Human Indoleamine 2,3-Dioxygenase

Thesis submitted for the degree of Doctor of Philosophy at the University of Leicester

by

Nektaria D. Papadopoulou, BSc Pharmaceutical Sciences, MSc Pharmaceutical & Analytical Sciences

Department of Chemistry
Faculty of Science
University of Leicester

July 2006

ProQuest LLC
789 East Eisenhower Parkway
P.O. Box 1346
Ann Arbor, MI 48106-1346

To Mum & Dad

Acknowledgements

I would like to thank my supervisor Dr. E. L. Raven for her guidance, support and help throughout the three years and Dr. B. Rawlings for helpful discussions on the progress of the project. Thanks also to Prof. A. W. Munro, Dr. K. J. McLean and Dr. H. E. Seward (University of Leicester, Biochemistry Department) for their expertise in redox potentiometry, magnetic circular dichroism (MCD) and electron paramagnetic resonance (EPR) spectroscopy. I would also like to thank Dr. R. Davydov (Northwestern University, Chemistry Department, Illinois) for his expertise in electron-nuclear double resonance (ENDOR) spectroscopy. I am also grateful to Dr. C. Metcalfe, Mr K. Singh, Dr. I. Macdonald, Dr. K. H. Sharp and Dr. M. Mewies for their assistance and encouragement. For financial support I am indebted to the BBSRC and the University of Leicester. Finally, I would like to thank my parents for their help and support.

Human Indoleamine 2,3-Dioxygenase

Nektaria D. Papadopoulou

Abstract

Indoleamine 2,3-dioxygenase (IDO) is a tryptophan degradation enzyme – it catalyses the oxidative cleavage of L-tryptophan to *N*-formylkynurenine – and is emerging as an important drug target. In this work, a bacterial expression system for human indoleamine 2,3-dioxygenase (rhIDO) has been developed and redox potentiometry, spectroscopy, kinetics and site directed mutagenesis have been used to characterise rhIDO and its substrate-binding properties.

Development of our understanding of the detailed mechanism of the IDO enzyme has been hampered by the limited quantities of pure enzyme that can be extracted from readily available sources. We have developed an efficient bacterial expression system for production of human IDO (hIDO) (Chapter 2) that utilizes a His-tag expression vector and have established reliable protocols for purification of the recombinant protein. In Chapter 3, we have used this expression system to examine the redox, spectroscopic and substrate-binding properties of the enzyme. The Fe^{3+}/Fe^{2+} reduction potential was found to be -30 ± 4 mV; in the presence of L-Trp, this value increases to $+ 16 \pm 3$ mV. Electronic, EPR and MCD spectroscopies indicate that ferric rhIDO (pH 6.6) exists as a mixture of six-coordinate, high-spin, water-bound heme and a low-spin species that contains a second nitrogenous ligand. There is an increase in the low-spin component at alkaline pH for rhIDO, but this is not due to hydroxide-bound heme. Substrate binding induces a conformational rearrangement and formation of low-spin, hydroxide-bound heme.

The role of two key histidine residues, H346A and H303A, was also examined in Chapter 4. Parallel spectroscopic, electrochemical and ligand binding analyses were consistent either with H303 as the sixth ligand or with H303 linked to a conformational change that affects the formation of the low-spin heme species. The first scenario is ruled out in light of the recently published crystal structure of rhIDO. Further analyses of the H303A variant indicated that this residue is not required for the formation of the low-spin, hydroxide-bound heme in the presence of substrate. The Fe^{3+}/Fe^{2+} reduction potential of H303A variant is $\approx$70 mV lower than that of rhIDO, leading to a destabilization of the ferrous-oxy complex , which is an obligate intermediate in the catalytic process (Chapter 4).

The detailed catalytic mechanism of IDO is still a matter of ongoing investigation. Although a structure for IDO is now available, the molecular details of substrate oxidation are still not defined. Mechanistic studies on the human or recombinant human enzyme have not been reported as yet. In Chapter 5, an investigation of the kinetic properties of rhIDO and the effects of pH and inhibitors and also spectroscopic studies on the obligate catalytic intermediates are presented for the first time.

Contents

Abbreviations

Amino Acids are abbreviated according to the three-letter codes recommended by the I.U.P.A.C Joint Commission on Biochemical Nomenclature (1985).

Enzymes

rIDO	rabbit indoleamine 2,3-dioxygenase
hIDO	human indoleamine 2,3-dioxygenase
rhIDO	recombinant human indoleamine 2,3-dioxygenase
TDO	tryptophan 2,3-dioxygenase
Mb	myoglobin
Hb	hemoglobin
HRP	horseradish peroxidase
DNase	deoxyribonuclease

Chemicals

Amp	ampicillin
DTT	dithiothreitol
dNTPs	deoxynucleotide triphosphates
EDTA	ethylenediaminetetraacetic acid
IPTG	isopropyl-β-D-thiogalactopyanoside
Kan	kanamycin
NTA	nitrilotriacetic acid
PMSF	phenylmethylsulphonyl fluoride
PVDF	polyvinylidene difluoride
SDS	sodium dodecyl sulphate
Tris	trizma base (tri[hydroxymethyl]aminomethane)
L-Trp	L-tryptophan

Techniques

CD	circular dichroism
ENDOR	electron nuclear double resonance
EPR	electron paramagnetic resonance
ESI-MS	electrospray ionisation mass spectrometry
FPLC	fast protein liquid chromatography
LB	Luria-Bertani broth
MALDI-Tof	matrix-assisted laser desorption ionisation – Time-of-flight
MCD	magnetic circular dichroism
NMR	nuclear magnetic resonance
PAGE	polyacrylamide gel electrophoresis
PCR	polymerase chain reaction
R_z	Reinheitzahl
SHE	standard hydrogen electrode
UV	ultra violet
Vis	Visible

Units/Symbols

A	Absorption
ε	absorption coeffecient
Å	Ångström (1 Å = 10^{-10} m)
°C	degrees Celcius
g	grams
kDa	kilo Daltons
l	litres
min	minutes
M	molar
rpm	revolutions per minute
mV	milliVolts
λ	wavelength

Miscellaneous

cDNA	complementary deoxyribonucleic acid
CT	charge transfer
E. coli	*Escherichia coli*
GVHD	graft *versus* host disease
IFN-γ	interferon gamma
IL-1α	interleukin alpha
ISRE	IFN-stimulable response element
MDL	Molecular Dimensions Ltd.
mRNA	messenger ribonucleic acid
NAD^+	nicotine adenine dinucleotide
$NADP^+$	nicotine adenine dinucleotide phosphate
PDB	Protein Data Bank
SOC	spin orbit coupling
TNF-α	tumor necrosis factor alpha

Chapter 1

Introduction

For many years it was generally assumed that the oxygen found in organic substances always came from water. A water molecule could be added to a double bond and the resulting alcohol dehydrogenated. Nevertheless, there were indications that small amounts of O_2 itself were essential, even to anaerobically growing cells (*1*). Prior to 1955, it was thought that the sole role of dioxygen in biological systems was an electron acceptor in dioxygen-utilizing oxidase or dehydrogenase reactions. In that year, Hayaishi *et al.* (*2*) and Mason *et al.* (*3*) independently demonstrated that ^{18}O – one or both oxygen atoms – was sometimes incorporated into organic compounds directly from $^{18}O_2$. Nowadays, a bewildering variety of oxygenases are known to function in forming essential metabolites such as sterols, prostaglandins, active derivatives of vitamin D, and amino acids. Thus, molecular oxygen in tissues serves two functions. One is to act as the ultimate hydrogen acceptor in the process of the biological oxidation of foodstuffs where the oxygen molecule is reduced to water, superoxide anion, or hydrogen peroxide. The other is the incorporation of molecular oxygen into dietary nutrients to yield cellular constituents or biologically active substances (*1*).

Hayaishi designated the enzymes that incorporate oxygen atoms from dioxygen as oxygenases. It is now known that oxygenases are extensively distributed in nature throughout the plant, animal, and microorganism kingdoms. The oxygenases can be further classified into two categories (*4*), monooxygenases and dioxygenases, depending on whether one or both the oxygen atoms from dioxygen are incorporated into the substrate (Figure 1.1). Monooxygenases require two electrons to reduce the second oxygen atom of dioxygen to water. The two electrons can come from a reducing agent like NADH (external monooxygenase) or from the substrate itself (internal monooxygenase). Similarly, dioxygenases are subcategorized into intermolecular and intramolecular varieties depending on whether the two oxygen atoms are incorporated into separate substrates or into a single molecule. Most dioxygenase enzymes require a metal cofactor (for reasons that are discussed in Section 1.2), which is most often Fe^{II} or Fe^{III}.

Monooxygenases

$S + O_2 + RedH_2 \Rightarrow SO + H_2O + Red$

Dioxygenases

$S + O_2 \Rightarrow SO_2$

Figure 1.1 Direct incorporation of molecular oxygen atoms into organic compounds. *S*, substrate; $RedH_2$, reductant.

This thesis is concerned with the biological oxidation of tryptophan. In biological systems, this reaction is the first and rate-limiting step in the kynurenine pathway (Figure 1.2). This is catalysed by two enzymes, namely tryptophan 2,3-dioxygenase (TDO) and indoleamine 2,3-dioxygenase (IDO). TDO was first isolated in 1937 (*5*) and IDO in 1967 (*6*) from rabbit small intestine. However, although there have been numerous functional studies on both TDO and IDO, structure/function investigations, in which the effect of protein structure on enzyme activity is examined, have not been possible. This is because: (a) there have been no efficient bacterial no efficient bacterial expression systems for either enzyme; and (b) because there are no structural data.

In this Chapter, the chemistry of dioxygen in relation to its biological activity is discussed and the information that is known about TDO and IDO and their relationships to other enzymes is summarised.

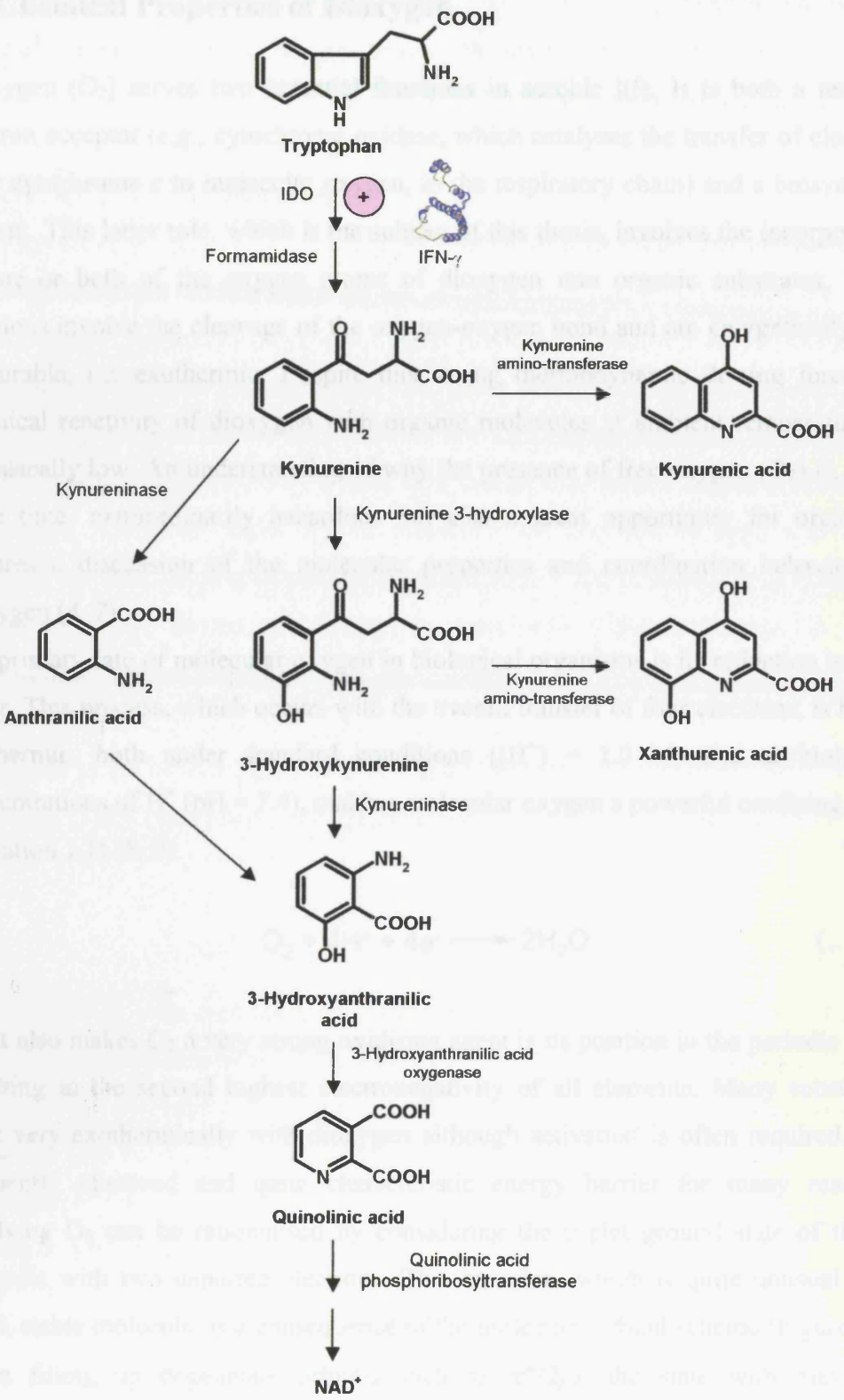

Figure 1.2 The kynurenine pathway of tryptophan degradation in mammalian cells.

1.1 Chemical Properties of Dioxygen

Dioxygen (O_2) serves two essential functions in aerobic life. It is both a terminal electron acceptor (*e.g.*, cytochrome oxidase, which catalyses the transfer of electrons from cytochrome *c* to molecular oxygen, in the respiratory chain) and a biosynthetic reagent. This latter role, which is the subject of this thesis, involves the incorporation of one or both of the oxygen atoms of dioxygen into organic substrates. These reactions involve the cleavage of the oxygen-oxygen bond and are energetically very favourable, *i.e.* exothermic. Despite this strong thermodynamic driving force, the chemical reactivity of dioxygen with organic molecules at ambient temperatures is intrinsically low. An understanding of why the presence of free oxygen (O_2) is, at the same time, extraordinarily hazardous but also a great opportunity for organisms requires a discussion of the molecular properties and coordination behaviour of dioxygen (*4, 7*).

The primary fate of molecular oxygen in biological organisms is its reduction to form water. This process, which occurs with the overall transfer of four electrons, is highly exothermic, both under standard conditions ($[H^+]$ = 1.0 M) and at biological concentrations of H^+ (pH = 7.4), making molecular oxygen a powerful oxidising agent (Equation 1.1) (*8, 9*).

$$O_2 + 4H^+ + 4e^- \longrightarrow 2H_2O \qquad (\ldots 1.1)$$

What also makes O_2 a very strong oxidising agent is its position in the periodic table, resulting in the second highest electronegativity of all elements. Many substances react very exothermically with dioxygen although activation is often required. This frequently observed and quite characteristic energy barrier for many reactions involving O_2 can be rationalised by considering the triplet ground state of the O_2 molecule with two unpaired electrons. This situation, which is quite unusual for a small, stable molecule, is a consequence of the molecular orbital scheme (Figure 1.3). When filling up degenerate orbitals such as $\pi^*(2p)$, the state with maximum multiplicity is favoured; in the case of dioxygen, triplet $^3O_2$ is favoured over singlet $^1O_2$ (*7*). In fact, $^3O_2$ with two unpaired electrons in the ground state is favoured over both singlet states $^1O_2$ ($^1\Delta$) and $^1O_2$ ($^1\Sigma$) by more than 90 and 150 kJ/mole, respectively (Figure 1.3).

Molecular oxygen is therefore a paramagnetic molecule (it is a diradical having two unpaired electrons). The two oxygen atoms share six electrons in their *2p* orbitals and the two unpaired electrons reside in the two antibonding $2p\pi x^*$ and $2p\pi y^*$ orbitals, leaving O_2 with a formal bond order of two (*8*). The lowest orbital available to accept an electron is an antibonding orbital.

Although dioxygen has a triplet ground state, essentially all stable organic compounds are singlets; *i.e.*, all of their electrons are paired. Direct reactions between the triplet and the singlet molecules to yield a singlet product are spin-forbidden because the chemical combination reaction rates are faster than spin inversion rates. Such reactions can proceed via the spin-allowed, but high energy formation of an unstable triplet intermediate, followed by a slow spin inversion to form a singlet product. The only easily oxidisable singlet organic molecules are thus able to react with triplet dioxygen by first forming resonance-stabilised (one-electron oxidised) radicals. For example, reduced flavins are thought to react with triplet dioxygen via initial formation of a caged radical pair (a triplet complex) followed by spin inversion to singlet products (*4, 10, 11*).

In contrast to the inherent difficulty of triplet dioxygen reacting with singlet organic molecules, it will react readily with organic radicals ($R^\bullet$), *i.e.* doublets (Equation 1.2).

$$R^\bullet + O_2 \longrightarrow RO_2^\bullet \qquad (\ldots 1.2)$$

Another way to overcome the high kinetic barrier inherent to the reactions of triplet O_2 is to utilise a transition metal ion such as iron or copper as the cofactor in enzymes that carry out biological oxidations. Transition metals in the appropriate oxidation states are able to react directly with triplet O_2 to form dioxygen adducts that can participate in reaction pathways leading either to the incorporation of oxygen atoms into organic substrates or to the oxidation of the organic substrates (*9*).

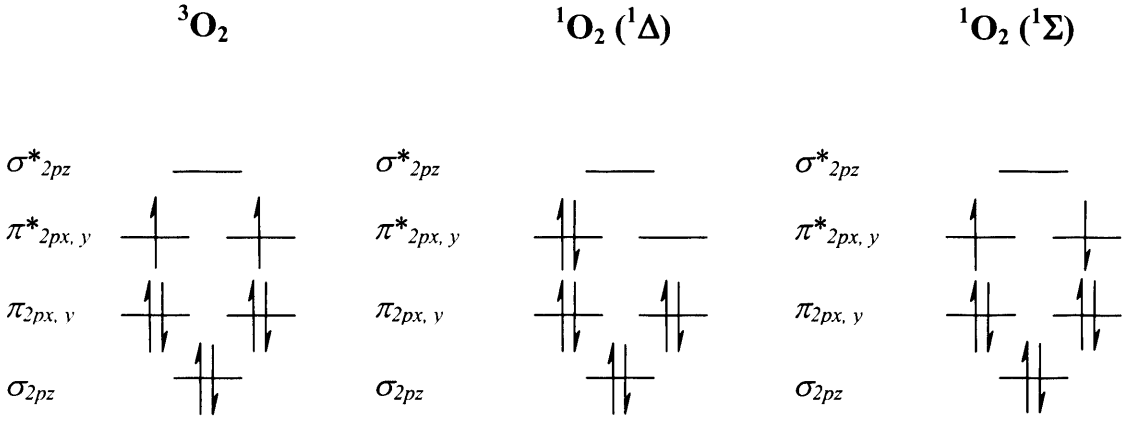

Figure 1.3 Molecular orbital diagrams for $^3O_2$, $^1O_2$ ($^1\Delta$) and $^1O_2$ ($^1\Sigma$).

1.2 Oxygen Activation by Metal Ions

There are many reasons why nature has chosen transition metals to transport, activate, and reduce O_2. First, most transition metals also contain unpaired electrons, allowing reactions with triplet O_2. Second, transition metals are relatively heavy atoms, which increases spin-orbit coupling (SOC), and thereby provide a quantum mechanical mechanism to change the spin-state of an electron. However, the SOC of the first-row transition metals is too small alone to allow for spin transitions. Third, transition metals often have several excited states with unpaired electrons close in energy to the ground state. This can also be used to enhance the probability of spin inversion (*12*). Transition metal ions, containing *3d* unpaired electrons, can use three strategies to activate dioxygen (*13*).

• *Orbital overlap with a metal ion.* Upon complexation of dioxygen to a transition metal ion containing unpaired *3d* electrons, the unpaired electrons in the dioxygen π^* orbitals are able to overlap with those on the metal ion (*8*). The reaction of such a transition metal-dioxygen with a singlet organic reagent is then allowed, provided that the overall number of unpaired electrons in the complex remains constant.

• *Single electron transfer.* The transition metals found in metallo-enzymes that activate dioxygen have two consecutive oxidation states (*e.g.* Fe^{II}/Fe^{III}, Cu^{I}/Cu^{II}), hence the metal centre is able to carry out single electron transfer to bound dioxygen. The $^3O_2$ oxygen ground state can accept a single electron to form superoxide – an allowed reaction – which is one possible route for oxygen activation. Superoxide can then participate in a variety of 1- or 2-electron chemical reactions (*14*).

A criticism of this route is that it is apparently energetically unfavourable. The reduction potential for the $O_2/O_2^{\bullet-}$ couple is -0.16 V in water at pH 7.0. The reduction potential for the Fe^{II}/Fe^{III} couple is +0.77 V. Therefore, the redox potential for the activation of dioxygen to superoxide by Fe^{II} is -0.93 V. However, the redox potentials for the Fe^{II}/Fe^{III} and dioxygen/superoxide couples in the metallo-enzyme would be dependent upon the particular microenvironment of the active site. It is also known that redox enzymes can strongly influence the redox potential of cofactors bound to their active sites, by selective stabilisation of the oxidised or the reduced form (*15*). Activation of dioxygen to superoxide has been observed in hemoglobin (*16*), and in EDTA-Fe^{III} complexes (*17*). Therefore, it is feasible that this route can be used by metallo-enzymes.

As already mentioned, single electron transfer to dioxygen can also take place from organic reagents which can access a stable radical intermediate. Thus, the reduced flavin cofactor found in flavoprotein hydroxylase enzymes is able to activate dioxygen via a single electron transfer to form a stable flavin semiquinone and superoxide, which then recombine to form a hydroperoxide intermediate (Figure 1.4, (*13*), (*18*)).

• *Reaction with a substrate radical.* Since the reaction of dioxygen via radical mechanisms is a spin-allowed process, reaction with a substrate radical is an alternative possible mechanism. It has been proposed that a substrate activation mechanism of this kind occurs in the intradiol catechol dioxygenases, where a bound catechol semiquinone intermediate attacks dioxygen to form a hydroperoxide radical (Figure 1.5, (*13*), (*19*)).

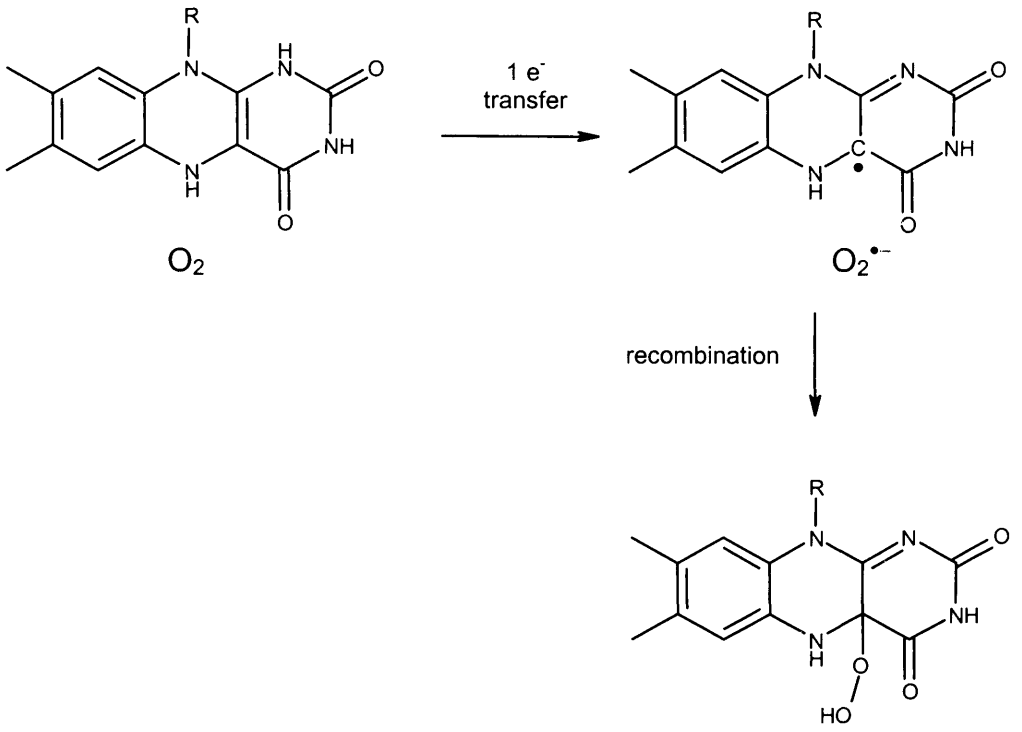

Figure 1.4 Activation of dioxygen by reduced flavin.

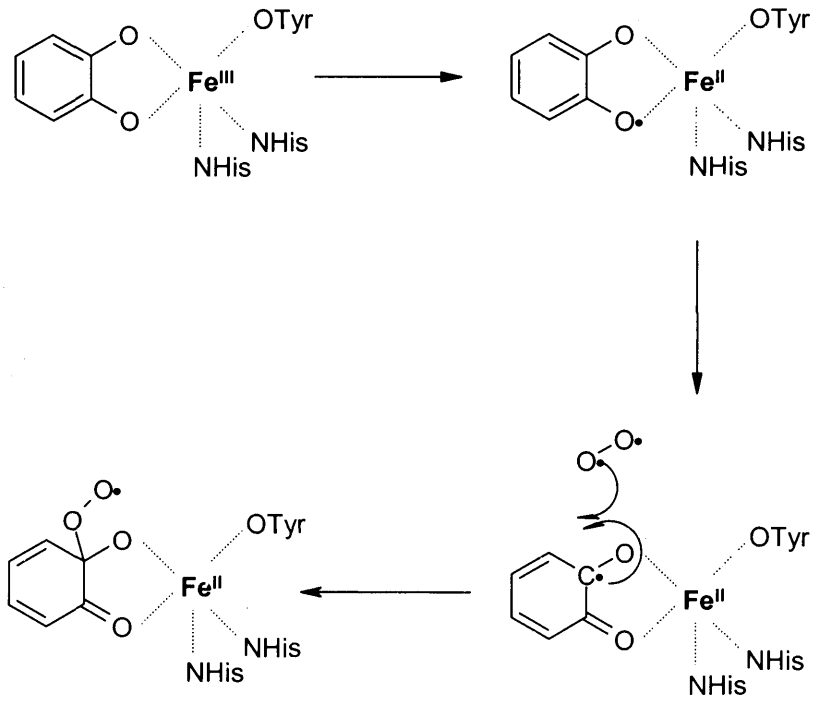

Figure 1.5 Substrate activation mechanism proposed for intradiol catechol cleavage.

1.3 Oxygen Activation by Iron

A lot of what we know about the intermediates involved in dioxygen activation comes from the studies of heme iron enzymes (those that contain iron in a porphyrin cavity). Examples include horseradish peroxidase and cytochrome P450 (*20-23*) and their synthetic analogues (*24*). The conjugated porphyrin ligand governs the pathways by which O_2 is activated. It makes low-spin states – an electronic arrangement in which most or all electrons on the metal ion are paired – accessible and stabilises highly oxidised iron intermediates.

The ligand environment in mononuclear nonheme iron enzymes, such as isopenicillin N synthase (*19*) and naphthalene dioxygenase, usually consists of a 2-histidine-1-carboxylate triad (*25*). The geometry is more flexible than that of the heme iron enzymes, allowing a more diverse chemistry. Low-spin states are less accessible in nonheme iron enzymes, and the formation of two accessible sites adjacent to one another is possible. These structural and electronic differences open up reaction pathways that are unavailable to heme iron (*19, 26, 27*). However, in general, the more reactive an intermediate, the more difficult it is to observe. As a result, very few of the intermediates shown in Figure 1.5 have been structurally characterised (*21*).

The widely accepted mechanism (*23*) of O_2 activation by heme iron enzymes (*21-23*) (Figure 1.6) involves the initial formation of a Fe^{II}-O_2 (A) or Fe^{III}-$O_2^{\bullet-}$ species, which converts to an end-on Fe^{III}-OOH (B) species upon addition of an electron. Alternatively, side-on peroxide may form (E) (*28*). Reduced iron (Fe^{II}) can react with oxygen to form potent biological oxidants. Borovic and colleagues showed that an oxidised Fe^{III}-O can be stabilised in a mononuclear nonheme environment by hydrogen bonds. Rohde *et al. (29)* report that Fe^{IV}=O (D) can also form in nonheme iron synthetic analogue.

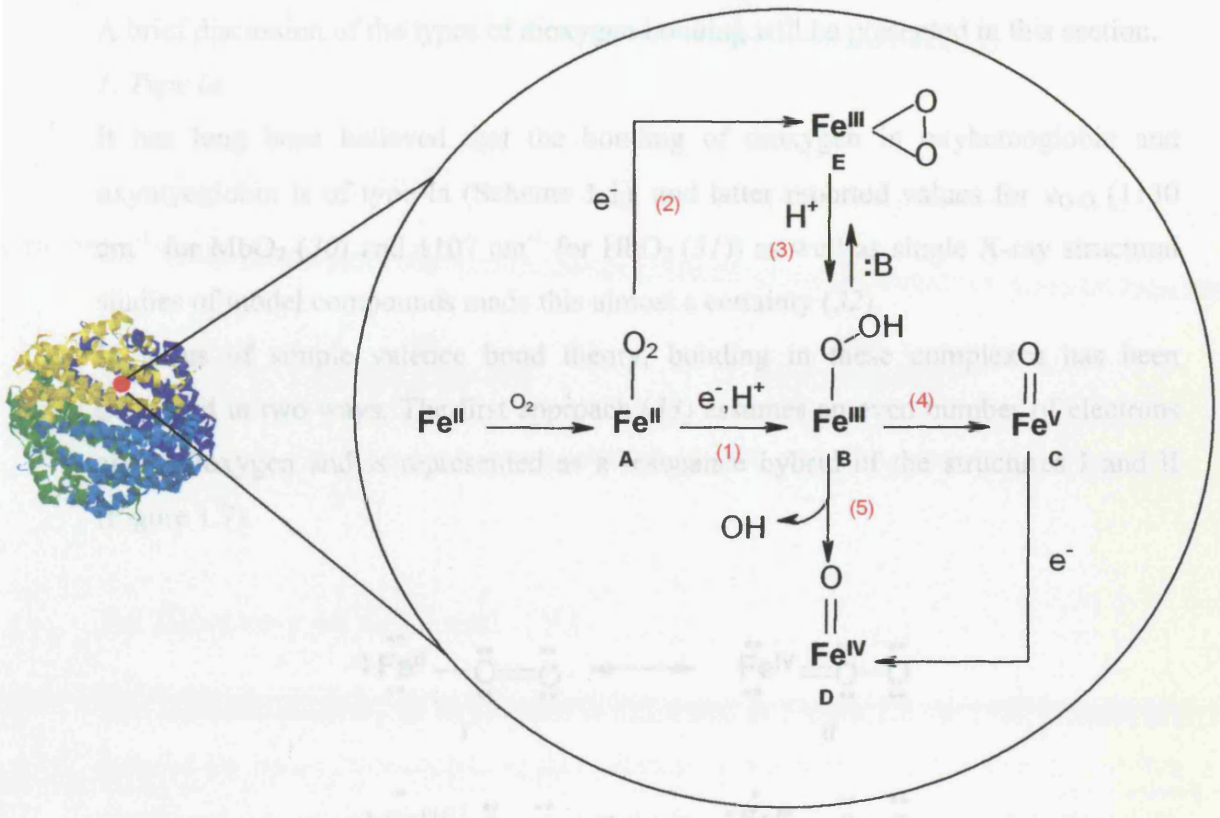

Figure 1.6 Mechanistic pathways available to iron in biology. Reduced iron (Fe^{II}) can react with oxygen to form potent biological oxidants. Proposed mechanistic pathways (1-5) and intermediates (A-E) are shown.

1.4 Nature of Bound Dioxygen

A brief discussion of the types of dioxygen bonding will be presented in this section.

1. Type Ia

It has long been believed that the bonding of dioxygen in oxyhemoglobin and oxymyoglobin is of type Ia (Scheme 1.1), and latter reported values for $\nu_{O\text{-}O}$ (1130 cm^{-1} for MbO_2 (*30*) and 1107 cm^{-1} for HbO_2 (*31*)) as well as single X-ray structural studies of model compounds made this almost a certainty (*32*).

In terms of simple valence bond theory, bonding in these complexes has been described in two ways. The first approach (*33*) assumes an even number of electrons about dioxygen and is represented as a resonance hybrid of the structures I and II (Figure 1.7).

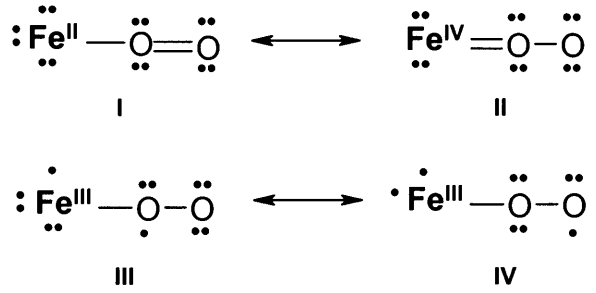

Figure 1.7 (A) Bonding of dioxygen in HbO_2, as proposed by Pauling. (B) Bonding of dioxygen in HbO_2, as proposed by Weiss.

The second approach (*34*) assumes an odd number of electrons on the coordinated dioxygen (structures III and IV, Figure 1.7). For either of these two structures, the metal is in a +3 oxidation state with the coordinated O_2 being formally $O_2^{\bullet-}$. For this bonding model, the unpaired spins on Fe^{III} and $O_2^{\bullet-}$ are reputedly coupled, thus allowing for the observed diamagnetism of the FeO_2 system.

2. Type IIa

Type IIa metal complexes (Scheme IIa), arising from the addition of O_2 to low-valent, coordinately unsaturated organometallic complexes (*e.g.*, $Cr(O_2)_4^{3-}$), have been recognised for many years. One major difference between this type of bonding and

the bonding observed in Ia complexes, is the coordination geometry, with the dioxygen being bound to the metal centre in a symmetric, triangular fashion, similar to that proposed by Griffith for the bonding of O_2 in oxyhemoglobin (*8*).

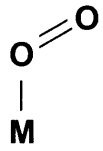

Ia
Superoxide-like

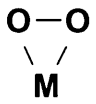

IIa
Peroxide-like

Scheme 1.1 Diagrammatic representation of Ia and IIa type metal-dioxygen complexes.

1.5 Discovery of TDO and IDO

The catabolic pathway of tryptophan is illustrated in Figure 1.2. In 1927 Kotake (*5*) isolated the major intermediate of this pathway, kynurenine, and the structure of this compound was established by Butenandt *et al.* in 1940 (*35*). The first enzymatic step, the formation of formylkynurenine, is the rate-limiting step in degradation of tryptophan. In 1936 Kotake and Masayama (*36*) isolated an enzyme that catalysed the conversion of tryptophan to formylkynurenine, and called it tryptophan pyrrolase. This enzyme was later called tryptophan 2,3-dioxygenase (TDO). The enzyme is found only in the liver, and is induced by administration of tryptophan. The TDO-catalysed oxidation reaction is the limiting step in tryptophan catabolism, as the formamidase was found to be in 600-fold excess. TDO concentration increases within several hours after administration of an active inducer, and returns to normal within 15-20 h after removal of the substance. TDO is induced by histidine and kynurenine, and to a lesser extent by tyrosine and phenylalanine. When large amounts of tryptophan, or tryptophan and hydrocortisone or hydrocortisone alone, are given to rats, the liver TDO activity increases from 5- to 10-fold over control levels. TDO was the first inducible enzyme system discovered in mammals (*37*).

It has been recognised for some time that elevated levels of various tryptophan metabolites can be found in the urine of patients suffering from a variety of diseases, such as rheumatoid arthritis, tuberculosis, leukaemia, Hodgkins disease, bladder

cancer, and prostrate disorders. However, TDO concentrations are not elevated in the liver in these patients. These findings suggested that TDO may not be the only enzyme initiating the catabolism of tryptophan (*38*). Kotake and Ito (*5*) found in 1937 that rabbits fed D-tryptophan excreted D-kynurenine in the urine (in 1980, hepatic tryptophan 2,3-dioxygenase in certain species of animals was found to cleave the pyrrole ring of the D-isomer, (*39*)). In 1950 Knox and Mehler (*37*) demonstrated that the primary product was formylkynurenine, and that a second enzyme, "formamidase", hydrolysed the formyl group of formylkynurenine to yield kynurenine and formic acid. Later, Tanaka and Knox (*40*) presented evidence that tryptophan pyrrolase is a hemoprotein containing protoporphyrin IX as its prosthetic group. In 1975, Hirata was able to demonstrate with the use of a heavy oxygen isotope ($^{18}O_2$) that molecular oxygen was directly incorporated into formylkynurenine (*41*).

In 1963, Hayaishi and colleagues isolated a second enzyme that catalysed conversion of tryptophan to kynurenine and in 1967, the same workers reported the discovery of an enzyme capable of oxidizing D-tryptophan to N-formyl-D-kynurenine in a homogenate of rabbit small intestine (*42, 6*). Unlike TDO, this enzyme is not found predominantly in the liver, but is distributed ubiquitously in nonhepatic organs of mammals, with the lung and placenta having the highest activities (*42, 43*). It has a wider spectrum of substrates than TDO and can utilise many indoleamine derivatives including L- and D-tryptophan, tryptamine, 5-hydroxytryptophan, and serotonin, and is therefore called indoleamine 2,3-dioxygenase (IDO) (Figure 1.8).

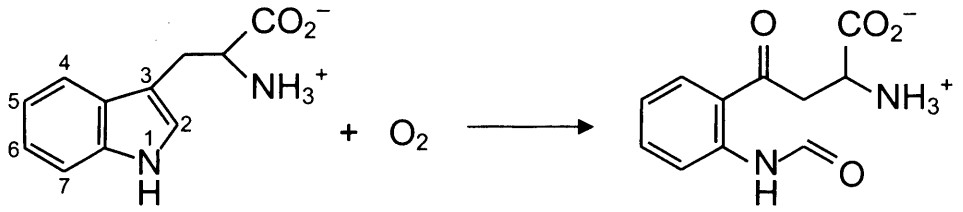

Tryptophan *N*-Formylkynurenine

Figure 1.8 Reaction catalysed by IDO, with IUPAC numbering indicated.

1.6 Distribution of IDO

IDO activity is distributed in various tissues of mammals such as rabbits, rats and mice, as reported by several workers.

In 1976, Hayaishi (*44*) reported that indoleamine 2,3-dioxygenase was ubiquitously distributed in almost all the rabbit tissues they have examined. The lowest value of IDO activity – with D and L-tryptophan as the substrate – was observed for the whole (rabbit) brain. Much higher activities were associated with the lower part of the intestine, the lung, and the colon. It should be emphasised that the observed activities were all dependent on superoxide anion for maximum activity and were inhibited by superoxide dismutase. In order to obtain further insight into the biological significance of this enzyme *in vivo*, Hayaishi and co-workers (*44*) investigated the metabolism of various indoleamines using tissue slices of intestine, perfusion of heart, and lung preparations, organ culture of pineal glands or direct infusion of radioactive substrates into the brains of intact animals. All these experiments supported the conclusion that this enzyme plays an important role in the metabolism and regulation of various indoleamines *in vivo*.

In 1985, Yamazaki *et al.* (*43*) presented a study undertaken to determine whether IDO exists in human beings. They have reported the presence and activity of IDO in various human tissues. The following Table 1 (*43, 44*), summarises the tissue distribution of IDO activity in human subjects. The indoleamine 2,3-dioxygenase activity was determined with various tissues of 9 human subjects, with L-tryptophan as substrate. Although there is considerable variation in the activity of each tissue, the activity was relatively high in the lung and small intestine, moderate in the spleen and stomach, and low in the other tissues. Activity in the nervous system could not be detected. IDO activity in the placenta was relatively high, but that in the umbilical cord and foetal membranes was low (<10 nmoles of kynurenine/ h / g of tissue). Unlike indoleamine 2,3-dioxygenase, tryptophan 2,3-dioxygenase – which, catalyses the same reaction as IDO – has been found, so far, only in the liver.

Table 1 Tissue distribution of indoleamine 2,3-dioxygenase activity in human subjects. [a] Activities were determined from 9 human subjects of various ages, sex and death cause, with L-tryptophan as substrate. The values listed above are average values form the 9 human subjects. * Activities were determined for the whole organ. – Not determined.

	Enzyme Activity (nmoles of kynurenine / h / g of tissue)	
Tissue	**Human[a]**	**Rabbit**
Brain	–	40
Colon*	33.40	1605×10^3
Epididymis	6.30	–
Heart	2.13	1000
Kidney*	50.22	8000
Lung	247.06	300×10^3
Pancreas	8.02	6000
Placenta	327.30	–
Rectum	3.00	15×10^3
Spleen	183.50	2000
Stomach*	20.98	1000

1.7 Involvement of IDO in Pathophysiological and Physiological Processes

There is a wealth of evidence linking IDO induction and kynurenine pathway metabolites to various physiological and pathophysiological conditions, including antimicrobial, antiviral, antiparasitic and antitumour activity, renal allograft rejection and various neurological disorders.

Before we discuss the involvement of IDO in these processes, it is important to remember some of the facts about tryptophan (Trp) (*45*):

(1) Trp provides a major part of niacinamide cofactors (NAD, NADP) for most animal species.

(2) Trp is essential for protein synthesis. Inadequate dietary intake of Trp (or any other essential amino acid) leads quickly to negative nitrogen balance, weight loss (mostly muscle mass) and possibly death.

(3) If any one essential amino acid is absent at the time it is needed for protein synthesis on the ribosome, the whole process of peptide synthesis is stopped, the incomplete peptide is rejected from the ribosome and the ribosome complex is disrupted. Provision of the deficient amino acid a few minutes after is needed does not restore protein synthesis.

(4) Significant re-utilisation of Trp occurs. Estimates of total protein synthesis per day suggests that 5 to 10 times more Trp is incorporated into protein than is provided by the daily requirement for Trp. Therefore, a large percentage of Trp released from breakdown of cells and proteins is usually reutilised.

The discovery of the kynurenine-niacin pathway and the description of liver Trp dioxygenase and its induction by glucocorticoids and stabilization by elevated Trp levels were helpful in trying to interpret early findings of elevated metabolite levels in a variety of apparently unrelated clinical conditions. However, the findings of a second enzyme which could also initiate the kynurenine pathway, namely indoleamine 2,3-dioxygenase (IDO) (*42, 43*), and many elegant studies showing that IDO was highly inducible by interferon-γ (IFN-γ) (*46-50*) (Figure 1.9), suddenly permitted new interpretations of much of the clinical data: infection, inflammatory processes, immune stimulation and any type which could induce production resulted in IDO induction and enhanced catabolism along the kynurenine pathway (*51*).

In contrast to the relatively simple Trp-metabolising role of hepatic TDO, which initiates the kynurenine pathway leading to the formation of pyridine nucleotide coenzyme (NAD), several possible physiological roles for IDO have been suggested. Most significantly, it is associated with the antiviral and antiproliferative activities of IFN-γ). Interferon γ (IFN-γ), a cytokine produced by activated T lymphocytes and natural killer cells, plays a vital role in host-cell defense against a variety of nonviral microbial pathogens, regulates immune responses, and inhibits cell growth (*52*). IFN-γ induces the synthesis of a number of gene products in cells. Several of the induced gene products have been implicated in the IFN-γ-mediated resistance to microbial infection (*Chlamydia psittaci, Taxoplasma gondii*) (*53, 54*). This includes the production of nitric oxide synthase, activation of macrophages, and starvation of tryptophan due to induction of IDO enzyme, which catalyses the first step in tryptophan degradation.

Although IFN-γ is the most potent inducer of IDO activity, other cytokines probably act, either directly or in combination with IFN-γ, to promote enzyme expression, *e.g.* interferon-α, interleukin-1α and tumor necrosis factor-α.

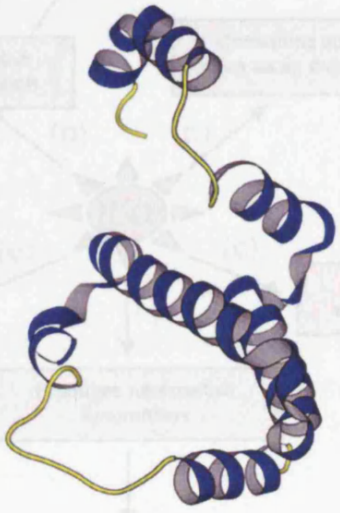

Figure 1.9 X-ray structures of IFN-γ (monomer) (1HIG). PDB ID number is shown in parentheses.

Tryptophan is a constituent for most proteins. In parallel, this amino acid represents a precursor for mainly two pivotal biochemical pathways: the generation of serotonin – a vasoconstrictor and a neurotransmitter that is also degraded by IDO – and the IDO-catalysed formation of a series of biologically active metabolites, referred to as kynurenines (*55*) (Figure 1.2). The enhanced activity of IDO along the kynurenine pathway must have a negative effect on the serotonin pathway. Indeed many patients receiving IFN-γ may develop evidence of depression, dementia as well as fatigue and weakness, conditions not uncommon in other conditions having enhanced immune system activity such AIDS (*56, 57*), infection, autoimmune diseases (*e.g.* organ transplant rejection, graft *versus* host disease (GVHD) (*45, 58*)) and related conditions (*45*).

The following Figure (Figure 1.10, modified from (*55*)) describes the multiplicity of effects of IDO induction and its possible role in pathophysiological conditions.

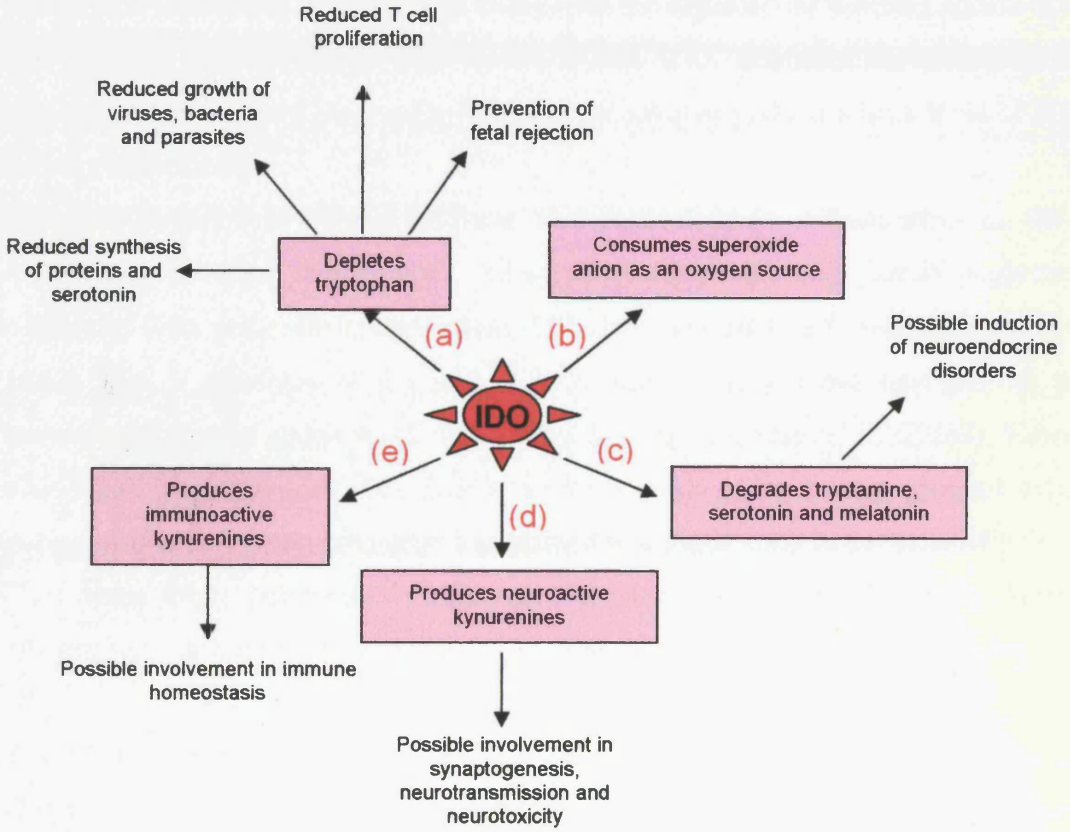

Figure 1.10 Multiplicity of effects of IDO induction and possible role in pathophysiological conditions. The scheme depicts the various physiological functions of the essential amino acid tryptophan, the possible consequences of its depletion, the effects of IDO activity on indole derivatives other than tryptophan and the postulated biological functions of tryptophan breakdown products (kynurenines).

In summary (Figure 1.10), by catalyzing the oxidative cleavage of the indole ring of tryptophan and thus depleting this essential amino acid, IDO impairs protein and serotonin biosynthesis, and limits microbial growth, and affects T cell proliferation, with possible implications in cell-mediated immune responses (Figure 1.10 (a)). As a consequence of inflammation, superoxide anion is liberated and serves as a substrate for IDO, and possibly at the maternal-fetal interface, clearance of free-radicals and inhibition of the serotonin vasoactive properties could represent a common, protective mechanism (Figure 1.10 (b)). Also, as previously mentioned, IDO acts on a variety of indole derivatives hence affecting the biology of important regulatory molecules, including, tryptamine, serotonin and melatonin, with potential implications for neuroendocrine functions (Figure 1.10 (c)). Tryptophan degradation leads to the formation of kynurenines, which display neuroactive and neurotoxic properties (Figure 1.10 (d)). Finally, selected kynurenines also exhibit immunoactive properties and could contribute to the control of immune homeostasis (*55*).

1.8 IDO and TDO cDNAs, Gene Structure of IDO and Bacterial Expression

The cDNA of human IDO was published in 1989 by Tone *et al.* (*59*) (Figure 1.11) and the primary structure of human IDO was deduced from sequences of cDNA clones. The open reading frame is 1209 nucleotides in length and encodes a protein containing 403 residues and having a molecular weight of 45,324 Da. A year later, Dai and Gupta (*60*), also reported the isolation of a cDNA clone of IDO (called C42). Its nucleotide sequence revealed an open reading frame coding for a polypeptide of 403 amino acids, which showed no homology with any known gene in the GenBank database.

In 1991, Habara-Ohkubo *et al.* (*61*) reported the isolation of cDNA clones encoding mouse IDO. The mouse IDO cDNA encodes a 407 amino acid protein with a molecular weight of 45,639 Da. The deduced amino acid sequence agreed with partial amino acid sequences derived from endopeptidase digestion of purified mouse IDO and revealed 61% homology with that of human IDO. Transient expression of the mouse IDO cDNA in COS-7 cells (bovine papillovirus) yielded a high level of IDO activity in the cells.

The gene structure of human IDO was also determined (*62*), from genomic DNA clones that encoded human IDO. Their restriction maps and partial nucleotide sequences were determined. The human IDO gene spanned 15 kilobase pairs with ten exons. The 5' terminus of the IDO mRNA was 33 nucleotides upstream of the translation initiation codon ATG. The 5' flanking region contained ISRE (*63*), X-box, and Y-box like sequences (*64*). Southern blot analysis of the human genomic DNA indicated that the human IDO gene was present in a single copy in the genome.

Two years later, polymerase chain reaction experiments carried out by Tone's laboratory, indicated that the human IDO gene could be assigned to chromosome 8 (*65*).

The complete amino acid sequence of rat liver TDO was reported by Maezono *et al.* (Figure 1.12) (*66*). According to the deduced amino acid sequence, the monomeric polypeptide of TDO consisted of 406 amino acid residues with a calculated molecular weight of 47,796 Da. It has 12 histidine residues around its hydrophobic region, which has homology with some heme proteins, suggesting that this hydrophobic region might be the core of TDO for the activity.

```
atggcacacgctatggaaaactcctggacaatcagtaaagagtaccatattgatgaagaa  60
taccgtgtgcgataccttttgaggacctgttagtcatttctcatggtataactacttctt
M  A  H  A  M  E  N  S  W  T  I  S  K  E  Y  H  I  D  E  E    20

gtgggctttgctctgccaaatccacaggaaaatctacctgatttttataatgactggatg  120
cacccgaaacgagacggtttaggtgtccttttagatggactaaaaatattactgacctac
V  G  F  A  L  P  N  P  Q  E  N  L  P  D  F  Y  N  D  W  M    40

ttcattgctaaacatctgcctgatctcatagagtctggccagcttcgagaaagagttgag  180
aagtaacgatttgtagacggactagagtatctcagaccggtcgaagctctttctcaactc
F  I  A  K  H  L  P  D  L  I  E  S  G  Q  L  R  E  R  V  E    60

aagttaaacatgctcagcattgatcatctcacagaccacaagtcacagcgccttgcacgt  240
ttcaatttgtacgagtcgtaactagtagagtgtctggtgttcagtgtcgcggaacgtgca
K  L  N  M  L  S  I  D  H  L  T  D  H  K  S  Q  R  L  A  R    80

ctagttctgggatgcatcaccatggcatatgtgtggggcaaaggtcatggagatgtccgt  300
gatcaagaccctacgtagtggtaccgtatacacaccccgtttccagtacctctacaggca
L  V  L  G  C  I  T  M  A  Y  V  W  G  K  G  H  G  D  V  R   100

aaggtcttgccaagaaatattgctgttccttactgccaactctccaagaaactggaactg  360
ttccagaacggttctttataacgacaaggaatgacggttgagaggttctttgaccttgac
K  V  L  P  R  N  I  A  V  P  Y  C  Q  L  S  K  K  L  E  L   120

cctcctattttggtttatgacgactgtgtcttggcaaactggaagaaaaaggatcctaat  420
ggaggataaaaccaaatacgtctgacacagaaccgtttgaccttctttttcctaggatta
P  P  I  L  V  Y  A  D  C  V  L  A  N  W  K  K  K  D  P  N   140

aagcccctgacttatgagaacatggacgttttgttctcatttcgtgatggagactgcagt  480
ttcggggactgaatactcttgtacctgcaaaacaagagtaaagcactacctctgacgtca
K  P  L  T  Y  E  N  M  D  V  L  F  S  F  R  D  G  D  C  S   160

aaaggattcttcctggtctctctattggtggaaatagcagctgcttctgcaatcaaagta  540
tttcctaagaaggaccagagagataaccacctttatcgtcgacgaagacgttagtttcat
K  G  F  F  L  V  S  L  L  V  E  I  A  A  A  S  A  I  K  V   180

attcctactgtattcaaggcaatgcaaatgcaagaacgggacactttgctaaaggcgctg  600
taaggatgacataagttccgttacgtttacgttcttgccctgtgaaacgatttccgcgac
I  P  T  V  F  K  A  M  Q  M  Q  E  R  D  T  L  L  K  A  L   200

ttggaaatagcttcttgcttggagaaagcccttcaagtgtttcaccaaatccacgatcat  660
aacctttatcgaagaacgaacctctttcgggaagttcacaaagtggtttaggtgctagta
L  E  I  A  S  C  L  E  K  A  L  Q  V  F  H  Q  I  H  D  H   220

gtgaacccaaaagcatttttcagtgttcttcgcatatatttgtctggctggaaaggcaac  720
cacttgggttttcgtaaaaagtcacaagaagcgtatataaacagaccgacctttccgttg
V  N  P  K  A  F  F  S  V  L  R  I  Y  L  S  G  W  K  G  N   240

ccccagctatcatacggtctggtgtatgaagggttctgggaagacccaaaggagtttgca  780
ggggtcgatagtctgccagaccacatacttcccaagacccttctgggtttcctcaaacgt
P  Q  L  S  D  G  L  V  Y  E  G  F  W  E  D  P  K  E  F  A   260

gggggcagtgcaggccaaagcagcgtctttcagtgctttgacgtcctgctgggcatccag  840
cccccgtcacgtccggtttcgtcgcagaaagtcacgaaactgcaggacgacccgtaggtc
G  G  S  A  G  Q  S  S  V  F  Q  C  F  D  V  L  L  G  I  Q   280

cagactgctggtggaggacatgctgctcagttcctccaggacatgagaagatatatgcca  900
gtctgacgaccacctcctgtacgacgagtcaaggaggtcctgtactcttctatatacggt
Q  T  A  G  G  G  H  A  A  Q  F  L  Q  D  M  R  R  Y  M  P   300

ccagctcacaggaacttcctgtgctcattagagtcaaatccctcagtccgtgagtttgtc  960
ggtcgagtgtccttgaaggacacgagtaatctcagtttagggagtcaggcactcaaacag
P  A  H  R  N  F  L  C  S  L  E  S  N  P  S  V  R  E  F  V   320

ctttcaaaaggtgatgctggcctgcgggaagcttatgacgcctgtgtgaaagctctggtc  1020
gaaagttttccactacgaccggacgcccttcgaatactgcggacacactttcgagaccag
L  S  K  G  D  A  G  L  R  E  A  Y  D  A  C  V  K  A  L  V   340

tccctgaggagctaccatctgcaaatcgtgactaagtacatcctgattcctgcaagccag  1080
agggactcctcgatggtagacgtttagcactgattcatgtaggactaaggacgttcggtc
S  L  R  S  Y  H  L  Q  I  V  T  K  Y  I  L  I  P  A  S  Q   360

cagccaaaggagaataagacctctgaagacccttcaaaactggaagccaaaggaactgga  1140
gtcggtttcctcttattctggagacttctgggaagttttgaccttcggtttccttgacct
Q  P  K  E  N  K  T  S  E  D  P  S  K  L  E  A  K  G  T  G   380

ggcactgatttaatgaatttcctgaagactgtgagaagtacaactgagaaatccctttg  1200
ccgtgactaaattacttaaaggacttctgacactcttcatgttgactctttagggaaaac
G  T  D  L  M  N  F  L  K  T  V  R  S  T  T  E  K  S  L  L   400

aaggaaggttaa                                                  1209
ttccttccaatt
K  E  G  *                                                     403
```

Figure 1.11 Nucleotide sequence of the gene encoding human IDO, together with the corresponding amino acid sequence. Nucleotide (italics) and amino acid (bold italics) are shown at the end of each line. The final stop codon is indicated with a *.

```
atgagtgggtgcccattttcaggaaacagtgtaggatatactttgaaaaacttatctatg   60
M  S  G  C  P  F  S  G  N  S  V  G  Y  T  L  K  N  L  S  M     20

gaagacaatgaagaagacggagctcaaactggtgtaaacagagccagcaaaggaggactt  120
E  D  N  E  E  D  G  A  Q  T  G  V  N  R  A  S  K  G  G  L     40

atctatggggactacttgcagttggagaagattttgaatgcacaagaacttcaaagtgaa  180
I  Y  G  D  Y  L  Q  L  E  K  I  L  N  A  Q  E  L  Q  S  E     60

atcaaagggaataaaatccacgacgagcacctctttattataactcaccaagcttatgaa  240
I  K  G  N  K  I  H  D  E  H  L  F  I  I  T  H  Q  A  Y  E     80

ctttggtttaaacaaattctctgggaacttgattctgttcgtgagatttttcaaaatggc  300
L  W  F  K  Q  I  L  W  E  L  D  S  V  R  E  I  F  Q  N  G    100

catgtcagggatgagaggaacatgctcaaggtgatgactcggatgcaccgtgtggtggtc  360
H  V  R  D  E  R  N  M  L  K  V  M  T  R  M  H  R  V  V  V    120

atcttcaagctcctggtacagcagttctcggttctggaaacaatgactgccttggacttc  420
I  F  K  L  L  V  Q  Q  F  S  V  L  E  T  M  T  A  L  D  F    140

aatgacttcagagagtacctgtctccagcatcaggcttccagagtcttcagttccggctg  480
N  D  F  R  E  Y  L  S  P  A  S  G  F  Q  S  L  Q  F  R  L    160

ctagaaaataagataggtgttcttcagagcttgagagtcccttacaacaggaaacactat  540
L  E  N  K  I  G  V  L  Q  S  L  R  V  P  Y  N  R  K  H  Y    180

cgtgataactttgaaggagactacaatgagctgctgctgaaatcggagcaggagcagacg  600
R  D  N  F  E  G  D  Y  N  E  L  L  L  K  S  E  Q  E  Q  T    200

ctattgcagctggtggaggcatggctggaacgcacacctggcttagagccacatggattc  660
L  L  Q  L  V  E  A  W  L  E  R  T  P  G  L  E  P  H  G  F    220

aatttctggggaaagtttgaaaaaaatatcttgaagggtctggaagaggagttcctaaag  720
N  F  W  G  K  F  E  K  N  I  L  K  G  L  E  E  E  F  L  K    240

attcaggcgaaaaaggactctgaagaaaaagaggaacagatggcagagttccggaagcag  780
I  Q  A  K  K  D  S  E  E  K  E  E  Q  M  A  E  F  R  K  Q    260

aaagaggtgctgctctgcttgttcgatgagaagcgtcatgactaccttctgagtaaaggt  840
K  E  V  L  L  C  L  F  D  E  K  R  H  D  Y  L  L  S  K  G    280

gaacgacgactgtcataccgtgcactccagggagcactgatgatatatttttacagggag  900
E  R  R  L  S  Y  R  A  L  Q  G  A  L  M  I  Y  F  Y  R  E    300

gagcctcgattccaggtccctttccagttgctgacctcacttatggacattgacacactc  960
E  P  R  F  Q  V  P  F  Q  L  L  T  S  L  M  D  I  D  T  L    320

atgaccaaatggagatataatcatgtgtgcatggtgcacaggatgctaggcagcaaggct 1020
M  T  K  W  R  Y  N  H  V  C  M  V  H  R  M  L  G  S  K  A    340

ggcactgggggatcctcaggctattattatctgcgctcaactgtgagcgacaggtacaag 1080
G  T  G  G  S  S  G  Y  Y  Y  L  R  S  T  V  S  D  R  Y  K    360

gtgttcgtggatttatttaacctctcatcgtacctggttccccgacactggataccaaag 1140
V  F  V  D  L  F  N  L  S  S  Y  L  V  P  R  H  W  I  P  K    380

atgaatccgatcattcacaagttcctttacacagctgagtacagcgacagctcctacttc 1200
M  N  P  I  I  H  K  F  L  Y  T  A  E  Y  S  D  S  S  Y  F    400

agcagcgatgaatcagattaa                                        1218
S  S  D  E  S  D  *                                            406
```

Figure 1.12 Nucleotide sequence of rat TDO cDNA and the deduced amino acid sequence. Nucleotide (italics) and amino acid (bold italics) are shown at the end of each line. The final stop codon is indicated with a *.

Recombinant expression systems for both rat liver TDO and human IDO have been reported. Rat liver TDO was first over-expressed in *E. coli* in 1996 by Ren *et al.* (*67*), TDO cDNA was incorporated into a pTrc99A expression vector, after introduction of convenient restriction sites, and it was also codon optimized for bacterial expression. DH5aF' strain of *E. coli* cells were transfected with this pTrc99A/TDO construct and expressed soluble, functionally active, tetrameric TDO protein in high yields.

The human IDO enzyme was expressed in *E. coli* EC538 containing the pQE9-IDO (histidine-tag expression vector) and pREP4 plasmids (*68*). IDO was expressed in high yields and purified to homogeneity in terms of electrophoretic and mass spectroscopic analysis, by a combination of phosphocellulose and nickel-agarose affinity chromatography.

The amino acid sequence of human IDO is aligned with that of human TDO, and the amino acid sequence identity (~ 16%) is shown in Figure 1.13.

```
hIDO                                    MAHAMENSWTISKEYHIDE
                                           |           |
hTDO  MSGCPFLGNNFGYTFKKLPVEGSEEDKSQTGVNRASKGGLIYGNYLHLEK

EVGFALPNPQENLPD-----FYNDWMFIAKH---------------LPD
      | ||              ||  |
VL-----NAQELQSETKGNKIHDEHLFIITHQAYELWFKQILWELDSVRE

LIESGQLRERVEKLNMLSIDHLTDHKSQRLARLVLGCITMAYVWGKGHGD
    |  |      |||         |  |  ||               |
IFQNGHVR---DERNMLKVVSRMHRVSVILKLLVQQFSILETMTALDFND

VRKVLPRNIAVPYCQLSKKLELPPILVYADCVLANWKKKDPNKPLTYENM
 |  |         |    ||                    ||     ||
FREYLSPASGFQSLQF-RLLE-------------------NKIGVLQNM

DVLFS---FRDGDCSKGFFLVSLLVEIAAASAIKVIPTVFKAMQMQERDT
 |       ||                            ||     |
RVPYNRRHYRDN--------------------------FKG---EENEL

LLKA-----LLEIASC-LEKALQVFHQIHDHVNPKAFFSVLRIYLSGW-K
|||      |||     ||              |  |          | |
LLKSEQEKTLLELVEAWLERT--------PGLEPHGF--------NFWGK

GNPQLSDGLVYEGFWEDPKEFAGGSAGQSSVFQ-CFDVLLGIQQTAGGGH
       ||  |      ||       |   ||    |||
LEKNITRGLEEEFIRIQAKEESEEKEEQVAEFQKQKEVLLS---------

AAQFLQDMRRYMPPAHRNFLCSLESNPSVREFVLSKGDAGLREAYDACVK
    | |  |                   |  ||||    |  | |
----LFDEKRH------------------EHLLSKGER--RLSYRALQG

ALVSLRSYHLQIVTKYILIPASQQPKENKTS-EDPSKLEAK---------
||             |   |  | |    ||  |   |  |
AL---------MIYFYREEPRFQVPFQLLTSLMDIDSLMTKWRYNHVCMV

--------GTGGTDLMNFLKTVRSTTEKSLLKEG            403
        ||||      |    |   |
HRMLGSKAGTGGSSGYHYLRSTVSDRYKVFVDLFNLSTYLIPRHWIPKMN


PTIHKFLYTAEYCDSSYFSSDESD                        ...
```

Figure 1.13 Sequence alignment of human IDO and human TDO. Amino acid residues conserved in the two sequences are indicated with a vertical line (|).

1.9 Similarities of IDO with TDO and Myoglobin

1.9.1 Similarities and Differences between the Two Dioxygenases

Both IDO and TDO are cytosolic (soluble) heme proteins that catalyse the conversion of L-Trp to N-formylkynurenine (Figure 1.9), the first and rate limiting step of the kynurenine pathway of L-Trp metabolism (Figure 1.7) (*1, 44*). Unlike TDO, IDO is not found predominantly in the liver, but is distributed ubiquitously in nonhepatic organs of mammals, with the lung and placenta having the highest activities. TDO has also been isolated from *Pseudomonas acidovorans*. IDO has a wider spectrum of substrates than TDO and can utilise many indoleamine derivatives including L- and D-Trp, tryptamine, 5-hydroxytryptophan and serotonin (5-hydroxytryptamine) (*42, 44, 69*). In terms of V_{max} and specificity constant (V_{max}/K_M), the other tryptophan derivatives are much poorer substrates than Trp. Since substrates for this dioxygenase must have the α-amino group of Trp, it was designated "indoleamine 2,3-dioxygenase" by Hayaishi (*42, 43, 69*).

Although both dioxygenases catalyse the same reaction, they are otherwise distinct (Table 2, modified from (*4*)). IDO uses superoxide anion and differs from TDO not only in organ distribution but in molecular weight (*37, 70*). Copper, once thought to be one of the cofactors for TDO, is not required for activity (*71*).

Table 2. Comparison of IDO and TDO.

Properties	IDO	TDO
Mol wt	45 000	191 000 (liver) 122 000 (*Pseudomonas*)
Subunits	1	4 (α_4 or $\alpha_2\beta_2$)
Carbohydrate	4.8%	None
Prosthetic group	Protoheme IX (1/molecule)	Protoheme IX (2/tetramer)
Oxygen source	O_2 (and $O_2^{\cdot-}$)	O_2
Substrates	L- and D-tryptophan, 5-hydroxy-L- and D-tryptophan, tryptamine, serotonin.	L-tryptophan (and D-tryptophan)
Turnover no. for L-Trp (s^{-1})	2	7 (liver), 17 (*Pseudomonas*)
Distribution		
- mammals	Ubiquitous (except liver)	Liver
- bacteria	None	*Pseudomonas acidovorans*
Inducers	Influenza virus, lipopolysaccharide, interferon γ	Tryptophan, tyrosine, histidine, phenylalanine, kynurenine, glucocorticoid, hydrocortisone

Both IDO and TDO are heme containing proteins, having protoheme IX, as the catalytic centre. Another notable distinction between these two dioxygenases is the cofactor requirement. Several non-specific reductants such as ascorbic acid, borohydride, and hydrogen peroxide can serve as reductive activators for TDO *in vitro* (*72*). These activators are required only to initiate the catalytic reaction by reducing the ferric (inactive) form; an autoxidation product that is probably a nonphysiological artefact in vitro, to the ferrous (active) form of TDO. On the other hand, IDO is highly autoxidisable, especially in the presence of O_2 and indoleamine substrates (*73*). Thus the dioxygenase requires superoxide anion ($O_2^{\bullet-}$) or a reductant such as ascorbic acid in either case in combination with methylene blue (or toluidine blue), an artificial dye, as cofactors *in vitro* (*74*). These cofactors are required not only to initiate but also to maintain the apparent maximal catalytic activity (*73, 75*). As candidates for the natural cofactor for IDO, tetrahydrobiopterin and dihydroriboflavin mononucleotide ($FMNH_2$) have been suggested (*76*). In 1989, a study by Sono (*72*)

on the activation mechanism of IDO has also suggested the presence of a physiological cofactor or cofactor system (xanthine oxidase-hypoxanthine) instead of $O_2^{\bullet-}$ or in combination with $O_2^{\bullet-}$. Thus, it is quite likely that such cofactor molecule would bind to the enzyme at a specific site. *In vitro*, catalase is required to protect the enzyme from hydrogen peroxide (H_2O_2), which is generated by the reducing system (*43*).

The amino acid sequence of rat liver TDO has been determined from its cDNA, and its molecular structure has been revealed to be that of a homotetramer, and it contains two protoheme IX per molecule (*66*). IDO is monomeric, and it has also been isolated and purified from human placenta (*70*) and mouse epididymims (*76*), and the amino acid sequences have been determined for the enzymes form these sources. The catalytic properties and substrate specificity of IDO from these sources are similar.

IDO can also been distinguished from TDO on the basis of antigenicity. Unlike TDO, IDO is not induced *in vivo* in lungs of mice by lipopolysaccharide (LPS) (*46*) or virus, by IFN-γ (*77*), and to a lesser extent by rHu-IFN-α A/D and a tumor necrosis factor (TNF) (*78*). *In vitro* studies have shown that all classes of IFN (α, β and γ) can induce IDO.

In contrast to a relatively simple Trp-metabolising role of hepatic TDO which initiates the kynurenine pathway leading to the formation of pyridine nucleotide coenzyme (NAD), several possible physiological roles for IDO have been suggested (these have already been discussed in section 1.7).

1.9.2 A Myoglobin Evolved from Indoleamine 2,3-Dioxygenase

It is well known that during evolution three types of respiratory proteins that can bind oxygen reversibly appeared. These are globins (myoglobin, hemoglobin), hemocyanin and hemerythrin. An organism usually expresses one of the three oxygen-binding proteins. Co-expression occurs rarely. The crystal structures of the three oxygen-binding proteins are quite different, implying that all three evolved from distinctly different ancestors. Globins carry a heme group: protoheme IX. The dioxygen binds to the sixth coordination site of the heme iron. On the other hand, hemocyanin and hemerythrin do not carry a heme group, and the oxygen binds directly to copper or iron atoms coordinated to amino acid side chains of the protein moiety (*79, 80*).

Most globins are composed of 140-160 amino acids (M_r 15-18 kDa). Although the amino acid sequence homology between the distantly-related globins is low – the amino acid identity between sperm whale and *Aplysia* myoglobins is about 25% – they have a very similar three-dimensional structures (the so-called myoglobin fold) (Figure 1.14) (*81*). An accidental evolutionary event of two or more duplications of a globin gene followed by their fusion sometimes results in a multidomain globin as seen in a blood clam, *Barbatia*, two-domain globin (M_r 32 kDa) (*82*), and a brine shrimp, *Artemia*, nine-domain globin (M_r 135 kDa) (*83*). These globins show no significant amino acid sequence homology with the usual globins composed of 140 to 160 residues.

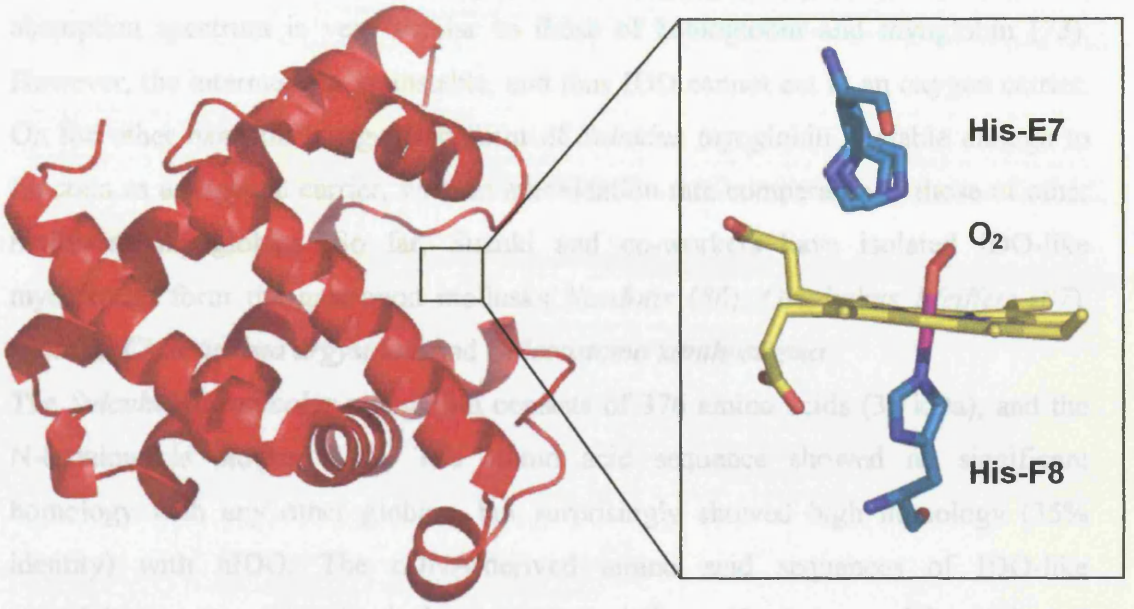

Figure 1.14 Ribbon diagram of the structure of oxygenated sperm whale myoglobin. The polypeptide chain, shown in red, is composed of eight α-helical regions, which are joined via nonhelical segments and folded, forming a compact tertiary structure. This structure is called the "myoglobin fold". The heme group, shown in yellow (box), is inserted in a pocket lined with hydrophobic amino acid side chains. The dioxygen molecule, shown in red, is at the centre of the heme. The proximal histidine (His-F8, in blue; the eighth residue of helix F), which is covalently bound to the heme iron, is conserved in all the myoglobins and hemoglobins studied so far. The distal histidine (His-E7, in blue; the seventh residue of helix E) occurs in many myoglobins and hemoglobins, stabilizing the bound oxygen via hydrogen bonding with it, but it is occasionally replaced by other residues.

In 1989, Suzuki and co-workers have isolated a myoglobin from the abalone (archaegastropod) *Sulculus diversicolor* (*84*). This myoglobin differed from all the myoglobins so far examined in the sense that the polypeptide chain has an unusual molecular mass of 39 kDa, which is about double the size of the usual myoglobin subunit; it contains only one heme per molecule, and the amino acid sequences of several internal peptides show no significant homology with other molluscan globins (*84*). Thus it was first assumed that *Sulculus* myoglobin has a two domain structure resulting from duplication of globin gene, but one of the two domains does not function as myoglobin. The cDNA-derived amino acid sequence showed that *Sulculus*

myoglobin is not a two-domain globin but has a significant homology with human IDO (*85*). As a reaction intermediate, IDO can take an oxygenated form, and its absorption spectrum is very similar to those of hemoglobin and myoglobin (*73*). However, the intermediate is unstable, and thus IDO cannot act as an oxygen carrier. On the other hand the oxygenated form of *Sulculus* myoglobin is stable enough to function as an oxygen carrier, with an autoxidation rate comparable to those of other molluscan myoglobins. So far, Suzuki and co-workers have isolated IDO-like myoglobins form the gastropod mollusks *Nordotis* (*86*), *Omphalius Pfeifferi* (*87*), *Battilus, Chlorostoma argystoma* and *Chlorostoma xanthostigma*.

The *Sulculus diversicolor* myoglobin consists of 376 amino acids (39 kDa), and the N-terminus is blocked (*85*). The amino acid sequence showed no significant homology with any other globins, but surprisingly showed high homology (35% identity) with hIDO. The cDNA-derived amino acid sequences of IDO-like myoglobins were determined from another abalone *Nordotis madaka* (*86*) and turbanshells *Battilus cornutus* and *Omphalius Pfeifferi* (*87*). The IDO-like myoglobins are aligned with human and mouse IDOs, and a homologue in the yeast *Saccharomyces cerevisiae* (Figure 1.15 (*88*)).

(A)

```
                1                                                  50                                                 100
Mb-Sulculus                      ADIQLSKYHVSKDIGFLLEP LQDVL PDYFAPWNRLAKSLPDLV ASHKFRDAVKEMPLLDSSK  LAGYRQKRLAHLQLV
Mb-Nordotis                    MADIQLSKYHVSKDIGFLLEP LQDVL PDYFEPWNRLAKSLPELV ASHKFRDAVKEMPLLDQSK  LAGYRQKRLAHLQLV
Mb-Turbo                         PRLDVAQFDVSMKTGFILEN PLTKL PAYFDAWNNLSSKMSQLV ASKGMRDEVKKLPVLDFNK  LNGPNEVKLGHLQLA
IDO-Human              MAHAMENSWTISKEYHIDEEVGFALPN PQENL PDFYNDWMFIAKHLPDLI ESGQLRERVEKLNMLSIDH  LTDHKSQRLARLVLG
IDO-Mouse           MALSKISPTEGSRRILEDHHIDEDVGFALPH PLVEL PDAYSPWVLVARNLPVLI ENGQLREEVEKLPTLSTDG  LRGHRLQRLAHLALG
Homolog-Yeast  MNNTSITGPQVLHRTKMRPLPVLEKYCISPHHGFLDDRLPLTRLSSKKYMKWEEIVADLPSLLQEDNKVRSVIDGLDVLDLDETILGDVRELRRAYSILG
                                                  **         *         *                 *         *         *

                                                 150                                                 200
Mb-Sulculus    LITSGYLWQEGEGGAVQRLPECVAKPLWNVSNDLGLKPVLTYGDVCLTNCR     VKGG       DIEVMYNLPGGAGT EWFLKVCGLVELTLGKGA
Mb-Nordotis    LITSGYLWQEGEGGAVQRLPECVSKPLWNVSNDLGLKPVLTFADICLTNCK     VKNG       DIEVMYNLPGGAGT EWFLKVCGLVELAFGKSG
Mb-Turbo       MMTSGYLWQNGLDDVPTSLPNCLAAPLYGIYEKYDIPPVMTYGDILLNNAI     AKGGPQP    ENISAIVDIPADKKDWDWYIGVSYMAEFEFAKAV
IDO-Human      CITMAYVWGKGHGDVRKVLPRNIAVPYCQLSKKLELPPILVYADCVLANWK     KKDPNKPLTYENMDVLFSFRDGDCSKGFFL VSLLVEIAAASAI
IDO-Mouse      YITMAYVWNRGDDDVRKVLPRNIAVPYCELSEKLGLPPILSYADCVLANWK     KKDPNGPMTYENMDILFSFPGGDCDKGFFL VSLLVEIAASPAI
Homolog-Yeast  FMAHAYIWASG  TPRDVLPECIARPLLETAHILGVPPLATYSSLVLWNFKVTDECKKTETGCLDLENITTINTFTGTVDE SWFYLVSVRFEKIGSACL
                    * * *       **     *          *       * *      *                          *    *

                                                 250                                                 300
Mb-Sulculus    QSVQNVLDGAKANDK  AKMTSGLTELTTTIGNMQAALAKMNDNLTPDEFYNVLRPFLGGFGGPA SPISGGLIYEGVSDAPVTMIGGSAAQSSAMQLLD
Mb-Nordotis    QAIQNVLDGAKANDK  AKMASGFTDLTAAIGNMQTALARMNENLTPEEFYNGVRPFLNGFGGPA SPISGGLVYEGVSDKPVTMIGGSAAQSSTMQVLD
Mb-Turbo       PALQNVFDGMDENND  DKIAAALKQIAEAAGNIQKTMGRFSEKLSADVLFPKMWAFFGGYGELT   LHDGLIFEGVKDQPIKMKGGNASQSPTLRVLD
IDO-Human      KVIPTVFKAMQMQER  DTLLKALLEIASCLEKALQVFHQIHDHVNPKAFFSVLRIYLSGWKGNP  QLSDGLVYEGFWEDPKEFAGGSAGQSSVFQCFD
IDO-Mouse      KAIPTVSSAVERQDL  KALEKALHDIATSLEKAKEIFKRMRDFVDPDTFFHVLRIYLSGWKCSS  KLPEGLLYEGVWDTPKMFSGGSAGQSSIFQSLD
Homolog-Yeast  NEGLQILRAIRSGDKGDANVIDGLEGLAATIERLSKALMEMELKCEPNVFYFKIRPFLAGWTNMSHMGLPQGVRY GAEGQYRIFSGGSNAQSSLIQTLD
                                                                  *         *   *         **    *         *

                                                 350                                                 400
Mb-Sulculus    NLLGVTHSPDK   QA      FLDEISNYMIPAHKQLLADLTKMPRKVPQIVA EAKDANLSKAYSGCVAALTQYRTYHIQVVTKYIVTA        S
Mb-Nordotis    GLLGITHSPEK   QA      FLDEIRNYMPPSHKQMLADLTNMPRKVPQVVA ETKDANLTKAFNGCVAAFVQYRSYHIQVVTKYIVTA        S
Mb-Turbo       NLLGIANQPER   TA      FIEEIMKYIQPNHRKFIQAVGE  RNLKARVD ASGNAGLKEAFQGLKAALSNLRNHHVQVVTKYIVQAF        E
IDO-Human      VLLGIQQTAGGGHAAQ       FLQDMRRYMPPAHRNFLCSLES NPSVREFVL SKGDAGLREAYDACVKALVSLRSYHLQIVTKYILIPASQQPKENK
IDO-Mouse      VLLGIKHEAGKESPAE       FLQEMREYMPPAHRNFLFFLES APPVREFVI SRHNEDLTKAYNECVNGLVSVRKHELAIVDTYIMKPSKKKPTDGD
Homolog-Yeast  ILLGVKHTANAAHSSQGDSKINYLDEMKKYMPRAHREFLYHLES VCNIREYVSRNASNRALQEAYGRCISMLKIFRDNHIQIVTKYIILPSNSKQHGSN
                *** *                    *   *                 *       *  *          *  *   *  **

                                                 450
Mb-Sulculus    K          SDSPKSLAYK       DTGKSDLIPFLKEVRDDTEKMQK
Mb-Nordotis    K          SDSPKSLAYK       DTGKSDLIPFLKEVRDDTEKVQQ
Mb-Turbo       K          NLPAAKQGEL       KPMKESAMKTVQGFRDDCK
IDO-Human      T          SEDPSKLEAK       GTGGTDLMNFLKTVRSTTEKSLLKEG
IDO-Mouse      K          SEEPSNVESR       GTGGTNPMTFLRSVKDTTEKALLSWP
Homolog-Yeast  KPNVLSPIEPNTKASGCLGHKVASSKTIGTGGTRLMPFLKQCRDETVATADIKNEDKN
```

(B)

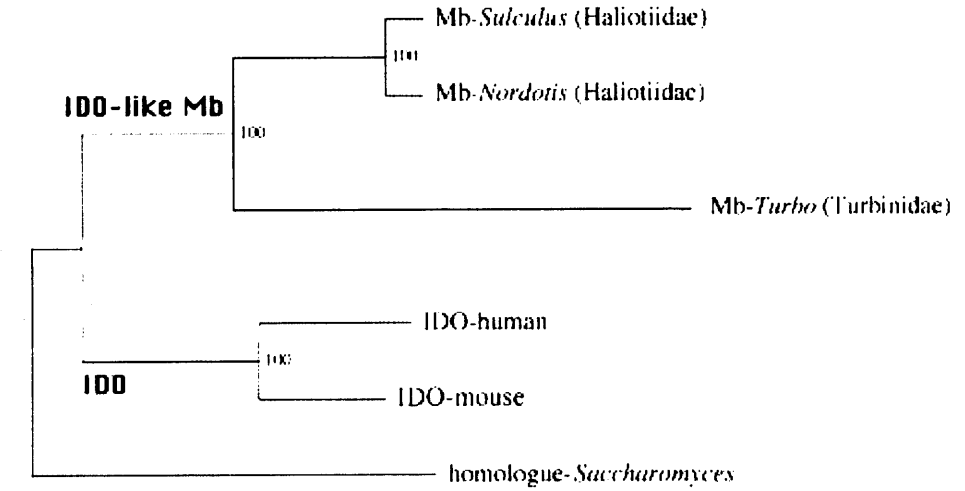

Figure 1.15 (A) Alignment of amino acid sequences of IDO-like myoglobins, IDOs and a homologue in yeast. Amino acid residue conserved in all sequences is indicated by asterisk. The boxed residues indicate the tentatively assigned distal and heme-binding proximal histidines. This alignment was obtained with the algorithm of Feng and Doolittle. **(B)** A phylogenetic relationship of IDOs, IDO-like myoglobins and a homologue in yeast. This tree was obtained with the NJ method in the PHYLIP package 3.5c.

Tryptophan induces spectral changes of *Turbo* metmyoglobin at different pH conditions (*88*), inducing changes in the heme environment. The same interaction has been witnessed for *Sulculus* myoglobin and it has been suggested that the interaction between tryptophan and the two IDO-like myoglobins is a relic of the IDO, conserved during molecular evolution. Tryptophan also affects the autoxidation rates of *Turbo* and *Sulculus* oxymyoglobins. The rate was about 20- and 25-times accelerated respectively, when compared with the rate in the absence of tryptophan. No IDO activity was determined for the two IDO-like myoglobins, suggesting that a non-catalytic binding site for tryptophan remains in or near the heme cavity (*85*).

1.10 Properties of Native (Rabbit) Indoleamine 2,3-Dioxygenase

1.10.1 Substrate Specificity

Since IDO was discovered in the rabbit intestine in 1967, numerous studies have been carried out concerning its catalytic properties.

Experiments carried out by Shimizu *et al.* (1978) (*42*) using a homogeneous enzyme preparation from rabbit intestine, had confirmed that the broad substrate specificity for various indoleamines was attributable to a single enzyme (rIDO). As previously reported, a single enzyme catalyzed the oxidative ring cleavage of D- and L-tryptophan, 5-hydroxy-D- and L-tryptophan, tryptamine and serotonin (*69*) (Table 3, (*42*)). The above studies suggested that the enzyme plays an important role in the metabolism of indoleamines. However, a marked substrate inhibition was observed by the L-isomers of tryptophan and 5-hydroxytryptophan (*89*). Just like the rabbit enzyme, the purified human enzyme exhibited broad substrate specificity; it oxidized D- and L-tryptophan, 5-hydroxy-D- and L-tryptophan, tryptamine (*70*). The above results have indicated that the human indoleamine 2,3-dioxygenase is essentially identical to the rabbit enzyme in terms of molecular and catalytic properties.

Table 3. Substrate specificity of native (rabbit) indoleamine 2,3-dioxygenase.

Substrate	Maximal turnover numbers mol/min/mol of enzyme	K_M μM
L-tryptophan	99	45
D-tryptophan	71	400
5-hydroxy-L-tryptophan	2.6	20
5-hydroxy-D-tryptophan	0.58	600
Tryptamine	0.29	75
Serotonin	0.17	100

Shimizu *et al.* have also demonstrated that the purified enzyme showed a peroxidase activity (in the presence of guaiacol or potassium iodide) with a turnover number nearly equal to that of the dioxygenase activity. However, the reaction rate rapidly declined in a few minutes after the addition of more H_2O_2. Peroxidase activity may be a non-specific activity of a hemoprotein or may be closely related to the primary dioxygenase activity.

1.10.2 Utilisation of Superoxide Anion

One of the unique features of IDO is that the ferric enzyme readily reacts with $O_2^{\bullet-}$ to yield the oxygenated enzyme ($Fe^{2+}O_2$) (*73*), which can also be generated by addition of O_2 to the ferrous enzyme (Fe^{2+}) (*90, 91*). This $O_2^{\bullet-}$-binding property of IDO is similar to those of horseradish peroxidase and catalase (*92, 93*). Possible utilisation of superoxide by IDO *in vivo* was examined by Hayaishi (*94*) and co-workers. When superoxide dismutase activity was suppressed by adding the inhibitor diethyldithiocarbamate, the intracellular IDO activity was markedly accelerated. Furthermore, addition of substrates (purines) of xanthine oxidase in the presence of methylene blue also enhanced the IDO activity in the cells. These results were indicative of intracellular utilisation of $O_2^{\bullet-}$ by IDO.

Sono (*95*) from his investigations on the roles of superoxide reached the following conclusions. Methylene blue acts as an electron mediator to the ferric dioxygenase.

With the increase in the amount of xanthine oxidase, the IDO activity is enhanced to a maximal level either in the presence or the absence of methylene blue when L-Trp is used as a substrate. In the absence of methylene blue, superoxide dismutase inhibits IDO activity, indicating that $O_2^{\bullet-}$ is the major reductant (activator) of IDO under these conditions.

Furthermore, a pulse radiolysis study (*90*) of the reaction of ferric IDO with $O_2^{\bullet-}$ has revealed that, under physiological conditions, utilisation of the superoxide anion by IDO is insignificant due to the presence of superoxide dismutase in cells. The only exceptions to this would be the case of a respiratory burst (*96-99*) – a metabolic event in which production of highly reactive oxidising agents, including oxidised halogens, oxidising radicals, and singlet oxygen, are generated. However, no particular connections between this extraordinary physiological condition and the IDO activity have been demonstrated. This leads to the conclusion, that in order for IDO to be active in tissues, a natural electron carrier (not as yet identified) must exist (*76*).

1.10.3 The Catalytic Cycle

The commonly proposed catalytic cycle of IDO is schematically illustrated in Figure 1.16. Under physiological steady-state conditions, the majority of the enzyme is likely to be in the active, ferrous form. However, *in vitro* catalysis starts from the inactive ferric form. The formation of the ferric enzyme–L-Trp form (K_D = 5.8 mM, pH 7.0 at 24 °C) (*72, 89*) is catalytically unfavorable and this probably justifies the substrate inhibition exclusively observed with L-Trp (and 5-hydroxy-Trp) for IDO (*6, 74*), but not for TDO. Thus, for IDO the ferric enzyme is either reduced to the active ferrous state, which binds to tryptophan and O_2 to form a ternary complex (Trp–Fe^{2+}–O_2) or, if $O_2^{\bullet-}$ is available, binds $O_2^{\bullet-}$ to generate an oxygenated form ($Fe^{2+}O_2$) followed by tryptophan binding. Equilibrium studies of the L-Trp to the CO-bound enzyme ($Fe^{2+}CO$)[1] suggested that the binding of Trp to the ferrous enzyme (K_D (13 μM), pH 7.0) rather than that of Trp to the oxygenated enzyme (K_D (350 μM), pH 7.0) is involved in a steady state of the catalytic reaction (*71, 89*). However, the reverse binding order has not been excluded. Once the ternary complex is formed, it decomposes to yield the ferrous enzyme and product. For TDO, the lower reaction

[1] Assuming that the CO-bound enzyme ($Fe^{2+}CO$) has a tryptophan-binding property similar to that of the oxygenated enzyme ($Fe^{2+}O_2$ or $Fe^{3+}O_2^{\bullet-}$).

sequence in Figure 1.16 is the principal catalytic cycle, since ferrous TDO does not readily bind O_2 in the absence of L-Trp (*100*).[2]

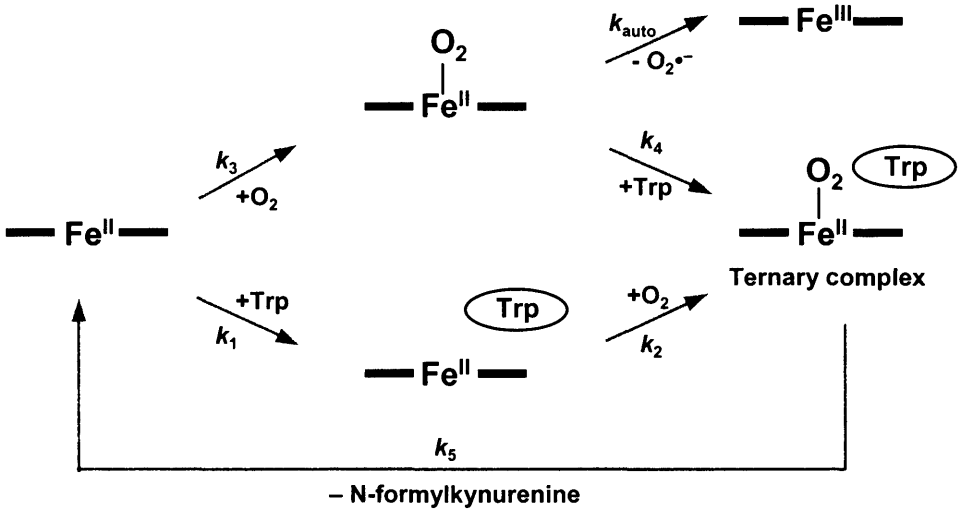

Figure 1.16 Proposed catalytic reaction cycles for IDO and TDO. The porphyrin macrocycle is abbreviated as a black line. The possible reaction intermediates and the rate constants are shown.

The turnover number for rabbit intestinal IDO is ~2 s^{-1} (*72, 42*) (17 s^{-1} for rat liver TDO (*101*)). However, in contrast to TDO, the O_2-bound IDO ($Fe^{2+}O_2$) is readily autoxidisable in the presence of substrate (autoxidation rates 2.8×10^{-2} s^{-1} and 4.7×10^{-4} s^{-1} at pH 7.0 and 25 °C, in the presence and absence of Trp, respectively) (*73, 91*). Thus, during the turnover, the enzyme autoxidises at a rate of 0.028 s^{-1}. The ferric enzyme generated needs to be reactivated (Equation 1.4).

$$\text{L-Trp}-\text{Fe}^{2+}-\text{O}_2 \rightarrow \text{Fe}^{3+} + \text{L-Trp} + \text{O}_2^{\bullet-} \qquad (\ldots 1.4)$$

[2] Note that, in the principal catalytic cycle, no redox changes of the enzyme heme iron are involved for either dioxygenase.

1.10.4 Tryptophan Analogues and Substituted Tryptophans as Mechanistic Probes.

As the structure of IDO is currently unknown, inhibition studies on this enzyme give insight into the structural requirements of the heme pocket substrate-binding site. Inhibition studies have been carried out on both the rabbit as well as the human IDO.

Up to 1984, little was known about the inhibitors of IDO, except that high concentrations (> 0.3 mM) of L-Trp, a substrate, inhibits this enzyme. On the other hand, it has already been shown that 5-hydroxy-Trp, serotonin, other indoleamines (IDO substrates) and L-(2,5-dihydro-phenyl)alanine inhibit TDO competitively. The latter was also shown to inhibit IDO competitively.

In 1984, Eguchi *et al.* (*102*) presented the first inhibition studies on IDO. They have showed that β-carboline derivatives[3] (Figure 1.17) inhibited both IDO (22-96% inhibition) and TDO (9-75% inhibition) activities from various sources. Among them, norharman was most potent for both enzymes from mammalian sources.

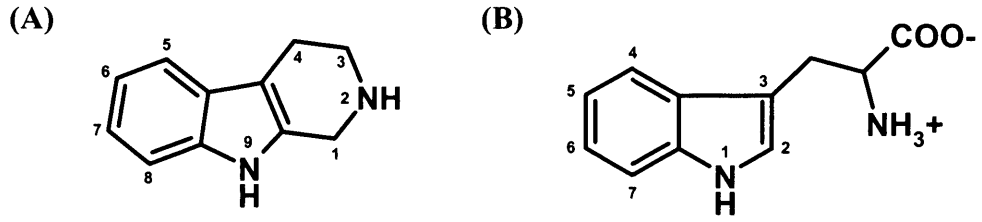

Figure 1.17 Structures of norharman (β-carboline) (A), tryptophan (B) and standard numbering of carbon and nitrogen atoms.

Norharman, a relatively large ligand, does not readily form complexes with myoglobin or horseradish peroxidase (HRP), can bind to IDO and TDO (*103*). Norharman binds directly to the heme iron of the enzyme as a nitrogen donor ligand. Thus, it competes with O_2 for the heme iron ferrous enzyme, resulting in the observed inhibition (*104*). *Pseudomonas* TDO was inhibited by a different spectrum of β-carbolines. Such a selective inhibition by the structure of substrate analogues was

[3] β-carbolines, naturally occurring in South American plants as harmala alkaloids, contain an indole ring structure within their molecules. They induce a characteristic tremor in experimental animals and hallucinations in man, and are reported to be potent inhibitors of type A monoamine oxidase.

more evident by the use of indole derivatives (*e.g.,* indole-3-acetamide, indole-3-acetonitrile and indole-3-acrylic acid). However, they showed no inhibition for IDO (*102*). These results suggested the difference of the structures of the active sites among these enzymes from various sources. Peterson *et al.* (*105, 106*) have also evaluated a series of 3-substituted β-carbolines for *in vitro* human IDO inhibition.

A later inhibition study (1991) (*107*), identified the first examples of potent competitive inhibitors of rabbit intestinal IDO. These inhibitors are 1-methyl-DL-tryptophan, β-(3-benzofuranyl)-DL-alanine (the oxygen analogue of Trp) and β-[3-benzo(b)thienyl]-DL-alanine (the sulphur analogue of Trp) (Figure 1.18). All three analogues showed competitive inhibition kinetics indicating that the analogues are binding to the same site on the enzyme as the substrate L-Trp. Of all the inhibitors tested, Sono and Cady found that the 1-methyl-DL-Trp analogue was the most potent. These results suggested that the free form of the indole NH is important for binding and that its replacement with more electron-inductive atoms such as sulfur and oxygen removes the ability of Trp to act as a substrate. In addition, the inability of 1-methyl-DL-Trp, which readily reacts with singlet oxygen (*108*), to serve as a substrate for the dioxygenase suggest that the singlet oxygen is not involved in the enzymic dioxygenation of Trp. Equilibrium binding studies suggested that the above tryptophan analogues bind to the enzyme in a manner that is similar to the physiological substrate. Furthermore, tryptophan analogues with substituents at the 4, 5 or 6 positions were found to be relatively good substrates (Figure 1.17 (B)). Curiously, however, analogues with substituents at position 7 no longer serve as substrates but instead are competitive inhibitors. The specificity of the enzyme towards substituted tryptophans shows that substitution of the phenyl ring of the indole is sterically unfavorable (*109*).

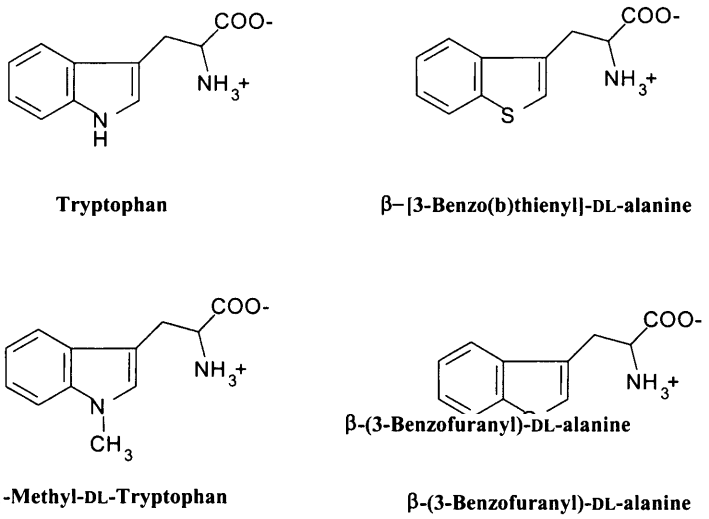

Figure 1.18 The structure of Trp and the first examples of Trp analogue competitive inhibitors of rabbit intestinal IDO. The Trp analogues all have substitutions at the indole nitrogen.

Further attempts to investigate the stereochemical requirements of the active site of human IDO included a wide variety of tryptophan analogues (*106*) and reached the following conclusions: (1) The 2,3 double bond in tryptophan is required for activity, *i.e.* planarity is required in this position, (2) the indole portion of the molecule binds in a lipophilic cleft and (3) the indole nitrogen is not absolutely necessary for binding at the active site.

A great number of tryptophan analogues, used throughout these inhibition studies, were able to bind to the tryptophan binding site. Hence, the active site of IDO must be fairly flexible to incorporate all the different sizes of the tryptophan analogues. It was also found that a dimer of Trp inhibited the activity of the enzyme, the active site could therefore, incorporate a molecule twice the size of that of tryptophan.

More recently, Li *et al.* (*110*) have reported the synthesis of optically active ring-A substituted tryptophans as IDO inhibitors.

1.10.5 Evidence for the Existence of Another Binding Site in IDO

To probe the active site of IDO, Sono (*72*) investigated the effects of 3-indolylethanol (or tryptophol) (IET), one of the known indole derivative effectors, and indole (IND) on the catalytic (V_{max}, K_M) and spectroscopic properties (optical absorption and CD) of the enzyme (Figure 1.19). This study has shown that IET enhances the V_{max} values

by 40-60% while IND lowers them by 12-24%. These effects of IET and IND on the V_{max} values may be attributed to the shift of the ferric (inactive) ↔ ferrous (active) equilibrium either to the right (IET) or to the left (IND) caused by the binding of these effectors to the enzyme in the steady state of the catalytic reaction. Both effectors induce clearly detectable spectral changes upon binding to the ferric and ferrous enzyme and its complexes with O_2, CO, CN^- and NO, both in the presence and absence of L-Trp. Moreover, additions of IND noticeably enhance the affinities of the ferrous-CO and the native ferric enzyme for L-Trp and the affinities of the ferric enzyme for cyanide and azide. These spectroscopic and equilibrium binding results provide evidence for the existence of another binding site near that for the substrate L-Trp and the heme iron for a possible natural cofactor or regulator for the enzyme.

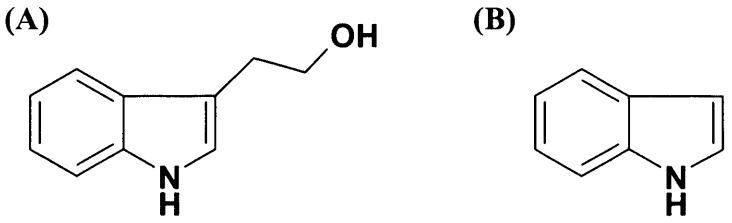

3-Indolylethanol (IET) Indole (IND)

Figure 1.19 (A) 3-Indolylethanol (IET); (B) Indole (IND)

1.10.6 Proposed Reaction Mechanisms

In contrast to heme iron and non-heme iron-containing monooxygenases such as P450 and methane monooxygenases (*111, 112*), respectively, which are able to oxygenate completely unactivated alkanes, IDO and TDO require a functionalized double bond for the substrate to help oxygen incorporation. In this respect, even singlet oxygen, a considerably reactive species, cannot react with alkanes or unactivated aromatic compounds.

The catalytic mechanism involves the cleavage of the aromatic carbon of the indole ring and a functionalised double bond on the substrate is required in order to incorporate oxygen. There have been two mechanisms proposed for this reaction, an ionic and a radical mechanism. The proposed ionic mechanism (Figure 1.20) (*113, 114*) proceeds via the deprotonation of the indole nitrogen by a base in the enzyme active site, which then stimulates the nucleophilic attack by the electron-rich indole carbon (third position) on the distal oxygen of the dioxygen bound to the heme. This results in a 3-indolenylperoxy-Fe^{2+} intermediate being formed (X), which could then be converted to N-formylkynurenine in one of two ways. The intermediate could undergo a Criegee rearrangement (*114*) producing another intermediate, which would then undergo further rearrangement to yield the product. The pathway may also proceed via a dioxetane intermediate, which would then rearrange to form N-formylkynurenine. However, although the formation of both of these intermediates is feasible there remains doubt about whether they occur *in vivo*.

The radical mechanism (Figure 1.20 (B)) was proposed by Wiseman *et al.* (*109*) and also involves the formation of the 3-indolenylperoxy-Fe^{2+} complex intermediate. In the radical mechanism however, the base-catalysed deprotonation of the indole nitrogen results in the formation of a Trp anion which reacts and ultimately leads to the formation of a Trp radical ($Trp^{\cdot}$) and heme-O_2 complex radical (Fe^{III}-$O_2^{\cdot-}$). These radicals combine to form the 3-indolenylperoxy-Fe^{2+} complex intermediate and it was proposed that this intermediate rearranges via the dioxetane pathway to form N-formylkynurenine.

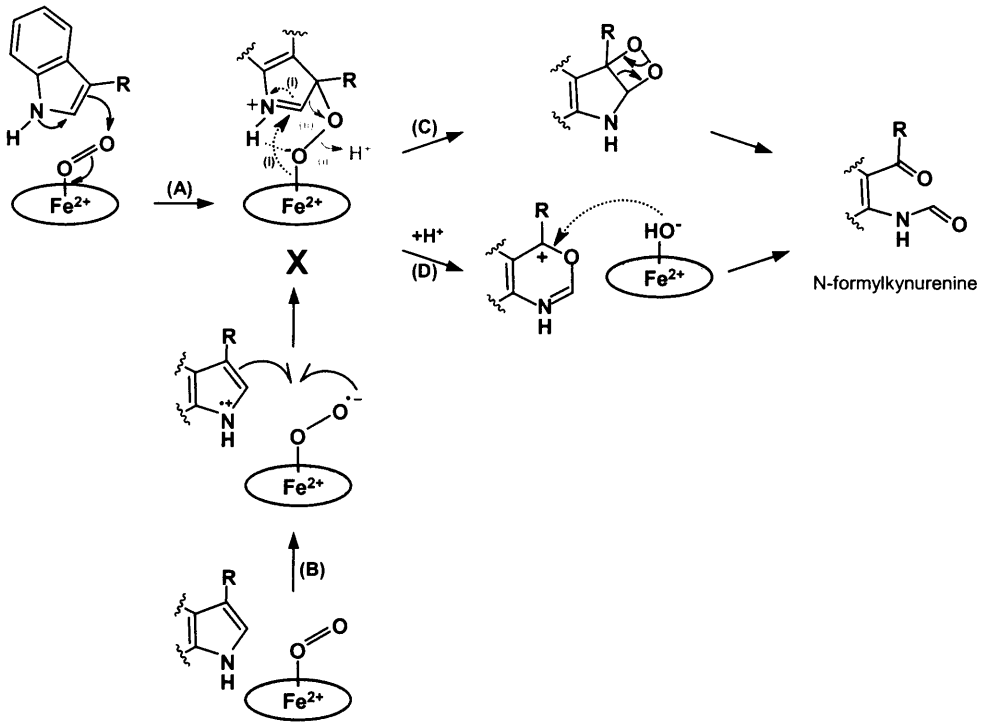

Figure 1.20 Possible mechanisms for the formation of N-formylkynurenine in IDO. All proposed mechanisms involve formation of a hydroperoxide intermediate **X**. Formation of **X** is thought to occur either by an ionic mechanism (A), or a radical pathway (B). Decay of **X** can occur through pathways (C) and (D). Base-catalysed loss of the indole proton is also possible and has been discussed previously in the literature, but is not *required* for addition at C^3: this means that product formation could occur in the absence of a catalytic base.

1.10.7 Heme-Iron Coordination Structures

All the enzyme intermediates (except the hydroperoxide intermediate *i.e.* X in Figure 1.20) involved in the catalytic cycle have been isolated and characterized for both IDO and TDO (except its Trp-free oxygenated form) (*42, 101, 115, 116*). The endogenous axial ligand coordinated to the heme prosthetic group has been shown to be histidine for both dioxygenases (*115, 116*). However, in the native ferric form IDO is six coordinate, apparently having a nitrogen donor as the sixth ligand *trans* to the proximal histidine, yet is predominantly high spin. On the other hand, water is a likely sixth ligand for ferric high-spin TDO as it is for ferric myoglobin (*115, 116*).

Upon addition of L-Trp to the ferric IDO and TDO, a spin-state change occurs, especially in the alkaline pH (pH > 7.5) resulting in a predominantly (~70% for IDO) or partially (30-50% for TDO) low-spin state. The binding of L-Trp in the distal pocket introduces significant conformational changes to the heme peripheral groups. The L-Trp also modifies the chemical environment of the distal pocket as reflected by the transition from a six-coordinate mixed-spin configuration to a low-spin configuration (*117*).

The ferrous enzyme and its complexes with O_2 as well as CO and NO exhibit spectral properties that are very similar to those of the analogous myoglobin derivatives (*89, 103, 118*). An addition of L-Trp to these dioxygenase derivatives causes slight spectral blue shifts in the Soret region. The L-Trp–Fe^{2+}–O_2 ternary complex was successfully generated and stabilized as a transient state for both dioxygenases at 5 °C for TDO (*100*) and below -20 °C in cryogenic mixed solvents for IDO (*118*).

1.11 Recent Developments and Unanswered Questions

Detailed mechanistic and functional information has been very difficult to obtain for IDO for two reasons. First of all, the lack of an efficient bacterial expression system. The first recombinant form of human IDO was reported in 1992. The protein was expressed in *E. coli* as a glutathione S-transferase (GST) fusion protein (*119*). However, this attempt was overall unsuccessful since the large GST tag (26 kDa) affected the activity of the enzyme and hampered structural analysis. Taking into account these problems, a more efficient *E. coli* expression system was developed by

Littlejohn *et al.* (*68*). A series of spectroscopic (resonance Raman (*120*), X-ray absorption near-edge structure (XANES) (*121*)) and site-directed mutagenesis studies (*122*) followed, which provided information on the nature of the active site of human IDO.

Second, until recently (*123*), there was no crystal structure available for IDO, which has severely hampered progress. The RIKEN laboratory in Japan has recently solved the structure of rhIDO (PDB ID 2D0T (4-phenylimidazole-bound, PI), 2D0U (cyanide-bound)). The overall structure revealed some interesting features. The protein was crystallized as a dimer (Figure 1.21), with a disulphide bridge formed between Cys308 residues from each monomer. The distance between the two monomers appears to be quite large (~13 Å), but a great number of water molecules form a hydrogen bond network between the two monomers. To date, there is no evidence in the IDO literature of the enzyme being a functional dimer, and it is known that dimerisation is a common crystallization artifact.

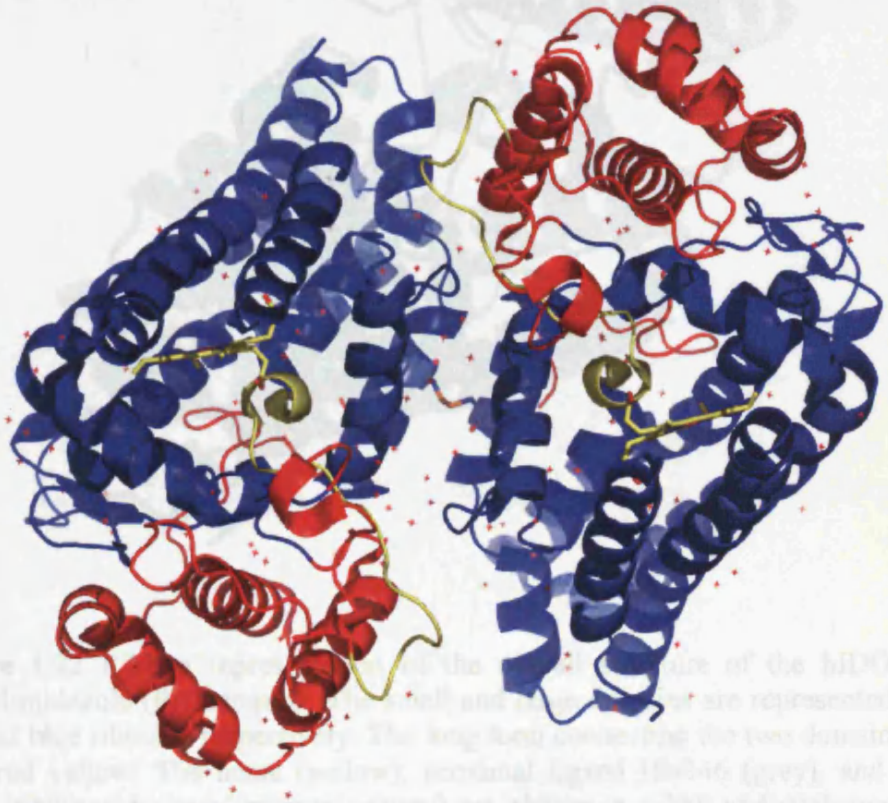

Figure 1.21 Crystal structure of rhIDO, showing the dimeric structure. The heme centres are shown in a stick model, the disulphide bridge between the two Cys308 residues is shown in the centre and water molecules are shown as red stars.

The overall structure shows two α-helical domains with the heme between them (Figure 1.22). IDO is folded in two distinct domains (small (red) and large (blue)), and the folding of each domain appeared to be unique.

The large domain is an all-helical domain and is comprised of 13 α-helices and two 3_{10} helices. Four long helices (G, I, Q and S) in the large domain run parallel to the heme plane. Helix Q provides an endogenous ligand (His346) for the heme iron at the fifth coordination position (proximal side). The heme binding pocket is created mainly by these four helices.

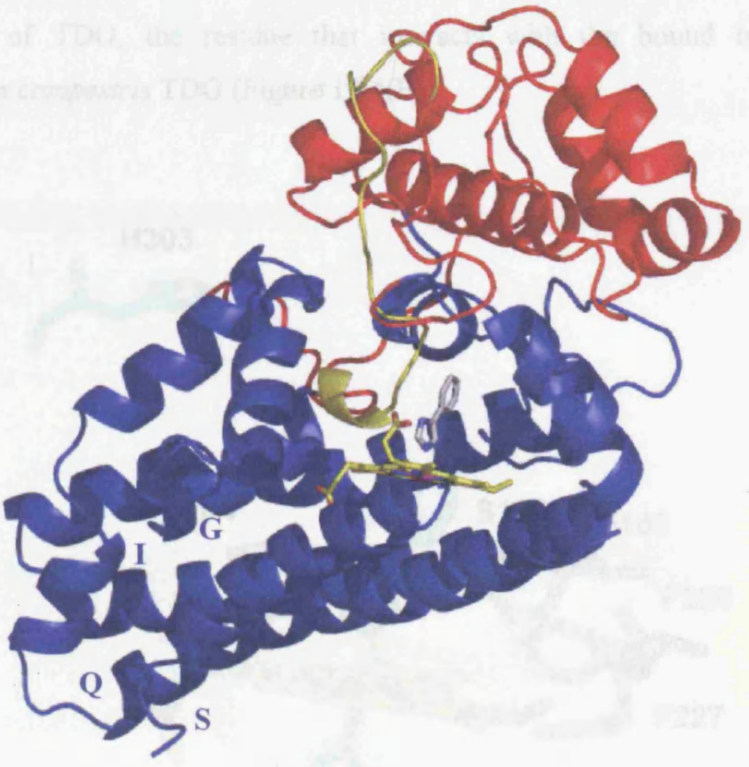

Figure 1.22 Ribbon representation of the overall structure of the hIDO–4-phenylimidazole (PI) complex. The small and large domains are represented by red and blue ribbons, respectively. The long loop connecting the two domains is coloured yellow. The heme (yellow), proximal ligand His346 (grey), and the heme inhibitor 4-phenylimidazole (grey) are shown in a ball-and-stick model. Helices G, I, Q and S of the large domain create the cavity for the heme.

The small domain and a long loop (residues 250-267, yellow) connecting the two domains above the sixth coordination site of the heme (distal side), cover the top of the heme pocket. Ala264 of the flexible loop is in close proximity to the iron.

The crystal structure of rhIDO also revealed a large abundance of hydrophobic residues around the heme centre (Phe163, Phe226, Phe227) (Figure 1.23), indicating a hydrophobic pathway for the entrance of the susbstrate. In the PI-bound form, Phe163 interacts with the phenyl group of PI in the π-π stacking. Ser167, which is located 3.7 Å above the 3-methyl group of the heme, is one of the closest residues to the iron.

A structural alignment between the PI-bound IDO and the Trp-bound TDO from *Xanthomonas campestris* (Figure 1.24(A)) (Professor S. K. Chapman, University of Edinburgh, personal communication to Dr E. Raven) showed that Ser167 is aligned with His55 of TDO, the residue that interacts with the bound tryptophan in *Xanthomonas campestris* TDO (Figure 1.24(B)).

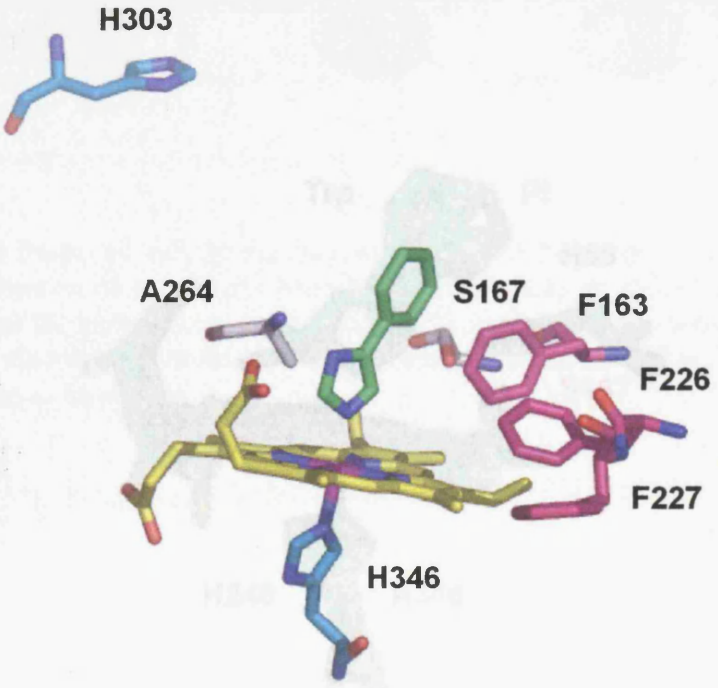

Figure 1.23 Active site of IDO-PI complex. The 7-proprionate of the heme points upward from the heme. Ser167 is the closest residue to the heme iron (3.7 Å). His303 is located ~15 Å away from the active, but in the interface of the small and large domain.

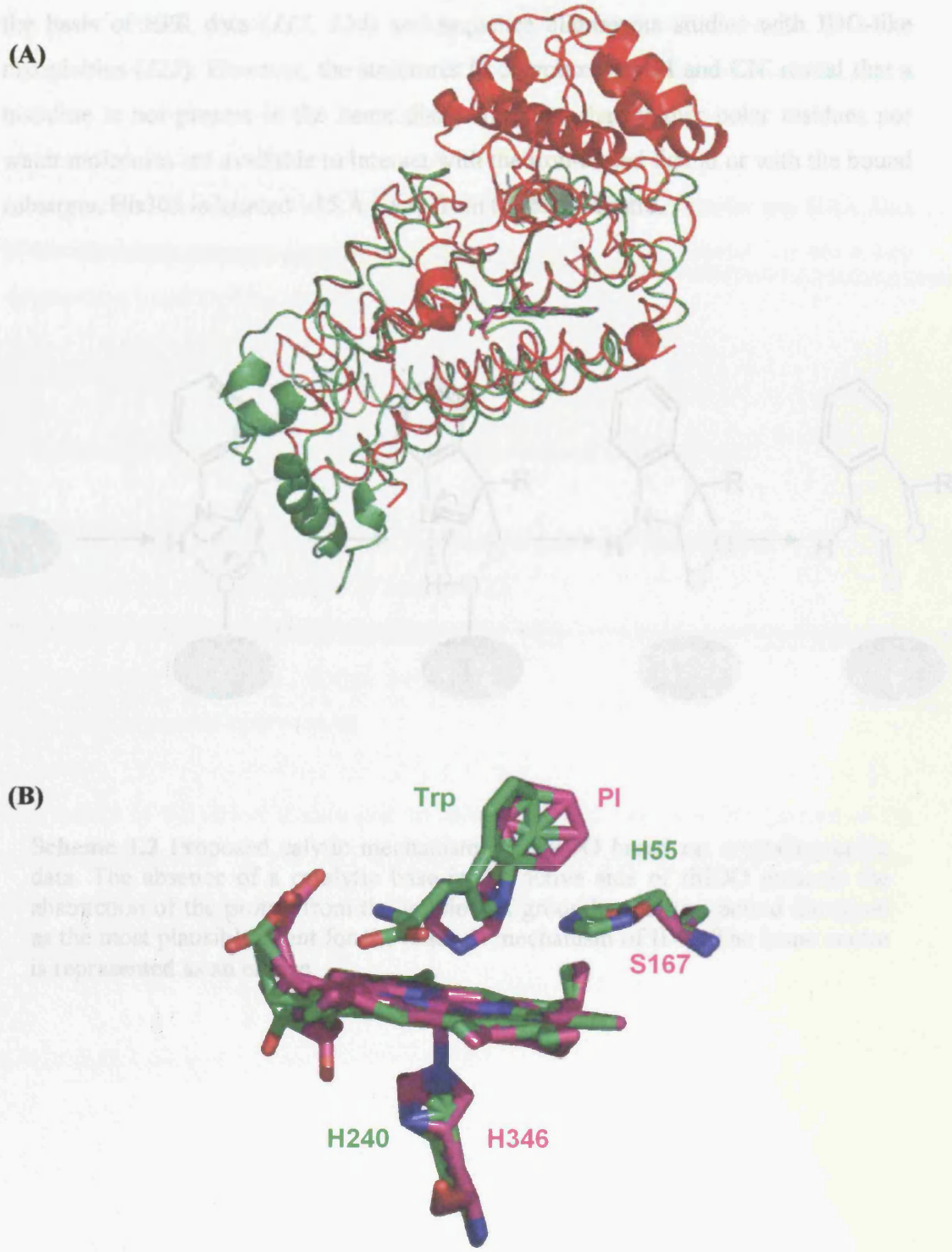

Figure 1.24 (A) Structural overlay between the IDO-PI complex (red) and the TDO-Trp complex (green). The heme centres are shown in a stick model. **(B)** Overlay of the active sites of the two dioxygenases (IDO, pink; TDO, green).

A histidine residue (His303) has been predicted to be a distal and catalytic residue on the basis of EPR data (*117, 124*) and sequence alignments studies with IDO-like myoglobins (*125*). However, the structures in complex with PI and CN^- reveal that a histidine is not present in the heme distal side, and that neither polar residues nor water molecules are available to interact with the iron-bound ligand or with the bound substrate. His303 is located ~15 Å away from the heme centre.

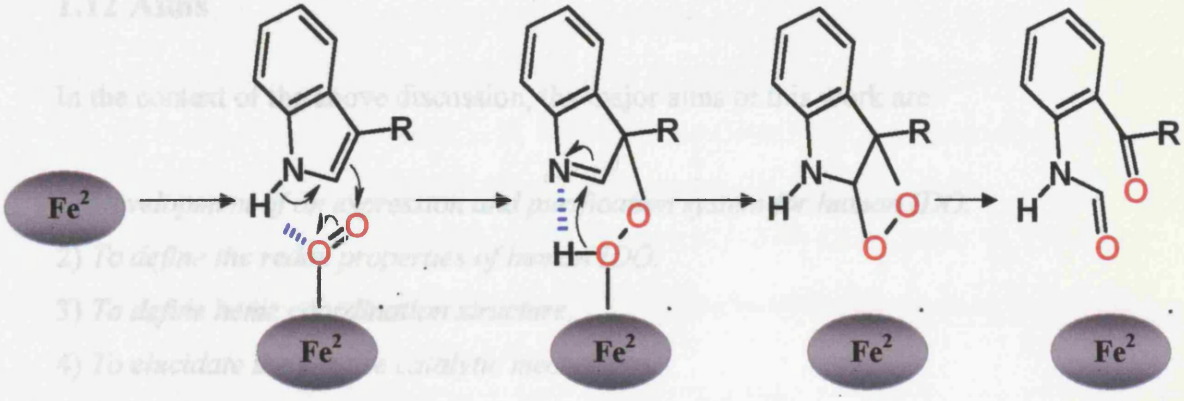

Scheme 1.2 Proposed calytic mechanism for rhIDO based on crystallographic data. The absence of a catalytic base in the active side of rhIDO presents the abstraction of the proton from the indole NH group by the iron-bound dioxygen as the most plausible event for the reaction mechanism of IDO. The heme centre is represented as an ellipse.

However, in related work, the crystal structure of TDO from *Xanthomonas campestris* has been solved (Professor S. K. Chapman, University of Edinburgh, personal communication to Dr E. Raven). Since the two dioxygenases catalyse the same reaction, the structure of TDO can play a vital role in the elucidation of the catalytic mechanism.

Finally, there is no information on the redox properties of the heme for any IDO. This is an important omission because the redox properties of the metal ion are a key determinant in controlling biological function.

1.12 Aims

In the context of the above discussion, the major aims of this work are:

1) *Development of an expression and purification system for human IDO.*
2) *To define the redox properties of human IDO.*
3) *To define heme coordination structure.*
4) *To elucidate the precise catalytic mechanism.*
5) *To gain structural information.*

The results of the above studies can be used to build a more detailed picture of the possible mechanism of the IDO enzyme, and the collective implications of these results can be used to inform our current understanding of the mechanism of IDO catalysis.

1.13 References

1. Hayaishi, O., Takikawa, O., Yoshida, R. (1990) *Prog. Inorg. Chem., 38*, 75.
2. Hayaishi, O., Katagiri, M., Rothberg, S. (1955) *J. Am. Chem. Soc., 77*, 5450-5451.
3. Mason, H. S., Fowlks, W. L., Peterson, L. (1955) *J. Am. Chem. Soc., 77*, 2914-2915.
4. Sono, M., Roach, M. P., Coulter, E. D., Dawson, J. H. (1996) *Chem. Rev., 96*, 2841-2887.
5. Kotake, Y., Ito, N. (1937) *J. Biochem. (Tokyo), 25*, 71-77.
6. Higuchi, K., Hayaishi, O. (1967) *Arch. Biochem. Biophys., 120*, 397-403.
7. Kaim, W., Schewederski, B. *Bioinorganic Chemistry: Inorganic Elements in the Chemistry of Life. An introduction and Guide*, Vol. Chapter 5.
8. Jones, R. D., Summerville, D. A., Basolo, F. (1979) *Chem. Rev., 79*, 139-179.
9. Valentine, J. S., Foote, C. S., Greenberg, A., Liebman, J. F. (1995) *Active Oxygen in Biochemistry*, Vol. Chapter 1.
10. Halliwell, B., Gutteridge, J. M. C. (1984) *Biochem. J. , 219*, 1.
11. Kemal, C., Chan, T. W., Bruice, T. C. (1977) *J. Am. Chem. Soc., 99*, 7272.
12. Jensen, K. P., Ryde, U. (2004) *J. Biol. Chem., 279*, 14561-14569.
13. Bugg, T. D. H. (2003) *Tetrahedron, 59*, 7075-7101.
14. Lee-Ruff, E. (1977) *Chem. Soc. Rev., 6*, 195-214.
15. Stephens, P. J., Jollie, D. R., Warshel, A. (1996) *Chem. Rev., 96*, 2491-1513.
16. Winterhalter, K. H. (1976) *Chimia, 30*, 9.
17. Brigelius, R., Spottl, R., Bors, W., Lengfelder, E., Saran, M., Weser, U. (1974) *FEBS Letters, 47*, 72-75.
18. Massey, V. (1994) *J. Biol. Chem., 269*, 22459-22462.
19. Que, L. J., Ho, R. Y. N. (1996) *Chem. Rev., 96*, 2607-2624.
20. Kovacs, J. A. (2003) *Science, 299*, 1024-1025.
21. Schlichting, I., Berendzen, J., Chu, K., Stock, A. M., Maves, S. A., Benson, D. E., Sweet, R. M., Ringe, D., Petsko, G. A., Sligar, S. G. (2000) *Science, 287*, 1615-1622.
22. Newcomb, M., Shen, R., Choi, S., Toy, P. H., Hollenberg, P. F., Vaz, A. D. N., Coon, M. J. (2000) *J. Am. Chem. Soc., 122*, 2677-2686.

23. Harris, D. L., Loew, G. H. (1998) *J. Am. Chem. Soc., 120*, 8941-8948.

24. Penner-Hahn, J. E., Eble, K. S., McMurry, T. J., Renner, M., Balch, A. L., Groves, J. T., Dawson, J. H., Hodgson, K. O. (1986) *J. Am. Chem. Soc., 108*, 7819-7825.

25. Que, L. J. (2000) *Nat. Struct. Biol., 7*, 182-184.

26. Solomon, E. I. (2001) *Inorg. Chem., 40*, 3656-3669.

27. Neese, F., Solomon, E. I. (1998) *J. Am. Chem. Soc., 120*, 12829-12848.

28. Karlson, A., Parales, J. V., Parales, R. E., Gibson, D. T., Eklund, H., Ramaswamy, S. (2003) *Science, 299*, 1039-1042.

29. Rohde, J., In, J., Lim, M., Brennessel, W. W., Bukowski, M. R., Stubna, A., Munck, E., Nam, W., Que, L. Jr. (2003) *Science, 299*, 1037-1042.

30. Maxwell, J. C., Volpe, J. A., Barlow, C. H., Caughey, W. S. (1974) *Biochem. Biophys. Res. Comm., 58*, 166-171.

31. Barlow, C. H., Maxwell, J. C., Wallace, W. J., Caughey, W. S. (1973) *Biochem. Biophys. Res. Comm., 55*, 91-95.

32. Collman, J. P., Gagne, R. R., Reed, C. A., Robinson, W. T., Rodley, G. A. (1974) *Proc. Nat. Acad. Sc., 71*, 1326-1329.

33. Pauling, L., Coryell, C. D. (1936) *Proc. Nat. Acad. Sc., 22*, 210.

34. Weiss, J. J. (1964) *Nature, 203*, 182-183.

35. Butenandt, A., Weidel, W., Becker, E. (1940) *Naturwissenschaften, 28*, 63-64.

36. Kotake, Y., Masayama, T. (1937) *Hoppe-Seyler's J. Physiol. Chem., 243*, 237-238.

37. Knox, W. E., Mehler, A. H. (1951) *Science, 113*, 237-238.

38. Hayaishi, O., Takikawa, O., Yoshida, R., Yasui, H. (1984) *Prog. Trypt. Ser. Res.*, 33-42.

39. Watanabe, Y., Fujiwara, M., Yoshida, R., Hayaishi, O. (1980) *Biochem. J., 189*, 393-405.

40. Tanaka, T., Knox, W. E. (1959) *J. Biol. Chem., 243*, 1162-1170.

41. Hirata, F., Hayaishi, O. (1975) *J. Biol. Chem., 250*, 5960-5966.

42. Shimizu, T., Nomiyama, S., Hirata, F., Hayaishi, O. (1978) *J. Biol. Chem., 253*, 4700-4706.

43. Yamazaki, F., Kuroiwa, T., Takikawa, O., Kido, R. (1985) *Biochem. J., 230*, 635-638.

44. Hayaishi, O. (1976) *J. Biochem., 79*, 13p-21p.

45. Brown, R. R. (1996) *Recent Adv. Trypt. Res., Plenum Press, New York*, 15-25.

46. Yoshida, R., Hayaish,i O. (1979) *Proc. Nat. Acad. Sc., 75*, 3998-4000.

47. Yoshida, R., Imanishi, J., Oku, T., Kishida, T., Hayaishi, O. (1981) *Proc. Nat. Acad. Sc., 78*, 129-132.

48. Takikawa, O., Habara-Ohkubo, A., Yoshida, R. (1990) *J. Immun., 145*, 1246-1250.

49. Ozaki, Y., Edelstein, M. P., Duch, D. S. (1988) *Proc. Nat. Acad. Sc., 85*, 1242-1246.

50. Werner, E. R., Felmayer, G., Fuchs, D., Hausen, A., Reibnegger, G., Watcher, H. (1989) *Biochem. J., 262*, 861-866.

51. Taylor, M. W., Feng, G. (1991) *FASEB J., 145*, 2516.

52. Gupta, S. L., Carlin, J. M., Pyati, P., Dai, W., Pfefferkorn, E. R., Murphy, M. J. (1994) *Infect. Immun., 62*, 2277-2284.

53. Byrne, G. I., Lehmann, L. K., Landry, G. J. (1986) *Infect. Immun., 53*, 347-351.

54. Pfefferkorn, E. R. (1984) *Proc. Nat. Acad. Sc. , 81*, 908-912.

55. Grohmann, U., Fallarino, F., Puccetti, P. (2003) *Trends Immun., 24*, 242-248.

56. Saito, K., Nowak, T. S., Markey, S. P., Heyes, M. (1993) *J. Neurochem., 60*, 180-192.

57. Sardar, A. M., Reynolds, G. P. (1995) *Neurosc. Letters, 187*, 9-12.

58. Holmes, E. W., Russell, P. M., Kinzler, G. J., Reckard, C. R., Flanigan, R. C., Thompson, K. D., Bermes, E. W. (1992) *Cytokine, 4*, 205-213.

59. Tone, S., Takikawa, O., Habara-Ohkubo, A., Kadoya, A., Yoshida, R., Kido, R. (1990) *Nuc. Acid Res., 18*, 367.

60. Dai, W., Gupta, S. L. (1990) *Biochem. Biophys. Res. Comm., 168*, 1-8.

61. Habara-Ohkubo, A., Takikawa, O., Yoshida, R. (1991) *Gene, 105*, 221-227.

62. Kadoya, A., Tone, S., Maeda, H., Minatogawa, Y., Kido, R. (1992) *Biochem. Biophys. Res. Comm., 189*, 530-536.

63. Fukunaga, R., Sokawa, Y., Nagata, S. (1984) *Proc. Nat. Acad. Sc., 81*, 5086-5090.

64. Dorn, A., Durand, B., Marfing, C., Le Meur, M., Benoist, C., Mathis, D. (1987) *Proc. Nat. Acad. Sc., 84*, 6249-6253.

65. Tone, S., Kadoya, A., Maeda, H., Minatogawa, Y., Kido, R. (1994) *Human Gen., 93*, 201-203.

66. Maezono, K., Tashiro, K, Nakamura, T. (1990) *Biochem. Biophys. Res. Comm., 170*, 176-181.

67. Ren, S., Liu, H., Licad, E., Correira, M. A. (1996) *Archives Biochem. Biophys., 333*, 96-102.

68. Littlejohn, T. K., Takikawa, O., Skylas, D., Jamie, J. F., Walker, M. J., Truscott, R. J. W. (2000) *Protein Express. Purif., 19*, 22-29.

69. Hirata, F., Hayaishi O. (1972) *Biochem. Biophys. Res. Comm., 47*, 1112-1118.

70. Takikawa, O., Kuroiwa, T., Yamazaki, F., Kido, R. (1988) *J. Biol. Chem., 263*, 2041-2048.

71. Ishimura, Y., Makino, R., Ueno, R., Sakaguchi, K., Brady, F. O., Feigelson, P., Aisen, P., Hayaishi, O. (1980) *J. Biol. Chem., 255*, 3835-3837.

72. Sono, M. (1989) *Biochem., 28*, 5400-5407.

73. Hirata, F., Ohnishi, T., Hayaishi, O. (1977) *J. Biol. Chem., 252*, 4637-4642.

74. Yamamoto, S., Hayaishi, O. (1967) *J. Biol. Chem., 242*, 5260-5266.

75. Ohnishi, T., Hirata, F., Hayaishi, O. (1977) *J. Biol. Chem., 252*, 4643-4647.

76. Ozaki, Y., Nichol, C. A., Duch, D. S. (1987) *Arch. Biochem. Biophys., 257*, 207-216.

77. Carlin, J. M., Borden, E. C., Sondel, P. M., Byrne, G. I.,. (1987) *J. Immun., 139*, 2414-2418.

78. Bianci, M., Bertini, R., Ghezzi, P. (1988) *Biochem. Biophys. Res. Comm., 152*, 237-242.

79. Suzuki, T., Imai, K. (1998) *Cel. Mol. Life Sc., 54*, 979-1004.

80. Vinogradov, S. N., Walz, D. A., Pohajdak, B., Moens, L., Kapp, O. H., Suzuki, T., Trotman, C. N. A. (1993) *Comp. Biochem. Phys., 106B*, 1-26.

81. Bolognesi, M., Bordo, D., Rizzi, M., Tarricone, C., Ascenzi, P. (1997) *Prog. Biophys. Mol. Biol., 68*, 29-68.

82. Naito, Y., Riggs, C. K., Vandergon, T. L., Riggs, A. F. (1991) *Proc. Nat. Acad. Sc., 88*, 6672-6676.

83. Manning, A. M., Trotman, C. N. A., Tate, W. P. (1990) *Nature, 348*, 653-657.

84. Suzuki, T., Furukohri, T. (1989) *Experientia, 45*, 998-1002.

85. Suzuki, T., Takagi, T. (1992) *J. Mol. Biol., 228*, 698-700.

86. Suzuki, T. (1994) *J. Prot. Chem., 14*, 9-13.

87. Kawamichi, H., Suzuki, T. (1998) *J. Prot. Chem., 17*, 651-656.

88. Suzuki, T., Kawamichi, H., Imai, K. (1998) *Comp. Biochem. Phys. B, 121*, 117-128.

89. Sono, M., Tanigushi, T., Watanabe, Y., Hayaishi, O. (1980) *J. Biol. Chem., 255*, 1339-1345.

90. Kobayashi, K., Hayashi, K., Sono, M. (1989) *J. Biol. Chem., 264*, 15280-15283.

91. Taniguchi, T., Sono, M., Hirata, F., Hayaishi, O., Tamura, M., Hayashi, K., Iizuka, T., Ishimura, Y. (1979) *J. Biol. Chem., 254*, 3288-3294.

92. Shimizu, N., Kobayashi, K., Hayashi, K. (1984) *J. Biol. Chem., 259*, 4414-4418.

93. Shimizu, N., Kobayashi, K., Hayashi, K. (1989) *Biochim. Biophys. Acta, 995*, 133-137.

94. Taniguchi, T., Hirata, F., Hayaishi, O. (1977) *J. Biol. Chem., 252*, 2774-2776.

95. Sono, M. (1989) *J. Biol. Chem., 264*, 1616-1622.

96. Badwey, J. A., Karnovsky, M. L. (1980) *Ann. Rev. Biochem., 49*, 695-726.

97. Fridovich, I. (1983) *Ann. Rev. Pharm. Toxicol., 23*, 239-257.

98. Chance, B., Sies, H., Boveris, A. (1979) *Physiol. Rev., 59*, 527-605.

99. Channock, S. J., El Benna, J., Smith, R. M., Babior, B. M. (1994) *J. Biol. Chem., 269*, 24519-24522.

100. Ishimura, Y., Nozaki, M., Hayaishi, O., Nakamura, T., Tamura, M., Yamazaki, I. (1970) *J. Biol. Chem., 255*, 1339.

101. Makino, R., Sakaguchi, K., Iizuka, T., Ishimura, Y. (1980) *J. Biol. Chem., 255*, 11883-11891.

102. Eguchi, N., Watanabe, Y., Kawanishi, K., Hashimoto, Y., Hayaishi, O. (1984) *Arch. Biochem. Biophys., 232*, 602-609.

103. Sono, M. (1990) *Biochem., 29*, 1451-1460.

104. Sono, M.,Cady, S. G. (1989) *Biochem., 28*, 5392-5399.

105. Peterson, A. C., La Loggia, A. J., Hamaker, L. K., Arend, R. A., Fisette, P. L., Ozaki, Y., Will, J. A., Brown, R. R., Cook, J. M. (1993) *Med. Chem. Res., 1993*, 473-482.

106. Peterson, A. C., Migawa, M. T., Martin, M. J., Hamaker, L. K., Czerwinski, K. M., Zhang, W., Arend, R. A., Fisette, P. L., Ozaki, Y., Will, J. A., Brown, R. R., Cook, J. M. (1994) *Med. Chem. Res., 3*, 531-544.

107. Cady, S. G., Sono, M. (1991) *Arch. Biochem. Biophys., 291*, 326-333.

108. Saito, I., Matsuura, T., Nakawaga, M., Hino, T. (1977) *Acc. Chem. Res., 10*, 346-352.

109. Leeds, J. M., Brown, P. J., McGeehan, G. M., Brown, F. K., Wiseman, J. S. (1993) *J. Biol. Chem., 268*, 17781-17786.

110. Li, X., Yin, W., Srirama Sarma, P. V. V., Zhou, H., Ma, J., Cook, J. M. (2004) *Tetrahedron Letters, 45*, 8569-8573.

111. Wallar, B. J., Lipscomb, J. D. (1996) *Chem. Rev., 96*, 2625.

112. Feig, A. L., Lippard, S. J. (1994) *Chem. Rev., 94*, 759.

113. Fraser, M. S., Hamilton, G. A. (1982) *J. Am. Chem. Soc., 104*, 4203-4211.

114. Muto, S. n. B., T. C. (1980) *J. Am. Chem. Soc., 102*, 7379-7381.

115. Sono, M.,Dawson, J. H. (1983) *Federation Proceedings, 42*, 1827-1827.

116. Uchida, K., Shimizu, T., Makino, R., Sakaguchi, K., Iizuka, T., Ishimura, Y., Nozawa, T., Hatano, M. (1983) *J. Biol. Chem., 258*, 2526-2533.

117. Sono, M.,Dawson, J. H. (1984) *Biochim. Biophys. Acta, 789*, 170-187.

118. Sono, M. (1986) *Biochem., 25*, 6089-6097.

119. Maeda, H., Tone, S., Kadoya, A. Iwamonoto, Y., Minatogawa, Y., Kido, R. (1992) *Advances Trypt. Res.*, 417-420.

120. Terentis, A. C., Thomas, S. R. Takikawa, O., Littlejohn, T. K., Truscott, R. J. W., Armstrong, R. S., Yeh, S., Stocker, R. (2002) *J. Biol. Chem., 277*, 15788-15794.

121. Aitken, J. B., Thomas, S. E., Stocker, R., Thomas, S. R., Takikawa, O., Armstrong, R. S., Lay, P. A. (2004) *Biochem., 43*, 4892-4898.

122. Littlejohn, T. K., Takikawa, O., Walker, M. J., Truscott, R. J. W. (2003) *J. Biol. Chem., 278*, 29525-29531.

123. Sugimoto, H., Oda, S., Otsuki, T., Hino, T., Yoshida, T., Shiro, Y. (2006) *Proc. Nat. Acad. Sc., 103*, 2611-2616.

124. Papadopoulou, N. D., Mewies, M., McLean, K. J., Seward, H. E., Svistunenko, D. A., Munro, A. W., Raven, E. L. (2005) *Biochem., 44*, 14318-14328.

125. Suzuki, T., Kawamichi, H., Imai, K. (1998) *Comp. Biochem. Physiol., Part B, 121*, 117-128.

Chapter 2

Bacterial Expression & Purification of Recombinant Human Indoleamine 2,3-Dioxygenase

2.1 Introduction

As discussed in Chapter 1 (Section 1.6), indoleamine 2,3-dioxygenase (IDO) activity is distributed in various mammalian tissues in rabbits, rats and mice. IDO is ubiquitously distributed in almost all the rabbit tissues that have been examined, with the lowest activity observed for the whole rabbit brain. IDO has been purified from rabbit intestine by a combination of streptomycin treatment, ammonium sulphate fractionation and affinity chromatography, to apparent homogeneity as judged by polyacrylamide gel electrophoresis and analytical centrifugation. This has shown that the native protein was monomeric of molecular weight 41,000 ± 1,000 (*1, 2*). IDO has also been isolated from various human tissues, like the placenta. The human enzyme was purified using the same methodology used to purify the rabbit enzyme. The enzyme activity was assayed in tissue homogenates containing methylene blue, ascorbic acid and catalase (*3*). Considering the low yield and the stringent and lengthy conditions required for the isolation of the human IDO, there is an urgent need for the development of an *Escherichia coli* expression system for purification of recombinant human indoleamine 2,3-dioxygenase (rhIDO). This allows the possibility of undertaking mutagenesis experiments to probe the function of one or a number of specific residues (*4*).

This Chapter will focus on the construction of a bacterial expression system for human IDO and the optimization of the purification methods. The optimized purification procedure (Chapter 6, Section 6.3.3) has revealed two components. Due to these findings, a major part of this Chapter will concentrate on the separation and identification of these two components. This work was used as a basis upon which kinetic, spectroscopic and site-directed mutagenesis studies on recombinant human IDO could subsequently be launched.

2.2 Results

2.2.1 Construction and Expression of the rhIDO

The polymerase chain reaction (PCR) was employed to modify the 5' and 3' ends of the human IDO cDNA (contained in pQKS7 vector, Stratagene™) to incorporate the *Kpn*I and *Sal*I restriction sites respectively. The modified gene was digested with *Kpn*I and *Sal*I restriction enzymes, ligated in the expression vector pQE30 (Qiagen™) and then was transformed into *E. coli* SG13009 carrying the repressor plasmid pREP4 (Figure 2.1). The bacterial colonies, containing both pQE30-IDO and pREP4 (ensures tightly regulated gene expression and confers resistance to kanamycin), were isolated on LB-agar plates containing 100 μg/ml ampicillin and 50 μg/ml kanamycin. The colonies carrying the pQE30-IDO in the correct orientation were identified by digestion of the extracted plasmid with restriction enzymes. In this system, a hexahistidyl tag is attached to the full-size IDO (403 amino acids) at the N-terminus with a spacer sequence of 7 amino acids. This spacer sequence is part of the remaining multiple cloning site (MCS) of the pQE30 vector, after addition of the IDO gene (Figure 2.2).

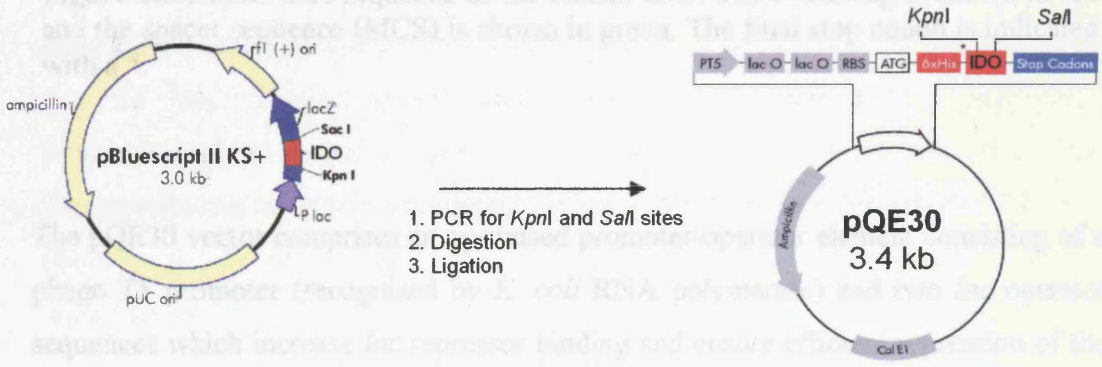

Figure 2.1 Diagrammatic representation of the construction of the pQE30-IDO vector, encoding the human IDO cDNA. IDO cDNA (red box) is cloned into the vector pQE30 (Qiagen™) and contains a hexahistidyl tag, there is a bacteriophage T5 promoter upstream of two *lac*O operators, a β-lactamase gene and *E. coli* origin of replication. Only relevant restriction sites are shown.

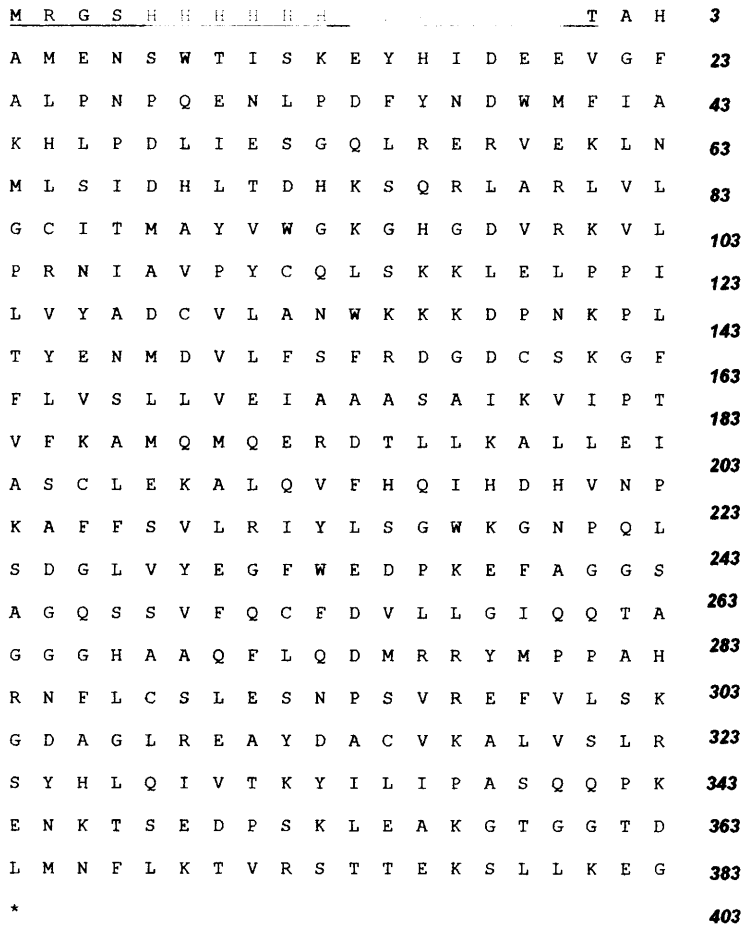

Figure 2.2 Amino acid sequence of the human IDO. The 6×His-tag is shown in red and the spacer sequence (MCS) is shown in green. The final stop codon is indicated with a *.

The pQE30 vector comprises an optimised promoter-operator element consisting of a phage T5 promoter (recognized by *E. coli* RNA polymerase) and two *lac* operator sequences which increase *lac* repressor binding and ensure efficient repression of the powerful T5 promoter. The synthetic ribosomal binding site, RBSII, provides high translation rates. The two strong transcriptional terminators (not shown in Figure 2.1), t_0 from phage λ and T1 from *rrnB* operon of *E. coli*, prevent read-through transcription and ensure stability of the expression construct. Finally the β-lactamase gene (*bla*) confers resistance to ampicillin at 100 μg/ml. The rhIDO expression is under the control of the phage T5 promoter and *lac* operator and it is repressed by the

lac repressor protein produced by the pREP4 repressor plasmid. Expression of the hexahistidyl tagged protein is achieved by addition of isopropyl-β-D-thiogalactopyrinoside (IPTG), which binds to the *lac* repressor protein and inactivates it.

Preliminary expression trials of the rhIDO according to previously published procedures (*5*) were unsuccessful. This was thought to be due to the fact that the *E. coli* cells were not thriving. Addition of the substrate (L-Trp, 50 mg/l) in the growth media eliminated this problem. However, induction of protein expression at 37 °C led to the isolation of recombinant enzyme with an atypical UV-visible spectrum possessing a significant shoulder at the Soret peak. This was thought to be due to the formation of inclusion bodies, which is a common problem encountered when using *E. coli* as the host for recombinant protein synthesis. In the case of inclusion bodies, *E. coli* does not fold the recombinant protein correctly. If the protein does not take up its correctly folded tertiary structure then it is usually insoluble and forms an inclusion body within the bacterium. To solve this problem, it was found that induction of protein expression must take place at 27 °C (*6*).

2.2.2 Purification and Handling of the rhIDO

Using the modified protocol, described in Chapter 6, recombinant human IDO was expressed in *E. coli* as a fusion protein to a hexahistidyl tag. An average of 5 days was required for complete isolation of the enzyme and the typical yield of purified enzyme was 2.1 mg/l in rich growth media. Figure 2.3 shows a 15% SDS-PAGE, bromophenol blue-stained gel that details the various stages in purification of rhIDO.

The purification of rhIDO was carried out using the procedure described in Chapter 6 (Section 6.3.3) (*6*). This protocol is a modified version of the suggested manufacturer's procedure (Qiagen™) in which a buffer – comprising 50 mM potassium phosphate pH 6.5, 300 mM potassium chloride and 50 mM imidazole – is used during the washing step, to disrupt the binding of dispersed histidine residues in non-tagged proteins and to prevent the nonspecific, low-affinity binding of background proteins to the Ni-NTA matrix. The column is developed using a linear gradient of 50 to 250 mM imidazole contained in the basal buffer (50 mM potassium phosphate containing 300 mM potassium chloride). Elution with imidazole resulted in binding of imidazole to the heme iron, which may obscure spectroscopic and

functional data. Another way of eluting protein from the column was to replace imidazole in the elution buffer with 1,2-dimethylimidazole (Scheme 2.1). The concentrations of 1,2-dimethylimidazole were the same with the corresponding imidazole concentrations in the manufacturer's procedures. This failed to displace the protein from the affinity chromatography column. This may be due to the weak interaction of the analogue with nickel resin (probably due to the methyl groups). Elution with a low pH (4.5) buffer was also attempted – the histidine residues in the 6×His tag have a pK_a of approximately 6.0 and will become protonated if the pH is reduced (pH 4.5-5.3). Under these conditions the 6×His-tagged protein can no longer bind to the nickel ions and will dissociate from the Ni-NTA resin. This procedure was observed to lead rapid enzyme precipitation on the Ni-NTA column. Since none of the above options were providing a satisfactory purification method we resorted to the purification procedure discussed in Chapter 6, in which the protein is eluted from the column with EDTA (100 mM). EDTA is a hexadentate ligand that chelates the Ni^{2+} atoms, resulting in the elution of the Ni-NTA-bound protein. Excess EDTA is subsequently removed by dialysis in sonication buffer (Appendix A).

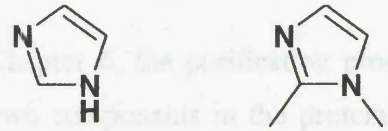

Imidazole **1,2-Dimethylimidazole**

Scheme 2.1 Chemical structures of imidazole and 1,2-dimethylimidazole

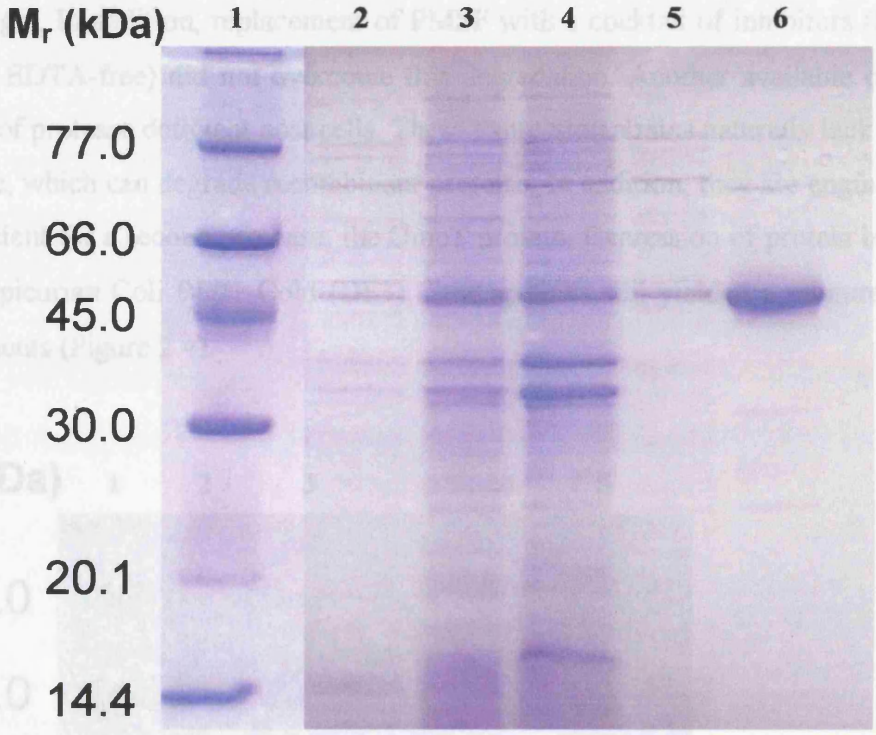

Figure 2.3 SDS-PAGE gel of samples taken during the purification of rhIDO. Lane **1** denotes the marker standards. The stages are: Lane **2** t = 0 hours, before induction; Lane **3** t = 24 hours, after induction with IPTG; Lane **4** = Cell free extract; Lane **5** = cell pellet; Lane **6** = rhIDO after the His-binding nickel column.

The recombinant enzyme expressed in *E. coli* is isolated as the holo-enzyme with a final R_Z (A_{404}/A_{280}) > 2.0. Attempts to increase the R_Z value by addition of exogenous heme after extraction of rhIDO from the cells was unsuccessful, indicating that the heme is efficiently incorporated during bacterial fermentation.

2.2.3 Investigation of a Possible Proteolytic Site of rhIDO

As already discussed in Chapter 6, the purification procedure, as described above, revealed the presence of two components in the protein sample during SDS-PAGE analysis. In order to investigate the origin of this second component several analytic techniques have been carried out and are presented below.

Although we have used PMSF (a protease inhibitor) during expression and purification of the recombinant protein, we still observed two components on the protein gel. In addition, replacement of PMSF with a cocktail of inhibitors (Roche™ Tablets EDTA-free) did not overcome this degradation. Another available option is the use of protease deficient host cells. These expression strains naturally lack the Lon protease, which can degrade recombinant proteins. In addition, they are engineered to be deficient for a second protease, the OmpT protein. Expression of protein in *E. coli* cells (Epicurian Coli BL21-Cold (DE3), Stratagene™) still yielded a mixture of two components (Figure 2.4).

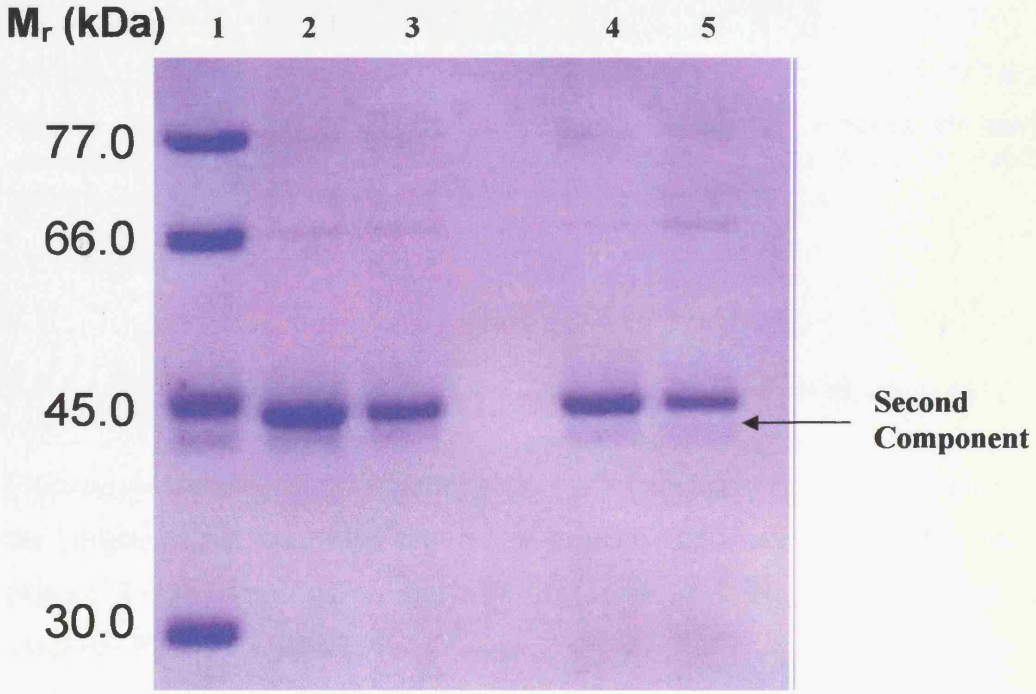

Figure 2.4 15% SDS-PAGE analyses of rhIDO expressed in two different strains of *E. coli* cells. Lane **1** denotes the marker standards. Lanes **2** and **3** = rhIDO expressed in SG13009 *E. coli* cells; Lanes **4** and **5** = rhIDO expressed in Epicurian Coli BL21-Gold (DE3) cells.

2.2.3.1 Protein Oxidation with Alkylating Agents after Reducing SDS Treatment

Reducing agents such as dithiothreitol (DTT) or 2-mercaptoethanol, used for the preparation of SDS-PAGE electrophoresis samples, cleave disulphide bonds into free sulphhydryl (SH) groups to allow proteins to unfold completely. However, the reducing agent can be oxidized during sample heating, which may allow these disulfide bonds to reform, leading to the appearance of 'ghost' bands in the high molecular weight area or precipitation at the sample application point on an SDS-PAGE gel. Blocking the reduced SH groups can prevent disulfide bonds from reforming. One common way to do this is to alkylate these SH groups with iodoacetamide. The iodoacetamide is added after boiling the reduced sample, but prior to loading the sample onto the SDS-PAGE gel. The alkylation reaction takes 15-20 minutes at room temperature.

As it is obvious from the following figure (Figure 2.5) that even after oxidation of rhIDO with iodoacetamide, the second component is still present on the SDS-PAGE gel. This suggests that this second, minor band is not an artifact of electrophoresis.

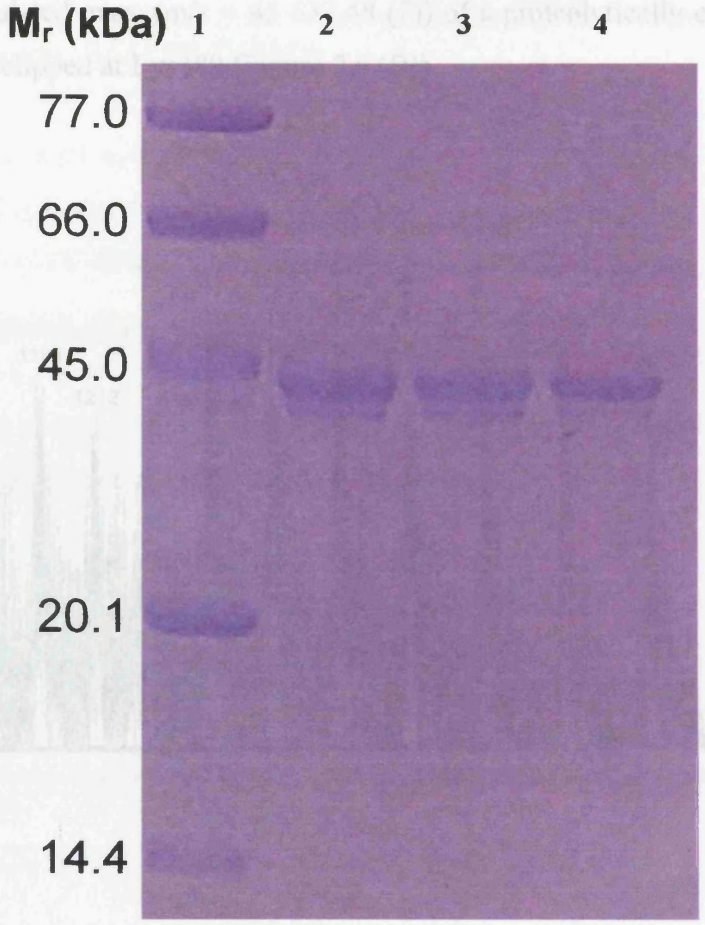

Figure 2.5 15% SDS-PAGE analyses of rhIDO. Lane **1** denotes the marker standards. Lanes **2** = SDS-reduced sample of rhIDO; Lanes **3** and **4** = rhIDO samples treated with iodoacetamide after reducing SDS treatment.

2.2.3.2 Electrospray Ionisation Mass Spectrometry (ESI-MS)

Electrospray ionization mass spectrometry was conducted in order to further evaluate the integrity of the recombinant wild-type protein. The charge distribution obtained (Figure 2.6 (A)) and the computationally constructed singularly charged mass spectrum (Figure 2.6 (B)) of the mixture of "intact" and "clipped" rhIDO gave two peaks at m/z 47,170.0 ± 1.8 and 45,643.0 ± 1.7, respectively[1]. The major peak at 47,170.0 corresponds to the calculated mass (m/z = 47,168.22 (*7*)) of the "intact" protein including the N-terminal His tag (Figure 2.2); the minor peak corresponds to

[1] An average molecular mass for the protein is calculated from the broad distribution of multiply charged species.

the calculated mass (m/z = 45 637.48 (*7*)) of a proteolytically cleaved version of the enzyme clipped at Lys389 (Figure 2.6 (B)).

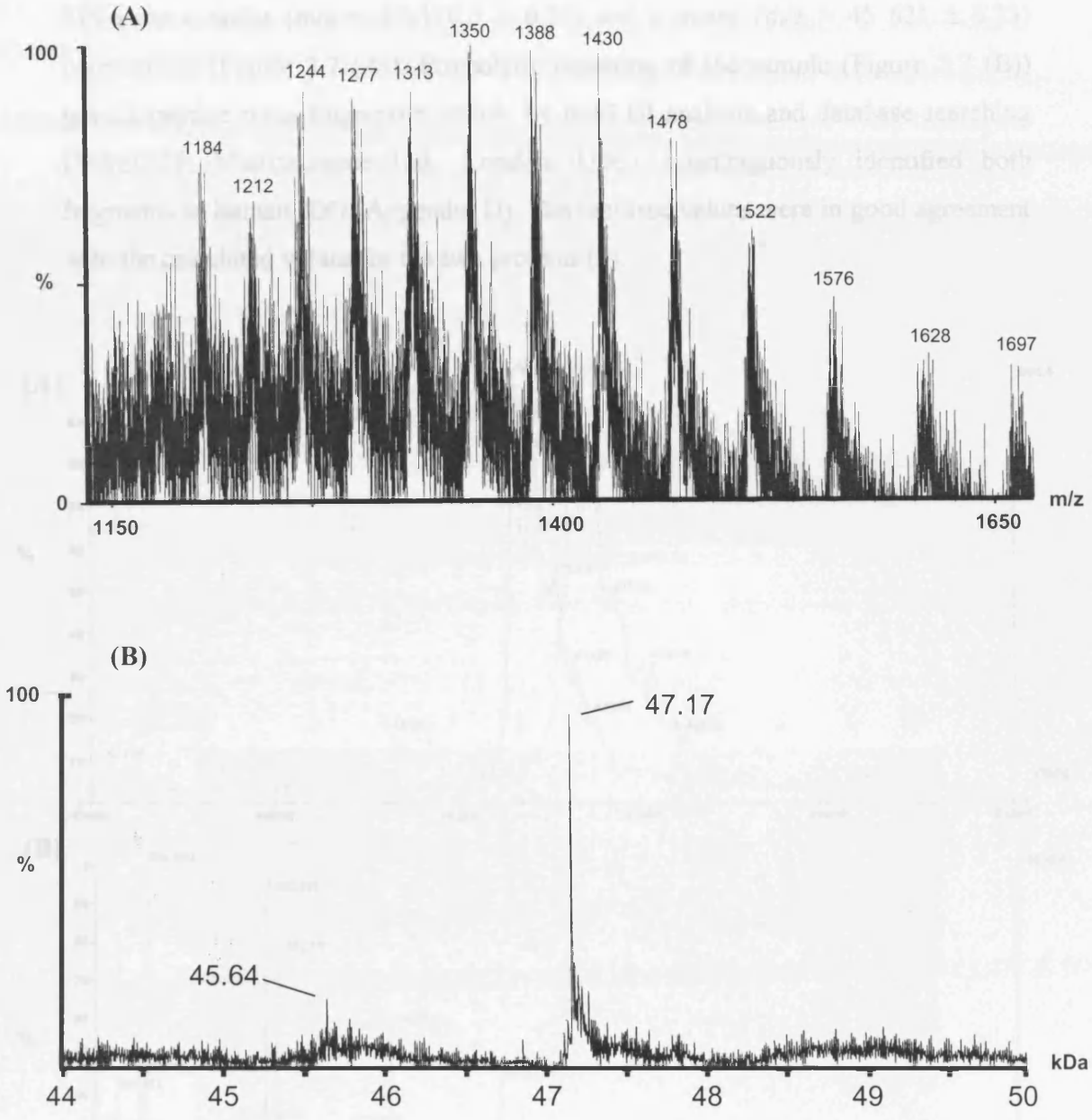

Figure 2.6 Mass spectrometric analysis of rhIDO. **(A)** A typical electrospray ionisation mass spectrum, which comprises of multiply charged protein species. **(B)** Computationally derived molecular mass for *holo* rhIDO.

2.2.3.3 Matrix-Assisted Laser Desorption Ionisation – Time-of-flight Mass Spectrometry (MALDI-Tof MS)

Analysis of a mixture of the "intact" and "clipped" forms of rhIDO using MALDI-Tof MS gave a major (m/z = 47 170.0 ± 0.24) and a minor (m/z = 45 621 ± 0.23) components (Figure 2.7 (A)). Proteolytic digestion of the sample (Figure 2.7 (B)) gave a peptide mass fingerprint which, by MALDI analysis and database searching (MASCOT, Matrixscience Ltd., London, U.K.), unambiguously identified both fragments as human IDO (Appendix D). The reported values were in good agreement with the calculated values for the two proteins (*7*).

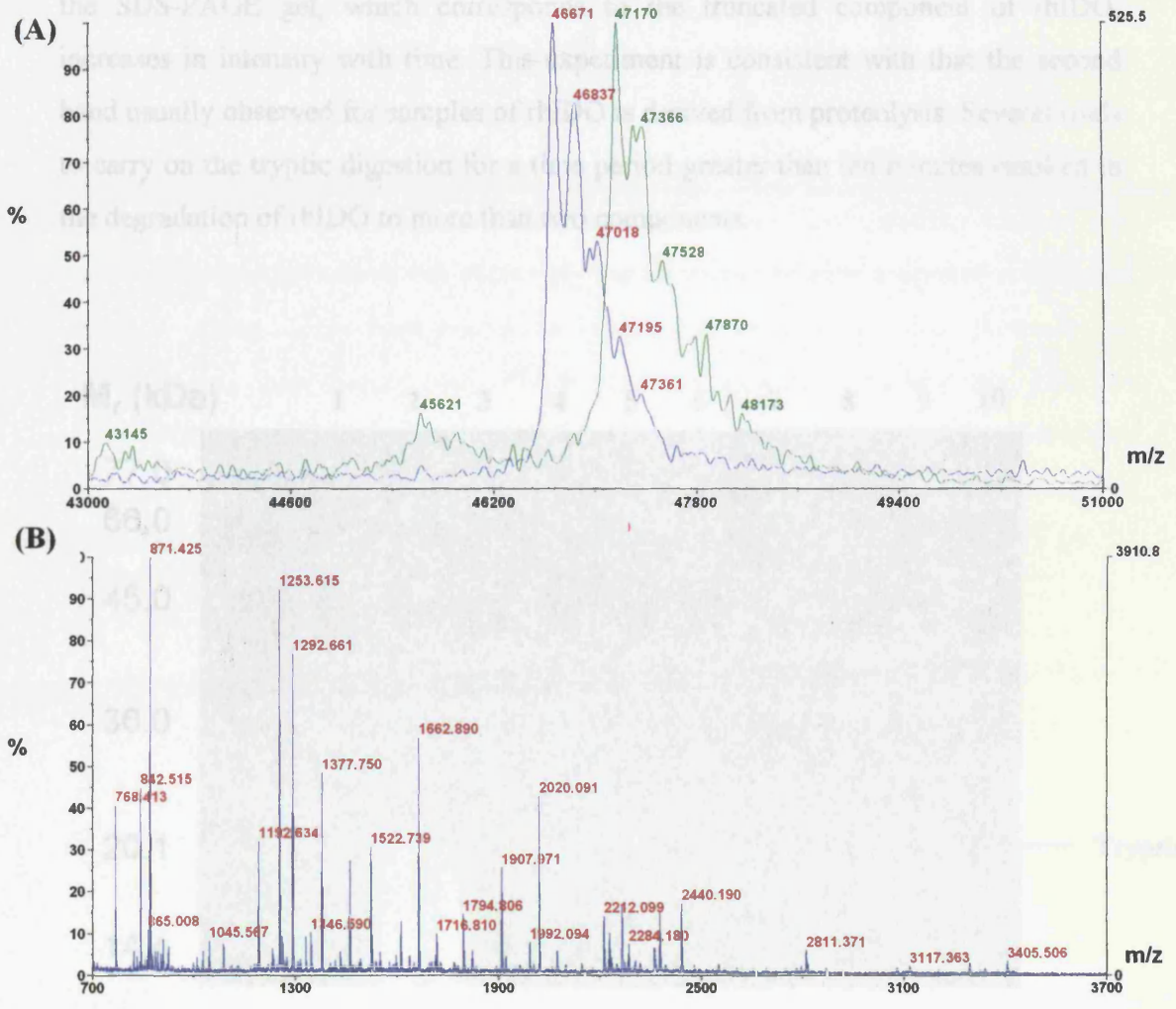

Figure 2.7 (A) MALDI-Tof spectrum of rhIDO. External calibration was achieved using comparable preparation of Baker's yeast enolase, which has a similar molecular weight to rhIDO. (blue spectrum = Baker's yeast, green spectrum = rhIDO) **(B)** Peptide mass fingerprint of rhIDO after tryptic digest.

2.2.3.4 Timed Tryptic Digest of rhIDO

The presence of the second component in the purified sample of the rhIDO has so far been identified by ESI and MALDI-TOF mass spectrometry. To unambiguously verify the presence of the proteolytic site at Lys389, a purified mixture of the 'intact' and 'clipped' rhIDO was subjected to tryptic digestion (Figure 2.8) by adding a solution of trypsin (0.7 mg/ml) at 37 °C. The reaction was monitored every minute for a period of ten minutes. Addition of a solution of trypsin inhibitor was used to cease the reaction, which was then loaded on a 15% SDS gel in order to monitor the results of the digestion.

From Figure 2.8, we can see that during the course of the reaction the minor band on the SDS-PAGE gel, which corresponds to the truncated component of rhIDO, increases in intensity with time. This experiment is consistent with that the second band usually observed for samples of rhIDO is derived from proteolysis. Several trials to carry on the tryptic digestion for a time period greater than ten minutes resulted in the degradation of rhIDO to more than two components.

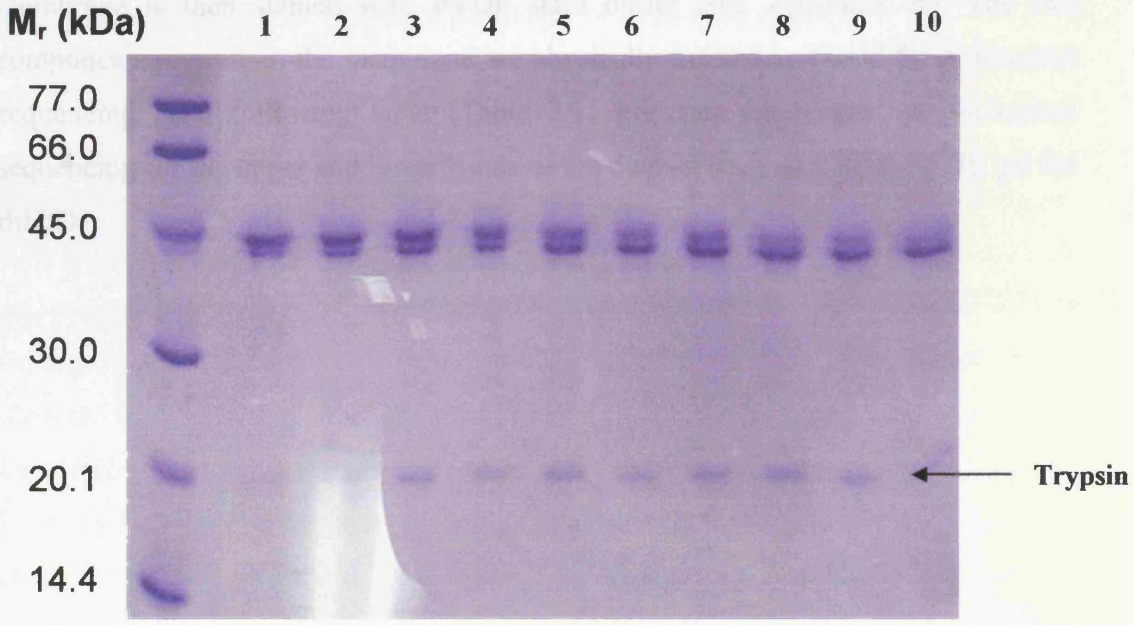

Figure 2.8 Timed tryptic digest of a purified sample of rhIDO. Lane **1** denotes the marker standards. Lanes **1-10** show the ten reactions between rhIDO and trypsin, where t = 1, 2, 3, …, 10 minutes.

2.2.3.5 N-Terminal Sequencing of the Two Components of rhIDO

N-terminal sequencing (or Edman degradation) is a useful method for the elucidation of the sequence of amino acids in a polypeptide chain. This technique is fully automated and it is capable of sequencing peptides containing up to about 20 amino acid residues. Peptide sequencing instruments automatically carry out all the reactions of the Edman degradation. The N-terminal derivatives are then analysed by reverse-phase HPLC.

After initial separation of the two rhIDO components on an SDS-PAGE gel, the two proteins are transferred (or blotted) electrophoretically from the acrylamide gel to a nitrocellulose membrane (Chapter 6, Figure 6.5) (see Chapter 6, Section 6.4.10). The gel and the nitrocellulose membrane, which has been previously soaked in PVDF (Polyvinylidene difluoride) transfer buffer (see Appendix A), are sandwiched between the two electrodes. A voltage is applied, *e.g.* 500 V or 125 mAmps constant current, which forces the two protein components to migrate form the SDS gel to the adjacent membrane. After ~ 90 minutes the membrane is removed and carefully washed with deionised water to remove any excess glycine. Removal of excess glycine is essential, since it causes high background in N-terminal sequencing. The nitrocellulose membrane is then stained with PVDF stain buffer (see Appendix A). The two components present on the membrane are physically excised and used for N-terminal sequencing. The following table (Table 2.1) presents the results of N-terminal sequencing for the upper and lower bands of the doublet seen on a SDS-PAGE gel for rhIDO.

	Low MW		High MW	
Cycle No	**Residue**	**Amount (pmoles)**	**Residue**	**Amount (pmoles)**
1	MET	9.09	MET	37.93
2	ARG	19.76	ARG	73.60
3	GLY	10.18	GLY	43.46
4	SER	3.26	SER	15.70
5	HIS	8.05	HIS	33.62
6	HIS	8.97	HIS	37.09
7	HIS	9.38	HIS	35.45
8	HIS	9.59	HIS	35.57
9	HIS	8.55	HIS	29.15
10	HIS	8.05	HIS	33.32
11	GLY	2.91	GLY	17.47
12	SER	0.84	SER	4.18
13	ALA	2.57	ALA	17.02
14			–	–
15			GLU	10.52

Table 2.1 N-terminal sequencing results for the two protein components present in a purified sample of rhIDO.

N-terminal sequencing clearly showed that the second band on the SDS-PAGE gel has the same starting sequence with the major component that is the 'intact' rhIDO, and not an impurity or an artifact of the electrophoresis (Figure 2.2).

2.2.3.6 Ion Exchange Chromatography

Ion-exchange chromatography using substituted cellulose/agarose anion exchangers, such as diethylaminoethyl (DEAE) and quaternary ammonium (Q) (Table 2.2), or cation exchangers such as carboxymethyl cellulose/agarose (CM) (Table 2.2) is frequently used and permits highly specific separation of proteins. Separation is obtained since different substances have different degrees of interaction with the ion exchanger due to differences in their charge densities. These interactions can be controlled by varying conditions such as ionic strength and pH. The differences in charge state of biological compounds are often considerable, and since ion chromatography is capable of separating species with very minor differences in properties, *e.g.* two proteins differing by only one charged amino acid, it is a very powerful separation technique.

Anion Exchangers	**Functional Group**
Diethylaminoethyl (DEAE)	$-OCH_2CH_2N^+H(CH_2CH_3)_2$
Quaternary ammonium (Q)	$-CH_2N^+(CH_3)_3$
Cation Exchangers	**Functional Group**
Carboxymethyl (CM)	$-OCH_2COO^-$

The isoelectric point (*p*I) value for the "intact" rhIDO, which is calculated from its cDNA sequence (including the 6×His tag) using the EMBL WWW gateway to isoelectric point (*8*), is 7.06. This value is in a good agreement with the value of 7.09 determined previously by isolectric focusing (*5*), and has shifted by approximately 0.16 from 6.9 of the native enzyme (*9*), as expected from the addition of the 6×His tag. Using the same method the *p*I value for the truncated form of rhIDO at Lys369 was calculated to be 6.85.

The starting buffer pH used for the separation is chosen so that substances to be bound to the exchanger are charged. The starting pH should be at least 1 pH unit above the isoelectric point value when anion exchangers are used.

In order to separate the two forms of rhIDO we have used a MonoQ anion exchanger. Several buffer systems have been tested (*e.g.* sodium phosphate, pH 8.0; potassium phosphate, pH 8.0; sodium carbonate pH 9.0) with different ionic strengths, but the best separation of the two components was obtained with Tris-HCl buffer (see Chapter 6, Section 6.4.9), using a stepwise ionic strength gradient. At pH 8.3 (pH of the buffer, 20 mM Tris-HCl) the two proteins have different charges, -7.0 for the 'intact' protein and -8.0 for the 'clipped' form, which allows us to separate the two components (Figure 2.9 (A)). The different fractions – containing either of the two forms of rhIDO – collected from the anion exchange chromatography column were applied on a SDS-PAGE gel to determine their identity (Figure 2.9 (B)).

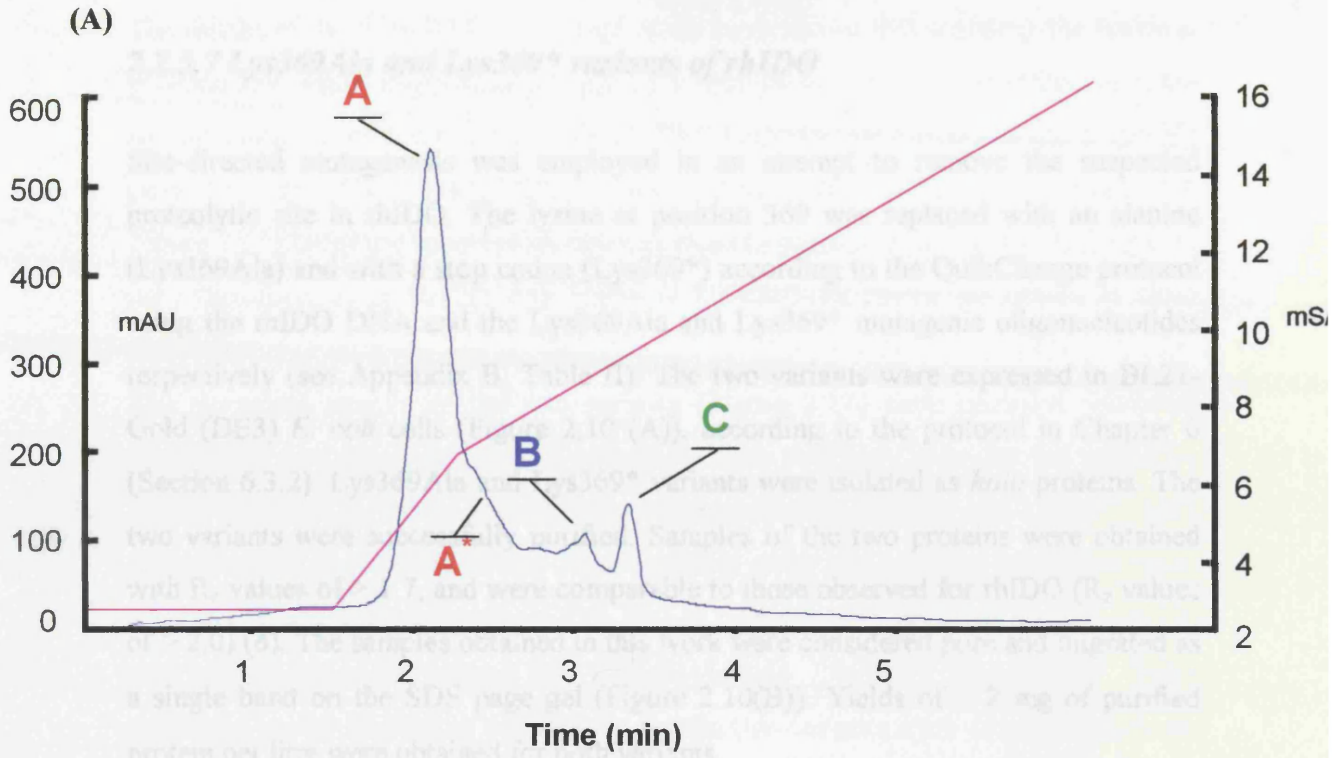

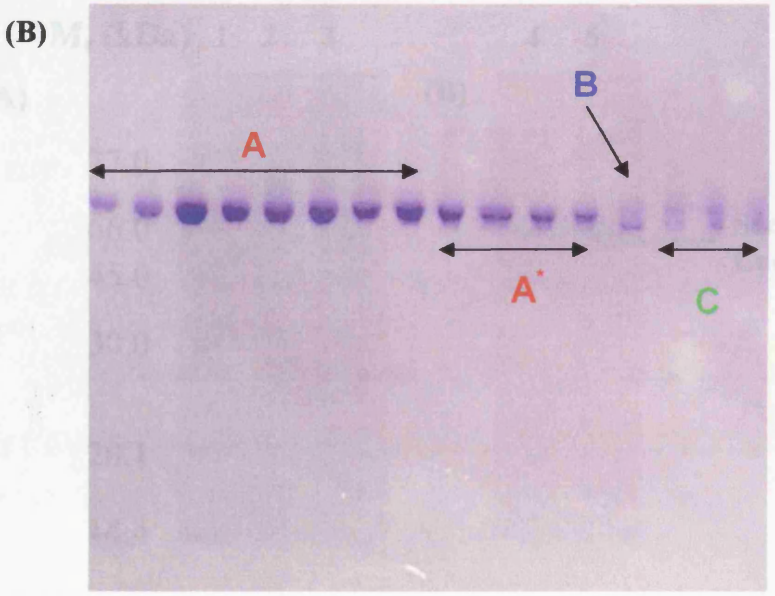

Figure 2.9 (A) FPLC trace for the separation of the two protein components present in a purified sample of rhIDO. **(B)** SDS-PAGE gel of the different fractions collected during the experiment. **A** = 'intact' rhIDO; **A*** = mixture of the two components; **B** = 'clipped' rhIDO; **C** = equal mixture of the two protein forms.

2.2.3.7 Lys369Ala and Lys369 variants of rhIDO*

Site-directed mutagenesis was employed in an attempt to remove the suspected proteolytic site in rhIDO. The lysine at position 369 was replaced with an alanine (Lys369Ala) and with a stop codon (Lys369*) according to the QuikChange protocol using the rhIDO DNA and the Lys369Ala and Lys369* mutagenic oligonucleotides respectively (see Appendix B, Table II). The two variants were expressed in BL21-Gold (DE3) *E. coli* cells (Figure 2.10 (A)), according to the protocol in Chapter 6 (Section 6.3.2). Lys369Ala and Lys369* variants were isolated as *holo* proteins. The two variants were successfully purified. Samples of the two proteins were obtained with R_z values of > 1.7, and were comparable to those observed for rhIDO (R_z values of > 2.0) (*6*). The samples obtained in this work were considered pure and migrated as a single band on the SDS page gel (Figure 2.10(B)). Yields of ~ 2 mg of purified protein per litre were obtained for both variants.

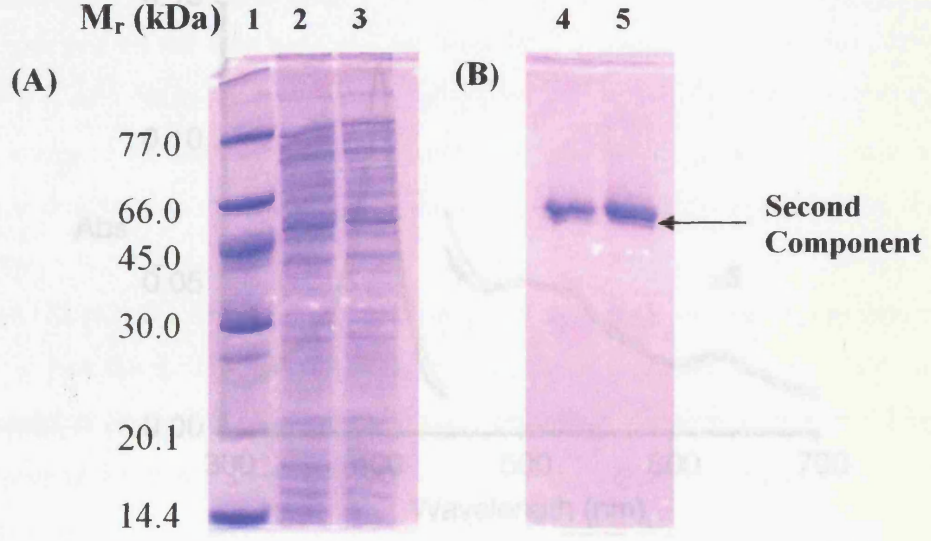

Figure 2.10 SDS-PAGE gel for the expression **(A)** and purification **(B)** of the Lys369A and Lys369* variants of rhIDO. **(A)** Lane **1** denotes the marker standards; Lane **2** cell free extract of Lys369A variant; Lane **3** cell free extract of Lys369* variant. **(B)** Lane **4** purified Lys369A variant; Lane **5** purified Lys369* variant. The minor band is present in both samples.

The results of the SDS-PAGE electrophoresis have shown that mutating the lysine at position 369, where tryptic-like proteolysis is thought to occur, has no effect, since the second minor component is still present. This suggests that Lys369 is not a specific proteolytic site. From the cDNA sequence of the rhIDO (Chapter 1, Section 1.7, Figure 1.11), there are other lysine residues close to position 369, *e.g.* Lys357, Lys353 *etc*. Therefore, even though one lysine is knocked-out, there are others in close proximity.

The electronic spectra of the two variants (Figure 2.11) were recorded following purification and they are in good agreement with published data for the wild-type rhIDO (Table 2.3). Molar absorption coefficients for Lys369Ala and Lys369* were determined as an average of two heme contents using the pyridine hemochromagen method (*10*) (Chapter 6, Section 6.4.2). Values of ε_{405} = 189 mM^{-1} cm^{-1} and ε_{405} = 170 mM^{-1} cm^{-1} were determined for Lys369Ala and Lys369*, respectively. These calculated molar absorption coefficients for the two variants were consistent with the published value for the wild-type rhIDO (*6*).

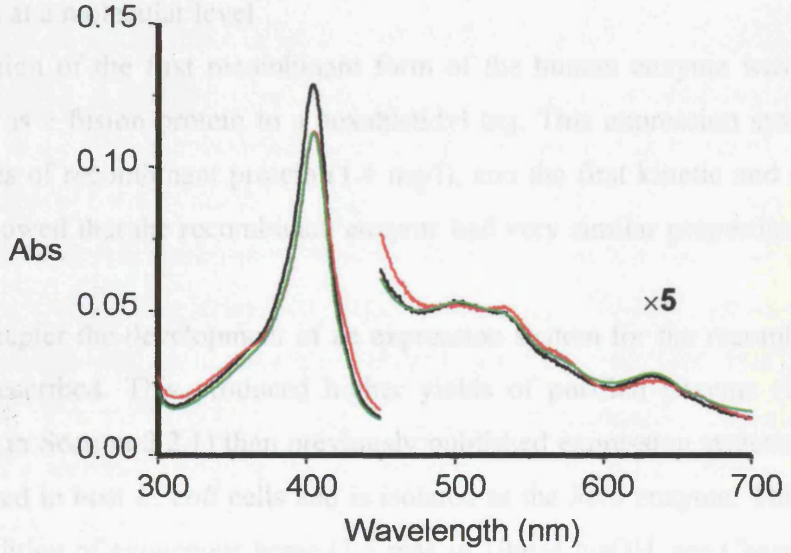

Figure 2.11 Electronic spectra of ferric rhIDO (black), Lys369Ala (red) and Lys369* (green). The visible region has been multiplied by a factor of five for clarity.

Table 2.3 Absorption maxima and absorption coefficients (in ( ), $mM^{-1}cm^{-1}$) for ferric and ferrous derivatives of Lys369A and Lys369* variants and wild-type rhIDO. ^{sh} = shoulder.

Derivative	λ_{max} (nm)		
	rhIDO	**Lys369A**	**Lys369***
ferric	404 (172), 500, 535, 633	405 (189), 500, 534, 633	405 (170), 500, 534, 570, 634, 666
ferrous	425, 527^{sh}, 558	428, 527^{sh}, 558	428, 527^{sh}, 558

2.3 Discussion

The functional properties of indoleamine 2,3-dioxygenase were reviewed in 1996 (*11*). At that time, all major kinetic, spectroscopic and functional studies had been carried out on the native rabbit intestinal enzyme. For the human enzyme, there is very little information available (*3, 4, 5, 12*). This lack of information, served as a catalyst for the development of new expression systems that can probe functional properties at a molecular level.

The isolation of the first recombinant form of the human enzyme was published in 2000 (*5*), as a fusion protein to a hexahistidyl tag. This expression system provided high yields of recombinant protein (1.4 mg/l), and the first kinetic and spectroscopic studies showed that the recombinant enzyme had very similar properties to the native enzyme.

In this Chapter the development of an expression system for the recombinant human IDO is described. This produced higher yields of purified enzyme (2.0 mg/l) (as discussed in Section 2.2.1) than previously published expression systems. The rhIDO is expressed in host *E. coli* cells and is isolated as the *holo* enzyme. This is achieved by the addition of exogenous heme (3.5 mM in 10mM NaOH, see Chapter 6, Section 6.3.2) in the LB medium during induction. Preliminary trials to add exogenous heme to the purified enzyme (by reconstitution) were unsuccessful, suggesting that the heme is efficiently incorporated during bacterial fermentation and that the heme binding cavity is buried inside the protein molecule.

Along with the optimization of the expression system for rhIDO, a series of studies have been carried out for the optimization of the purification procedures available for 6×His tagged proteins. The manufacturer's purification protocol (Qiagen™) suggests

the incorporation of high concentrations of imidazole in the wash and elution buffers. It is widely known that imizadole binds strongly to the heme iron, so an alternative procedure had to be devised in order to avoid obscuring the spectroscopic and functional data obtained for the recombinant enzyme. Replacement of imidazole with 1,2-dimethylimidazole failed to produce the same interactions that imidazole has with the Ni-NTA column. An alternative protocol for purifying 6×His tagged proteins describes the development of the affinity chromatography column using low pH buffers (pH 4.5-5.3), which effectively dissociated the bound protein from the Ni-NTA matrix. Due to the fact that rhIDO is very sensitive to changes in pH and that its stability range lies between pH 6.0 and pH 8.5, this protocol was not suitable for the purification of rhIDO and led to precipitation of the protein on the nickel column. Elution of the protein by using high concentrations of EDTA (100 mM), a bidentate ligand, results in the dissociation of the tagged protein from the column along with the nickel atoms. Excess EDTA is effectively removed by dialysis in storing buffer (see Appendix A). This modified protocol provides us with purified enzyme that can be confidently used to perform kinetic, spectroscopic and functional studies.

A major part of this Chapter is focused on the investigation of a suspected proteolytic site on rhIDO, a problem that has been encountered in previous work (*5, 13*). Littlejohn *et al.* (*5*) have reported the existence of a second component, which proved to be a 'clipped' form of the rhIDO, generated by a tryptic-like cleavage of the 'intact' enzyme, lacking 14 amino acid residues from the C-terminus. These results were obtained by electrospray ionization mass spectrometry (ESI-MS), which demonstrated that the purified samples consisted of two proteins with molecular sizes of 46,976 and 45,437 Da. The proteolytic site (Lys403) was determined by N- and C-terminal analysis. To prevent cleavage by an endogenous trypsin-like protease in the host bacterial cell, a serine protease inhibitor, phenylmethylsulfonyl fluoride (PMSF), was added to the LB medium during the induction phase, and to all buffers used for purification. In the above work it was claimed that they have managed to overcome this tryptic-like proteolysis in host bacterial cells by addition of this serine protease inhibitor (PMSF). The presence of the serine protease inhibitor resulted in the isolation of only the 'intact' protein as judged by SDS-PAGE electrophoresis and mass spectrometric analysis.

Although we have included the serine protease inhibitor in the growth media and to all the buffers used for purification, we could not prevent the cleavage of the recombinant enzyme by an endogenous protease in host bacterial cells. Addition of an array of protease inhibitors, in the form of a complete inhibitor cocktail (Roche™), during sonication still failed to protect the protein from proteolysis. Several experimental procedures, discussed in this Chapter (e.g., tryptic digestion, ESI-MS and MALDI-Tof spectrometry, N-Terminal sequencing and use of alkylating agents during SDS-PAGE electrophoresis) have suggested the presence of a proteolytic site after Lys369. With the knowledge that the presence of a second, although minor, truncated form of the enzyme in the purified sample could affect the kinetic and structural charactersation of rhIDO, we have developed an anion exchange method that successfully separated the two components. Numerous control experiments were carried out on pure mixtures of the 'intact' and 'clipped' components as well as on FPLC-purified samples of 'intact' rhIDO to determine the effect of the minor component on the kinetic, redox, or spectroscopic properties of the enzyme (presented in the following chapters). We were not able to detect any measurable differences in any of the experiments presented in this thesis.

The true identity of this proteolytic site is still elusive. *E. coli* might be degrading the recombinant protein. Exactly how *E. coli* can recognize the foreign protein, and thereby subject it to preferential turnover, is not known. Degradation of recombinant proteins can be reduced by using a mutant of *E. coli* strain that is deficient in one or more of the proteases responsible for protein degradation. In this Chapter we have presented the results of expressing rhIDO in Epicurian BL21-Gold (DE3) *E. coli* cells that lack the Lon and OmpT proteases. Expression in this host cells still resulted in the degradation of the rhIDO. There are examples in nature that proteolysis is of importance. For example, the intracellular machinery responsible for apoptosis depends on a family of proteases, called *caspases*. Caspases have a cysteine residue in their active site and cleave their target proteins at specific aspartic acids. Caspases are synthesised in the cell as inactive precursors, or *procaspases*, which are activated by other caspases (proteolytic cascade). It is not known if proteolysis of human IDO *in vivo* occurs, but proteolytic activation can be a possible scenario. In 1978, three different forms of the rabbit intestinal enzyme were evident upon isoelectric focusing (*1*). It was concluded that the three forms of the native enzyme had the same

molecular weight but different net charges. It is therefore apparent that proteolytic cleavage is a common trend between the native rabbit intestinal, recombinant human IDOs and recombinant TDO.

2.4 References

1. Shimizu, T., Nomiyama, S., Hirata, F., Hayaishi, O. (1978) *J. Biol. Chem., 253*, 4700-4706.
2. Hayaishi, O. (1976) *J. Biochem., 79*, 13p-21p.
3. Yamazaki, F., Kuroiwa, T., Takikawa, O., Kido, R. (1985) *Biochem. J., 230*, 635-638.
4. Littlejohn, T. K., Takikawa, O., Walker, M. J., Truscott, R. J. W. (2003) *J. Biol. Chem., 278*, 29525-29531.
5. Littlejohn, T. K., Takikawa, O., Skylas, D., Jamie, J. F., Walker, M. J., Truscott, R. J. W. (2000) *Protein Express. Purif., 19*, 22-29.
6. Papadopoulou, N. D., Mewies, M., McLean, K. J., Seward, H. E., Svistunenko, D. A., Munro, A. W., Raven, E. L. (2005) *Biochem., 44*, 14318-14328.
7. http://ca.expassy.org/tools/peptide-mass.html.
8. EMBL http://www.embl-heidelberg.de/cgi/pi-wrapper.pl.
9. Takikawa, O., Kuroiwa, T., Yamazaki, F., Kido, R. (1988) *J. Biol. Chem., 263*, 2041-2048.
10. Antonini, M., Brunori, E. (1971) *Hemoglobin and Myoglobin and their Reactions with Ligands.*, North Holland Publishers, Amsterdam.
11. Sono, M., Roach, M. P., Coulter, E. D., Dawson, J. H. (1996) *Chem. Rev., 96*, 2841-2887.
12. Terentis, A. C., Thomas, S. R. Takikawa, O., Littlejohn, T. K., Truscott, R. J. W., Armstrong, R. S., Yeh, S., Stocker, R. (2002) *J. Biol. Chem., 277*, 15788-15794.
13. Manandhar, S. P. (2002) *Inter. Congr. Series, 1233*, 161-169.

Chapter 3

Redox and Spectroscopic Properties of Recombinant Human Indoleamine 2,3-Dioxygenase

3.1 Introduction

As highlighted in Chapter 1, development of our understanding of the detailed mechanism of the IDO enzyme has been hampered by the limited quantities of pure enzyme that can be extracted and purified from readily available sources. To date, almost all studies on the purified enzyme have been carried out with rabbit indoleamine 2,3-dioxygenase (rIDO). For the human enzyme (hIDO), there is very little functional or spectroscopic information available (*1-5*). Indeed the dioxygenase was first isolated from rabbit intestine, and the enzyme was invariably purified with the heme iron in the ferric (Fe^{3+}) state (*6*). In this work, we have developed an efficient bacterial expression system (Chapter 2) for the production of recombinant human IDO (rhIDO) and have used this to examine the spectroscopic properties (electronic and EPR, MCD and CD properties) of the enzyme.

To date, the heme iron coordination structure of IDO (from various sources) and of L-Trp binding has been investigated by EPR, MCD and CD spectroscopy (*7*), site-directed mutagenesis (*1*) and resonance Raman spectroscopy (*2*), but no definitive picture of the active site of the dioxygenase has emerged. Although the crystal structure of hIDO has been recently published (*8*), the nature of the substrate binding and the iron–oxygen interactions remain unclear. In addition there is no information on the redox properties of the heme for either rIDO or hIDO. This is an important omission because the redox properties of the metal ion are a key determinant in controlling biological function. To begin to address these deficiencies, we have examined in detail the spectroscopic and redox properties of the substrate-bound and substrate-free rhIDO, which are presented in this Chapter.

3.2 Results

3.2.1 Electronic Properties of rhIDO

3.2.1.1 Electronic Absorption Spectra of rhIDO

The electronic spectrum of rhIDO was recorded (Figure 3.1(A)) following purification. There are no reported wavelength maxima for human IDO (hIDO); we have therefore compared wavelength maxima with the corresponding maxima for the wild-type rabbit enzyme, for which most of the published data have been obtained. The spectrum of the ferric form of rhIDO (λ_{max} = 404, 500, 535, and 633 nm) has maxima that are consistent with a mixed population of high- and low-spin heme species. Wavelength maxima of 406 and 630 nm for rhIDO have been previously reported (*9*). This spectrum shows no evidence for formation of a hydroxide-bound heme (in the visible region) with increasing pH (Figure 3.1 (B)): there are no substantial changes in the peak positions or intensities in the pH range of 5.5-10.7, although there is a drop in the Soret band above pH ≈8.5 (Figure 3.1(B), inset), which can be attributed to partial denaturation of the protein. Above pH ≈9 and below pH ≈5, the enzyme was not stable enough to allow meaningful data collection. Ferric rIDO has also a pH-independent electronic spectrum, as reported by Uchida *et al.* (*10*).

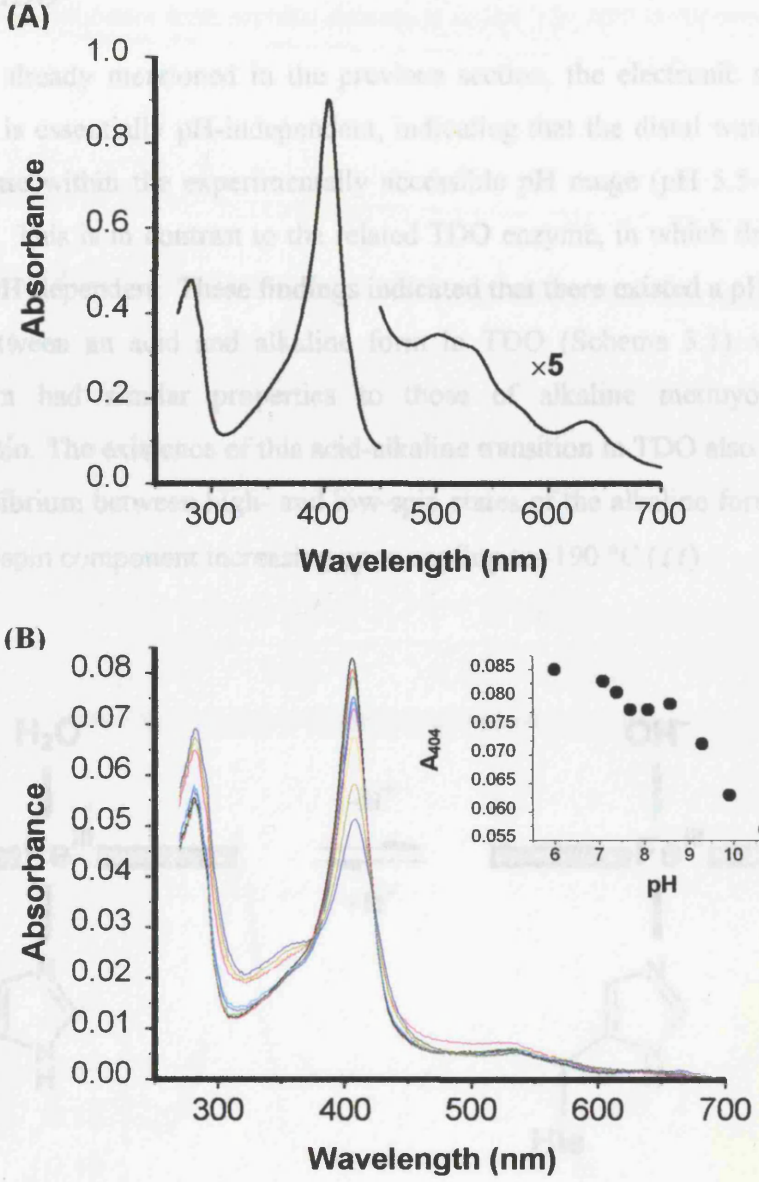

Figure 3.1 **(A)** UV-visible spectrum of ferric rhIDO (pH 8.0 and 25.0 °C). Absorbance values in the visible region have been multiplied by a factor of five. **(B)** pH dependency of the electronic spectrum of ferric rhIDO. (Inset) Plot of absorbance changes in the Soret band of ferric rhIDO upon changes in pH (1 mM potassium phosphate, pH 6.0 at 25 °C).

3.2.1.2 Acid-Alkaline Transition and Thermal Spin Equilibrium of the Heme in Ferric rhIDO

As we have already mentioned in the previous section, the electronic spectrum of ferric rhIDO is essentially pH-independent, indicating that the distal water molecule does not titrate within the experimentally accessible pH range (pH 5.5-10.7 in our experiments). This is in contrast to the related TDO enzyme, in which the electronic spectrum is pH-dependent. These findings indicated that there existed a pH-dependent transition between an acid and alkaline form in TDO (Scheme 3.1) and that the alkaline form had similar properties to those of alkaline metmyoglobin and methemoglobin. The existence of this acid-alkaline transition in TDO also suggested a thermal equilibrium between high- and low-spin states of the alkaline forms of TDO, with the low-spin component increasing upon cooling to -190 °C (*11*).

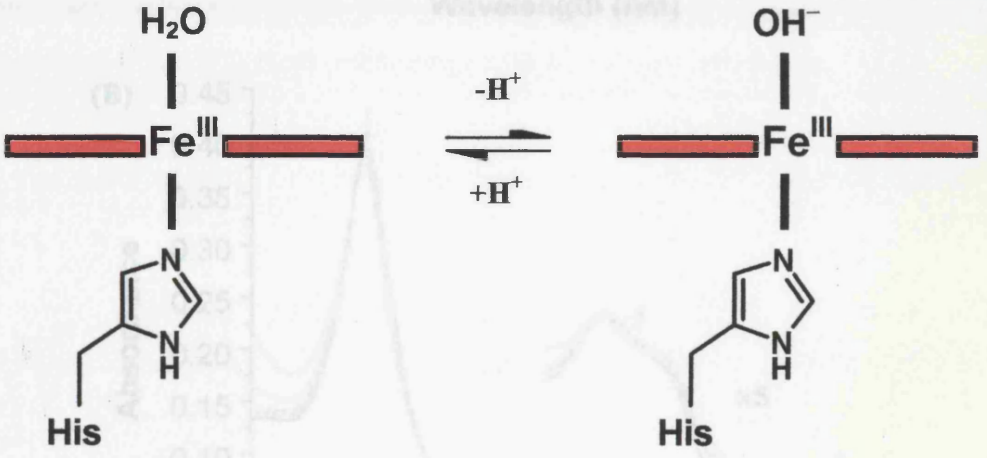

Scheme 3.1 Diagrammatic representation of the acid-alkaline transition in rat liver TDO.

A thermal spin equilibrium was determined for rhIDO in the absence (Figure 3.2(A)) and presence of L-Trp (Figure 3.2(B)) by increasing the temperature from 5 °C to 55 °C at alkaline pH. Under these conditions, the low-spin component of rhIDO increased with concomitant decreases in the high-spin bands when the temperature

was lowered from 55 °C to 5 °C. In contrast, elevation of the temperature increased the high-spin components with parallel decreases in the low-spin components.

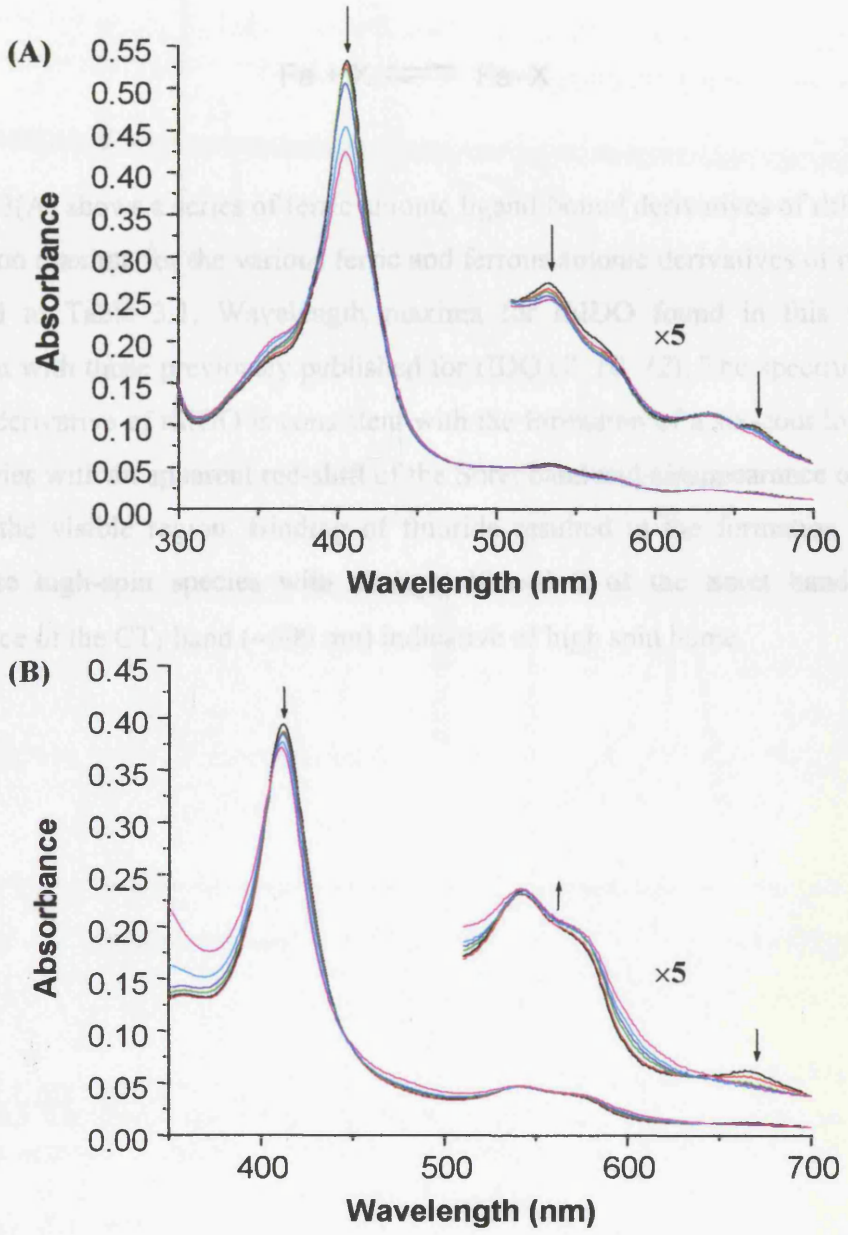

Figure 3.2 Temperature dependent electronic spectra of **(A)** ferric rhIDO in 0.2 M Tris-HCl, pH 8.8 in the absence of L-Trp and **(B)** those of ferric rhIDO in 0.2 M Tris-HCl in the presence of 10 mM L-Trp. The enzyme concentration employed was 30 μM and arrows indicate the direction of change in absorbance upon successive changes in temperature (5 °C = black; 55 °C = magenta).

3.2.1.3 Binding of Anionic Ligands to rhIDO

The simplest of all heme protein reactions are those involving iron-centred ligand (X) binding, Equation 3.1.

$$Fe + X \rightleftharpoons Fe\text{–}X \qquad \ldots (3.1)$$

Figure 3.3(A) shows a series of ferric anionic ligand-bound derivatives of rhIDO. Absorption maxima for the various ferric and ferrous anionic derivatives of rhIDO are presented in Table 3.1. Wavelength maxima for rhIDO found in this work are consistent with those previously published for rIDO (*7, 10, 12*). The spectrum for the cyanide derivative of rhIDO is consistent with the formation of a six-coordinate, low-spin species with an apparent red-shift of the Soret band and disappearance of the CT_1 band in the visible region. Binding of fluoride resulted in the formation of a six-coordinate high-spin species with a slight blue-shift of the Soret band and the appearance of the CT_1 band (~600 nm) indicative of high spin heme.

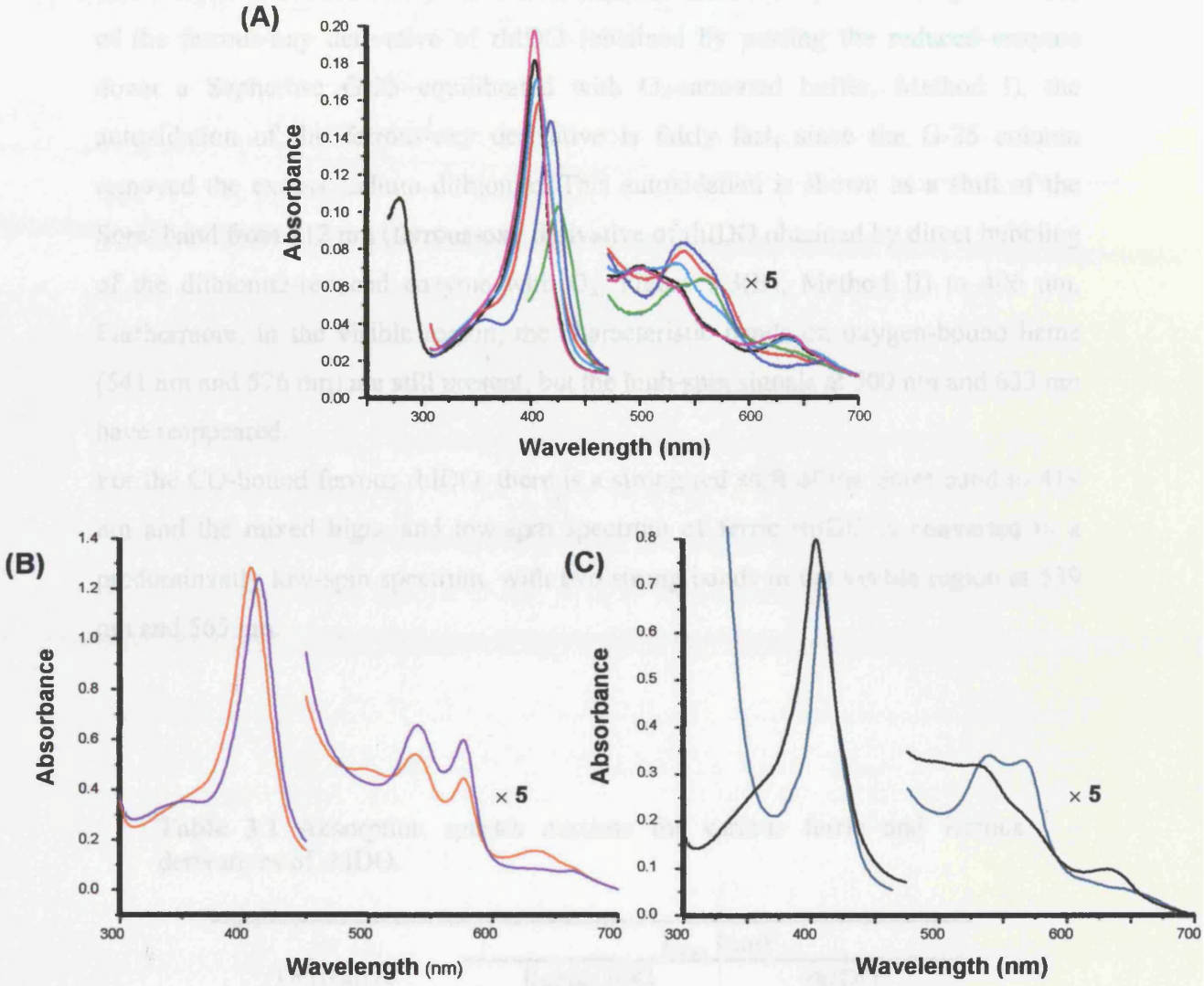

Figure 3.3 Electronic spectra of **(A)** ferric, ferrous and the ferric anionic ligand-bound derivatives of rhIDO. Conditions: 100 mM potassium phosphate, pH 7.0, 25 °C; ferric (black); ferric + L-Trp (red); ferrous (green); CN^- (blue); N_3^- (cyan); F^- (magenta). **(B)** Ferrous-oxy derivatives, Method I = orange, Method II = violet (for details of Methods I and II see text); **(C)** Ferric rhIDO and ferrous CO-bound rhIDO.

The ferrous-oxy derivative of rhIDO could be generated by two different protocols (see Chapter 6, Section 6.4.4). As is clear from the electronic spectrum (Figure 3.3(B) of the ferrous-oxy derivative of rhIDO (obtained by passing the reduced enzyme down a Sepharose G-25 equilibrated with O_2-saturated buffer, Method I), the autoxidation of the ferrous-oxy derivative is fairly fast, since the G-25 column removed the excess sodium dithionite. This autoxidation is shown as a shift of the Soret band from 412 nm (ferrous-oxy derivative of rhIDO obtained by direct bubbling of the dithionite-reduced enzyme with O_2, Figure 3.3(B), Method II) to 406 nm. Furthermore, in the visible region, the characteristic bands on oxygen-bound heme (541 nm and 576 nm) are still present, but the high-spin signals at 500 nm and 633 nm have reappeared.

For the CO-bound ferrous rhIDO, there is a strong red shift of the Soret band to 419 nm and the mixed high- and low-spin spectrum of ferric rhIDO is converted to a predominantly low-spin spectrum, with two strong bands in the visible region at 539 nm and 565 nm.

Table 3.1 Absorption spectra maxima for various ferric and ferrous derivatives of rhIDO.

Derivative	λ_{max} (nm)	
	Rabbit IDO	rhIDO
Ferric	406, 500, 534, 570, 632	404, 500, 535, 633
Ferric + L-Trp	412, 540, 576	411, 540, 576
Ferrous	429, 558	425, 527^{sh}, 558
Ferrous-oxy	415, 544, 577	412, 539, 576
Ferrous-CO	420, 539, 570	419, 539, 565
Ferric-azide	416.5	414, 535, 572, 634
Ferric-cyanide	428, 532, 562	419, 540, 570
Ferric-fluoride	402, 488, 608	404, 497, 537, 572, 632

3.2.1.4 Investigation of L-Trp Binding and its pH Dependency

Binding of L-Trp to ferric rhIDO leads to the formation of a low-spin species (λ_{max} = 411, 540 and 576 nm, Figure 3.3(A)). Comparison with other heme proteins (*e.g.* horseradish peroxidase (pH 12.3): λ_{max} = 414, 543, 573 nm; horse heart myoglobin (pH 10.9, mixed high-spin/low-spin): λ_{max} = 411, 485^{sh}, 541, 583, 593^{sh} nm, (*13*)) indicates that the spectrum for rhIDO arises from formation of a low-spin, hydroxide-bound heme. This new substrate-bound species is now pH-dependent (Figure 3.4), with low-spin heme dominating at alkaline pH. A pK_a of 6.7 ± 0.1 can be extracted from a plot of the absorbance at 406 nm *versus* pH (Figure 3.4, inset). To quantify the binding interaction, the equilibrium binding constant, K_D, for binding of L-Trp to ferric IDO was measured. At pH 7.0, a value for K_D of 0.57 ± 0.05 mM was determined. This binding constant varies with pH (Figure 3.5(A)) indicating that it is sensitive to titration of another group. A fit of these data to a single proton process yields a pK_a of 7.8 ± 0.1 (Equation 3.2) (*14*).

$$Abs_{406} = (K_D A_i + [\text{L-Trp}]_{tot} A_f)/(K_D + [\text{L-Trp}]_{tot}) \quad \ldots (3.2)$$

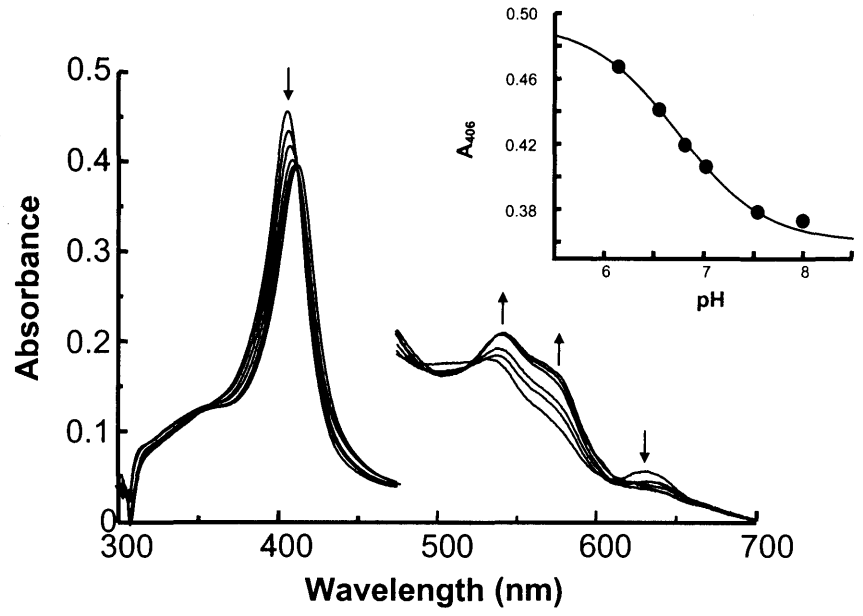

Figure 3.4 pH dependence of the UV-visible spectra of rhIDO in the presence of 20 mM L-Trp. (Inset) Fit of the absorbance at 406 nm to a single proton process. Absorbance values in the visible region have been multiplied by a factor of five; and arrows indicate the direction of change in absorbance upon successive changes in pH.

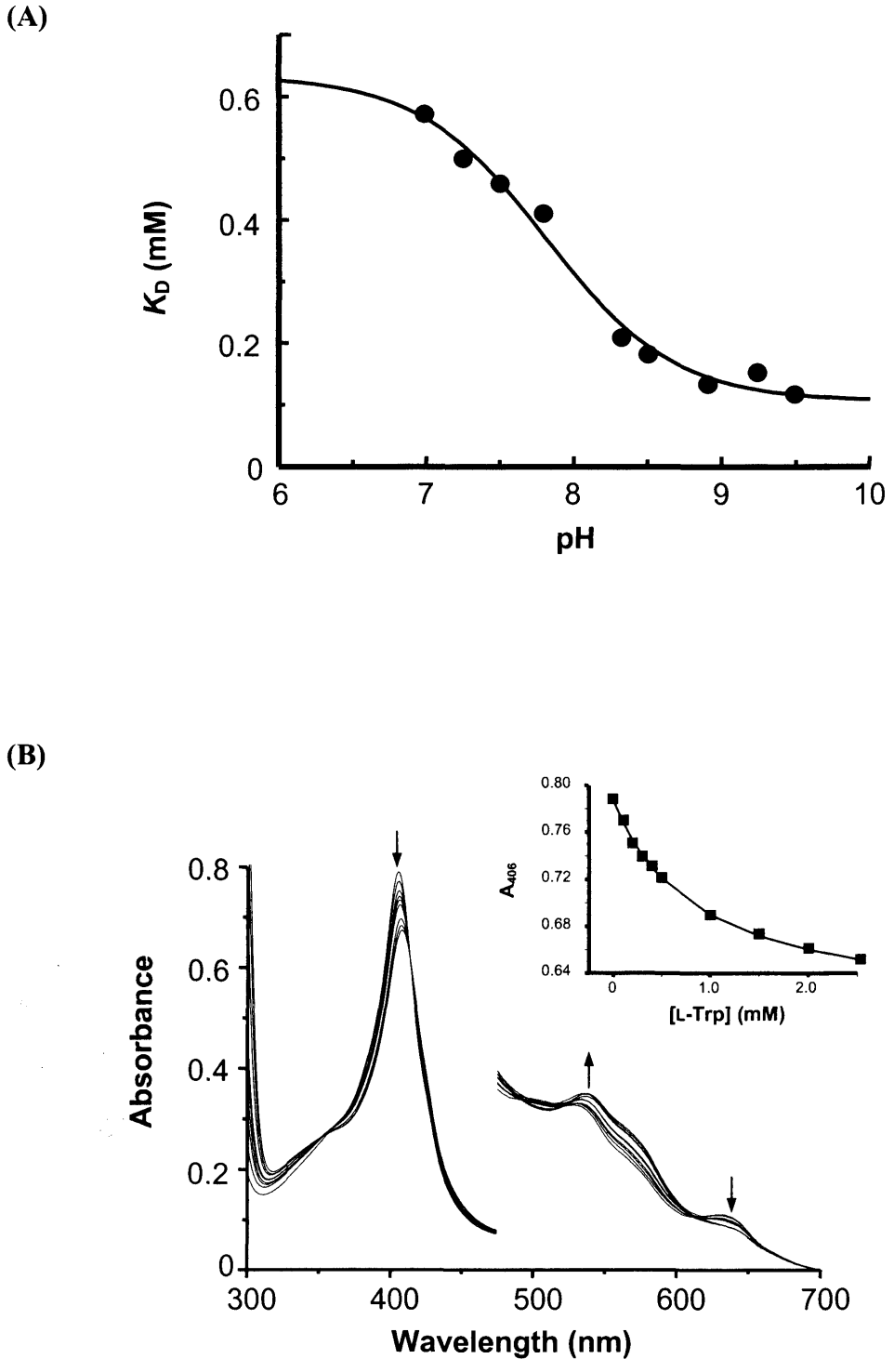

Figure 3.5 (A) Plot of the equilibrium binding constant, K_D, versus pH for binding L-Trp to ferric rhIDO. Data were fitted to a single proton process (Chapter 6, Equation 6.11). **(B)** Representative data set for the determination of K_D at pH 7.0. The visible region has been multiplied by a factor of five, and arrows indicate the direction of change in absorbance upon successive additions of L-Trp. (Inset) Fit of data at 406 nm to Equation 3.2 (conditions: 50 mM potassium phosphate at 25.0

3.2.2 Magnetic Circular Dichroism (MCD) Spectrosopy

3.2.2.1 MCD Spectroscopy of Ferric rhIDO at Acidic and Alkaline pH

UV-visible and near-IR MCD spectra of rhIDO at pH 6.6 (Figures 3.6(A) and 3.6(B), respectively) are characteristic of ferric heme, showing both low- and high-spin features. MCD spectra for rabbit IDO have been published previously (*7, 10*), but did not include measurements in the near-IR region from which very detailed information can be obtained. For rhIDO, the Soret crossover is at 410 nm and its peak-trough intensity is in between the values expected for a purely low-spin (120-160 $M^{-1}cm^{-1}T^{-1}$) or high-spin species (5-25 $M^{-1}cm^{-1}T^{-1}$). Low-spin bands dominate the visible region but a negative feature at 641 nm is part of a high-spin ligand-metal charge transfer derivative, CT_2. Spectra in the near-IR region (Figure 3.6(B)) are also consistent with a mix of high- and low-spin species. In this case, two CT bands are observed at 1040 and 1570 nm. The 1570 nm band arises from ligand-metal charge transfer from the porphyrin to the ferric *d*-orbitals of low-spin iron (CT_{ls}) and its position is consistent with bis-nitrogenous ligation (*15, 16*). The MCD spectra of high-spin heme species also contain ligand-metal CT bands, CT_1 and CT_2, which shift with changes in axial ligation (*13, 17*). The CT_2 band is observed as the negative trough of the derivative in the visible region (see above). The feature at 1040 nm is the positive lobe of the CT_1 derivative, and the negative lobe of this band is obscured by the more intense CT_{ls} band at 1570 nm. This negative lobe obscures in turn the vibrational side band of the CT_{ls} feature. Together, the positions of $CT_{1,2}$ are consistent with coordination of a nitrogen ligand and a second, neutral ligand to the heme (*e.g.* histidine/water). The intensities of the transitions suggest roughly equal populations of high- and low-spin heme at this pH.

At pH 8.0 (Figure 3.6(A)), there is an increase in intensity in the Soret and visible regions, reflecting an increase in low-spin heme content, and a decrease in the CT_2 band (641 nm), reflecting a decrease in high-spin heme content. In the near-IR region, the 1040 nm feature has decreased to a similar extent (15% of total heme population) and the more intense CT_{ls} feature at 1570 nm now has a vibrational sideband at 1346 nm. There are no major changes wavelength maxima of the CT bands compared to pH 6.6, which suggests that the two dominant species observed at acidic pH (low-spin bis-nitrogenous and high-spin histidine/water) are unchanged. In contrast to previous work (*2*), there is no evidence at room temperature for the formation of a

histidine/hydroxide species at alkaline pH, in agreement with the observation that the UV-visible spectrum of rhIDO is pH-independent. Histidine/hydroxide coordination is characteristic of intense $CT_{1,2}$ bands which are shifted to lower wavelength compared to histidine/neutral ligand species (*13, 17, 18*).

3.2.2.2 MCD Spectroscopy of Ferric rhIDO in the Presence of L-Trp

In the presence of L-Trp at pH 8.0, there is a clear increase in intensity throughout the Soret and visible regions, which indicates an increase in low-spin heme. The high-spin CT_2 band at 641 nm (Figure 3.6(A)) is diminished in intensity and accounts for only ≈7% of the total heme species. There are shifts in the bands throughout the visible region that indicate formation of a new low-spin species; this is confirmed in the near-IR spectrum, where a new feature at 1000 nm is observed. The shift in peak wavelength from the position of the CT_1 positive lobe, the absence of a corresponding CT_2 band in the visible region and the clear vibrational sideband in the second CT_{ls} feature suggest that this band is a CT_{ls} feature arising from a new low-spin species rather than from a feature of high-spin CT_1 band. Its maximum at 1000 nm is similar to that observed for hydroxide-bound myoglobin (1035 nm) (*13, 19*) and hydroxide-bound horseradish peroxidase at pH 12.3 (1100 nm) (*20, 21*) both of which have histidine/hydroxide ligation at room temperature. The second CT_{ls} feature at 1515 nm is shifted by ~60 nm from its maximum in the absence of tryptophan but remains in the range expected for histidine/nitrogenous axial ligation and there are no changes in the corresponding EPR species (g_z = 2.94) on binding of L-Trp which suggests no major changes in ligation or ligand conformation in this species. The intensity of this band accounts for ≈30% of the heme population.

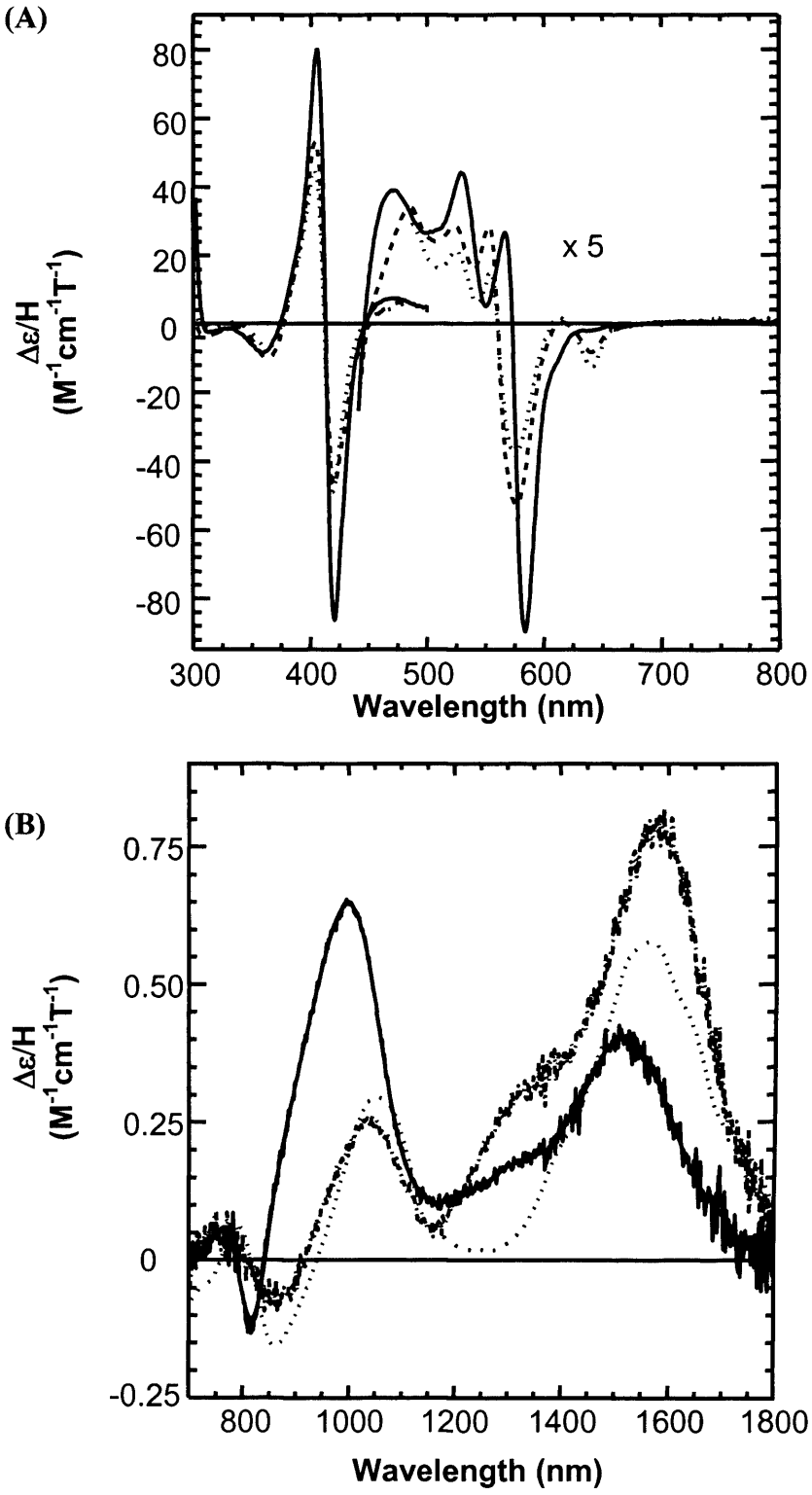

Figure 3.6 Room-temperature MCD at 6 T in the UV-visible (A) and near-IR (B) regions of ferric rhIDO at pH* 6.6 (• • •, [rhIDO] = 132 μM in both cases), ferric rhIDO at pH* 8.0 (– – –, [rhIDO] = 35 and 169 μM in the Soret and visible/near-IR, respectively), and ferric rhIDO at pH* 8.0 in the presence of 20 mM L-Trp (—, [rhIDO] = 45 and 224 μM, respectively).

3.2.2.3 MCD Spectroscopy of Ferrous rhIDO

The spectrum of ferrous rhIDO (Figure 3A.7) contains an asymmetric Soret feature with a positive peak at 436 nm, positive features at 524, 552 and ~770 nm, and negative features at 532 and 592 nm. The spectrum is similar to ferrous myoglobin (*22, 23*) and ferrous horseradish peroxidase (*24*), both of which contain 5-coordinate, high-spin heme. We therefore assign ferrous rhIDO as containing a 5-coordinate high-spin heme as the single species, with histidine as the fifth (proximal) ligand. There is no evidence for low-spin heme, which suggests that any internal (nitrogenous) ligands present in the ferric form are no longer coordinated.

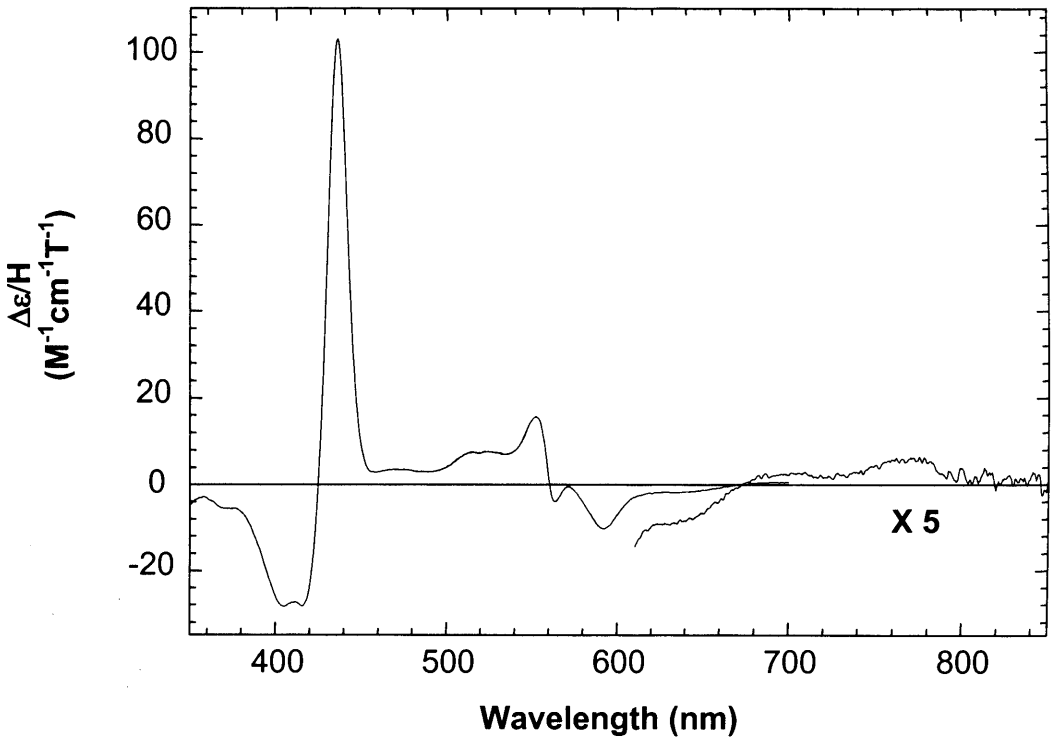

Figure 3.7 Room-temperature MCD spectra at 6 T of ferrous rhIDO (66 μM) at pH* 6.6.

3.2.3 Electron Paramagnetic Resonance (EPR) Spectroscopy

EPR spectra for human IDO have not been published, although rabbit IDO has been examined (*7*). The EPR spectrum of rhIDO at pH 6.6 (Figure 3.8(A)) contains high- and low-spin species with g-values of g = 5.96, 5.53 and 1.99 and g = 2.94, 2.25 and 1.50, respectively. Rhombic g-values of 2.94, 2.25 and 1.50 are associated with bis-histidine-ligation, in which the histidine planes are near parallel (*16, 25, 26*). The high-spin signals are slightly rhombic with splitting on the g_{xy} feature at g = 5.7.

At pH 8.0 (Figure 3.8(B)), the high-spin signals are diminished with respect to the low-spin species, the latter accounting for ≈80% of the heme population at 10.8 K. Minor but sharp features at g = 2.52 and 1.86 (middle g-value obscured) represent a low-spin species whose g-values are consistent with those seen in histidine/hydroxide coordination: since there is no evidence of histidine/hydroxide coordination in the MCD spectra at room temperature (as discussed above, Figure 3.6), this probably reflects a freezing-induced artefact. There are numerous examples in the heme literature (particularly the peroxidase literature, see for example (*27*)) of water/histidine coordinated heme producing, when frozen at cryogenic temperatures, a fraction of low-spin heme species for which there is no evidence at ambient temperatures. The factors that influence this are not known.

On addition of L-Trp at pH 8.0, sharp rhombic signals (g = 2.52, 2.19 and 1.86) are observed (Figure 3.8(C)) that arise from low-spin heme and are associated with histidine/hydroxide coordination. Minor signals from high-spin heme (g = 5.96) and the other low-spin species (g_z = 2.94) are also present in this spectrum.

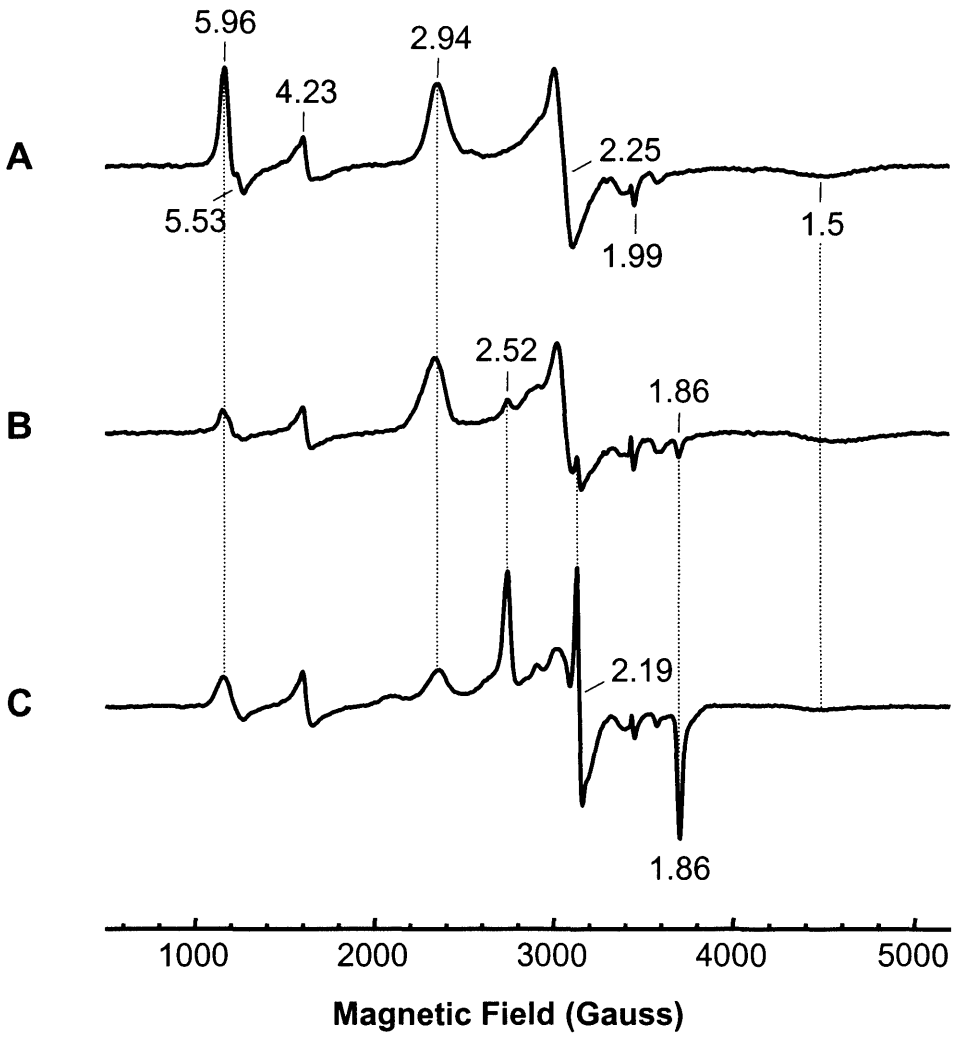

Figure 3.8 Perpendicular mode X-band EPR spectra of ferric rhIDO at pH 6.6 (A), ferric rhIDO at pH 8.0 (B), and ferric rhIDO in the presence of 20 mM L-Trp at pH 8.0.

3.2.4 Circular Dichroism Spectroscopy

The ferric form of rhIDO showed negative Cotton effects in the Soret region as shown in Figure 3.9(A). The intensity value of ~-0.8 ([ϑ], mdeg) at ~400 nm for ferric rhIDO in the absence of L-Trp was considerably lower than that obtained for the rabbit intestinal dioxygenase ([ϑ] = -12 mdeg, (*10*)). Upon addition of a saturating amount of L-Trp, the trough position of ferric rhIDO shifted to longer wavelength and an increase in the intensity, to -1.3 mdeg, was observed associated with the peak shift. It appears that the shift of the CD peak position is related to the spin state conversion induced by substrate binding. The changes in the CD intensity reflect another kind of change in the structure, such as changes in the interaction between the heme

prosthetic group and nearby aromatic amino acid residue(s) from the protein moiety. A conformational change induced by the interaction between the heme and the added substrate, L-Trp, is a possible cause of the changes in the CD intensity. In conclusion, from the rhIDO structure (Chapter 1, Figure 1.21) and the above CD observations, it can be suggested that upon substrate binding the residues that line the distal site (or even His303, which is located further away, somewhere in the interface between the two domains) move closer to the heme centre causing changes in the CD spectrum.

The far UV CD spectrum of ferric rhIDO (Figure 3.9(B)) was obtained to investigate its secondary structure. The far UV CD spectra obtained by Littlejohn *et al.* (*1*) were further analysed using the K2D deconvolution program. This analysis showed that the wild type IDO protein exhibited a structure consisting of 31% α-helical, 11% β-sheet, and 58% random coil.

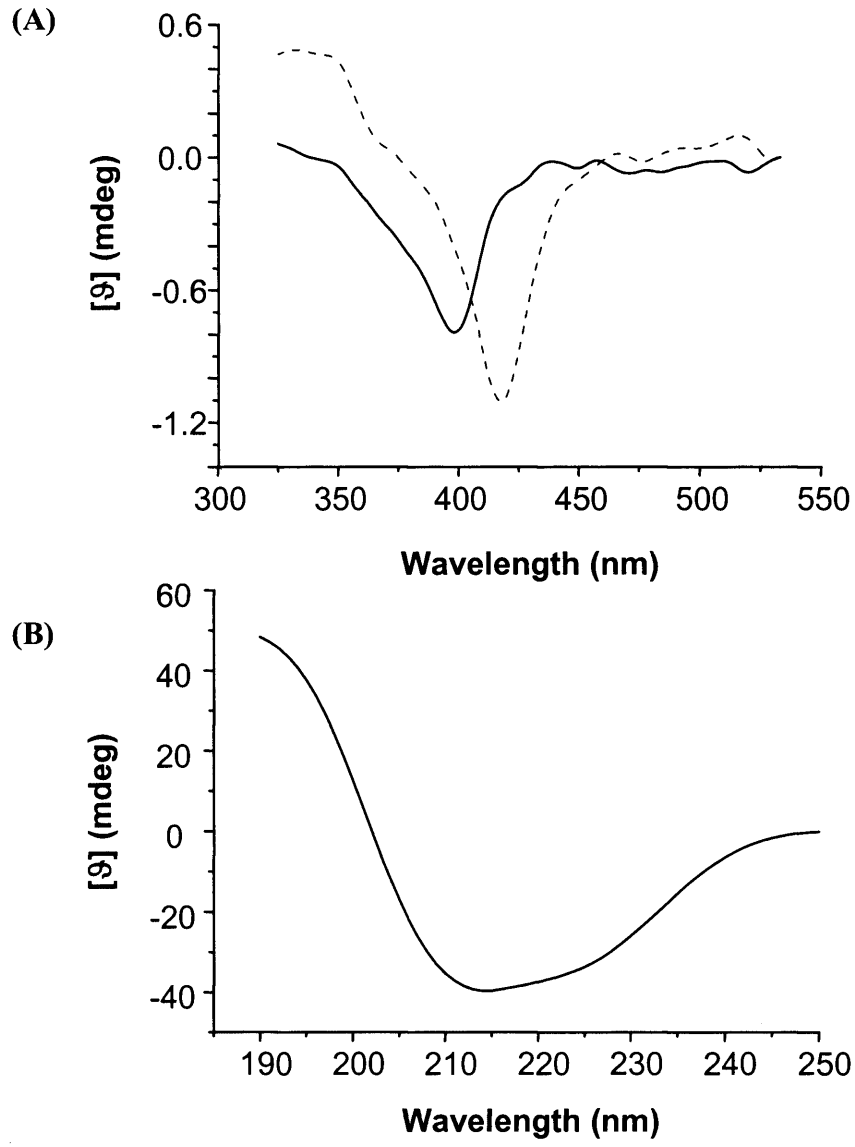

Figure 3.9 Circular dichroism analyses of ferric wild type rhIDO (30 μM) (A) in the visible region (320-600 nm) in the absence (—) and presence (– – –) of 20 mM L-Trp, and (B) in the far-UV region (190-260 nm). The CD spectra were conducted in 100 mM potassium phosphate buffer, pH 8.0.

3.2.5 Redox Potentiometry

3.2.5.1 Redox Titrations on rhIDO in the Absence and Presence of L-Trp

Selected spectra obtained during anaerobic redox titration of rhIDO are shown in Figure 3.10(A). The redox process was clearly reversible, with no sign of hysteresis in the oxidative or reductive directions; spectra collected in the oxidative and reductive stages were near identical at equivalent potentials. Clean isosbestic points were observed indicating only two absorbing species. Control experiments confirmed that the observed reduction potential was not altered in the presence of the minor (cleaved) component (Appendix D). Data sets are all consistent with each other for both "intact" and "clipped" forms of the enzyme (Table 3.2). Clearly the "clipping" has no effect on the heme thermodynamics. On reduction of rhIDO there is a decrease in intensity of the Soret band and a shift to longer wavelength, consistent with the formation of ferrous heme. Data were fitted to a single electron process (Nernst equation) at either 407 nm (Figure 3.10(B)) or 429 nm (Figure 3.10(C)); these analyses at different wavelengths gave results that were within error of one another. The reduction potential (average value from data at 407 and 429 nm) was –30 ± 4 mV.

Table 3.2 Summary of redox potential obtained for both the "intact" and "clipped" forms of rhIDO.

Enzyme		A_{407} Potential	A_{429} Potential
"Intact"	–L-Trp	- 31 ± 3 mV	- 26 ± 4 mV
"Clipped"	–L-Trp	- 27 ± 3 mV	- 34 ± 4 mV
	+L-Trp	+16 ± 1 mV	+18 ± 2 mV

In the presence of 15 mM L-Trp (Figure 3.11), similar absorbance changes were observed. In this case, the reduction potential was 16 ± 3 mV (Figure 3.11, inset), an increase of 46 mV over the value for the substrate-free enzyme.

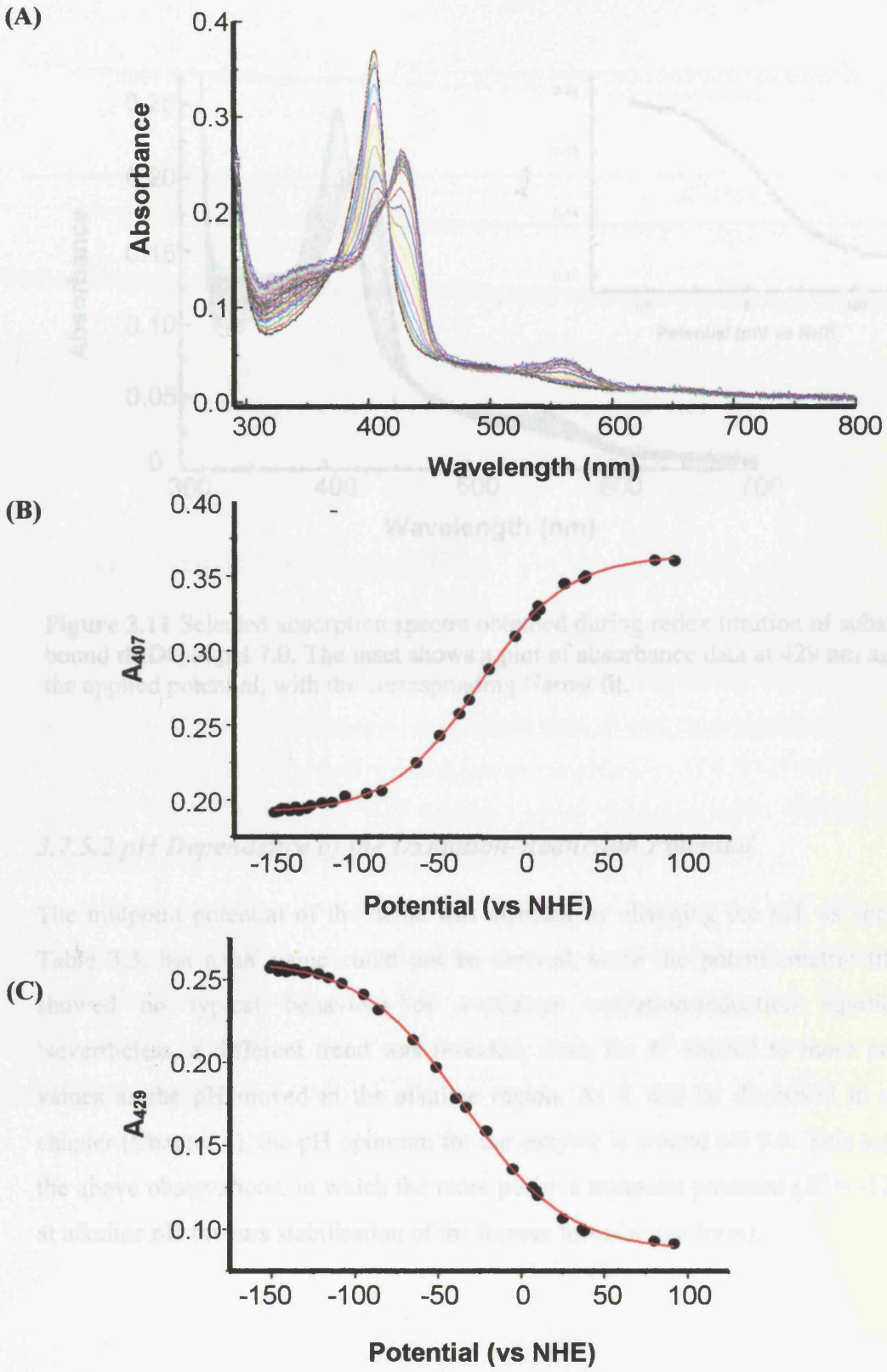

Figure 3.10 (A) Spectral redox titration for the "clipped" form of IDO. Soret peak shifts from ~405 nm to ~ 428 nm. Isosbestics at ~ 406 nm and 370 nm. Smaller reduced peak accumulates at ~ 559 nm in α/β region. The titration is fully reversible without hysteresis. (B) Data fit at 407 nm to single electron Nernst function. E^0 value of –27 ± 3 mV. (C) Data fit at 429 nm to single electron Nernst function. E^0 value of –34 ± 3 mV.

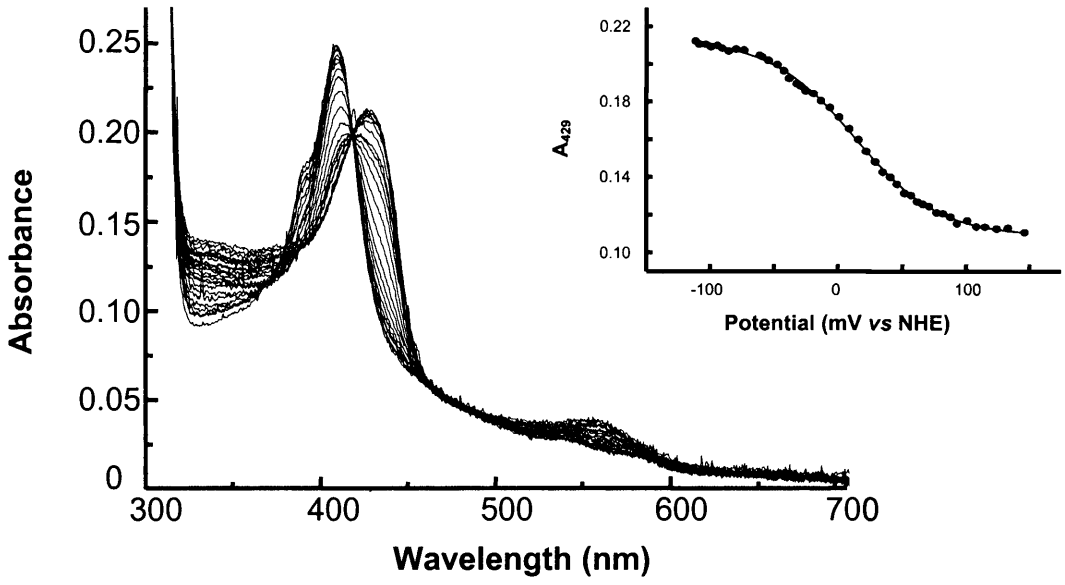

Figure 3.11 Selected absorption spectra obtained during redox titration of substrate-bound rhIDO at pH 7.0. The inset shows a plot of absorbance data at 429 nm against the applied potential, with the corresponding Nernst fit.

3.2.5.2 pH Dependence of the Oxidation-Reduction Potential

The midpoint potential of the heme was affected by changing the pH, as shown in Table 3.3, but a pK value could not be derived, since the potentiometric titration showed no typical behaviour of 1-electron oxidation-reduction equilibrium. Nevertheless, a different trend was revealed, since the E^0 shifted to more positive values as the pH moved in the alkaline region. As it will be discussed in a later chapter (Chapter 4), the pH optimum for the enzyme is around pH 8.0. This supports the above observations, in which the more positive midpoint potential (E^0 = -13 mV) at alkaline pH favours stabilisation of the ferrous form (active form).

Table 3.3 pH dependence of the oxidation-reduction potential in rhIDO, in the absence of L-Trp.

pH	E^0 (mV)
6.0	-50
6.5	-34
7.0	-34
7.5	-20
8.0	-13

3.2.6 Crystallisation Screens

The purity of the rhIDO enzyme used for the crystallisation experiments is of importance. The purity of rhIDO was determined by measuring Reinheitzahl (R_Z) values (the ratio of the absorbance of the Soret peak at 404 nm and that of the protein peak at 280 nm) and by polyacrylamide gel electrophoresis (SDS-PAGE). The protein was then further purified by Fast Protein Liquid Chromatography (FPLC) (Figure 3.12). All screens were prepared as described in Chapter 6 (Section 6.6).

Commercial screens were attempted and Molecular Dimensions Ltd (MDL) screen (I), solution 17 (MDL1-01), which contained 0.1 M imidazole at pH 6.5 and 1.0 M sodium acetate trihydrate, seemed to provide favourable conditions for the protein. The protein retained its colour, whereas most of the screen solutions resulted in protein precipitation.

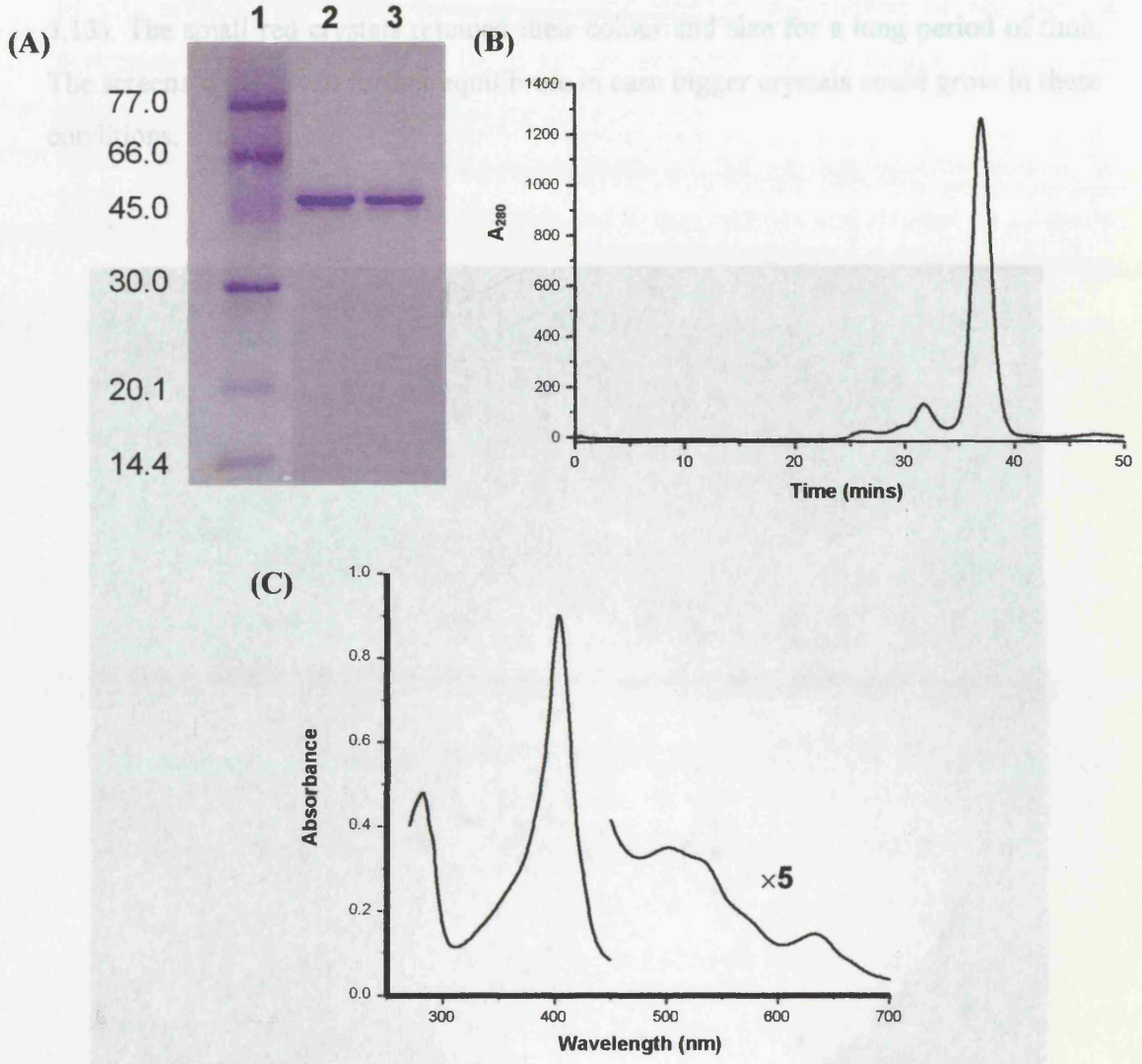

Figure 3.12 (A) SDS-PAGE gel of the FPLC purified rhIDO. From the left: standard markers (lane 1) FPLC-purified samples of rhIDO (lanes 2 and 3). (B) FPLC trace of rhIDO. Conditions: Superdex 75 HR 10/30 gel filtration column, 0.15 M potassium phosphate, pH 7.0, 200 µl injection of purified rhIDO, run time 50 minutes, protein has a retention time of 37 mins. (C) UV-visible absorption spectrum of ferric rhIDO.

Therefore further screens were prepared based around these conditions (see Chapter 6, Section 6.6), which yielded small quasi-red crystals (bundles of crystals) (Figure 3.13). The small red crystals retained their colour and size for a long period of time. The screens were left to further equilibrate in case bigger crystals could grow in these conditions.

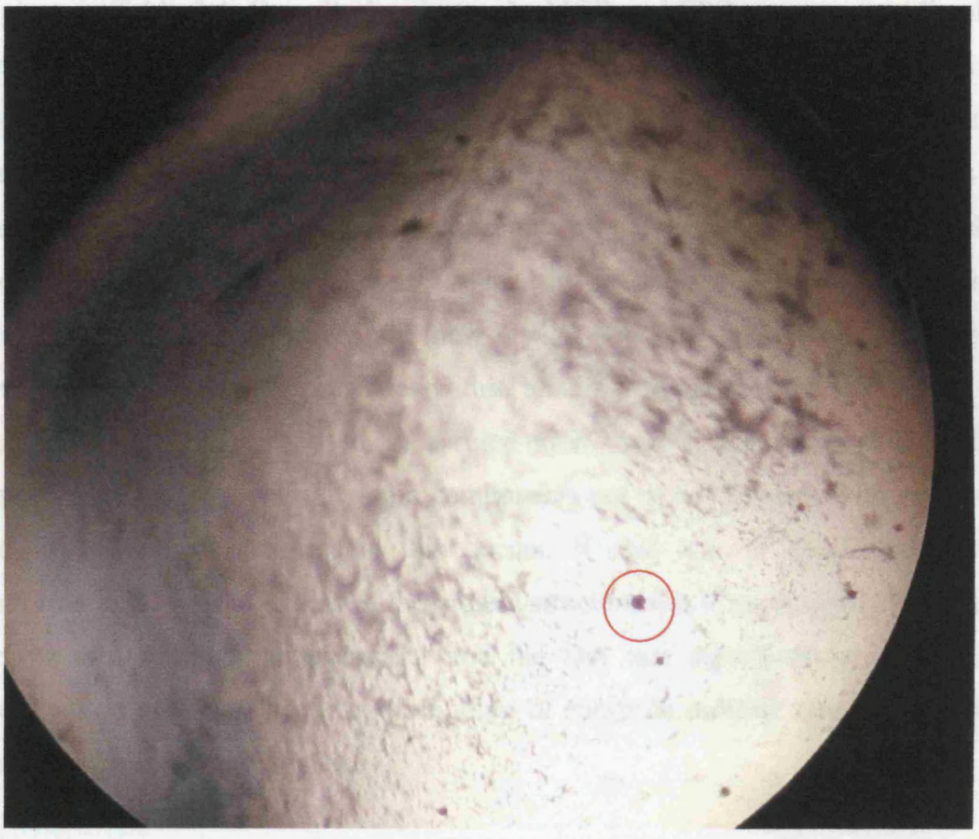

Figure 3.13 Bundles of small red crystals (magnified).

3.3 Discussion

In this section, the major findings are discussed in the context of our current understanding of the nature of the heme environment, the mechanism of substrate binding, and the redox properties of the IDO enzyme.

Heme coordination environment. A summary of the various species present in solution for ferric rhIDO at different pHs and in the presence and absence of substrate is given in Table 3.4. Overall, the electronic, MCD and EPR spectra at acidic pH are clearly consistent with the presence of two distinct species in solution: a high-spin and a low-spin heme species in approximately equal population. The high-spin species is confirmed by MCD as arising from histidine/water ligation. Similar conclusions were reached using resonance Raman spectroscopy (*2*). The low-spin species, which has been observed previously (*2, 7*), is assigned by MCD as being consistent with bis-nitrogenous ligation. However, the new crystal structure for human IDO does not have any potential ligating residues within bonding distance of the iron. Hydroxide-ligation, as previously proposed (*2*), is ruled out by the MCD analyses. It is not known whether the high-spin and low-spin components are in equilibrium with one another and, if so, on what timescale this occurs. If they are in equilibrium, then a conformational rearrangement of the protein structure would presumably be necessary for the two forms to interconvert (and the fact that significant changes in iron coordination geometry occur upon binding of substrate indicate that conformational changes of this kind are realistic).

Table 3.4 Distribution of heme species in ferric rhIDO at different pHs in the presence and absence of substrate, as determined from MCD and EPR analyses. HS = high-spin heme; LS = low-spin heme. n.d. = not detected. The percentages stated are derived from MCD intensities and errors on percentages are estimated as ± 5%.

Proximal/distal ligand	- Trp		+ Trp
	pH 6.6	pH 8.0	pH 8.0
His / H_2O (HS)	50%	35%	7%
His / X (LS)	50%	65%	33%
His / OH^- (LS)	n.d	n.d	60%

The electronic spectrum of ferric rhIDO is essentially pH-independent, indicating that the distal water molecule does not titrate within the experimentally accessible pH range (pH 5.5 – 10.7 in our experiments). This is in contrast to the related L-tryptophan 2,3-dioxygenase enzyme (which catalyses the same reaction as IDO), in which the electronic spectrum is pH-dependent (*11*). The electronic spectra are consistent with the MCD data, which clearly indicate that there is essentially no hydroxide-bound heme at either pH 6.6 or 8.0. There is an increase in low-spin heme at pH 8.0, but this is due to an increase in the bis-histidine species and not to the formation of hydroxide-bound heme. An increase in the low-spin component at alkaline pH has also been observed by resonance Raman and assigned as hydroxide-bound heme. Our data show that this assignment is incorrect, which would explain the reported (*2*) failure to detect any $\nu_{Fe\text{-}OH}$ stretching frequency at alkaline pH.

Several possibilities can be considered for the co-existence of low- and high-spin components observed in the MCD, EPR and electronic spectra of rhIDO: (a) an equilibrium ligand exchange between a strong field ligand and a weak field ligand; (b) an acid-base transition; and (c) a thermal spin equilibrium between the high- and low-spin states. Among them, the ligand exchange reaction is unlikely because such reaction may not occur under the frozen conditions. For the second possibility, we could not detect any transition in MCD, EPR and optical spectra by changing the pH between 6.0 and 8.0. Then the last possibility is also likely, but we could not unambiguously demonstrate a thermal equilibrium since the temperature-dependent spectral changes observed were very small. Temperature-dependent spin equilibria have been demonstrated with both *Pseudomonas* and rat liver TDO (*11*).

Substrate binding. MCD and EPR spectra confirm that the predominant species present in the substrate-bound form of rhIDO is hydroxide-bound heme. This is consistent with resonance Raman spectra for the substrate-bound derivative of human IDO (*2*) and previous MCD/EPR spectra for rabbit IDO (*7*). In contrast to the ferric enzyme, the spectrum of this substrate-bound species is now pH-dependent and a pK_a of 6.7 was derived (Figure 3.4, (inset)). The spectroscopic changes reflect titration of an ionisable residue that affects binding of L-Trp, which explains the appearance of high-spin signals at acidic pH (weaker binding at acidic pH). The pH-dependence of the binding interaction can also be determined separately by measuring the change in K_D with pH (Figure 3.5(A); pK_a = 7.8). The two pK_a values are in reasonable

agreement and are assumed, but not unambiguously confirmed, to report on the same process. This is discussed in more detail below.

A comparison of the pH-dependent properties of substrate-free and substrate-bound rhIDO provides new information that is particularly informative in terms of our understanding of the substrate binding process. That the spectrum of ferric rhIDO shows no evidence for formation of a hydroxide-bound heme is an unexpected observation in view of the fact that several other heme proteins with known histidine/water coordination – including the closely related L-tryptophan 2,3-dioxygenase enzyme – have titratable distal water molecules (*e.g.* myoglobin (*28*), leghemoglobin (*29*) and cytochrome *c* peroxidase (*30, 31*). A conveniently positioned hydrogen-bond acceptor – usually, but not exclusively, the distal histidine residue – is the normal way in which deprotonation of the bound water is facilitated. Why, then, does the distal water molecule in ferric rhIDO not titrate in a similar manner? The most reasonable explanation is that, in the absence of substrate, there is no suitable hydrogen-bond acceptor able to stabilise hydroxide formation. This would be consistent with the structure of human IDO (*8*), in which no potential hydrogen bonding residues are observed in the distal pocket. It has previously been proposed (*2*) that a direct hydrogen bond between the distal histidine and the distal water molecule in ferric IDO, but this is only consistent with the pH-independent spectrum of the ferric form if the pK_a of the bound water is unaffected by the hydrogen bond or if it is lowered to such an extent as to still be outside accessible pH range. The fact that pH-dependent behaviour is observed in the tryptophan-bound form presumably means that substrate binding induces a conformational change within the overall protein structure that favours deprotonation, such that a suitable (pH-dependent) hydrogen-bond acceptor is now accessible. One possible scenario that accounts for our observed data is depicted in Scheme 3.2. Here, the binding of substrate leads to a hydrogen-bonding interaction between an unspecified active site acid/base group, the bound substrate and the distal water molecule. In the absence of substrate (Scheme 3.2), no such hydrogen-bonding interaction occurs. This would be consistent with the pH-dependent spectrum of the substrate-bound enzyme and the pH-dependence of L-Trp binding, because L-Trp can now act as a proton donor/acceptor, shuttling a proton between the distal water molecule and the acid/base group. The pH-dependencies observed in this work would therefore be assigned as arising from titration of one of the residues indicated in Scheme 3.2, but we cannot unambiguously assign these pK_as

at this stage. At present, the new crystallographic information (*8*) gives no further insight because the structure of the substrate-bound form is not known.

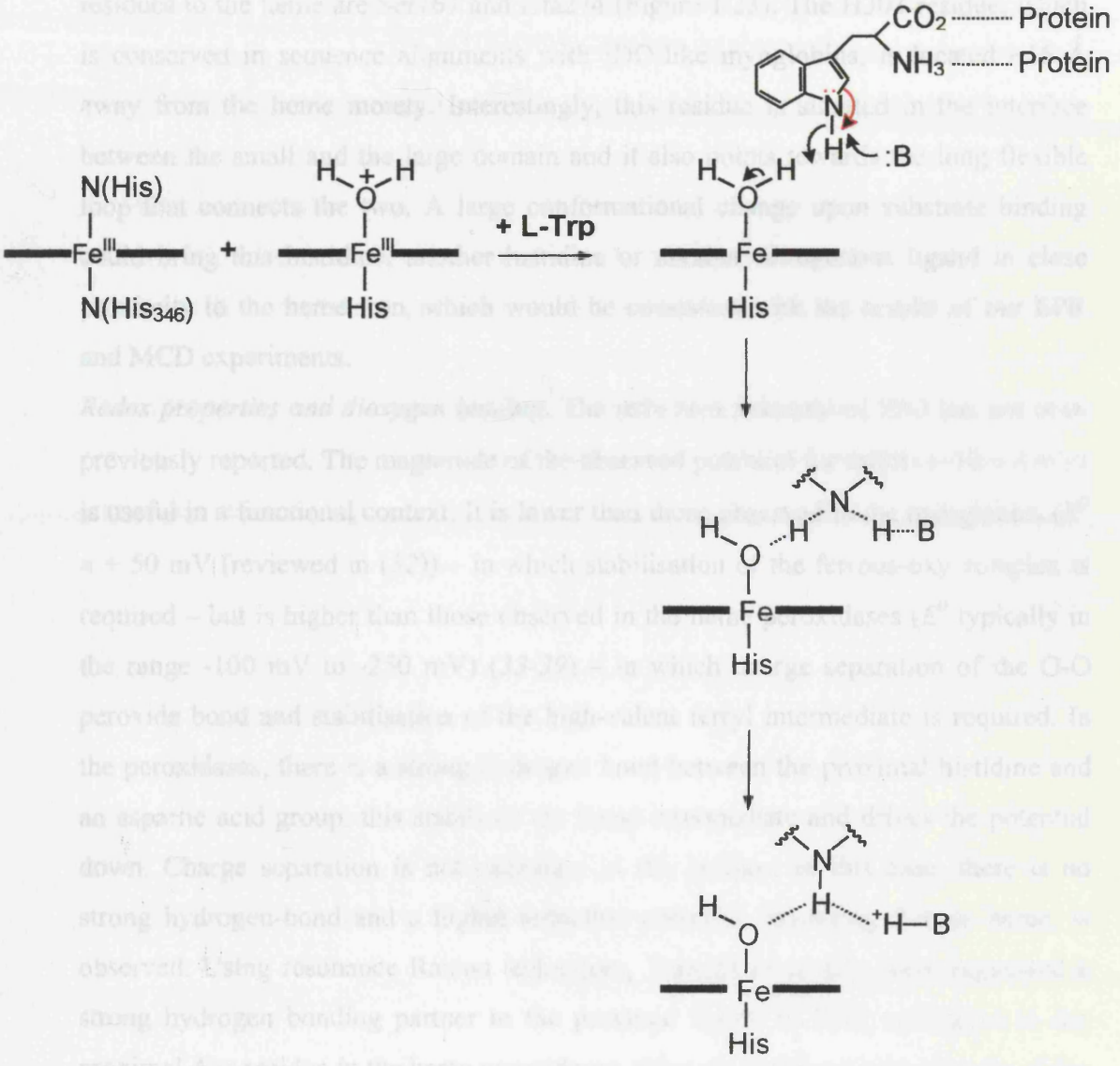

Scheme 3.2 Proposed mechanism for substrate binding and hydrogen-bond formation in rhIDO. The red curly arrow indicates an alternative root for hydrogen-bond formation in rhIDO in the absence of an acid/base group in the enzyme's active site.

As we have already discussed in Chapter 1 (Section 1.11), a histidine residue has been predicted by spectroscopy and sequence alignments to be located in the distal side of the heme in IDO, but the recent crystallographic data are not consistent with these previous data because the closest histidine is 18 Å from the heme. The closest residues to the heme are Ser167 and Ala274 (Figure 1.23). The H303 residue, which is conserved in sequence alignments with IDO-like myoglobins, is located ~15 Å away from the heme moiety. Interestingly, this residue is situated in the interface between the small and the large domain and it also points towards the long flexible loop that connects the two. A large conformational change upon substrate binding could bring this histidine, another histidine or another nitrogenous ligand in close proximity to the heme iron, which would be consistent with the results of our EPR and MCD experiments.

Redox properties and dioxygen binding. The reduction potential of IDO has not been previously reported. The magnitude of the observed potential for rhIDO (–30 ± 4 mV) is useful in a functional context. It is lower than those observed in the myoglobins (E^0 ≈ + 50 mV (reviewed in (*32*)) – in which stabilisation of the ferrous-oxy complex is required – but is higher than those observed in the heme peroxidases (E^0 typically in the range -100 mV to -250 mV) (*33-39*) – in which charge separation of the O-O peroxide bond and stabilisation of the high-valent ferryl intermediate is required. In the peroxidases, there is a strong hydrogen bond between the proximal histidine and an aspartic acid group: this stabilises the ferryl intermediate and drives the potential down. Charge separation is not necessary in the globins: in this case, there is no strong hydrogen-bond and a higher reduction potential, favouring ferrous heme, is observed. Using resonance Raman techniques, Terentis *et al.* (*2*) have suggested a strong hydrogen bonding partner to the proximal ligand in IDO, analogous to the proximal Asp residue in the heme peroxidases, although in this case the identity of the hydrogen bonding partner is not known (Asp274 has been suggested, however (*1*)). Based on comparisons with the reported reduction potentials for the peroxidases, the potential for rhIDO is substantially higher than would be expected if a strong hydrogen bond from His346 really does exist.

pH dependence studies of the redox potential of rhIDO, revealed that the potential shifts to more positive values in order to accommodate a more stable ferrous form. This is in very good agreement with the fact the enzyme's pH optimum is ~8.

Upon binding of substrate, there is a 46 mV increase in reduction potential for rhIDO, reflecting additional stabilisation of the ferrous derivative. This increase has not been reported previously and is analogous to, but less than, the corresponding increase in reduction potential (~130-140 mV) observed in both cytochrome $P450_{cam}$ (*40*) and P450 BM3 (*41*) on binding of substrates (camphor and fatty acids, respectively). For P450, this large increase in reduction potential acts as a switch, to turn on electron transfer to the ferric heme. For IDO, it is not clear at this stage whether heme reduction precedes substrate binding or *vice versa*, but a thermodynamic stabilisation of the reduced form would clearly favour catalytic reduction prior to substrate binding. We note, however, that the potentials of substrate-free and substrate-bound forms of IDO are more positive than their P450 counterparts (potentials typically in the range –350 to –400 mV for substrate-free P450s and –200 to –250 for the substrate-bound forms) – perhaps, with its higher potential, IDO does not need to depend on a substrate-induced mechanism for stabilisation of catalytically-active ferrous heme.

3.4 References

1. Littlejohn, T. K., Takikawa, O., Walker, M. J., Truscott, R. J. W. (2003) *J. Biol. Chem., 278*, 29525-29531.
2. Terentis, A. C., Thomas, S. R. Takikawa, O., Littlejohn, T. K., Truscott, R. J. W., Armstrong, R. S., Yeh, S., Stocker, R. (2002) *J. Biol. Chem., 277*, 15788-15794.
3. Suzuki, T., Kawamichi, H., Imai, K. (1998) *Comp. Biochem. Physiol., Part B, 121*, 117-128.
4. Yamazaki, F., Kuroiwa, T., Takikawa, O., Kido, R. (1985) *Biochem. J., 230*, 635-638.
5. Aitken, J. B., Thomas, S. E., Stocker, R., Thomas, S. R., Takikawa, O., Armstrong, R. S., Lay, P. A. (2004) *Biochem., 43*, 4892-4898.
6. Hayaishi, O. (1985) *Biken J., 28*, 39-49.
7. Sono, M.,Dawson, J. H. (1984) *Biochim. Biophys. Acta, 789*, 170-187.
8. Sugimoto, H., Oda, S., Otsuki, T., Hino, T., Yoshida, T., Shiro, Y. (2006) *Proc. Nat. Acad. Sc., 103*, 2611-2616.
9. Littlejohn, T. K., Takikawa, O., Skylas, D., Jamie, J. F., Walker, M. J., Truscott, R. J. W. (2000) *Protein Express. Purif., 19*, 22-29.
10. Uchida, K., Shimizu, T., Makino, R., Sakaguchi, K., Iizuka, T., Ishimura, Y., Nozawa, T., Hatano, M. (1983) *J. Biol. Chem., 258*, 2526-2533.
11. Makino, R., Sakaguchi, K., Iizuka, T., Ishimura, Y. (1980) *The Journal of Biological Chemistry, 255*, 11883-11891.
12. Sono, M., Tanigushi, T., Watanabe, Y., Hayaishi, O. (1980) *J. Biol. Chem., 255*, 1339-1345.
13. Seward, H. E. (1999) in *PhD Thesis, University of East Anglia.*
14. Patel, N., Jones, D. K., Raven, E. L. (2000) *Eur. J. Biochem., 267*, 2581.
15. McKnight, J., Cheesman, M. R., Thimson, A. J., Miles, J. S., Munro, A. W. (1993) *Eur. J. Biochem., 213*, 683-687.
16. Gadsby, P. M. A., Thomson, A. J. (1990) *J. Am. Chem. Soc., 112*, 5003-5011.
17. Watmough, N. J., Cheesman, M. R., Butler, C. S., Little, R. H., Greenwood. C., Thomson, A. J. (1998) *J. Am. Chem. Soc., 30*, 55-62.

18. Patel, N., Seward, H. E., Svensson, A., Gurman, S. J., Thimson, A. J., Raven, E. L. (2003) *Archives Biochem. Biophys., 418*, 197-204.

19. Eglinton, D. G., Gadsby, P. M. A., Sievers, G., Peterson, J., Thimson, A. J. (1983) *Biochim. Biophys. Acta, 742*, 648-658.

20. Foote, N., Gadsby, P. M. A., Berry, M. J., Greenwood, C., Thomson, A. J. (1987) *Biochem. J. , 246*, 659-668.

21. Kobayashi, N., Nozawa, T., Hatano, M. (1977) *Biochim. Biophys. Acta, 493*, 340-351.

22. Bolard, G., Garnier, A. (1972) *Biochim. Biophys. Acta, 263*, 535-549.

23. Springall, J., Stillman, M. J., Thomson, A. J. (1976) *Biochim. Biophys. Acta, 453*, 494-501.

24. Nozawa, T., Kobayashi, N., Hatano, M. (1976) *Biochim. Biophys. Acta, 427*, 652-662.

25. Palmer, G. (1985) *Biochem. Soc. Trans., 13*, 548-560.

26. More, C., Belle, V., Asso, M., Fournel, A., Roger, G., Guigliarelli, B., Bertrand, P. (1999) *Biospec., 5*, S3-18.

27. Yonetani, T., Anni, H. (1987) *J. Biol. Chem., 262*, 9547-9554.

28. Antonini, M., Brunori, E. (1971) *Hemoglobin and Myoglobin and their Reactions with Ligands.*, North Holland Publishers, Amsterdam.

29. Jones, D. K., Badii, R., Rosell, F. I., Lloyd, E. (1998) *Biochem. J. , 330*, 983-988.

30. Foshay, M. C., Vitello, L. B., Erman, J. E. (2004) *Biochem., 43*, 5065-5072.

31. Turano, P., Ferrer, J. C., Cheesman, M. R., Thomson, A. J., Banci, I., Mauk, A. G. (1995) *Biochem., 34*, 13895-13905.

32. Raven, E. L., Mauk, A. G. (2001) *Adv. Inorg. Chem., 51*, 1-49.

33. Conroy, C. W., Tyma, P., Daum, P. H., Erman, J. E. (1978) *Biochim. Biophys. Acta, 537*, 62-69.

34. Goodin, D. B., McRee, D. E. (1993) *Biochem., 32*, 3313-3324.

35. Harbury, H. A. (1957) *J. Biol. Chem., 225*, 1009-1024.

36. Millis, C. D., Cai, D., Stankovich, M. T., Tien, M. (1989) *Biochem., 28*, 8484-8489.

37. Jones, D. K., Dalton, D. A., Rosell, F. I., Raven, E. L. (1998) *Archives Biochem. Biophys., 360*, 173-178.

38. Tanaka, M., Ishimori, K., Morishima, I. (1998) *Biochem., 37*, 2629-2638.

39. Yamada, H., Makino, R., Yamazaki, I. (1975) *Archives Biochem. Biophys., 169*, 344-353.

40. Sligar, S. G. (1976) *Biochem., 15*, 5399-5406.

41. Daff, S., Chapman, S. K., Turner, K. L., Holt, R. A., Govindaraj, S., Poulos, T. L., Munro, A. W. (1997) *Biochem., 36*, 13816-13823.

Chapter 4

His346Ala, His303Ala & Arg304Ala Variants of Recombinant Human Indoleamine 2,3-Dioxygenase

4.1 Introduction

Heme proteins, such as IDO, are the most extensively studied of all metalloproteins. All heme proteins carry iron coordinated to protoporphyrin IX (Figure 4.1). The four coordination sites provided by the porphyrin ring are not sufficient to satisfy the coordination requirements of iron. Normally, groups from the heme-binding protein occupy the remaining coordination sites. The common coordinating functional groups are the imidazole nitrogen of histidine, the phenoxide group of tyrosine, the sulfur of methionine and cysteine, and the carboxylate group of aspartic acid and glutamic acid. In both myoglobin and hemoglobin, the heme is attached to the protein through a histidine residue to the fifth coordination position on the iron (proximal ligand). A second histidine (the distal ligand) occupies space immediately above the sixth coordination position of the iron, and coordination is through an oxygen molecule, not directly to the iron. Although only the primary structure of IDO has been determined (*1, 2*), there have been extensive equilibrium studies undertaken to investigate the binding properties of both substrate and oxygen with the additional objective to identify the proximal and distal heme ligands.

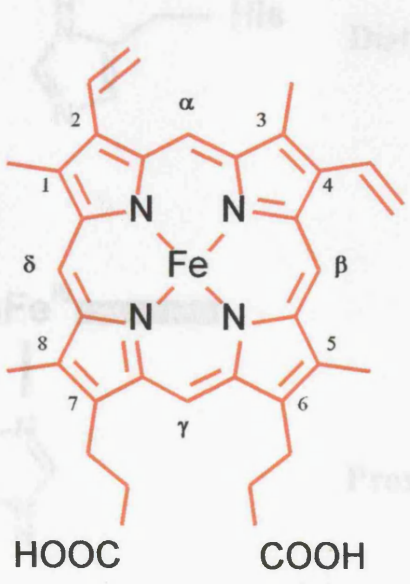

Figure 4.1 The tetra-pyrrole structure of heme b (protoporphyrin IX), the prosthetic group of indoleamine 2,3-dioxygenase. The methane bridges are designated α, β, γ and δ.

EPR, MCD and CD spectroscopic studies have been carried out over the years to determine the properties of the IDO heme pocket and the nature of the proximal and distal heme ligands. On the basis of MCD studies the ferric and ferrous IDO closely resembled that of myoglobin and horseradish peroxidase (*3*, *4*); however, the environment of the IDO heme pocket is similar to, but the size is considerably larger than, the binding heme pocket of myoglobin. This observation is supported by data showing that the heme pocket of IDO allows access to the inhibitors norharman and 4-phenylimidazole (*5*). EPR spectra (*6*), suggested that the fifth (proximal) ligand of the heme was nitrogen, probably from a histidine imidazole ring. The sixth (distal) ligand in substrate-free IDO was proposed to be histidine imidazole ring nitrogen (*3*, *4*) based on MCD spectroscopy. Uchida *et al.* (*3*) suggested that, in the substrate-bound ferric IDO, the sixth ligand was also a histidine. This contrasted with Sono and Dawson (*4*), who showed that the observed changes in MCD upon L-Trp were consistent with hydroxide-bound heme. The findings suggested that both the proximal and distal heme ligands in substrate-free IDO were histidines, as in myoglobin and hemoglobin (Scheme 4.1).

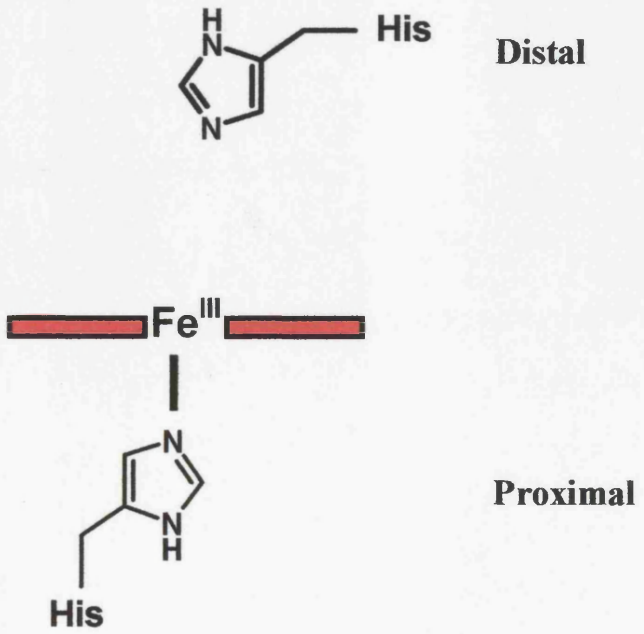

Scheme 4.1 Diagrammatic representation of the active site of IDO. The red boxes represent the heme.

Later sequence alignment studies by Suzuki *et al.* (*7*) (see also Chapter 1, 1.9.2) between mollusc IDO-like myoglobins, human IDO, mouse IDO and a homologue in yeast revealed a 37% sequence identity. From these studies, there are two histidine residues at position 335 and 380 (Figure 1.15 A, boxed) that are conserved in all the sequences, one of which is most likely to correspond to the heme-binding proximal histidine. If histidine-380 is assigned to the heme-binding proximal histidine, then histine-335 may be assigned to the distal histidine by analogy with usual myoglobins and hemoglobins. In our amino acid sequence for the rhIDO (Chapter 2, Figure 2.2) these two residues have been identified as histidine-346 (proximal) and histidine-303 (distal).

During the early part of this work, the crystal structure of rhIDO was unknown, hence to investigate the hypothesis of that the proximal and distal heme ligands are imidazole nitrogen, we undertook alanine replacement site-directed mutagenesis of the two key histidine residues to generate two new variants, His346Ala and His303Ala. Spectroscopic, electrochemical and ligand binding analyses have been undertaken with the aim of establishing the heme ligation of the new variants and assess the effect of the mutations on the properties of the proteins. The data are compared with rhIDO.

4.2 Mutagenesis, Expression, Isolation and Purification

Preparation of the His346Ala, His303Ala and Arg304Ala variants of rhIDO using site-directed mutagenesis was conducted according to the Quickchange™ protocol (Stratagene), using the rhIDO encoded gene and the His346Ala and His303Ala mutagenic oligonucleotides, respectively (see Appendix B, Table II). Sequence of the whole rhIDO gene confirmed the desired mutation. The His346Ala, His303Ala and Arg304Ala variants were expressed, isolated and purified according to published procedures (*8*) (Chapter 6, Section 6.3). Variant His346Ala was isolated as *apo*-protein, whereas His303Ala variant was isolated as a *holo*-protein. Reconstitution of the variants by addition of appropriate volumes of hemin, was not possible for the His303Ala variant. Purified proteins (2.5 mg/l) were obtained with $R_Z > 1.2$ (for His303Ala) (pH 7.9 and 25 °C, 100 mM potassium phosphate) and migrated as a single band on a SDS-PAGE gel (Figure 4.2).

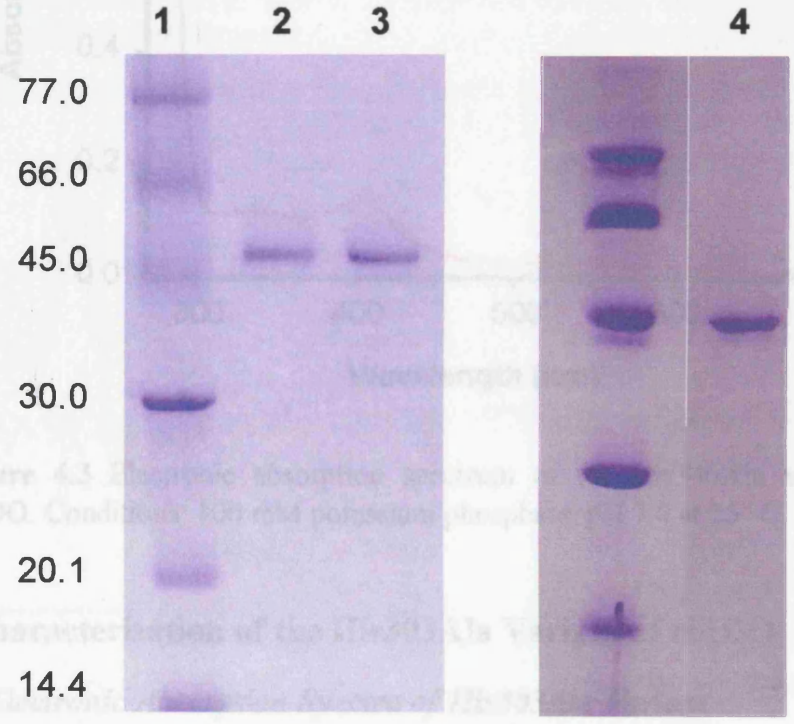

Figure 4.2 SDS-PAGE gel of variants of rhIDO. Lane **1** denotes the marker standards; Lane **2** His303Ala variant of rhIDO; Lane **3** His346Ala variant of rhIDO; Lane **4** Arg304Ala variant of rhIDO.

4.3 Results

4.3.1 Characterisation of the His346Ala Variant of rhIDO

4.3.1.1 Electronic Absorption Spectrum of His346Ala Variant

UV and visible spectroscopy was conducted on the purified His346Ala variant. This mutant has very low absorbance at 404 nm, indicating that it does not bind heme (Figure 4.3). A similar site-directed mutagenesis study was carried out by Littlejohn *et al.* (*9*), in which they have identified His346 and Asp274 as the essential residues for the heme binding and catalytic function of human IDO.

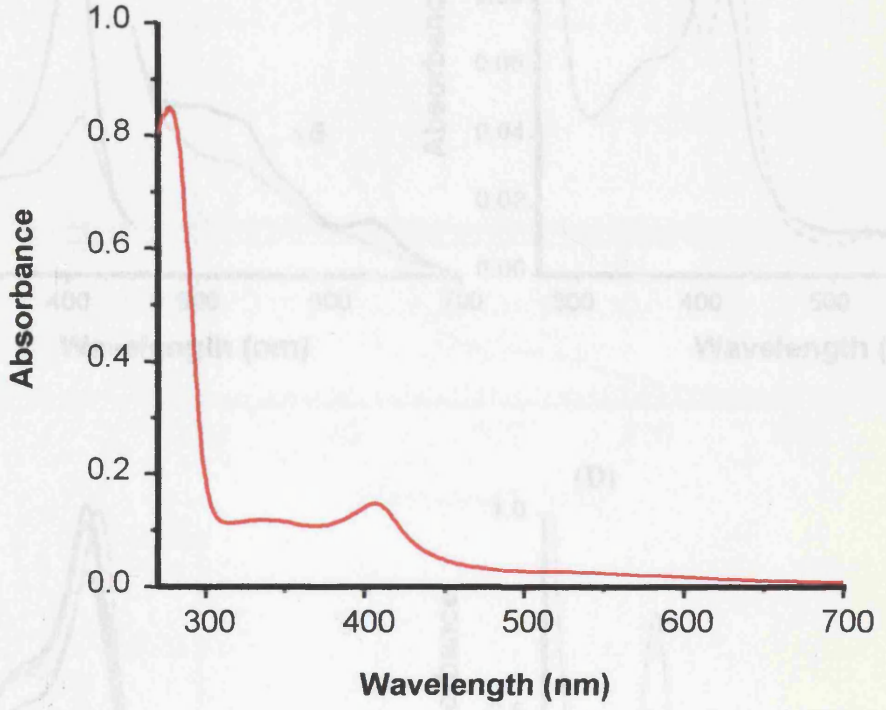

Figure 4.3 Electronic absorption spectrum of the His346Ala variant of rhIDO. Conditions: 100 mM potassium phosphate, pH 7.0 at 25 °C.

4.3.2 Characterisation of the His303Ala Variant of rhIDO

4.3.2.1 Electronic Absorption Spectra of His303Ala Variant

The UV-visible spectrum of ferric His303Ala (λ_{max} = 408, 531, 568 nm, Figure 4.4(A), Table 3B.1) shows that the Soret band has red-shifted compared to rhIDO, but is still characteristic of high-spin heme. This spectrum is pH-independent, as observed

for rhIDO. The spectrum of ferrous His303Ala is essentially identical to that of rhIDO (Figure 4.4(B), Table 4.1). Cyanide binds to His303Ala, as evidenced by the change in the electronic spectrum and its similarity to that of rhIDO. There is a decrease in intensity of the Soret band on addition of azide to His303Ala, but no corresponding changes in the visible region that indicate formation of the expected low-spin heme (Figure 4.4 (C)).

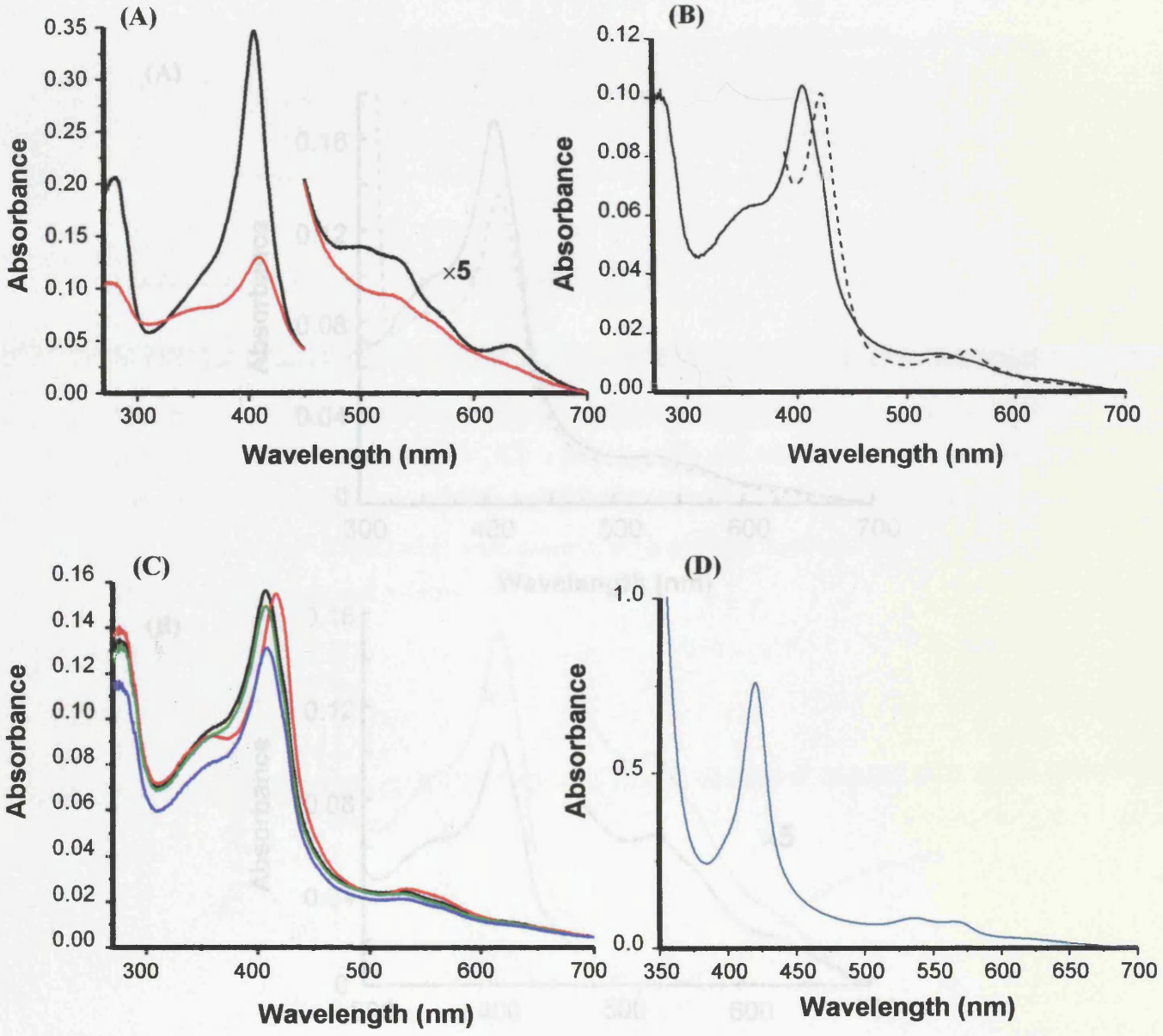

Figure 4.4 (A) UV-visible spectra of ferric rhIDO and ferric His303Ala variant (pH 7.9 and 25 °C). Absorbance values in the visible region have been multiplied by a factor of 5. (B) UV-visible spectra of ferric His303Ala and ferrous His303Ala (pH 7.9 and 25 °C). (C) Electronic spectra of ferric anionic ligand-bound derivatives of His303Ala variant (pH 8.0 and 25 °C) (black: ferric His303Ala; red: CN^-; green: F^-; blue: N_3^-). (D) UV-visible spectra of the CO-bound His303Ala variant (pH 7.9 and 25 °C).

On binding of L-Trp at pH 8.0 (Figure 4.5 (A)), the Soret band shifts to a value (λ_{max} = 411 nm) that is characteristic of low-spin heme formation and that is similar to that observed for rhIDO, but in the visible region there is no measurable change as observed for rhIDO. Formation of the ferrous–oxy complex of the His303Ala variant was not observed under identical conditions used for the formation of the ferrous–oxy complex for rhIDO (Figure 3.3(B)). The identical experiment gave no characteristic oxy peaks in the visible region and no shift in the Soret peak (Figure 4.5(B)).

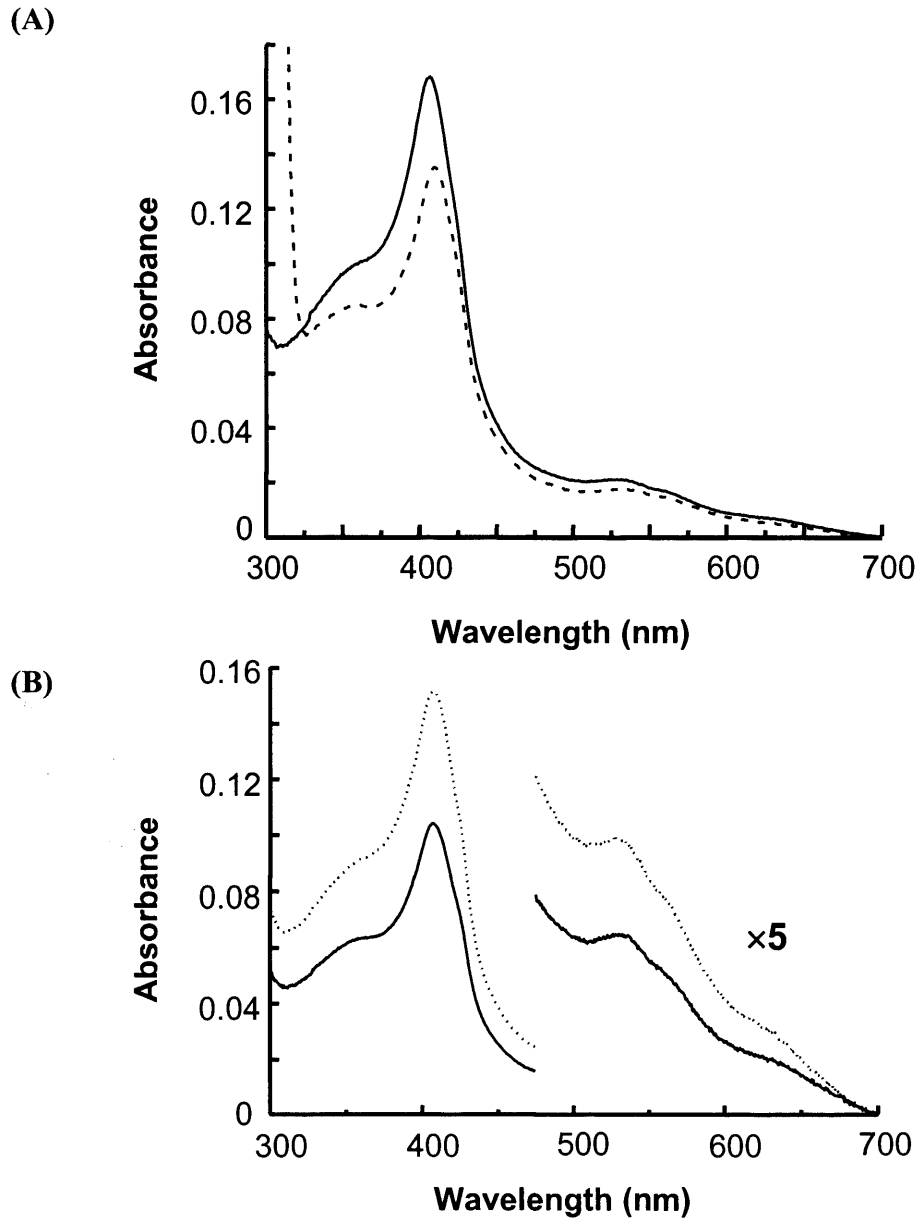

Figure 4.5 (A) UV-visible spectrum of ferric His303Ala in the absence (—) and presence of (– – –) of 20 mM L-Trp (pH 7.9 and 25 °C). (B) UV-visible spectra of the ferric (—) and ferrous-oxy (•••) derivatives of His303Ala variant (100 mM potassium phosphate at pH 7.9 and 25 °C).

Table 4.1 Absorption maxima and absorption coefficients (in ( ), mM^{-1} cm^{-1}) for various ferric and ferrous derivatives of rhIDO and His303Ala variant..

Derivative	λ_{max} (nm)	
	rhIDO	His303Ala
Ferric	404 (172), 500, 535, 633	408 (108), 531, 568
Ferric + L-Trp	411, 540, 576	411, 531, 568
Ferrous	425, 527, 558	425, 529, 568
Ferrous-oxy	412, 539, 565	nd
Ferrous-CO	419, 539, 565	420, 437, 567
Ferric-azide	414, 535, 572, 634	408, 531, 568
Ferric-cyanide	419, 540, 570	417, 533, 563
Ferric fluoride	404, 497, 537, 572, 632	407, 531, 568

4.3.2.2 Circular Dichroism (CD) Spectroscopy

A CD spectrum of the His303Ala variant of rhIDO was acquired to determine whether the selected mutation affected the protein secondary structure of IDO structure of IDO. The far UV CD spectrum (Figure 4.6) of the variant, with comparison to the wild type rhIDO, exhibited similar structural compositions. These data indicate that site-directed mutagenesis of individual residues did not grossly affect the protein secondary structure.

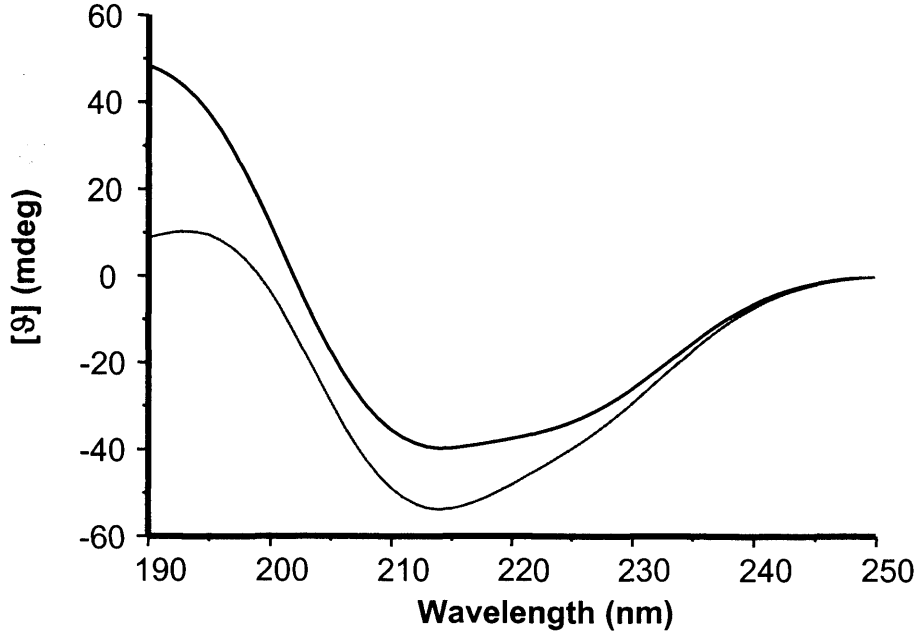

Figure 4.6 Far-UV circular dichroism spectra of wild type (black) and His303Ala variant (~ 30 μM). CD spectra were conducted in 100 mM potassium phosphate, pH 8.0 and 25 °C.

4.3.2.3 Electron Paramagnetic Resonance (EPR) Spectroscopy

EPR analyses indicate that the ferric derivative (Figure 4.7(A)) of His303Ala variant has a much higher proportion of high-spin heme (g = 5.98, 5.53, 2.00) than for rhIDO. Significantly, the low-spin signals arising from the low-spin, bis-nitrogenous species (g = 2.96, 2.29 and 1.50) are very considerably diminished (the very weak signal that does remain probably arises from coordination of another strong field ligand). The low-spin signals (g = 2.47, 2.19 and 1.86) associated with hydroxide ligation in rhIDO are broader for His303Ala, which suggests the presence of a range of conformers. Addition of L-Trp (Figure 4.7(B)) leads to an increase in low-spin heme at g = 2.53, 2.19 and 1.86: these sharp signals are consistent with a hydroxide-bound heme species that is in a defined conformation, rather than a range as observed above. An MCD spectrum of His303Ala could not be obtained because the sample was unstable during repeated exchange into D_2O.

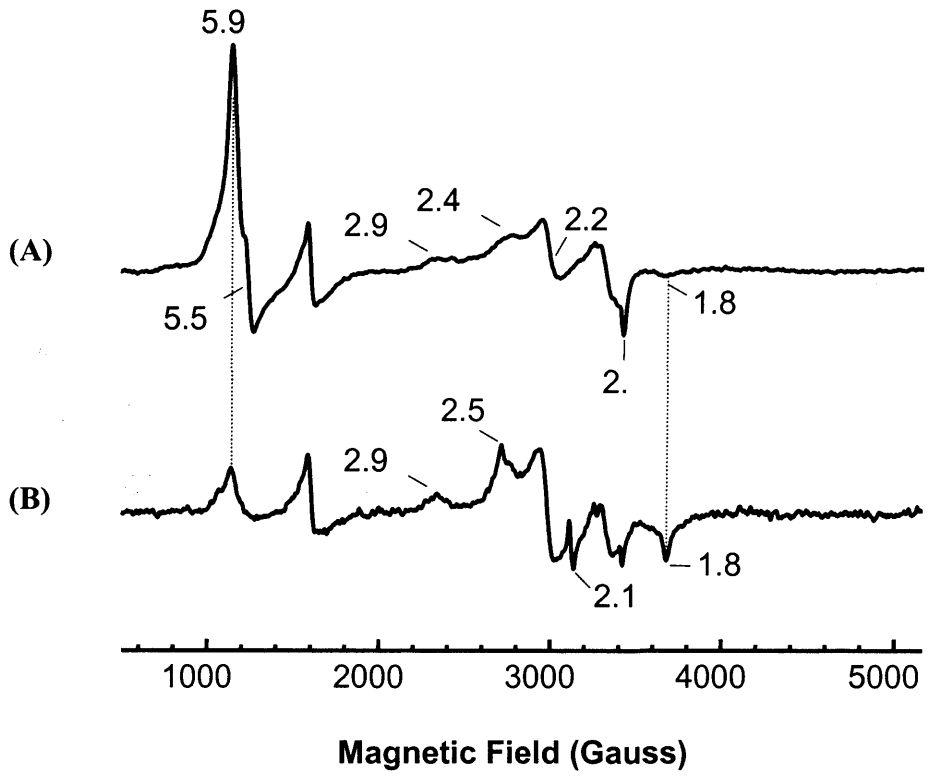

Figure 4.7 Perpendicular mode X-band EPR spectra of ferric His303Ala (A) and ferric His303Ala in the presence of 20 mM L-Trp (pH 7.5) (B).

4.3.2.4 Redox Potentiometry

Selected spectra obtained during redox titration of H303A are shown in Figure 4.8. Data obtained at 423 nm (to monitor formation of ferrous heme) were fitted to a single electron process (Nernst equation) and gave a reduction potential of –99 ± 2 mV, representing a destabilisation of the ferrous heme of almost 70 mV compared to rhIDO.

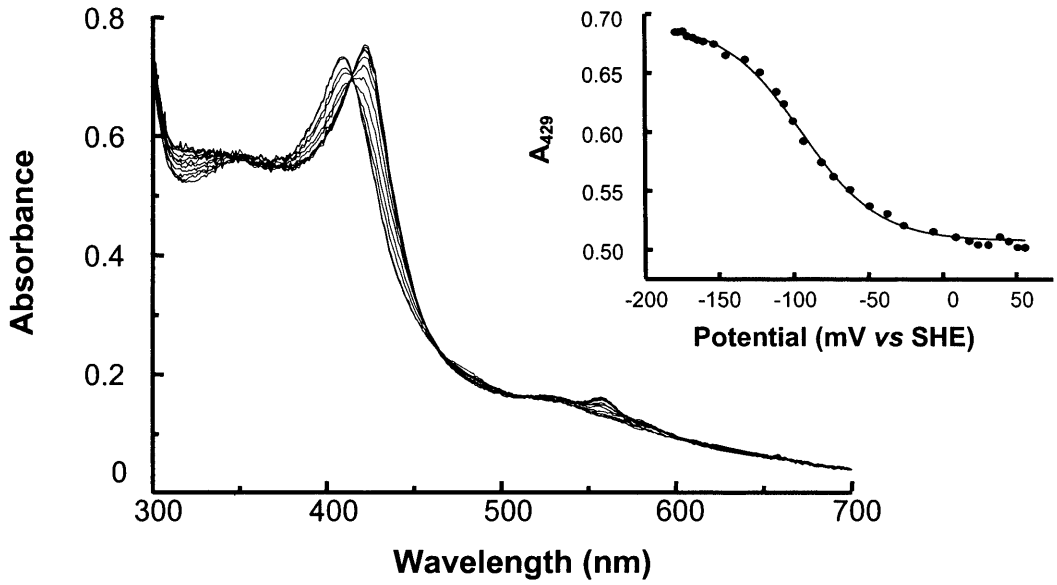

Figure 4.8 Redox titration of His303Ala at pH 8.0, with a fit of the data at 429 nm to the Nernst equation shown in the inset.

4.3.2.5 Steady State Kinetics

The His303Ala variant was observed to be capable of steady state oxidation of L-Trp at pH 8.0 under conditions identical to those used for rhIDO, with values for k_{cat} and K_M of 2.7 ± 0.1 s^{-1} and 15 ± 1.0 μM, respectively (k_{cat}/K_M = 0.18 $\mu M^{-1}s^{-1}$). This is in agreement with previous steady state analyses on the His303Ala variant (*9*).

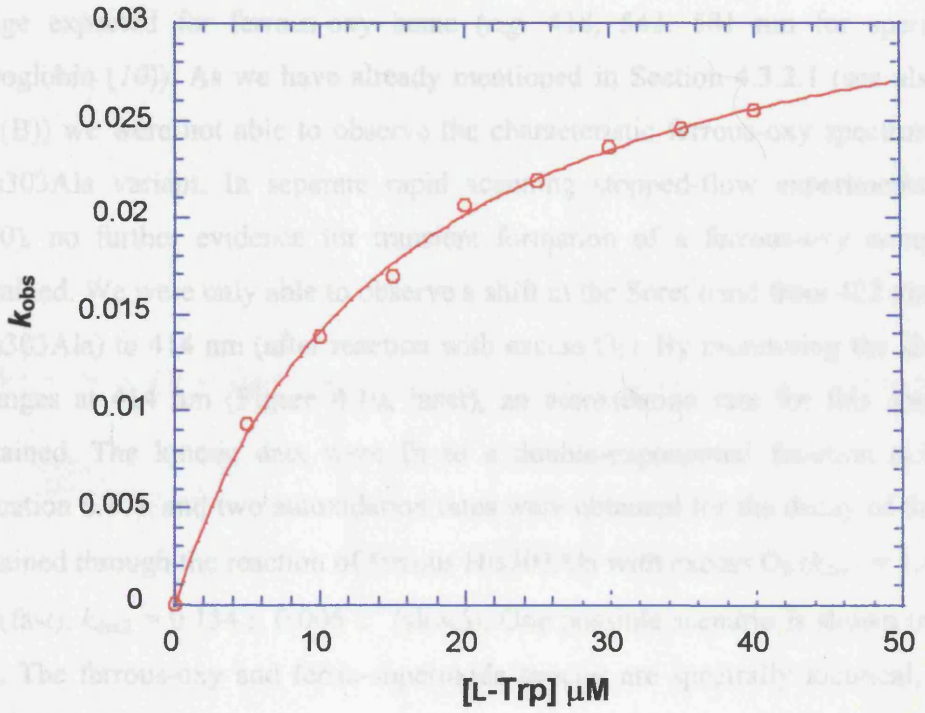

Figure 4.9 Steady state oxidation of L-Trp by His303Ala variant of rhIDO. Conditions: [His303Ala] = 25 nM, 25 °C, potassium phosphate 100 mM, pH 8.0. Reactions were initiated by addition of His303Ala. The solid red line is a fit of the data to the Michaelis-Menten Equation (Chapter 6, Equation (6.13)).

4.3.2.6 Formation of the Ferrous-Oxy Derivative

To check whether this decrease in reduction potential was functionally significant, we tested whether destabilisation of the ferrous derivative may affect stability of the catalytic ferrous-oxy intermediate. Under conditions that resulted in clean formation of the ferrous-oxy complex for rhIDO, formation of the ferrous-oxy complex for His303Ala was not observed. Hence, for rhIDO a species with wavelength maxima of 412, 539, 576 nm (Figure 3.3(C) and Table 4.1) was obtained: these maxima are in the range expected for ferrous-oxy heme (*e.g.* 418, 543, 581 nm for sperm whale myoglobin (*10*)). As we have already mentioned in Section 4.3.2.1 (see also Figure 4.5(B)) we were not able to observe the characteristic ferrous-oxy spectrum for the His303Ala variant. In separate rapid scanning stopped-flow experiments (Figure 4.10), no further evidence for transient formation of a ferrous-oxy complex was obtained. We were only able to observe a shift in the Soret band from 422 nm (ferrous His303Ala) to 414 nm (after reaction with excess O_2). By monitoring the absorbance changes at 414 nm (Figure 4.10, inset), an autoxidation rate for this species was obtained. The kinetic data were fit to a double-exponential function (Chapter 6, Equation 6.17), and two autoxidation rates were obtained for the decay of the species obtained through the reaction of ferrous His303Ala with excess O_2 (k_{dec1} = 1.40 ± 0.02 s^{-1} (fast), k_{dec2} = 0.154 ± 0.006 s^{-1} (slow)). One possible scenario is shown in Scheme 4.1. The ferrous-oxy and ferric-superoxide species are spectrally identical, but they have different autoxidation rates. At this stage we cannot unambiguously assign these autoxidation rates. The slower autoxidation rate (k_{dec2}) may be due to the fact that some ferrous-oxy species are being reformed, since the reaction mixture will still contain Fe^{II}-rhIDO and oxygen. The above observation can also be attributed to the heterogeneity of the sample. Comparison of these values with the ones obtained for the rhIDO ferrous-oxy decay, k_{dec1} = 0.982 ± 0.01 s^{-1} and k_{dec2} = 0.008 ± 0.001 s^{-1}, suggests that the ferrous-oxy complex of the His303Ala is more unstable than the wild type species (These will be discussed in detail in Chapter 5). Attempts to increase the yield of the ferrous-oxy derivative by addition of imidazole (to 10 mM) – which has been shown to recover hydrogen-bonding interactions with bound ligands (*11*) – were unsuccessful.

$$Fe^{II}–O_2 \longleftrightarrow Fe^{III}–O_2^{\bullet-} \xrightarrow[k_{dec1}]{} Fe^{III} + O_2^{\bullet-}$$

Scheme 4.1 Possible decay intermediate of the ferrous-oxy species of the His303Ala variant.

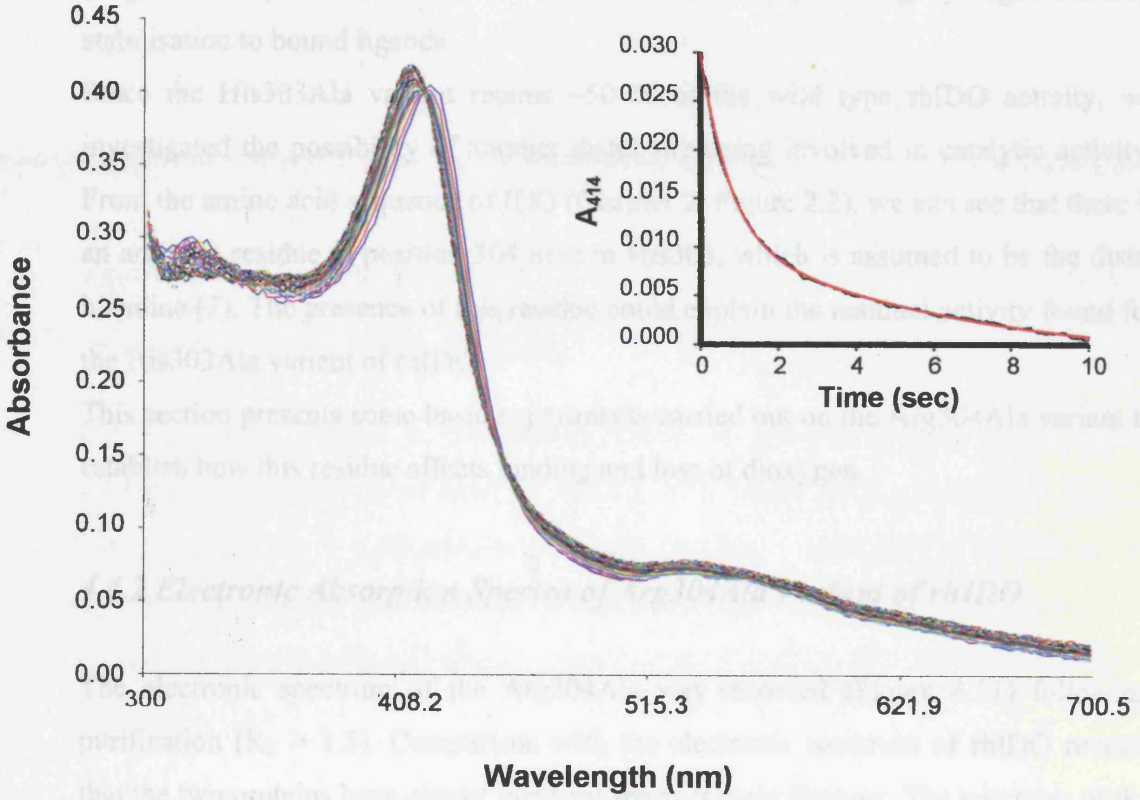

Figure 4.10 Time-dependent spectral changes for the formation of the ferrous-oxy complex of the His303Ala variant (8 μM). The reaction was monitored over a time base of 0.5 seconds at 25 °C. Conditions: 100 mM potassium phosphate, pH 8.02. 40 spectra were collected. The inset shows a biphasic kinetic trace for the decay of the His303Ala ferrous-oxy complex (black line) obtained at high $[O_2]$ (600 μM). The solid red line is a fit of the data to double-exponential function (Equation 6.18). The decay was followed over a period of 10 seconds.

4.4 Characterisation of the Arg304Ala Variant of rhIDO

4.4.1 Introduction

From the discussion in Chapter 1, on the oxygen binding properties of myoglobins from several sources, it is clear that the residue in the distal site controls the ligand binding affinity of myoglobin and is important for the stabilisation of the ferrous-oxy species. This residue is usually a histidine in the vertebrate myoglobins, however, there is much more variation in its identity in the nonvertebrate myoglobins. For example, *Aplysia* myoglobin contains a valine as the distal residue (in the place of histidine). This residue is not able to participate in hydrogen bonding interactions, but X-ray and NMR studies have indicated that the arginine residue in the distal pocket (ArgE10) compensates for the absence of histidine by providing hydrogen-bonding stabilisation to bound ligands.

Since the His303Ala variant retains ~50 % of the wild type rhIDO activity, we investigated the possibility of another distal site being involved in catalytic activity. From the amino acid sequence of IDO (Chapter 2, Figure 2.2), we can see that there is an arginine residue at position 304 next to His303, which is assumed to be the distal histidine (*7*). The presence of this residue could explain the residual activity found for the His303Ala variant of rhIDO.

This section presents some basic experiments carried out on the Arg304Ala variant to establish how this residue affects binding and loss of dioxygen.

4.4.2 Electronic Absorption Spectra of Arg304Ala Variant of rhIDO

The electronic spectrum of the Arg304Ala was recorded (Figure 4.11) following purification (R_Z > 1.5). Comparison with the electronic spectrum of rhIDO reveals that the two proteins have almost identical spectroscopic features. The spectrum of the ferric form of Arg304Ala variant (λ_{max} = 404, 500, 536, 572^{sh}, 633 nm) has maxima that are consistent with a mixed population of high- and low-spin heme species. This spectrum is pH-independent, like for the wild type rhIDO.

For the rhIDO, the wild high- and low-spin species were assigned as arising from a six-coordinate, water-bound heme derivative, and from coordination of a distal histidine residue (probably His303) to the heme respectively (*8*). Molar absorption

coefficient for Arg304Ala was determined as an average of two heme contents using the pyridine hemochromagen method (*10*) (Chapter 6, Section 6.4.2). A value of ε_{404} = 189 mM^{-1} cm^{-1} was determined for the Arg304Ala variant.

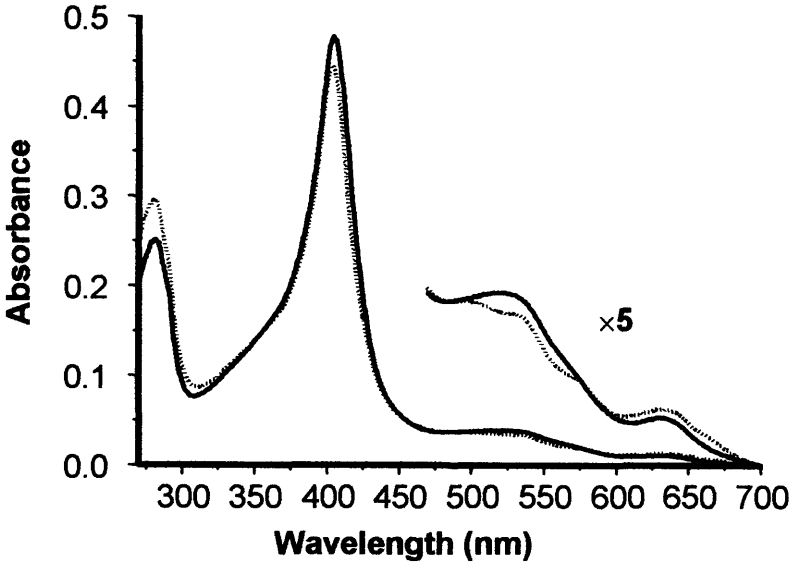

Figure 4.11 UV-visible spectra (pH 8.0 and 25.0 °C) of ferric rhIDO (—) and ferric Arg304Ala variant (——). Absorbance values in the visible region have been multiplied by a factor of five for clarity.

The Arg304Ala variant is catalytically active at pH 8.0 (Figure 4.12), under conditions identical to those used for rhIDO, with values for k_{cat} and K_M of 3.56 ± 0.19 s^{-1} and 7.72 ± 1.42 μM, respectively (k_{cat}/K_M = 0.46 $\mu M^{-1}s^{-1}$). This is in agreement with steady state analyses on the rhIDO (k_{cat} = 3.3 ± 0.1 s^{-1} and K_M = 9.5 ± 0.7 μM, k_{cat}/K_M = 0.347 μM^{-1} s^{-1}).

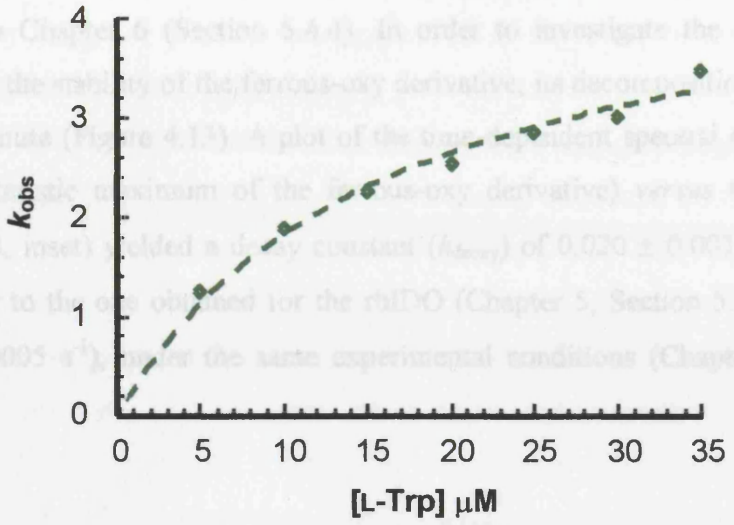

Figure 4.12 Steady state oxidation of L-Trp by Arg304Ala variant of rhIDO. Conditions: [Arg304Ala] = 25 nM, 25 °C, potassium phosphate 100 mM, pH 8.0. Reactions were initiated by addition of Arg304Ala. The dashed green line is a fit of the data to the Michaelis-Menten Equation (Chapter 6, Equation (6.13)).

4.4.3 Formation of the Ferrous-Oxy Derivative

The ferrous-oxy derivative of the Arg304Ala variant (Figure 4.13) was prepared as described in Chapter 6 (Section 6.4.4). In order to investigate the effects of this mutation on the stability of the ferrous-oxy derivative, its decomposition was monitor over ~ 1 minute (Figure 4.13). A plot of the time-dependent spectral changes at 576 nm (characteristic maximum of the ferrous-oxy derivative) *versus* time (minutes) (Figure 4.13, inset) yielded a decay constant (k_{decay}) of 0.020 ± 0.0013 s^{-1}, which is very similar to the one obtained for the rhIDO (Chapter 5, Section 5.2.3.2) (k_{decay} = 0.011 ± 0.0005 s^{-1}), under the same experimental conditions (Chapter 6, Equation 6.18).

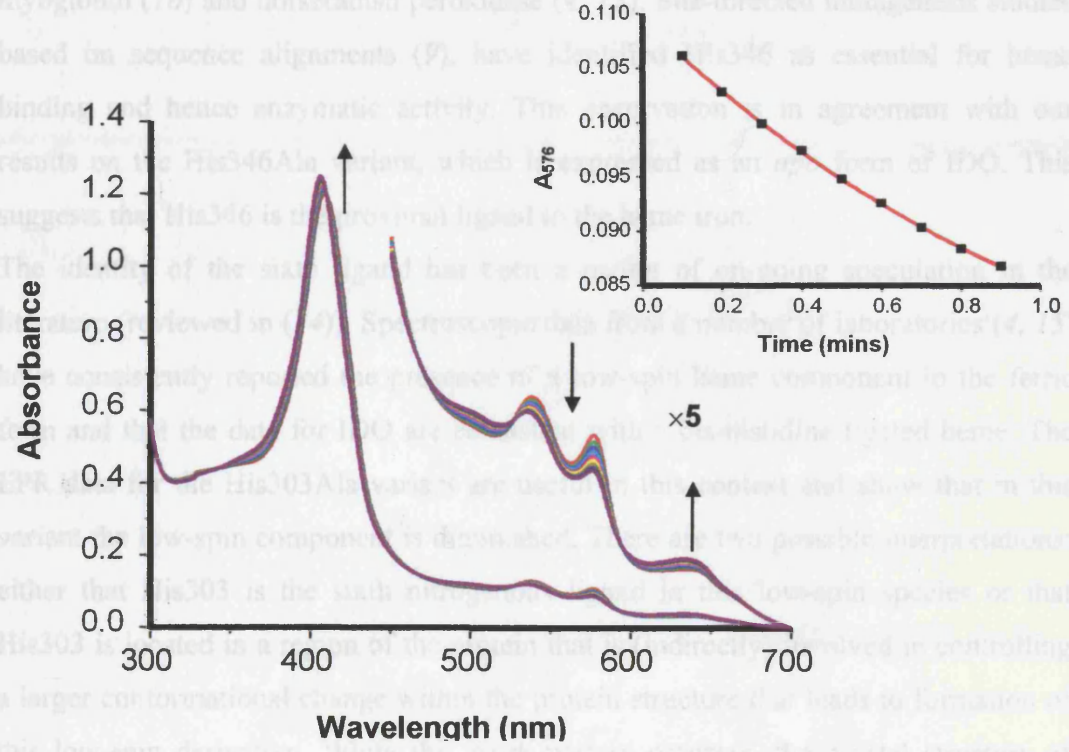

Figure 4.13 Representative data set for the decomposition of the ferrous-oxy complex of the Arg304Ala variant. (Inset) A fit of data at 576 nm to a first order exponential decay. Conditions: 100 mM potassium phosphate, pH 8.0, 25 °C, [Arg304Ala] = 7 μM.

4.5 Discussion

In this Chapter we have attempted to define the heme-iron coordination environment of rhIDO by using site-directed mutagenesis. Since the crystal structure of IDO has only been solved recently (*12*), the only previous 'structural' information available comes from spectroscopic studies (*3, 4, 8*), and from sequence alignments between IDOs and IDO-like myoglobins (*7*). These sequence alignment studies have proved vital for the identification of residues in the proximal and distal sites of the heme moiety in IDO.

Extensive spectroscopic studies on the rabbit intestinal IDO revealed the identity of the fifth and sixth ligand to the heme iron to be a histidine imidazole and a sterically hindered histidine imidazole respectively, by comparison to previous studies on myoglobin (*10*) and horseradish peroxidase (*4, 13*). Site-directed mutagenesis studies based on sequence alignments (*9*), have identified His346 as essential for heme binding and hence enzymatic activity. This observation is in agreement with our results on the His346Ala variant, which is expressed as an *apo* form of IDO. This suggests that His346 is the proximal ligand to the heme iron.

The identity of the sixth ligand has been a matter of on-going speculation in the literature (reviewed in (*14*)). Spectroscopic data from a number of laboratories (*4, 15*) have consistently reported the presence of a low-spin heme component in the ferric form and that the data for IDO are consistent with a bis-histidine-ligated heme. The EPR data for the His303Ala variant are useful in this context and show that in this variant the low-spin component is diminished. There are two possible interpretations: either that His303 is the sixth nitrogenous ligand in this low-spin species or that His303 is located in a region of the protein that is (indirectly) involved in controlling a larger conformational change within the protein structure that leads to formation of this low-spin derivative. While this work was in progress, the crystal structure of rhIDO was published, (Figure 4.14 (A)). It shows that His303 is situated ~15 Å away form the bound inhibitor (4-phenylimidazole), which immediately eliminates the possibility that this residue is the sixth coordination ligand of the heme. The second scenario appears to be more plausible, since His303 is located near the interface of the two domains (Figure 4.14 (B)), which are connected with a large loop (residues 250-267, shown in red). It is possible that removal of His303 might therefore lead to large

conformational changes (observed by spectroscopic methods) that affect the population of low-spin heme.

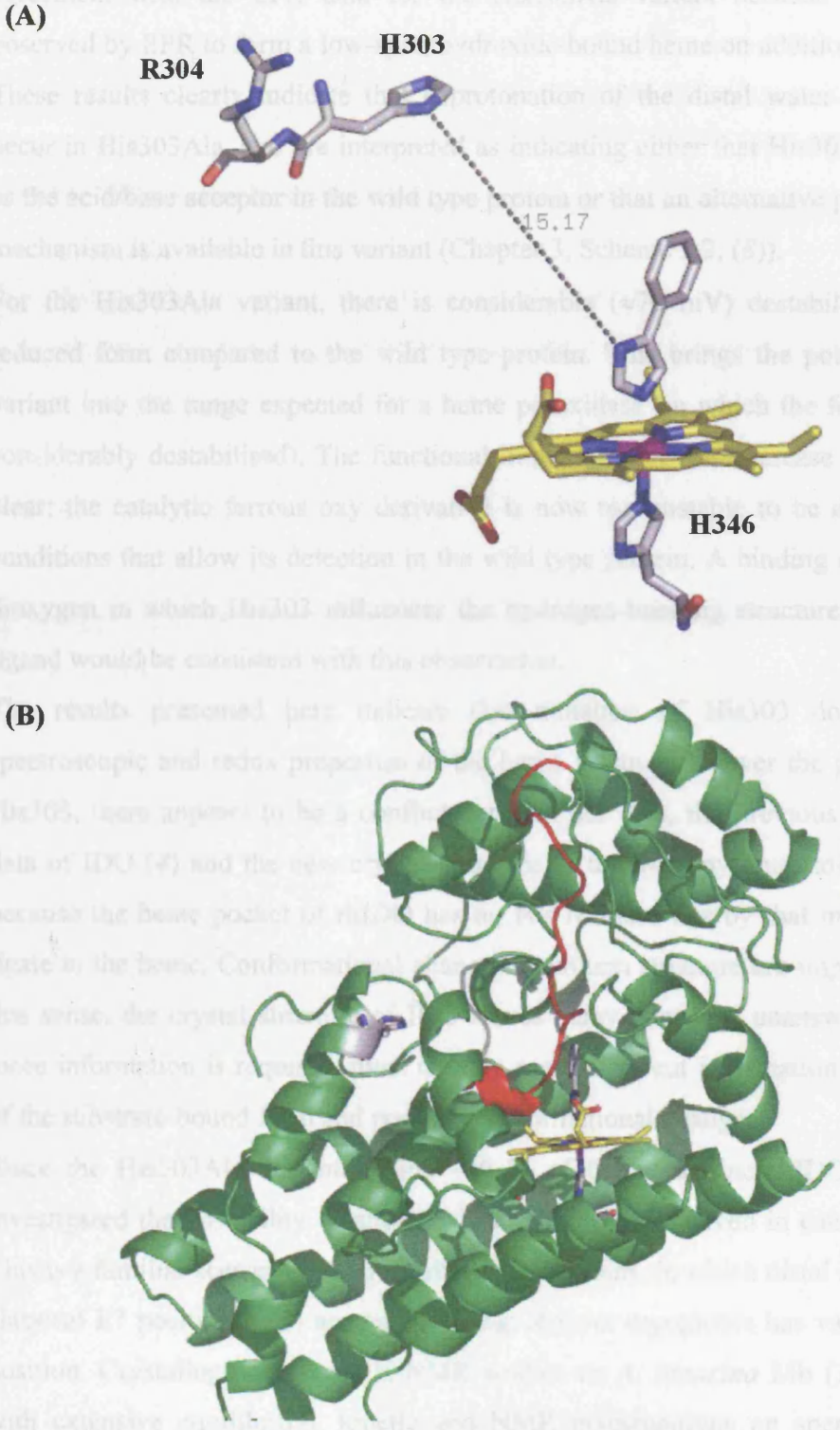

Figure 4.14 (A) Ball-and-stick model of the active site of IDO-PI complex. Residues His346, His303, Arg304 and the bound inhibitor (PI) are shown in grey. Heme is shown in yellow. **(B)** Structure of IDO-PI complex. The long loop connecting the two domains is coloured in red. Residue His303 (grey) is shown near the interface of the two domains.

The fact that His303Ala is catalytically competent for L-Trp turnover suggests that substrate binding is not critically dependent on the presence of this residue. This is in agreement with the EPR data for the His303Ala variant because His303Ala is observed by EPR to form a low-spin, hydroxide-bound heme on addition of substrate. These results clearly indicate that deprotonation of the distal water molecule can occur in His303Ala, and are interpreted as indicating either that His303 does not act as the acid/base acceptor in the wild type protein or that an alternative proton transfer mechanism is available in this variant (Chapter 3, Scheme 3.2, (*8*)).

For the His303Ala variant, there is considerable (≈70 mV) destabilisation of the reduced form compared to the wild type protein. This brings the potential for this variant into the range expected for a heme peroxidase (in which the ferrous form is considerably destabilised). The functional implication of this decrease in potential is clear: the catalytic ferrous oxy derivative is now too unstable to be detected under conditions that allow its detection in the wild type protein. A binding orientation for dioxygen in which His303 influences the hydrogen-bonding structure of the bound ligand would be consistent with this observation.

The results presented here indicate that mutation of His303 does affect the spectroscopic and redox properties of the heme group. Whatever the precise role of His303, there appears to be a conflict between our data, the previous spectroscopic data of IDO (*4*) and the new crystal structure of the 4-phenylimidazole-bound form because the heme pocket of rhIDO has no His residues nearby that might plausibly ligate to the heme. Conformational changes in protein structure are implicated but, in this sense, the crystal structure of IDO leaves many questions unanswered. Clearly, more information is required, most notably more clear-cut information on the nature of the substrate-bound form and possible conformational changes.

Since the His303Ala variant retains ~50 % of the wild type rhIDO activity, we investigated the possibility of another distal site being involved in catalytic activity. This is a familiar scenario in nonvertebrate myoglobins, in which distal residues at the classical E7 position (His) are replaced, *e.g. Aplysia* myoglobin has valine at the E7 position. Crystallographic and ^{1}H-NMR studies on *A. limacina* Mb (*16, 17*), along with extensive equilibrium, kinetic and NMR investigations on sperm whale Mb variants, have suggested that a nearby arginine residue (position E10) provides an an alternative mechanism of ligand stabilisation (*18-20*). In the amino acid sequence of

rhIDO, an arginine residue is located at position 304, exactly adjacent to His303. This arginine residue could participate in hydrogen bonding interactions with the bound dioxygen in wild type rhIDO and in the His303Ala variant.

Site-directed mutagenesis studies, in which the Arg304 residue has been replaced with an alanine, were carried out in order to investigate the effects of this residue on the enzymatic activity and oxygen stabilisation. The newly formed variant (Arg304Ala) has nearly identical spectroscopic and kinetic features with the wild type rhIDO. Spectroscopic studies on the formation and decomposition of the ferrous-oxy derivative of this variant, have shown no distinct differences with the wild type, indicating that this residue is not involved in ligand stabilisation in rhIDO.

4.6 References

1. Dai, W., Gupta, S. L. (1990) *Biochem. Biophys. Res. Comm., 168*, 1-8.
2. Tone, S., Takikawa, O., Habara-Ohkubo, A., Kadoya, A., Yoshida, R., Kido, R. (1990) *Nuc. Acid Res., 18*, 367.
3. Uchida, K., Shimizu, T., Makino, R., Sakaguchi, K., Iizuka, T., Ishimura, Y., Nozawa, T., Hatano, M. (1983) *J. Biol. Chem., 258*, 2526-2533.
4. Sono, M.,Dawson, J. H. (1984) *Biochim. Biophys. Acta, 789*, 170-187.
5. Sono, M. (1990) *Biochem., 29*, 1451-1460.
6. Shimizu, T., Nomiyama, S., Hirata, F., Hayaishi, O. (1978) *J. Biol. Chem., 253*, 4700-4706.
7. Suzuki, T., Kawamichi, H., Imai, K. (1998) *Comp. Biochem. Physiol., Part B, 121*, 117-128.
8. Papadopoulou, N. D., Mewies, M., McLean, K. J., Seward, H. E., Svistunenko, D. A., Munro, A. W., Raven, E. L. (2005) *Biochem., 44*, 14318-14328.
9. Littlejohn, T. K., Takikawa, O., Walker, M. J., Truscott, R. J. W. (2003) *J. Biol. Chem., 278*, 29525-29531.
10. Antonini, M., Brunori, E. (1971) *Hemoglobin and Myoglobin and their Reactions with Ligands.*, North Holland Publishers, Amsterdam.
11. Newmyer, S., Ortiz de Montellano, P. R. (1996) *J. Biol. Chem., 271*, 14891-14896.
12. Sugimoto, H., Oda, S., Otsuki, T., Hino, T., Yoshida, T., Shiro, Y. (2006) *Proc. Nat. Acad. Sc., 103*, 2611-2616.
13. Yonetani, T., Yamamoto, H., Erman, J. E., Leighh, J. S., Reed, G. H. (1972) *J. Biol. Chem., 247*, 2447-2455.
14. Sono, M., Roach, M. P., Coulter, E. D., Dawson, J. H. (1996) *Chem. Rev., 96*, 2841-2887.
15. Sono, M. (1986) *Biochem., 25*, 6089-6097.
16. Qin, J., La Mar, G. N., Ascoli, F., Bolognesi, M., Brunori, M. (1992) *J. Mol. Biol., 224*, 891-897.
17. Conti, E., Moser, C., Rizzi, M., Mattevi, A., Lionetti, C., Coda, A., Ascenzi, P., Brunori, M., Bolognesi, M. (1993) *J. Mol. Biol., 233*, 498-508.

18. Cutruzolla, F., Travaglini-Allocatelli, C., Brancaccio, A., Brunori, M. (1996) *Biochem. J., 314*, 83-90.

19. Smerdon, S. J., Krzywda, S., Brzozowsi, A. M., Davies, G. J., Wilkinson, A. J., Brancaccio, A., Cutruzzola, F., Travaglini-Allocatelli, C., Brunori, M.,Li, T., Brantley, R. E., Carver, T. E., Eich, R. F., Singleton, E., Olson, J. S. (1995) *Biochem., 34*, 8715-8725.

20. Draghi, F., Miele, A. E., Travaglini-Allocatelli, C., Vallone, B., Brunori, M., Gibson, Q. H., Olson, J. S. (2002) *J. Biol. Chem., 277*, 7509-7519.

Chapter 5

Spectroscopic & Mechanistic Studies on Recombinant Human Indoleamine 2,3-Dioxygenase

5.1 Introduction

The detailed catalytic mechanism of indoleamine 2,3-dioxygenase (IDO) is still a matter of ongoing investigation. For many years, the absence of crystallographic data for the enzyme resulted in very little structural and mechanistic information being available. Although a structure for IDO is now available (*1*), there is no information on the likely substrate binding site, which means that the molecular details of substrate oxidation are still not defined. As has already been discussed in Chapter 1 (Section 1.8.3.3), the catalytic cycle (Figure 5.1) is known to include a redox state change in the heme iron ($Fe^{2+} \rightarrow Fe^{3+}$), dioxygen binding and L-Trp binding. It is also suggested that the enzyme forms a ternary complex (Fe^{2+}–O_2–L-Trp). However, the order in which these events occur remains unclear. From earlier studies (*2*), it is known that L-Trp has higher affinity for the enzyme than dioxygen; however, this does not rule out the binding of dioxygen before L-Trp and it is also possible that the cycle proceeds via both routes.

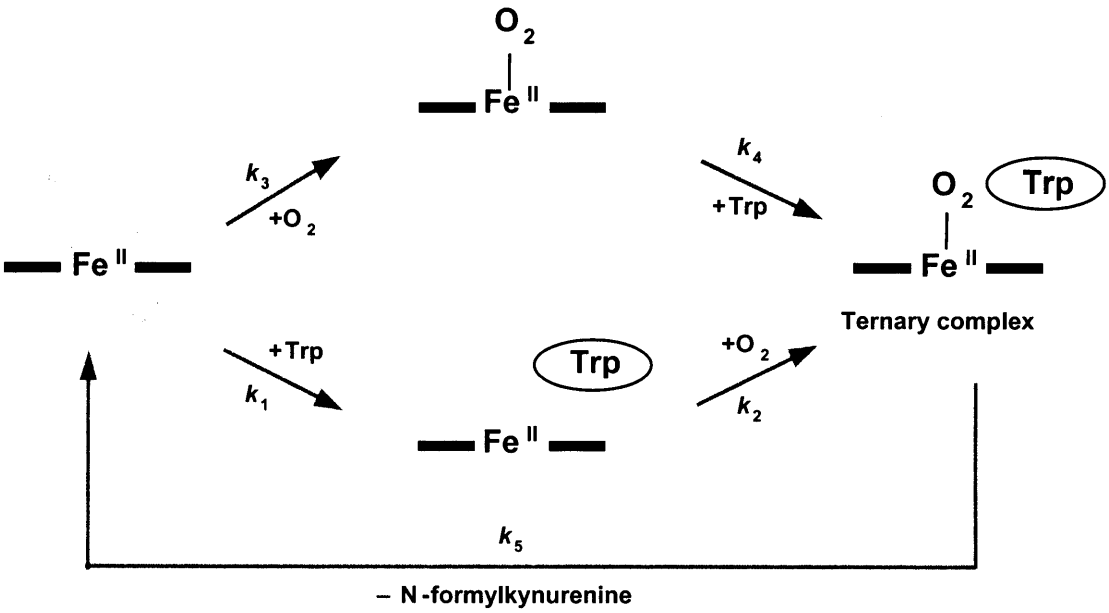

Figure 5.1 The catalytic mechanism of IDO. The porphyrin macrocycle is abbreviated as a black solid line. The possible reaction intermediates and the rate constants are shown.

These two reactions pathways for the enzyme have been deduced from kinetic studies carried out on the native rabbit intestinal IDO. On the other hand, mechanistic studies on the human or recombinant human enzyme have not been reported as yet. As a consequence, the first part of this Chapter describes, for the first time, an investigation of the kinetic properties of the recombinant human IDO, which have been made possible by the development of an expression system that provided enzyme in yields sufficient for kinetic work. A series of steady-state and transient state kinetic studies were performed on the recombinant human IDO in an attempt to define the kinetic behavior of the enzyme. As well as basic parameters (K_M and k_{cat}), we have examined the influence of pH and inhibitors. Using a combination of rapid-scanning and multimixing methods, we have examined the formation and decay of the ferrous-oxy and ternary complexes of rhIDO, which are obligate intermediates in the catalytic cycle.

The implication of IDO in many neurological and autoimmune disorders has been extensively discussed in Chapter 1, and therefore, characterization of the binding site is important, especially in the absence of a crystal structure for the substrate-bound derivative. The remainder of this chapter will focus on characterization of the substrate binding pocket of rhIDO using tryptophan analogues as mechanistic probes. These analogues also have the potential to act as inhibitors of the dioxygenase (see Chapter 1, Section 1.8.3.4). Finally, we have carried out preliminary EPR/ENDOR experiments in order to examine the nature of the ferrous-oxy species in IDO. At the end of this Chapter, the implications of these data are discussed in terms of our current understanding of IDO catalysis.

5.2 Results

5.2.1 Steady State Analysis of Substrate Oxidation

Previous analysis of the rabbit intestinal IDO has shown that the enzyme exhibits conventional Michaelis-Menten kinetic behaviour when L-Trp and other tryptophan derivatives (*e.g.* 5-hydroxytryptophan) are used as substrates (*2-8*). In this present study, a similar observation for rhIDO is observed. A plot of the initial rate of dioxygenase activity (V/[E] s^{-1}), where V is the initial rate and [E] is the enzyme concentration in the reaction mixture) *versus* L-Trp concentration (μM) shows a hyperbolic response (100 mM potassium phosphate, [rhIDO] = 1μM). The data were fitted to the Michaelis-Menten equation (Equation 6.13) and are shown in Figure 5.2. Steady state oxidation of L-Trp at pH 8.0 gave values for k_{cat} and K_M of 3.3 ± 0.1 s^{-1} and 9.5 ± 0.7 μM, respectively (k_{cat}/K_M = 0.35 $\mu M^{-1}s^{-1}$). There is no reported k_{cat} for hIDO; K_M has been previously reported (*9*) as ≈ 20 μM, in agreement with the value obtained here.

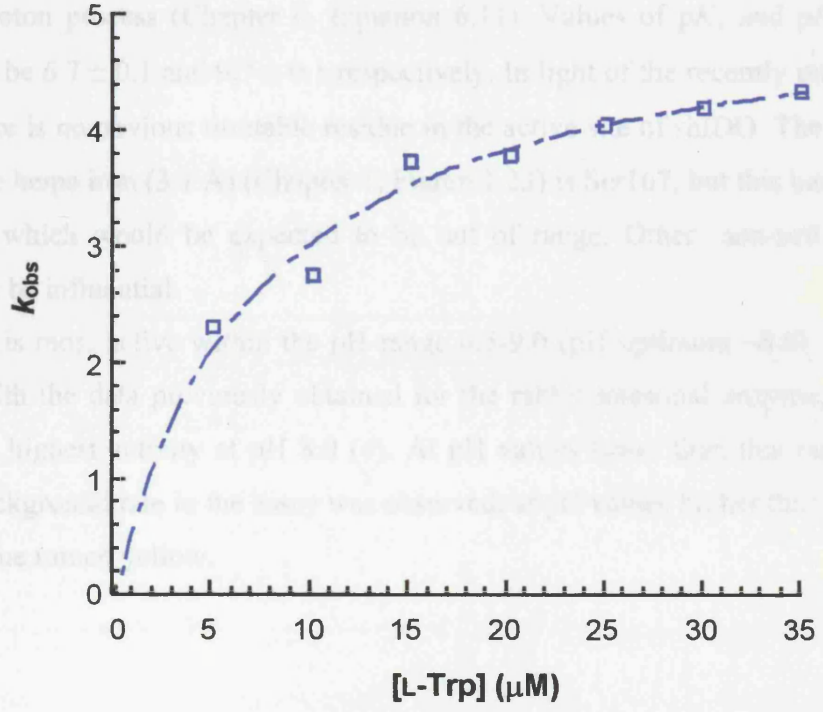

Figure 5.2 Steady state oxidation of L-Trp by rhIDO. Conditions: 1 μM, 25.0 °C, 100 mM potassium phosphate, pH 8.0. Reactions were initiated by addition of rhIDO. The blue dashed line is a fit of the data to the Michaelis-Menten equation (Chapter 6, Equation 6.13).

The recombinant human enzyme also shows activity towards tryptophan analogues, such as D-Trp and 5-hydroxytryptophan; the steady state kinetic parameters are summarised in Table 5.1.

Table 5.1 Steady state kinetic parameters for the oxidation of L-Trp, D-Trp and 5-OH-Trp by rhIDO.

Substrate	k_{cat} (sec^{-1})	K_M (mM)
L-Trp	3.3 ± 0.1	$9.5\times10^{-3} \pm 0.7\times10^{-3}$
D-Trp	5.2 ± 0.1	3.2 ± 0.3
5-OH-Trp	0.06 ± 0.002	0.027 ± 0.003

5.2.2 pH-Dependent Steady State Analysis

To further examine the steady-state behaviour of rhIDO, a pH-dependent profile of L-Trp oxidation was generated. The plot of the specificity constant (k_{cat}/K_M, μM^{-1} s^{-1}) versus pH is shown in Figure 5.3 (see also Table 5.2). rhIDO exhibited a broad bell-shaped kinetic profile, and the data were fitted to the Henderson-Hasselbach equation for a two proton process (Chapter 6, Equation 6.11). Values of pK_1 and pK_2 were calculated to be 6.7 ± 0.1 and 9.7 ± 0.1 respectively. In light of the recently published structure there is no obvious titratable residue in the active site of rhIDO. The closest residue to the heme iron (3.7 Å) (Chapter 1, Figure 1.23) is Ser167, but this has a high pK_a (~ 13), which would be expected to be out of range. Other, non-active site, residues may be influential.

The enzyme is most active within the pH range 6.5-9.0 (pH optimum ~8.0). This is consistent with the data previously obtained for the rabbit intestinal enzyme, which also exhibits highest activity at pH 8.0 (*4*). At pH values lower than this range, an excessive background rate in the assay was observed; at pH values higher than pH 9.3 methylene blue turned yellow.

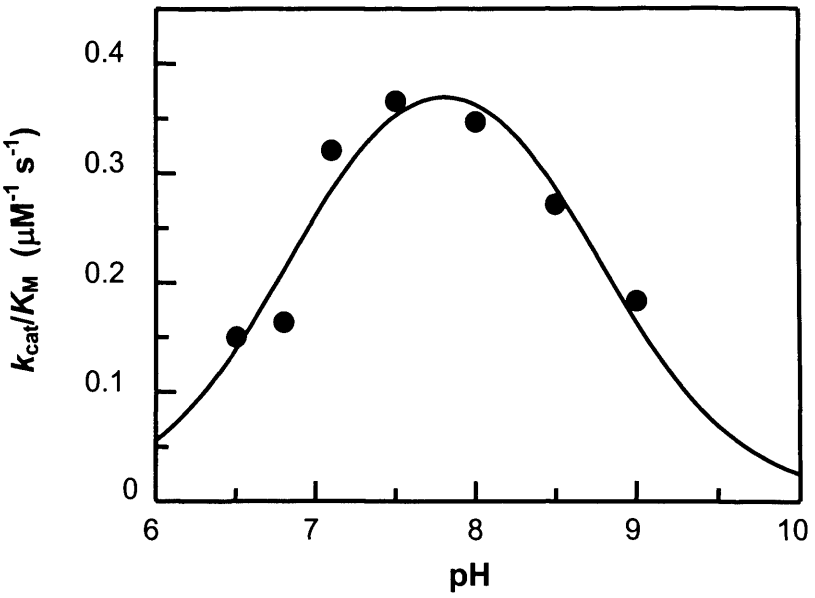

Figure 5.3 pH-dependent steady state kinetic profile for the oxidation of L-Trp by rhIDO. The solid line is a fit of the data to the Henderson-Hasselbach equation for a two proton process. Assays were conducted in 100 mM potassium phosphate buffer, 25.0 °C, [rhIDO] = 1 μM, [L-Trp] = 10 mM. Reactions were initiated by addition of rhIDO.

Table 5.2 Steady state parameters for the oxidation of L-Trp by rhIDO as function of pH.

pH	k_{cat} (s^{-1})	K_M (μM)	k_{cat}/K_M (μM^{-1} s^{-1})
6.5	1.9 ± 0.1	12.7 ± 1.4	0.15
6.8	1.6 ± 0.1	9.8 ± 1.2	0.16
7.1	2.6 ± 0.1	8.1 ± 0.7	0.32
7.5	3.3 ± 0.1	9.0 ± 1.0	0.37
8.0	3.3 ± 0.1	9.5 ± 0.7	0.35
8.5	2.2 ± 0.1	8.1 ± 0.8	0.27
9.0	1.6 ± 0.1	8.7 ± 1.6	0.18

5.2.3 Transient State Kinetics of rhIDO

In the present study we are focusing on the study of the ferrous-oxy (Figure 5.4(A)) and ternary (Figure 5.4(B)) complexes of rhIDO, which are obligate intermediates of the catalytic cycle. This is obtained by using rapid-scanning techniques, which are commonly used for the identification of transient intermediates in related heme proteins.

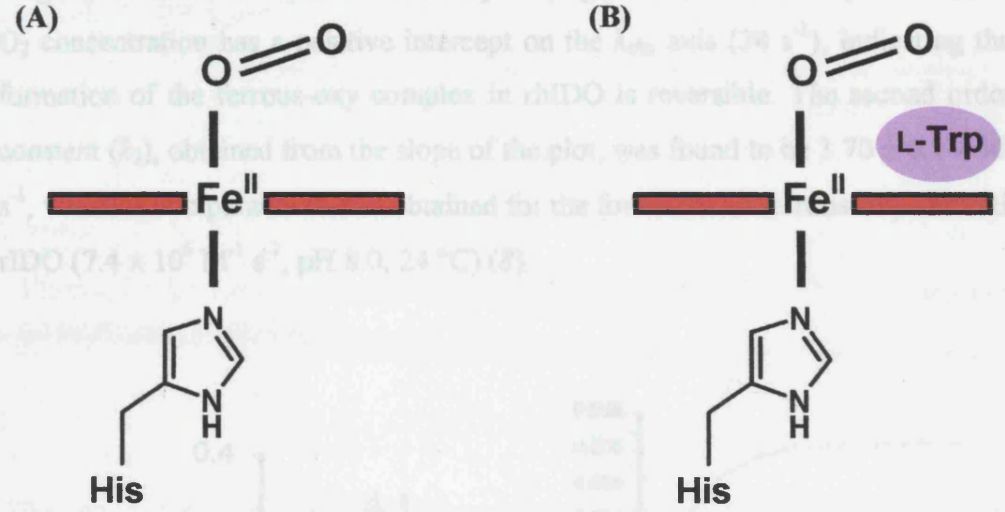

Figure 5.4 Diagrammatic representations of the ferrous-oxy (A) and ternary (B) complexes of rhIDO.

5.2.3.1 Spectra of the Ferrous-Oxy Complex of rhIDO

Photodiode array experiments were undertaken (100 mM potassium phosphate, pH 8.02, 25 °C) to determine the spectrum of the ferrous-oxy derivative of rhIDO (Figure 5.5) immediately after reaction of ferrous rhIDO with dioxygen. This was obtained by mixing the reduced enzyme (reduced with sodium dithionite, 0.2 mM) with an oxygen saturated buffer solution (1.2 mM, 25 °C, see Chapter 6). The reaction was monitored over a time base of 0.5 seconds (200 spectra were collected). The wavelength maxima (λ_{max} = 416, 539, 576 nm) were identical with those observed when the complex was detected using conventional UV-visible spectroscopy (Chapter 3).

5.2.3.2 Formation of the Ferrous-Oxy Complex of rhIDO

The rate of the ferrous-oxy derivative formation was determined by measuring absorbance changes at 416 nm (100 mM potassium phosphate, pH 8.0, degassed and bubbled with O_2 at 25 °C for 1 hour, $[O_2] \approx 1.2$ mM). All kinetic traces were monophasic and fitted to a single exponential function (Chapter 6, Equation 6.17) (Figure 5.5, inset). The observed pseudo-first order rate constants (k_{obs}) obtained at different concentrations of O_2 were linearly proportional to O_2 concentration in the range of 10 to 60-fold excess over enzyme (Figure 5.6). The fitted plot of k_{obs} *versus* O_2 concentration has a positive intercept on the k_{obs} axis (34 s^{-1}), indicating that the formation of the ferrous-oxy complex in rhIDO is reversible. The second order rate constant (k_3), obtained from the slope of the plot, was found to be $3.70 \pm 0.1 \times 10^5$ M^{-1} s^{-1}, which is comparable to that obtained for the formation of ferrous-oxy derivative of rIDO (7.4×10^6 M^{-1} s^{-1}, pH 8.0, 24 °C) (*8*).

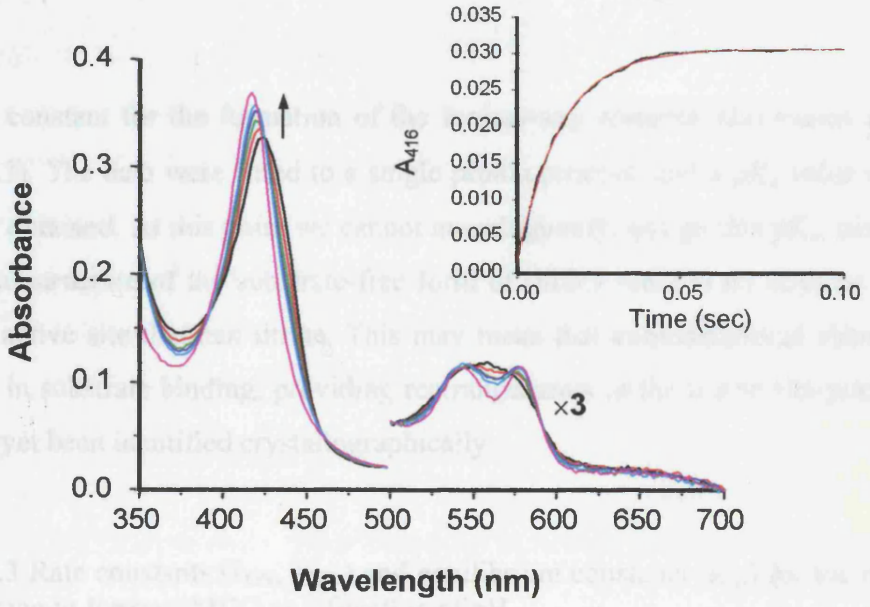

Figure 5.5 Time-dependent spectroscopic changes for the formation of the ferrous-oxy complex of rhIDO. Conditions: 100 mM potassium phosphate (degassed and bubbled with O_2 at 25 °C for 1 hour, $[O_2] \approx 1.2$ mM), pH 8.0, 25 °C, [rhIDO] = 10 μM. Black spectrum: ferrous rhIDO; Magenta spectrum: ferrous-oxy rhIDO ($[O_2] = 0.6$ mM). The *inset* shows a typical transient trace for the reaction followed as an increase in absorbance.

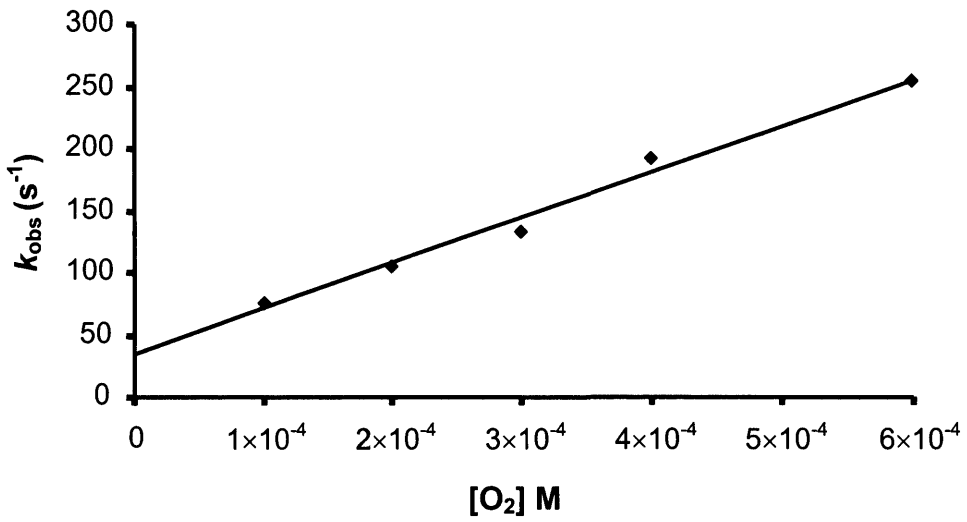

Figure 5.6 Linear dependence of k_{obs} for the formation of the ferrous-oxy complex on dioxygen concentration.

The rate constant for the formation of the ferrous-oxy complex (k_3) varies with pH (Table 5.3). The data were fitted to a single proton process, and a pK_a value of 6.2 ± 0.06 was obtained. At this point we cannot unambiguously assign this pK_a, since from the crystal structure of the substrate-free form of rhIDO there is no obvious residue near the active site that can titrate. This may mean that conformational changes are involved in substrate binding, providing rearrangements in the active site pocket that have not yet been identified crystallographically.

Table 5.3 Rate constants (k_{ON}, k_{OFF}) and equilibrium constants (K_{eq}) for the binding of dioxygen to ferrous rhIDO as a function of pH.

pH	k_{ON} (M^{-1} s^{-1})	k_{OFF} (s^{-1})	K_{eq} (M^{-1})
6.0	6.53×10^5	38.2	1.70×10^4
7.0	4.23×10^5	37.0	1.14×10^4
8.0	3.70×10^5	34.0	1.09×10^4
8.5	3.60×10^5	20.0	1.80×10^4

In order to further investigate the above observations of hydrogen bonding interactions preliminary EPR/ENDOR studies have been carried out on oxyferrous rhIDO that has been cryoreduced by γ-irradiation at 77 K, in collaboration with Dr. Roman Davydov (Department of Chemistry, Northwestern University, Illinois).

The EPR spectrum of the irradiated frozen oxyferrous-rhIDO (Figure 5.7) clearly shows the presence of a hydroperoxo intermediate ($Fe^{3+}OOH$), observed as a 'pair' of signals. The majority form of this intermediate has a g-tensor typical of most hydroperoxo ferriheme species previously studied (g_2 = 2.30). A minor form of this species exhibits an unusual g-tensor, g_1 = 2.35. The two observed g-values of 2.32 and 2.35 are in good agreement with the ones observed for $P450_{cam}$, and indicate the presence of two different conformations of the dioxygen molecule in the parent oxyferrous state or rhIDO (*10*). Both these conformers are hydrogen bonded; in the absence of an obvious hydrogen-bonding residue in the crystal structure, we suggest that this may be to a water molecule present in the active site of the dioxygenase. This is in agreement with the fact the cytochromes P450 recruit water molecules upon oxygenation (proton delivery on oxygenation). A distinguishing feature of monooxygenases is their ability to reductively cleave the O–O bond of dioxygen to generate a "reactive oxygen" species (Fe^{IV}=O, Compound I) capable of oxygen atom insertion into hydrocarbon substrates. At first it was proposed that the P450 proximal thiolate ligand serves as a strong internal electron donor to facilitate O–O bond cleavage to generate the high-valent iron-oxo intermediate (the "push" effect) (*11*). But the "big push" of the cysteinate proximal ligand cannot, by itself, accomplish the cleavage of the O–O bond. Sligar (*12*) has proposed a distal charge relay involving two distal side amino acids, Thr252 and Asp251 in $P450_{cam}$, to carry out the proton donation. Further refinement of the role of these amino acids suggested that the oxygen of Thr252 positions a water molecule to deliver protons to the iron-bound peroxide.

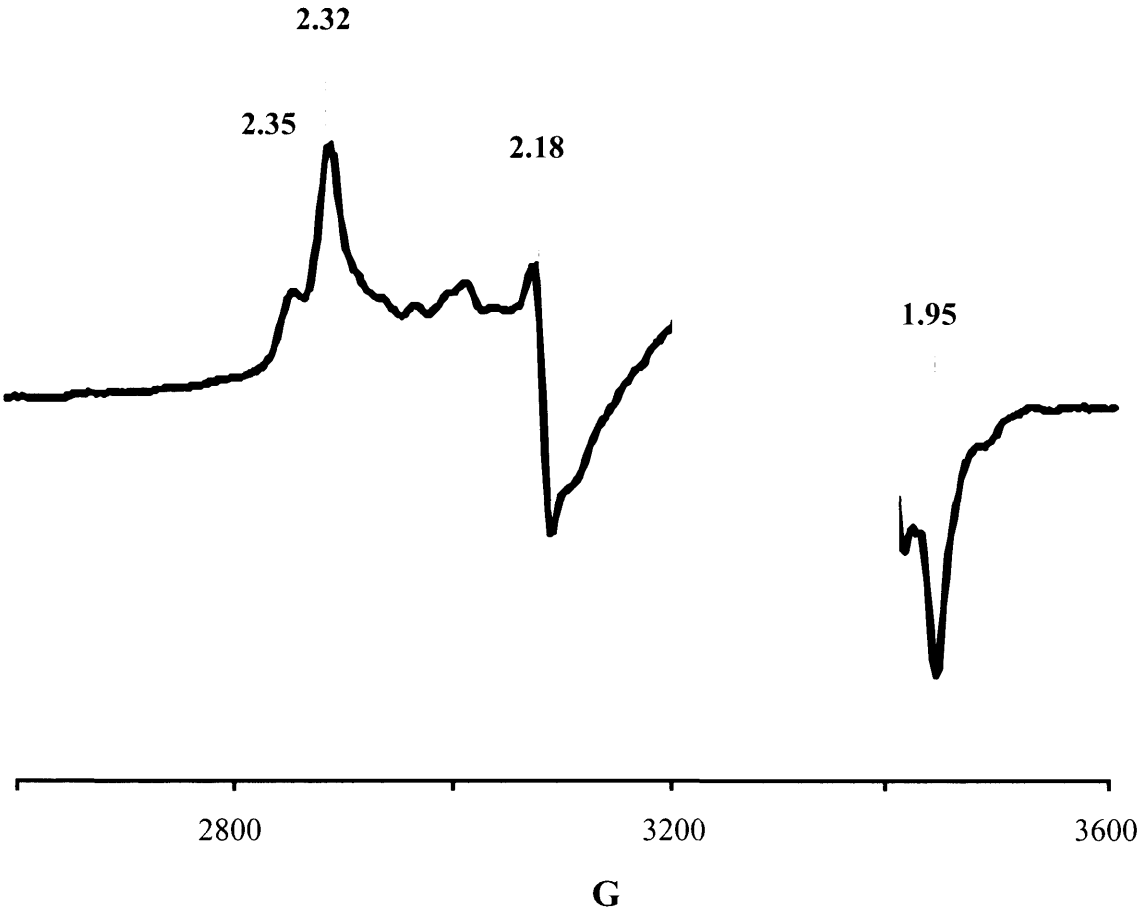

Figure 5.7 20 K X-band EPR spectrum of oxyferrous rhIDO cryoreduced at 77K. Conditions: 100 kHz modulation amplitude 5 G, microwave power 20 mW, microwave frequency 9.100 GHz, and T = 77 K.

As the temperature is annealed to 173 K, the hydroperoxo intermediate with the unusual g-tensor (g_1 = 2.35) becomes dominant. Hence, upon stepwise annealing of the hydroperoxo intermediate seen above (Figure 5.7), the two forms relax with no changes in g-values and we observe an exchange in intensity of the two conformers, with the (g_1 = 2.35) dominating the spectrum (Figure 5.8).

These results show that the product of reduction exhibits multiple EPR-active forms and hence the parent oxyferrous intermediate can be inferred to exist in multiple substates. It also suggests that the Fe–O–O angle is changing upon annealing, probably due to steric constraints by residues or water molecules of the distal pocket.

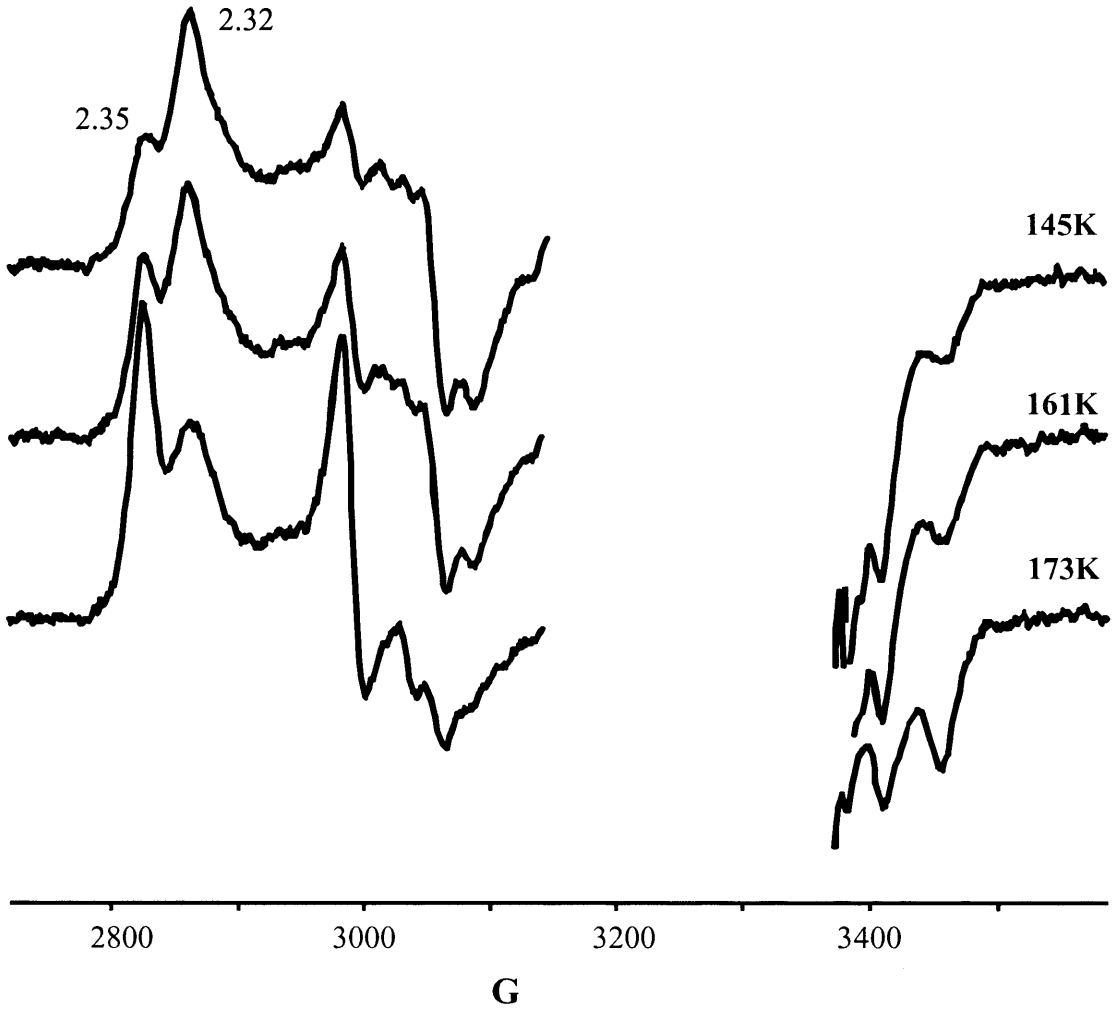

Figure 5.8 X-band EPR spectra of oxyferrous rhIDO cryoreduced and after annealing at indicated temperatures. Conditions: 100 kHz modulation amplitude 5 G, microwave power 20 mW, microwave frequency 9.100 GHz, and T = 77 K. 2.32 and 2.35 labels need to be clearer here.

A proton ENDOR spectrum (Figure 5.9) of the cryoreduced oxy rhIDO in H_2O and D_2O (D_2O/40% d_2-ethylene glycol) buffers was collected at $g_2 = 2.32$, and shows the presence of an exchangeable proton assigned to a hydrogen bond from a distal residue or water molecule to the "peroxo" moiety.

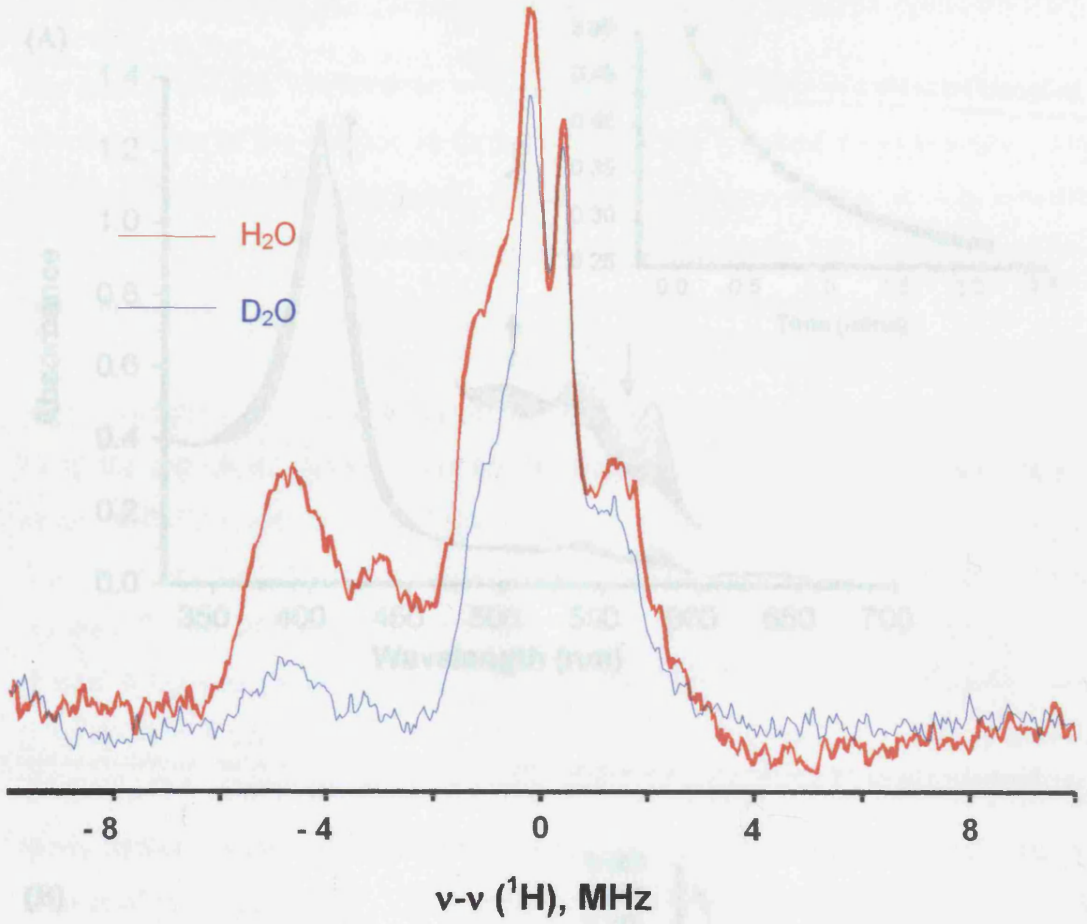

Figure 5.9 ^{1}H ENDOR spectrum of the cryoreduced oxyferrous rhIDO in H_2O (red) and D_2O (blue) buffers. Conditions: modulation frequency 100 kHz, modulation amplitude 1.5 G, microwave frequency 35 GHz, microwave power 35 db, sweep rate 0.5 MHz/s, RF power 10 W, RF broadening 60 kHz.

We were also able to monitor the decomposition of the ferrous-oxy complex using UV-visible spectroscopy (Figure 5.10(A)). In this case the reaction was monitored over a longer time base (~ 2 minutes). A plot of the changes in absorbance at 576 nm *versus* time (minutes), yielded a k_{dec} for the ferrous-oxy complex of 0.011 s^{-1} (Figure 5.10(A), inset). In the presence of L-Trp (100 μM) (Figure 5.10(B)), the k_{dec} for the oxy derivative changes to 0.0043 s^{-1} (Figure 5.10(B), inset).

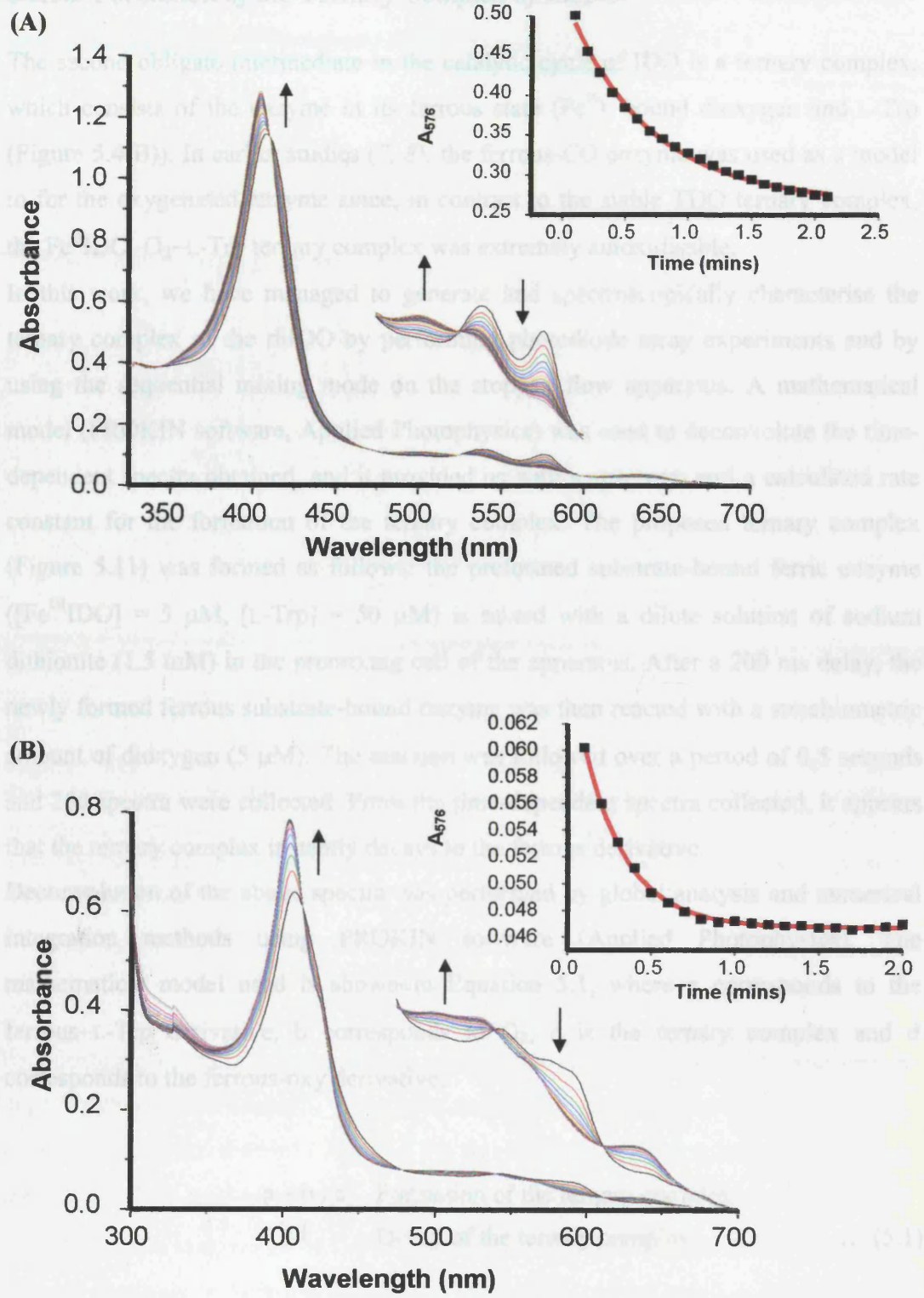

Figure 5.10 Representative data set for the decomposition of the ferrous-oxy complex of rhIDO in the absence (A) and the presence (B) of L-Trp. Insets (A) and (B) fit of data at 576 nm to a first order exponential decay (Chapter 6, Equation 6.18). Conditions: 100 mM potassium phosphate, pH 8.0, 25 °C, [L-Trp] = 100 μM, [rhIDO] = 4 μM.

5.2.3.3 Formation of the Ternary Complex of rhIDO

The second obligate intermediate in the catalytic cycle of IDO is a ternary complex, which consists of the enzyme in its ferrous state (Fe^{II}), bound dioxygen and L-Trp (Figure 5.4(B)). In earlier studies (*7, 8*), the ferrous-CO enzyme was used as a model to for the oxygenated enzyme since, in contrast to the stable TDO ternary complex, the Fe^{II}IDO–O_2–L-Trp ternary complex was extremely autoxidisable.

In this work, we have managed to generate and spectroscopically characterise the ternary complex of the rhIDO by performing photodiode array experiments and by using the sequential mixing mode on the stopped flow apparatus. A mathematical model (PROKIN software, Applied Photophysics) was used to deconvolute the time-dependent spectra obtained, and it provided us with a spectrum and a calculated rate constant for the formation of the ternary complex. The proposed ternary complex (Figure 5.11) was formed as follows: the preformed substrate-bound ferric enzyme ([Fe^{III}IDO] = 5 μM, [L-Trp] = 50 μM) is mixed with a dilute solution of sodium dithionite (1.5 mM) in the premixing cell of the apparatus. After a 200 ms delay, the newly formed ferrous substrate-bound enzyme was then reacted with a stoichiometric amount of dioxygen (5 μM). The reaction was followed over a period of 0.5 seconds and 200 spectra were collected. From the time-dependent spectra collected, it appears that the ternary complex instantly decays to the ferrous derivative.

Deconvolution of the above spectra was performed by global analysis and numerical integration methods using PROKIN software (Applied Photophysics). The mathematical model used is shown in Equation 5.1, where a corresponds to the ferrous–L-Trp derivative, b corresponds to O_2, c is the ternary complex and d corresponds to the ferrous-oxy derivative.

$$\begin{aligned} a + b &\rangle c \quad \text{Formation of the ternary complex} \\ c &\rangle d \quad \text{Decay of the ternary complex} \end{aligned} \qquad \ldots (5.1)$$

The following figure (Figure 5.11) shows the calculated spectra for the three components of the above reaction. The spectrum obtained for the ternary complex has maxima of 412, 542 and 582 nm. The mathematical model employed to obtain the

spectra of the intermediates of this reaction, also provided us with a calculated rate constant for formation of the ternary complex ($k_{ternary}$) of ~ 1×10^7 M^{-1} s^{-1}.

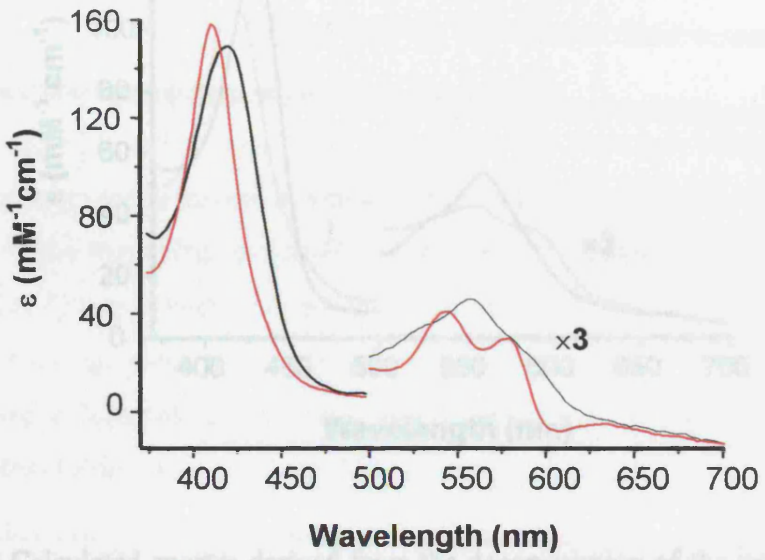

Figure 5.11 Calculated spectra derived from the deconvolution of the time-dependent spectra for the formation of the ternary complex of rhIDO. The red line corresponds to the calculated spectrum of the ternary complex (Fe^{II}rhIDO–L-Trp–O_2); the black line corresponds to the Fe^{II}–L-Trp derivative. The visible region has been magnified by a factor of 3.

To investigate the decay of the ternary complex, the reaction was monitored over a longer timebase (131 seconds). The calculated spectra derived from the decay of the ternary complex are shown in Figure 5.12, in which the black spectrum has maxima (428, 529^{sh}, 559 nm) and corresponds to the Fe^{II}rhIDO–L-Trp derivative. The red spectrum – with maxima of 417, 556 and 589 nm – is very similar to the previously assigned spectrum of the ternary complex. Hence from the information obtained from the above experiment we can draw a scheme for the formation and decay of this intermediate in the catalytic cycle of rhIDO (Scheme 5.1)

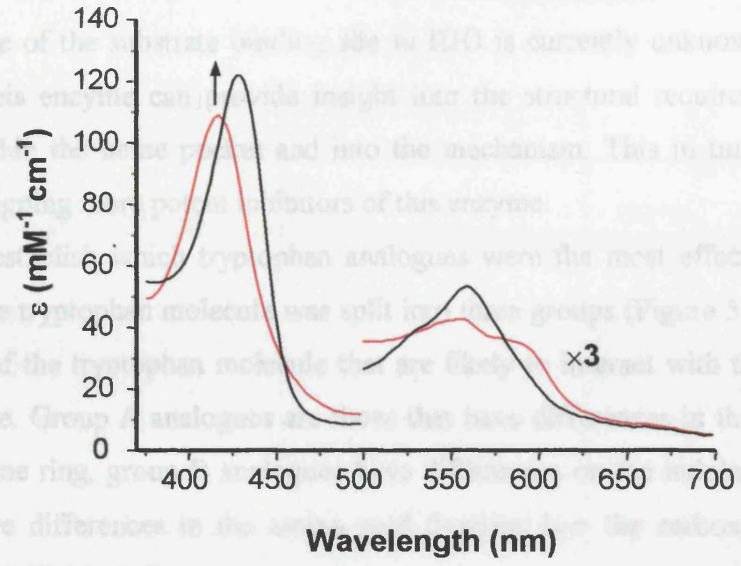

Figure 5.12 Calculated spectra derived from the deconvolution of the time-dependent spectra for the decay of the ternary complex of rhIDO. The black spectrum is represents the Fe^{II}rhIDO–L-Trp derivative of rhIDO; the red line corresponds to the ternary complex (Fe^{II}rhIDO–O_2–L-Trp).

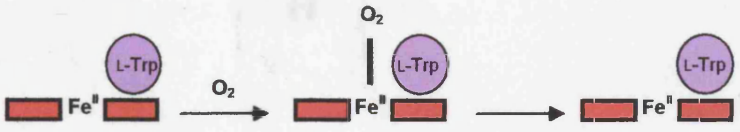

Scheme 5.1 Diagrammatic representation of the formation and decay of the ternary complex of rhIDO. The red box represents the heme.

5.2.4 Inhibition Studies on rhIDO

5.2.4.1 Introduction

As the nature of the substrate binding site in IDO is currently unknown, inhibition studies on this enzyme can provide insight into the structural requirements of the substrate within the heme pocket and into the mechanism. This in turn may prove useful in designing more potent inhibitors of this enzyme.

In order to establish which tryptophan analogues were the most effective potential inhibitors, the tryptophan molecule was split into three groups (Figure 5.13) based on the regions of the tryptophan molecule that are likely to interact with the enzyme in the active site. Group A analogues are those that have differences in the substituents on the benzene ring, group B analogues have differences on the indole nitrogen and group C have differences in the amino acid function (*i.e.* the carboxylic acid and amino groups) (Table 5.4).

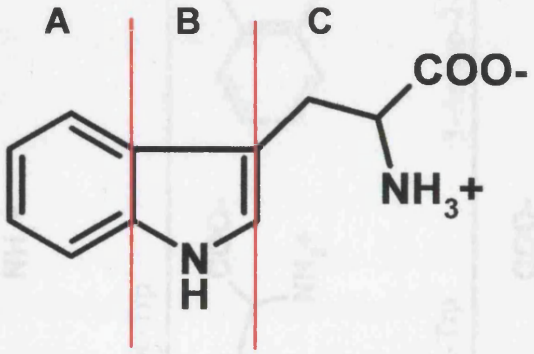

Figure 5.13 Chemical structure of the tryptophan molecule. The dashed red lines indicate the three groups of tryptophan analogues that have substituents on the specified parts of the molecule.

Table 5.4 The chemical structures of tryptophan analogues belonging in the three groups of analogues used in this study.

Group A	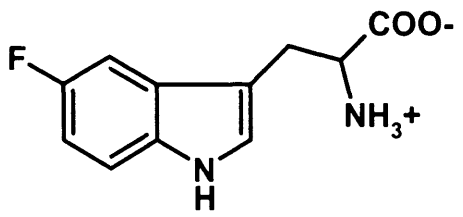		
	5-Fluoro-DL-Trp		
Group B	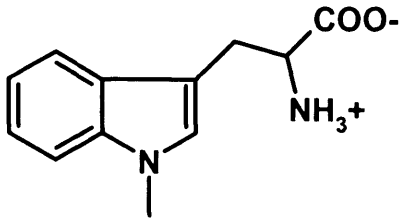	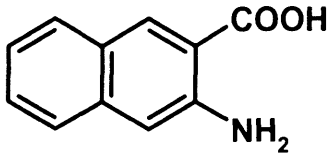	
	1-Methyl-DL-Trp	3-Amino-2-Napthoic Acid	
Group C	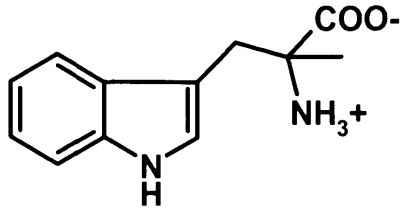	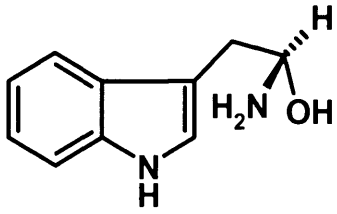	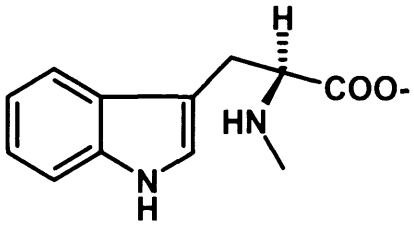
	α-Methyl-DL-Trp	L-Tryptophanol	N-Methyl-L-Trp

5.2.4.2 Group A Analogues

Only one group A analogue was examined, this was 5-fluoro-DL-Trp, which has a fluorine atom substituted at carbon five on the benzene ring and is a mixture of D- and L-isomers. The structure of this analogue is shown in Table 5.4. Six different concentrations of this inhibitor were used to study its effect on the initial rate of the enzyme activity. On the basis of the crystal structure (*1*), it is suspected that this part of the normal tryptophan molecule binds in a hydrophobic region, probably close to Phe163, Phe226 and Phe227 (Chapter 1, Figure 1.23).

The plots of initial rate (V/[E] s^{-1}) against [L-Trp] at each analogue concentrations are shown in Figure 5.14. These plots show that for 5-fluoro-DL-Trp concentrations in the range 50-200 μM the V_{max} varies very little but at lower concentrations (10 and 20 μM) the maximum rate varies. This may be because higher concentrations of the analogue are required to have an effect. Plots of V/[E] (s^{-1}) *versus* [L-Trp], gave a k_{cat} value of 2.60 ± 0.11 s^{-1} and a K_M value of 12.11 ± 1.61 μM. This is a 21% decrease in k_{cat} indicating that some inhibition of rhIDO is occurring.

Figure 5.15 shows the Lineweaver-Burk plot for this analogue from which it can clearly be seen that as the inhibitor concentration increases the slope of the trendline tends to increase corresponding to the increase in K_M (slope of the Lineweaver-Burk plot is equal to K_M/V_{max}). The intercept does not greatly vary except for lower inhibitor concentrations. This pattern most closely resembles competitive inhibition at higher concentrations because the K_M increases but the V_{max} remains largely unchanged. However, at lower concentrations the pattern is more like non-competitive inhibition as there is higher variation in the V_{max}, therefore, as the inhibitor displays properties of both competitive and non-competitive inhibition it is likely that the inhibition occurring is a more complicated example of mixed inhibition. As the slope of the Lineweaver-Burk plot is changing it has been plotted against the inhibitor concentration to produce a secondary plot (Figure 5.16). From this secondary plot a K_i value of 90 μM can be estimated from the x-axis intercept signifying that this analogue is a relatively strong inhibitor of rhIDO.

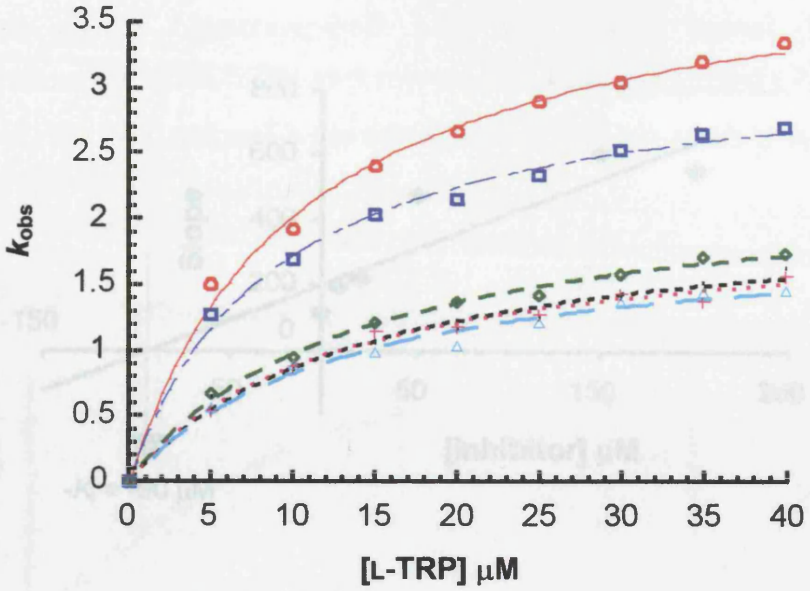

Figure 5.15 Steady state oxidation of L-Trp by rhIDO in the presence of increasing concentrations of 5-fluoro-DL-Trp (10 (o), 20 (□), 50 (◊), 75 (---), 100 (+) and 200 (Δ) μM). Conditions: 1 μM, 25.0 °C, 100 mM potassium phosphate, pH 8.0. Reactions were initiated by addition of rhIDO. The kinetic data were fitted to the Michaelis-Menten equation (Chapter 6, Equation 6.13).

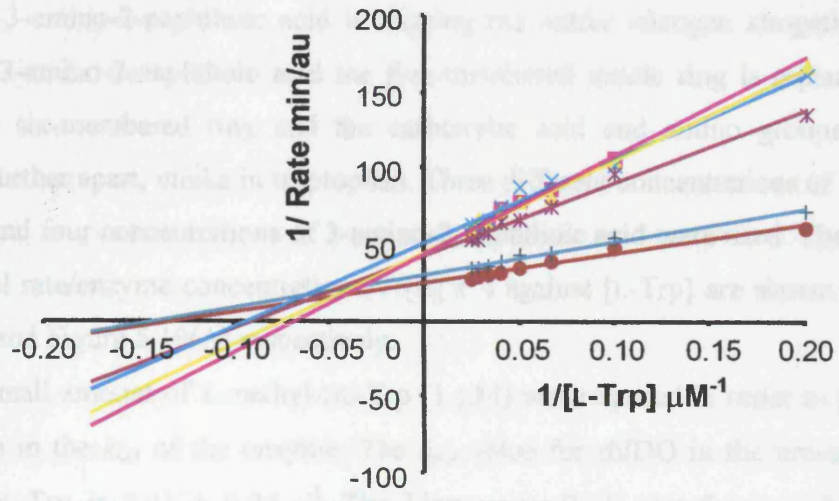

Figure 5.15 The Lineweaver-Burk plot derived from the kinetic data from Figure 5.13.

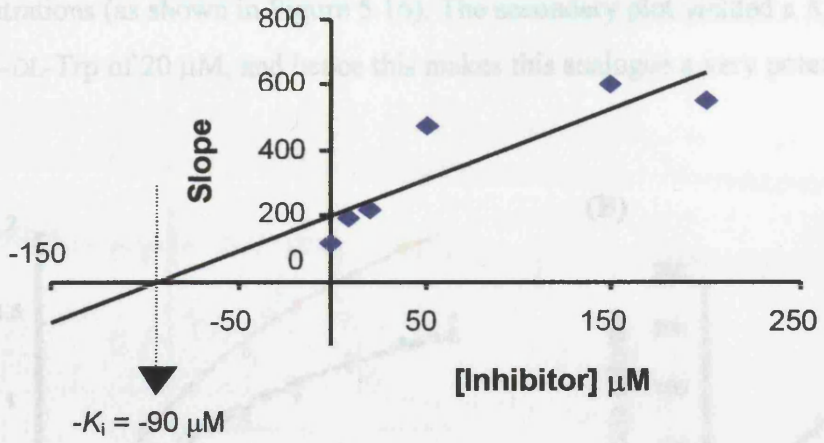

Figure 5.16 A secondary plot derived from the Lineweaver-Burk plot to determine the inhibition constant K_i for 5-fluoro-DL-Trp.

5.2.4.3 Group B Analogues

Two group B analogues were examined; these were 1-methyl-DL-Trp and 3-amino-2-naphthoic acid, which each has differences in the indole ring of tryptophan. 1-methyl-DL-tryptophan has a methyl group substituted for the hydrogen on the indole nitrogen whereas 3-amino-2-naphthoic acid is missing the indole nitrogen altogether (Table 5.4). In 3-amino-2-naphthoic acid the five-membered indole ring is replaced by an aromatic six-membered ring and the carboxylic acid and amino groups are also pushed further apart, unlike in tryptophan. Three different concentrations of 1-methyl-DL-Trp and four concentrations of 3-amino-2-naphthoic acid were used. The plots for the initial rate/enzyme concentration (V/[E] s^{-1}) against [L-Trp] are shown in Figure 5.17(A) and Figure 5.19(A) respectively.

Only a small amount of 1-methyl-DL-Trp (1 μM) was required in order to produce a reduction in the k_{cat} of the enzyme. The k_{cat} value for rhIDO in the presence of 1-methyl-DL-Trp is 2.41 ± 0.24 s^{-1}. The Lineweaver-Burk plot for 1-methyl-DL-Trp (Figure 5.17(B)) indicates that this analogue is a competitive inhibitor. This is further emphasised in the large increase in K_M of the enzyme for the substrate L-Trp when 1-methyl-DL-Trp is present. This also indicates that the presence of 1-methyl-DL-Trp

must decrease the affinity of the enzyme for the substrate. The slope (K_M/V_{max}) of the trendlines in the Lineweaver-Burk plot were plotted against the inhibitor concentrations (as shown in Figure 5.16). The secondary plot yielded a K_i value for 1-methyl-DL-Trp of 20 μM, and hence this makes this analogue a very potent inhibitor.

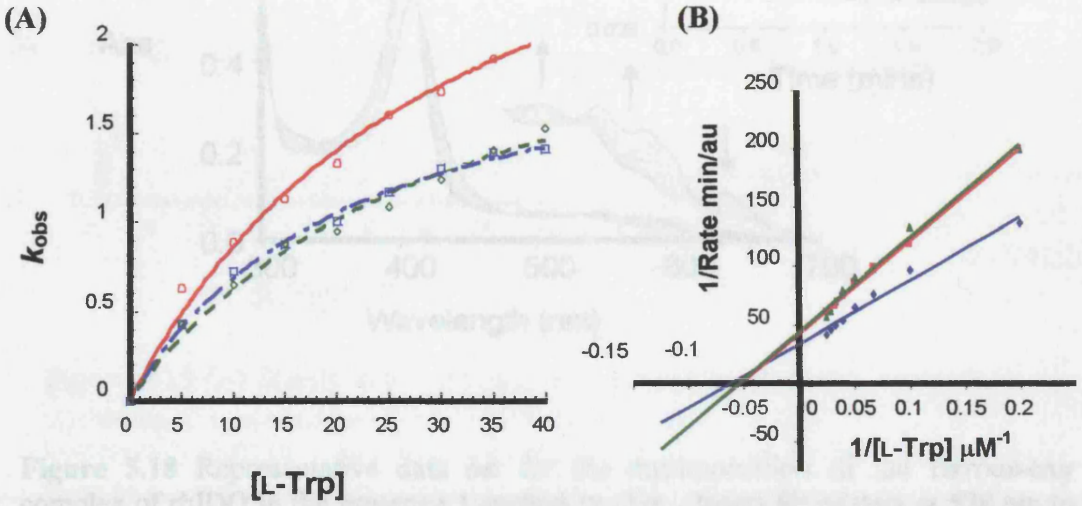

Figure 5.17 (A) Steady state oxidation of L-Trp by rhIDO in the presence of increasing concentrations of 1-methyl-DL-Trp (1(o), 5 (□) and 10 (◊) μM). (B) The Lineweaver-Burk plot derived from the kinetic data from (A), where the red line corresponds to 1 μM [inhibitor], the blue line to 5 μM [inhibitor] and the green line to 10 μM [inhibitor]. Conditions: 1 μM, 25.0 °C, 100 mM potassium phosphate, pH 8.0. The reaction was initiated by addition of rhIDO. The kinetic data were fitted to the Michaelis-Menten equation (Chapter 6, Equation 6.13).

Due to the fact that 1-methyl-DL-Trp has proven to be the most potent inhibitor we have also investigated how this analogue affects the stability of the ferrous-oxy derivative of rhIDO. This was examined by monitoring the decay of the ferrous-oxy rhIDO in the presence of the inhibitor (Figure 5.18). A plot of the absorbance changes at 576 nm *versus* time (minutes) (Figure 5.16, wrong figure inset) yielded a decay constant (k_{dec}) of 0.0043 ± 0.0002 s^{-1}, which is identical to the k_{dec} obtained for the ferrous-oxy complex in the presence of the substrate.

The above result suggests that the inhibitor, like the substrate, favours the stability of the ferrous-oxy form.

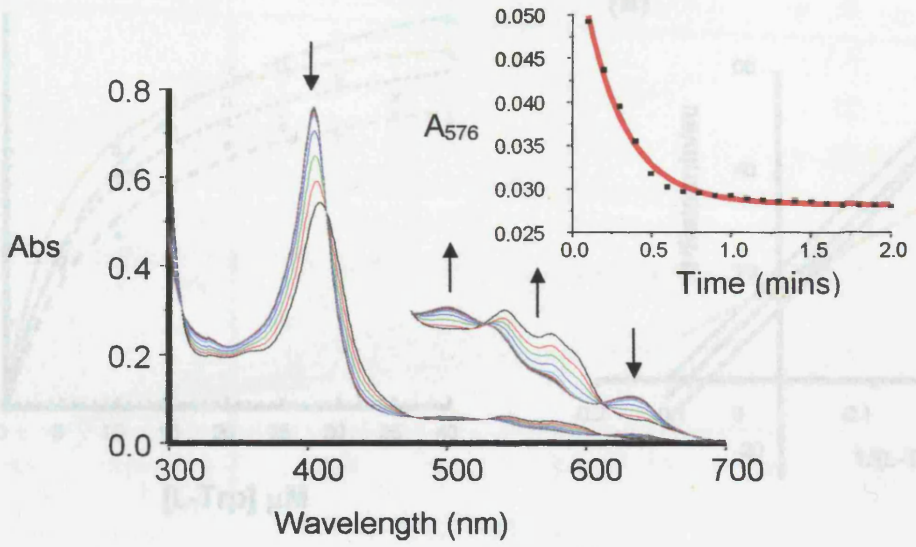

Figure 5.18 Representative data set for the decomposition of the ferrous-oxy complex of rhIDO in the presence 1-methyl-DL-Trp. (Inset) Fit of data at 576 nm to a first order exponential decay (Equation 5.1). Conditions: 100 mM potassium phosphate, pH 8.0, 25 °C, [1-methyl-DL-Trp] = 100 μM, [rhIDO] = 4 μM.

Unlike 1-methyl-DL-Trp, much larger concentrations of 3-amino-2-napthoic acid (25 μM) were required to produce a detectable enzyme inhibition. A k_{cat} value of 3.86 ± 0.81 s^{-1} was obtained in the presence of 3-amino-2-naphthoic acid (Figure 5.19(A)). 3-Amino-2-naphthoic acid is a much less potent inhibitor than 1-methyl-DL-Trp, the Lineweaver-Burk plot (Figure 5.19(B)) is also less conclusive: there is no change in slope apart from at 50 μM suggesting that the analogue largely follows uncompetitive kinetics as there are changes in the intercept.

The K_M value remains largely unchanged. The K_i value obtained from a secondary plot (intercept of the Lineweaver-Burk plot *versus* [inhibitor]) is 290 μM; this analogue therefore, is a relatively weak inhibitor in comparison to 1-methyl-DL-tryptophan and 5-fluoro-DL-tryptophan. This small inhibition contradicts previous inhibition studies that have found this compound to be a very potent inhibitor, causing 75% inhibition (*13*).

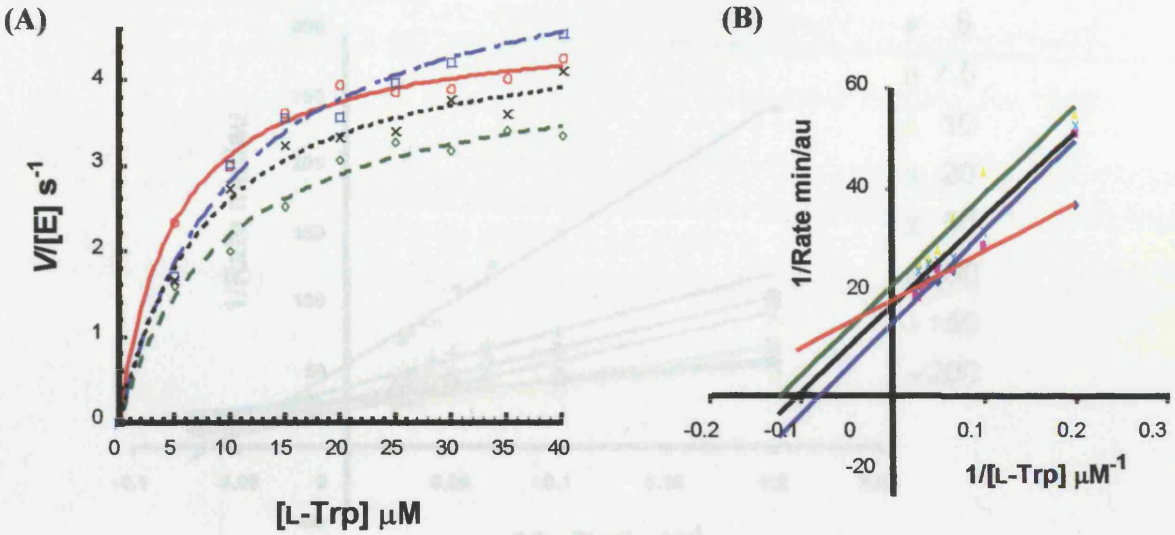

Figure 5.19 (A) Steady state oxidation of L-Trp by rhIDO in the presence of increasing concentrations of 3-amino-2-napthoic acid (25 (o), 50 (□), 75 (◊), and 100 (×) μM). (B) The Lineweaver-Burk plot derived from the kinetic data from (A), where the red line corresponds to 25 μM [inhibitor], the blue line to 50 μM [inhibitor], the green line to 75 μM [inhibitor], and the black line to 100 μM [inhibitor]. Conditions: 1 μM, 25.0 °C, 100 mM potassium phosphate, pH 8.0. The reaction was initiated by addition of rhIDO. The kinetic data were fitted to the Michaelis-Menten equation (Chapter 6,

5.2.4.4 Group C Analogues

Group C analogues have differences in the amino acid function. These analogues are α-methyl-DL-Trp, L-tryptophanol and N-methyl-L-Trp (Table 5.4). From these three analogues only α-methyl-DL-tryptophan exhibited considerable inhibition. A k_{cat} value of 2.65 ± 0.13 s^{-1} was obtained, which corresponds to a decrease of the enzyme activity by 20%. A Lineweaver-Burk plot of different α-methyl-DL-tryptophan concentrations (Figure 5.20) reveals differences in both the slope and the intercept, which as for 5-fluoro-DL-tryptophan appears to show a mixed form of inhibition (Figure 5.13). From the secondary plot of the intercept of the Lineweaver-Burk plot against the inhibitor concentration gives an estimate of the K_i as 130 μM, corresponding to the apparent reduction in the k_{cat} .

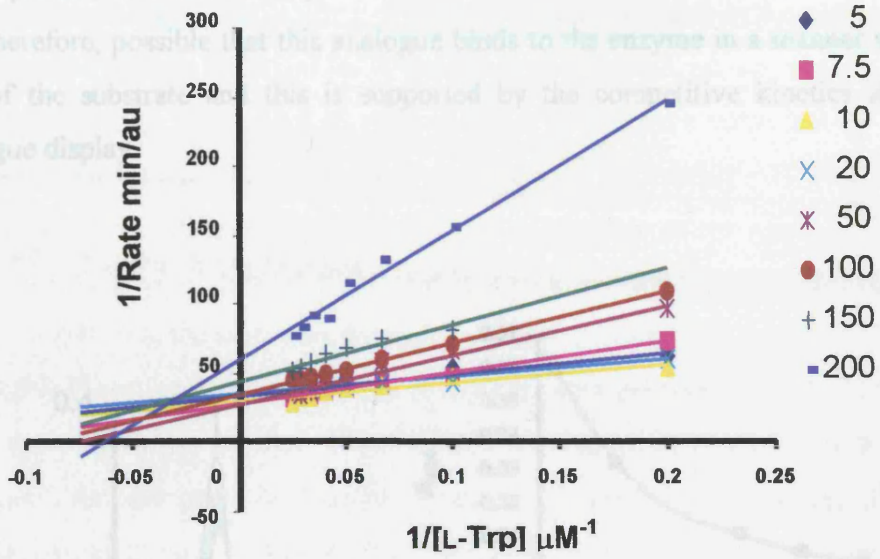

Figure 5.20 The Lineweaver-Burk plot derived from the kinetic data for the oxidation of L-Trp by rhIDO in the presence of α-methyl-DL-Trp (5-200 μM). Conditions: 1 μM, 25.0 °C, 100 mM potassium phosphate, pH 8.0.

5.2.4.5 Effects of Inhibitors on the Absorption Spectra of rhIDO

The effect that the inhibitors have on the UV-visible absorption spectrum of the protein was also examined by addition of the inhibitor to the native enzyme. From the six analogues used during these inhibition studies, only 1-methyl-DL-Trp caused any significant changes in the protein spectrum. Addition of 1-methyl-DL-Trp, the most potent inhibitor, causes significant changes in the visible region similar to those observed upon addition of L-Trp (Figure 5.21). The presence of the inhibitor causes a red shift of the Soret peak from 404 nm to 408 nm, accompanied with an increase in the low-spin signals (537, 577 nm) and a concomitant decrease of the high-spin signals (635 nm). To quantify the binding interaction, the equilibrium binding constant, K_D, for binding of 1-methyl-DL-Trp to ferric rhIDO was measured (Figure 5.22, inset). At pH 8.0, a value for K_D of 0.92 ± 0.03 mM was determined. This value

suggests that the enzyme has lower affinity for the inhibitor compared to the substrate (K_D at pH 8.0, 0.41 ± 0.04 mM).

It is therefore, possible that this analogue binds to the enzyme in a manner similar to that of the substrate and this is supported by the competitive kinetics that these analogue display.

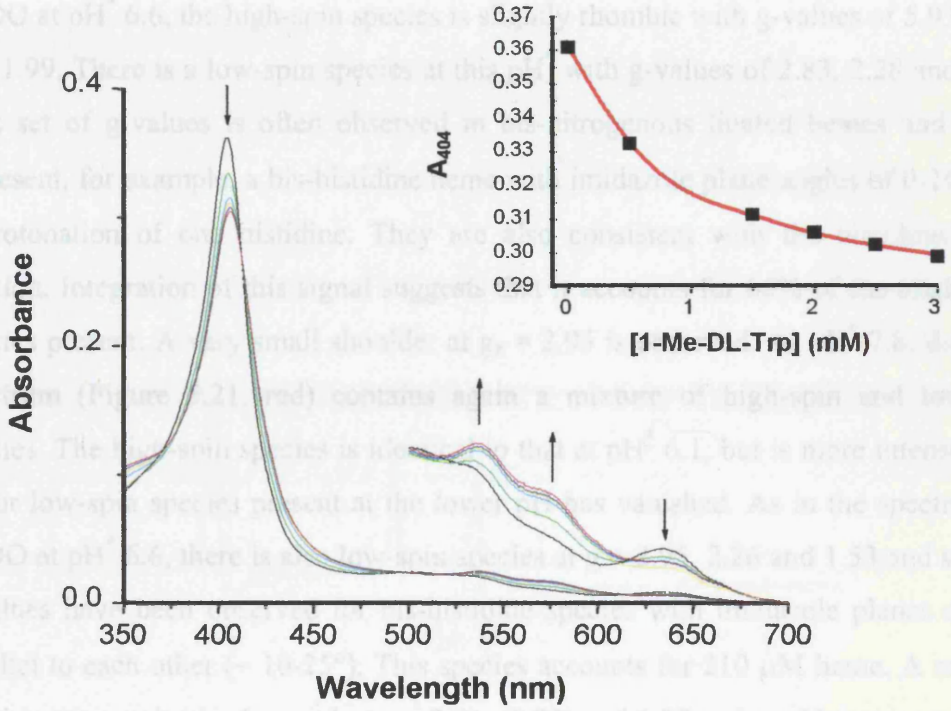

Figure 5.21 Representative data for the determination of K_D at pH 8.0. The visible region has been multiplied by a factor of 5, and arrows indicate the direction of change in absorbance upon successive additions of 1-methyl-DL-Trp (0-3 mM). Inset: Fit of data at 404 nm to Equation 6.10 (conditions: 100 mM potassium phosphate, pH 8.0, 25 °C, [rhIDO] = 2 μM). there are not many data points on that fit.

5.2.4.6 EPR and MCD Spectra of 1-Me-DL-Trp–Bound rhIDO

To further investigate the binding of this tryptophan analogue in the active site of the recombinant protein, EPR and MCD experiments were carried out, and the results are shown in Figures 5.21 and 5.22 respectively. Spectra were collected by Dr Harriet Seward in the laboratories of Professor A J Thomson (University of East Anglia).

The form of the EPR spectrum of rhIDO in the presence of the inhibitor (pH* 6.1) is consistent with a mixture of high- and low-spin species (Figure 5.21, black). Like rhIDO at pH* 6.6, the high-spin species is slightly rhombic with g-values of 5.93, 5.51 and 1.99. There is a low-spin species at this pH* with g-values of 2.83, 2.28 and 1.66. This set of g-values is often observed in bis-nitrogenous ligated hemes and could represent, for example, a bis-histidine heme with imidazole plane angles of 0-10° or a deprotonation of one histidine. They are also consistent with the histidine/amine ligation. Integration of this signal suggests that it accounts for 66% of the total heme species present. A very small shoulder at g_z = 2.95 is observed. At pH* 7.8, the EPR spectrum (Figure 5.21, red) contains again a mixture of high-spin and low-spin species. The high-spin species is identical to that at pH* 6.1, but is more intense. The major low-spin species present at the lower pH has vanished. As in the spectrum of rhIDO at pH* 6.6, there is also low-spin species at g = 2.95, 2.26 and 1.53 and similar g-values have been observed for bis-histidine species with imidazole planes almost parallel to each other (~ 10-25°). This species accounts for 210 μM heme. A second, less intense species is observed at g = 2.71, (2.22) and 1.77 and could represent either histidine/histidinate ligation or partial coordination of 1-methyl-DL-Trp via the amine. The low-spin species observed in rhIDO at g = 2.83, 2.28, and 1.66 could arise from the inhibitor amine group coordinating to the heme or a bis-histidine or histidine/histidinate species. The low-spin species observed in the EPR spectrum at pH* 7.8 is similar to that observed in rhIDO at pH* 6.6 and could arise from the changes in the coordination of His303 or coordination of His303.

The form of the MCD spectrum at pH* 6.1, is consistent with a majority ferric high-spin species at room temperature. The Soret crossover is at 407 nm (3 nm lower than in rhIDO at pH 6.6) and there is a CT_2 band at 640 nm (Figure 5.22(A), black). There are traces of low-spin heme in the spectrum and this is reflected in the intensity of the Soret derivative. The near-IR region (Figure 5.22(B), black) contains a CT_1 derivative

with a crossover at 1100 nm, which suggests histidine/water ligation at the heme. There is a small CT_{ls} peak at 1560 nm, which is assigned to bis-nitrogeneous ligation. At pH* 7.8, the MCD spectrum contains a mixture of high- and low-spin species. Throughout the UV/visible region (Figure 5.22(B), red) the low-spin form predominates, shifting the Soret crossover to 410 nm and increasing its intensity. However, there still is a clear CT_2 band at 640 nm but this has halved in intensity. In the near-IR region (Figure 5.22(B), red), a peak at 1035 nm is the positive lobe of the obscured CT_1 derivative. There is a large CT_{ls} feature at 1555 nm, which is consistent with bis-nitrogeneous ligation.

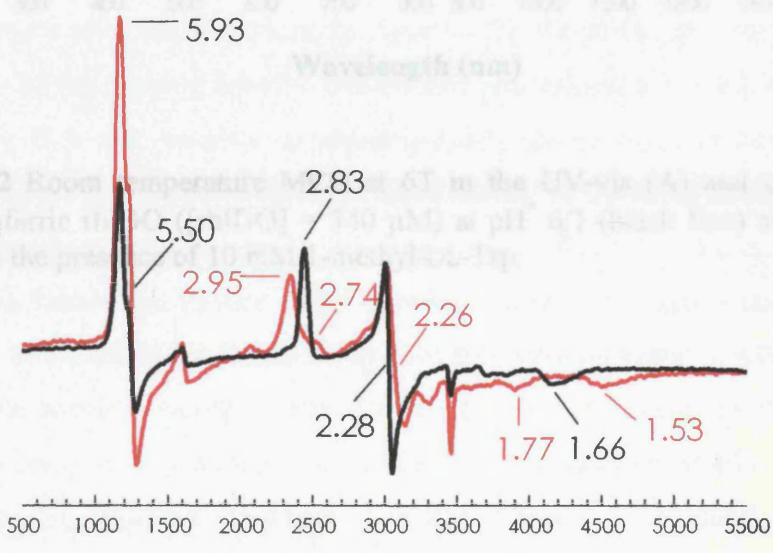

Figure 5.21 Perpendicular mode X-band EPR spectra of ferric rhIDO ([rhIDO] = 340 μM) in the presence of 10 mM 1-methyl-DL-Trp at pH* 6.1 (black line) and pH* 7.8 (red line).

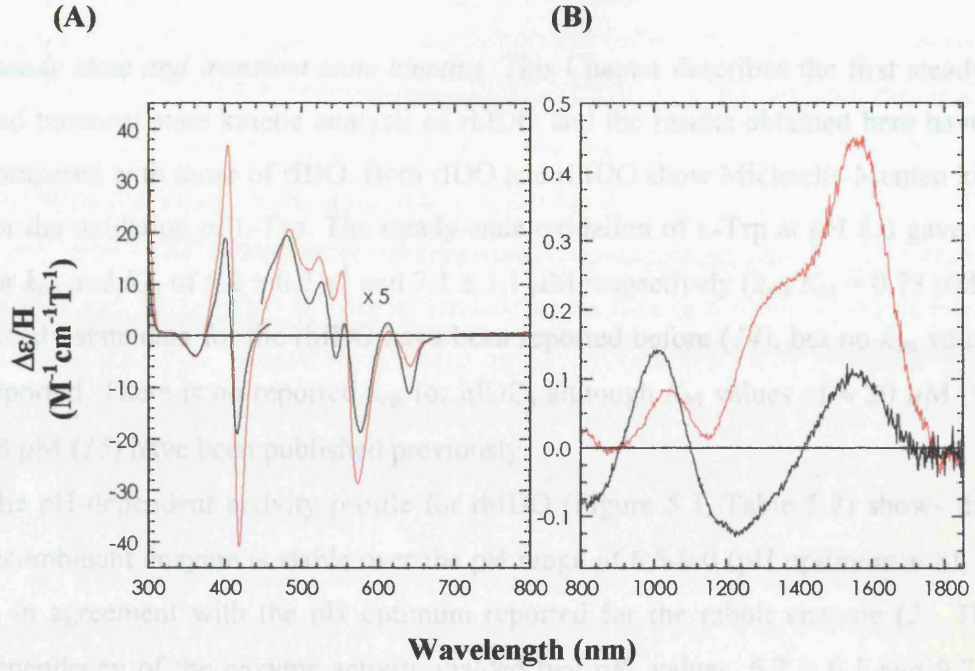

Figure 5.22 Room temperature MCD at 6T in the UV-vis (A) and near-IR (B) regions, of ferric rhIDO ([rhIDO] = 340 μM) at pH* 6.1 (black line) and pH* 7.8 (red line) in the presence of 10 mM 1-methyl-DL-Trp.

5.3 Discussion

Steady state and transient state kinetics. This Chapter describes the first steady state and transient state kinetic analysis of rhIDO and the results obtained here have been compared with those of rIDO. Both rIDO and rhIDO show Michaelis-Menten kinetics for the oxidation of L-Trp. The steady-state oxidation of L-Trp at pH 8.0 gave values for k_{cat} and K_M of 5.2 ± 0.2 s^{-1} and 7.1 ± 1.1 μM respectively (k_{cat}/K_M = 0.73 μM^{-1} s^{-1}). Steady-state data for the rhIDO have been reported before (*14*), but no k_{cat} value was reported. There is no reported k_{cat} for hIDO, although K_M values of ≈ 20 μM (*9*) and 18 μM (*15*) have been published previously.

The pH-dependent activity profile for rhIDO (Figure 5.3, Table 5.2) shows that the recombinant enzyme is stable over the pH range of 6.5-9.0 (pH optimum ≈ 8), which is in agreement with the pH optimum reported for the rabbit enzyme (*2*). The pH dependency of the enzyme activity yielded two pK_a values, 6.7 ± 0.1 and 9.7 ± 0.1 respectively. It is not possible to unambiguously assign these titration processes, however because there is no obvious titratable residue in the heme active site, Ser167 is one of the closest residues to the iron and it is located 3.7 Å above the 3-methyl group of the heme: this residue could possibly ionise in the active site but its pK_a would have to be lowered substantially (pK_a of the hydroxyl group in solution is ~13). One possible scenario would be that the pK_a of the distal serine residue might be changing to compensate a stronger interaction with the substrate at alkaline pH (were we observe the optimum enzymatic activity). On the other hand, site-directed mutagenesis studies on the Ser167Ala variant of rhIDO showed no changes in the dioxygenase activity, although a pH-dependency analysis was not carried out (*1*).

Transient state kinetics for the formation and decomposition of the oxyferrous and the ternary derivatives of rhIDO have not been previously reported. The rate constant for the formation of the oxyferrous intermediate varies with pH, and a pK_a value of 6.2 ± 0.06 was determined. As previously discussed, the only residue in close proximity to the heme iron is Ser167, however we cannot say with certainty that what we observe is the ionisation of this residue.

The committed portion of the catalytic monooxygenation of substrate by cytochromes P450 and other dioxygen-activating enzymes (*16*) begins with one-electron reduction of the dioxygen-bound ferroheme ($Fe^{2+}O_2$), to generate an intermediate assigned as peroxoferriheme ($Fe^{3+}O_2^{2-}$). This intermediate is converted to a hydroperoxoferric

heme intermediate ($Fe^{3+}OOH$), which then accepts a second proton and undergoes heterolytic O–O cleavage to produce compound I ($Fe^{IV}O$), which is the catalytically active species. Through cryoreduction EPR/ENDOR measurements on the oxyferrous rhIDO we were able to identify a hydroperoxo intermediate (g = 2.32, 2.35), which is similar to that observed for cytochrome P450cam (*10*) and which exists as to different conformers. These conformers derive from two conformations of the parent oxy-species and are possibly hydrogen bonded to a residue or a water molecule present in the catalytic site. Water recruitment upon oxygenation is a common trend in cytochromes P450. Another possibility would also be that upon dioxygen (or substrate) binding large conformation changes introduce a titratable residue in the active site of the dioxygenase.

Along with the oxyferrous intermediate the ternary complex (Fe^{II}IDO–O_2–L-Trp) is also an obligate intermediate in the catalytic cycle of IDO. This is a transient species and previous attempts to detect this intermediate were carried out at really low temperatures (-30 °C) and in the presence of organic solvents. In this work we have managed to detect the ternary complex for the human enzyme at room temperature and in the presence of physiological buffers. The wavelength maxima for this important intermediate are 412, 542 and 582 nm (Figure 5.11) and its rate of formation was calculated to be ~ 1×10^7 M^{-1} s^{-1}. Monitoring of the decomposition of this intermediate revealed that after its formation, the L-Trp molecule is released first and then the oxygen molecule (Figure 5.12).

Inhibition Studies. From the pH-dependency steady-state studies it is clear that the enzyme is most efficient at pH 8.0, therefore, all subsequent inhibition studies were carried out at this pH.

The only Group A analogue, 5-fluoro-DL-Trp, showed a 21% inhibition of the rhIDO activity. The presence of this inhibitor in the steady-state assay mixture caused a slight increase of the K_M value suggesting that its presence decreases the affinity of the enzyme for its physiological substrate. A decrease in the specific activity was also observed, indicating a decrease in the efficiency of the enzyme, which is in agreement with the decrease in its catalytic activity. An inhibition constant (K_i) of 90 μM suggests that 5-fluoro-DL-Trp is a relatively potent inhibitor of rhIDO. This supports the suggestion that this region of the Trp molecule binds to a lipophilic cleft, as fluorine compounds are lipophilic. This is in absolute agreement with the crystal

structure of rhIDO (*1*), which revealed a great abundance of hydrophobic residues (Phe163, Phe226, and Phe227). The presence of the fluorine atom on the phenyl ring of L-Trp interferes with the π-stacking interactions with the phenylalanine residues present in the active site.

1-Methyl-DL-Trp (Group B) has proved to be the most potent inhibitor of rhIDO, with a K_i value of 20 μM. The observed increase in the K_M value (28 μM) in the presence of the inhibitor, suggests that this analogue inhibits IDO in a competitive fashion. This Trp analogue lacks the indole proton therefore once bound in the enzyme's active site the catalytic reaction can no longer proceed (Chapter 1, Figure 1.20).

From the Group C analogues tested in these studies, only α-methyl-DL-Trp exhibited moderate inhibition (K_i = 130 μM). This is not unexpected as, although none of the potential hydrogen bonds are removed, they are possibly pushed further apart by the methyl group.

5.4 Conclusions and Future Directions

In summary, the results in this Chapter have indicated that formation of the first committed intermediate in the catalytic cycle – ferrous-oxy rhIDO – is fast. A spectroscopically distinct species that is consistent with formation of a ternary complex has also been identified. ENDOR data indicate that the ferrous oxy species exists in two conformations and evidence for protonation of this species has been observed. The most potent inhibitor for rhIDO is the 1-methyl-DL-Trp, which is found to be a competitive inhibitor and must therefore be binding at the substrate binding site.

Together, the results presented in this Chapter provide preliminary information on the mechanism and the likely catalytic intermediates. At present, however, there are a large number of questions that are still unresolved for IDO, including the nature of the substrate binding site, the role of conformational changes in formation of the ferrous-oxy and substrate-bound forms, the physiological reductase, and the role (if any) of pH in these processes. The results in this thesis present a framework against which more detailed answers to some of these questions can be developed in the future.

5.5 References

1. Sugimoto, H., Oda, S., Otsuki, T., Hino, T., Yoshida, T., Shiro, Y. (2006) *Proc. Nat. Acad. Sc., 103*, 2611-2616.
2. Sono, M., Tanigushi, T., Watanabe, Y., Hayaishi, O. (1980) *J. Biol. Chem., 255*, 1339-1345.
3. Sono, M. (1990) *Biochem., 29*, 1451-1460.
4. Shimizu, T.. Nomiyama, S., Hirata, F., Hayaishi, O. (1978) *J. Biol. Chem., 253*, 4700-4706.
5. Yamamoto, S., Hayaishi, O. (1967) *J. Biol. Chem., 242*, 5260-5266.
6. Higuchi, K., Hayaishi, O. (1967) *Arch. Biochem. Biophys., 120*, 397-403.
7. Hirata, F., Ohnishi, T., Hayaishi, O. (1977) *J. Biol. Chem., 252*, 4637-4642.
8. Taniguchi, T., Sono, M., Hirata, F., Hayaishi, O., Tamura, M., Hayashi, K., Iizuka, T., Ishimura, Y. (1979) *J. Biol. Chem., 254*, 3288-3294.
9. Takikawa, O., Kuroiwa, T., Yamazaki, F., Kido, R. (1988) *J. Biol. Chem., 263*, 2041-2048.
10. Davydov, R., Perera, R., Jin, S., Yang, T., Bryson, T., Sono, M., Dawson, J., Hoffman, B. (2005) *Journal of the American Chemical Society. 127*, 1403-1413.
11. Dawson, J., Iolm, R., Trudell, J. R., Barth, G., Linder, R., Bunnenberg, E., Djerassi, C., Tang, S. C. (1976) *Journal of the American Chemical Society, 98*, 3707.
12. Gerber, N. C., Sligar, S. G. (1994) *The Journal of Biological Chemistry, 269*, 4260.
13. Peterson, A. C., Migawa, M. T., Martin, M. J., Hamaker, L. K., Czerwinski, K. M., Zhang, W., Arend, R. A., Fisette, P. L., Ozaki, Y., Will, J. A., Brown, R. R., Cook, J. M. (1994) *Med. Chem. Res., 3*, 531-544.
14. Littlejohn, T. K., Takikawa, O., Walker, M. J., Truscott, R. J. W. (2003) *J. Biol. Chem., 278*, 29525-29531.
15. Southan, M. D., Truscott, R. J. W., Jamie, J. F., Pelosi, L., Walker, M. J., Maeda, H., Iwamoto, Y., Tone, S. (1996) *Med. Chem. Res.*, 343-352.
16. Sono, M., Roach, M. P., Coulter, E. D., Dawson, J. H. (1996) *Chem. Rev., 96*, 2841-2887.

Chapter 6

Experimental

6 Experimental

This Chapter describes the experimental methods and techniques used throughout this thesis.

6.1 Materials & Stock Solutions

All chemicals were obtained from commercial sources and used without further purification unless otherwise stated. All glycerol was sterilised. All buffers and solutions were made using deionised water (PURELAB option DV 35) and are listed in Appendix A.

6.2 cDNA of Human Indoleamine 2,3-Dioxygenase

The cDNA of human indoleamine 2, 3-dioxygenase (rhIDO) was a kind gift of Dr. Sohan Gupta (Hipple Cancer Research Center) (*1*) and was the starting point for protein expression, of rhIDO and preparation of site-directed variants.

6.2.1 Oligonucleotides

Complementary oligonucleotides (29-35 bases in length) were designed to have ~15 bases either side of the residue to be mutated and end in G or C (See Appendix B). The melting temperatures (T_m) of primers were calculated according to Equation (6.1),

$$T_m = 81.5 + 0.41(\%\,GC) - 675/N - \%\,\text{mismatch} \qquad \ldots (6.1)$$

where *N* is the primer length in bases, % GC is the percentage of mismatching bases in the primer and % mismatch is the percentage of mismatching bases in the primer. All these numbers are rounded to whole numbers for the formula.

The mfold program (IDT SciTools, http://biotools/idtdna.com/mfold) (*2*) was used to predict any secondary structures. The primers were synthesised and purified by the Protein and Nucleic Acid Chemistry Laboratory, University of Leicester and by Invitrogen™. The complementary pairs of oligonucleotides containing the appropriate

mismatch bases (indicated in red), depicted in Table II in Appendix B, were used to prepare the variants of rhIDO studied in this thesis.

6.2.2 Site-Directed Mutagenesis

Site-directed mutagenesis, using the appropriate pair of oligonucleotides, was carried out using the Quickchange™ mutagenesis kit (Stratagene). Reactions were prepared in thin-walled PCR tubes. Each reaction was set-up as in Table 6.1. All chemicals were added in the order listed in Table 6.1 – with the exception of the DNA polymerase (*pfuTurbo™* or *pfuUltra™*), which was added later – to a thin-walled PCR tube and kept on ice. The DNA polymerase was supplied in the kit along with 10× reaction buffer and the dNTP mix. The template was pQKS7 vector containing the rhIDO gene (50-100 ng/μl). The reaction contained 125 μg of each primer.

Water	16-17
10× Buffer	2.5
dNTP	0.5
Template	1-2
Primer F	0.5
Primer R	0.5
DNA Polymerase	0.5

Table 6.1 Reaction volumes used in site directed mutagenesis PCR (μl).

The tubes were then centrifuged (13,000 rpm, ~10 seconds) and the PCR block (Perkin Elmer, 480 DNA Thermocycler) turned on with the programs set as in Table 6.2.

Number of Cycles	Temperature (°C)	Time (s)
1	95	120
16	95	30
	Primer T_m- 5 °C*	30
	72	300
1	72	600
	4	30

Table 6.2 Temperature cycler program for site directed mutagenesis. * See Equation 6.1.

In the 16 cycles, the time at 72 °C (5 minutes) was calculated from the size of the template (1 minute per kb) and the annealing temperature was calculated using Equation (6.2).

$$\text{Primer } T_m - 5 = \text{Primer annealing temperature} \quad \ldots (6.2)$$

When the block reached 94 °C, the *pfuTurbo* or *pfuUltra* was added, a drop of nujol oil (DNase-free) was added to the surface of each reaction and the tubes put in the cycler. PCR products were analysed using 1% agarose gel electrophoresis.

Digestion of the methylated and hemimethylated parental DNA was carried out by the addition of *Dpn*I (1 µl, standard solution in the kit). Mixtures were then centrifuged (1 minute) and immediately incubated at 37 °C for 1 hour to digest the parental DNA. The reaction product was transformed into 50 µl of super-competent *Epicurian Coli* XL1-Blue cells (Stratagene) in pre-chilled Falcon® 2059 Tubes (15 ml), and stored on ice for 30 minutes. The cells were heat-pulsed at 42 °C for 45 seconds, returned to ice for 2 minutes and incubated with shaking for one hour at 37 °C, 250 rpm with 0.5 ml preheated LB-media (42 °C). The transformants were plated onto LB agar plates containing ampicillin (50 µg/ml) and incubated at 37 °C overnight. To confirm the identity of the transformants, a single colony from the overnight plates was selected and incubated into 10 ml LB media containing 100 µg/ml ampicillin overnight at 37 °C with vigorous shaking (250 rpm). Mutant DNA was isolated from overnight cultures using the Qiagen mini-plasmid system following the manufacturer's instructions and using the buffers, resins and tubes provided.

6.2.3 Isolation of DNA

The rhIDO DNA was extracted from cells using a QIAprep® Spin Miniprep kit (Qiagen Cat. No. 27104) from 10 ml overnight cultures using a microcentrifuge. The protocol from the kit (QIAprep® Miniprep handbook, p22) was followed, except the eluting step was performed with sterile water (not EB buffer, see Appendix A). The cells were pelleted in a microcentrifuge tube, 1 ml media at a time, at 13,000 rpm for 2 minutes discarding the supernatant each time. The pellet was then resuspended in buffer P1 (250 µl, with RNase added, and stored at 4 °C, see Appendix A). Buffer P2

(250 µl, see Appendix A) was added and the tube was gently inverted 4-6 times, after which N3 buffer (350 µl, see Appendix A) was added and the tube inverted 4-6 times. The tube was centrifuged (13,000 rpm) for 10 minutes. The supernatant was added to a QIAprep spin column and centrifuged for 1 minute at 13,000 rpm discarding the flow through. The column was washed with PB buffer (500 µl, see Appendix A) and centrifuged at 13,000 rpm for 1 minute discarding the flow through. The column was then washed with PE (750 µl, with ethanol added, see Appendix A) and centrifuged for 1 minute at 13,000 rpm discarding the flow through. The column was centrifuged for 1 minute at 13,000 rpm to remove residual ethanol. The column was placed in a clean 1.5 ml microcentrifuge tube with sterile water (50 µl) in the centre of the column and left standing for 1 minute before centrifuging at 13,000 rpm for 1 minute. The DNA sample obtained was stored at -80 °C. The isolated DNA concentration was calculated using Equation (6.3).

$$A_{260} \times 50 \times \text{Dilution factor} = \text{DNA concentration (ng/µl)} \quad \ldots (6.3)$$

6.2.4 Agarose Gel Electrophoresis

Agarose gels (1.0% w/v) (5.5 cm × 8.5 cm) containing ethidium bromide (20 µl of 10 mg/ml, stored at 4 °C) were cast on a horizontal bed with a well comb and covered in TAE buffer. The comb was removed and samples of isolated DNA (10 µl and 2µl loading buffer (Fermentas)) loaded into the wells. A well was also loaded with 6 µl of 1 Kb DNA ladder (Fermentas, Generuler™). The gel was run for one hour applying a 100 mA current, and DNA was visualised by placing under a UV light.

6.2.5 DNA Sequencing

Sequencing of the entire recombinant mutant or rhIDO-coding gene was performed to ensure that no spurious mutations had arisen during the mutagenic reactions. The Protein and Nucleic Acid Chemistry Laboratory (PNACL) at the University of Leicester carried out all DNA sequencing. It was performed by automated fluorescent sequencing on an Applied Biosystems 373-Stretch machine and the data analysed using the program SeqED (Applied Biosystems). The sequencing primers used are listed in Table I in Appendix B.

6.2.6 Transformation of the Recombinant DNA into Competent E. coli Cells

The sequenced DNA (5 μl) was placed in prechilled Falcon® 2059 Propylene Tubes (15 ml). Competent cells (SG13009 (for rhIDO) and BL21-Gold (DE3) (for rhIDO variants), 70 μl) were added; the reactions were swirled to mix solutions and placed on ice for 30 minutes. A heat shock of the solution at 42 °C, for 90 seconds, was followed by incubation on ice for 2 minutes. The reactions were then incubated with 0.5 ml of Psi Broth (see Appendix A) at 37 °C, shaking for 90 minutes at 225 rpm. The cultures were then pelleted, 300 μl of the supernatant media were removed and the remaining 200 μl of supernatant solution was used to resuspend the bacterial pellets. The cultures were then plated on LB ampicillin agar plates. A single colony from the overnight plate was selected and incubated into LB media (10 ml) containing 100 mg/ml ampicillin and 5 mg/ml L-Trp at 37 °C with vigorous shaking at (225 rpm). DNA was isolated from the overnight cultures using Qiagen Mini-plasmid® kit and analysed as above using agarose electrophoresis and the DNA was re-sequenced to confirm the mutation.

6.3 Bacterial Expression & Purification

6.3.1 Constuction of Expresion Vector pQKS7

The construction of the expression vector and preliminary expression trials in *E. coli* were carried out by Dr Martin Mewies. PCR was employed to modify the 5' and 3' ends of the gene to incorporate *Kpn*I and *Sal*I restriction sites respectively. Primer sequences for the forward and reverse primers were, respectively: forward 5'-GACTACAGGTAC/CGCACACGACTATGGAAAACTCC for the *Kpn*I restriction site (underlined) (*3*); reverse 5'-GGG/TCGACTTAACCTTCCTTCAAAAGGGA for the *Sal*I restriction site. The PCR fragment was digested with the relevant restriction enzymes and the modified gene sub-cloned into the pQE-30 vector (Qiagen) containing an N-terminal hexa-histidine tag. The new N-terminal sequence for the recombinant enzyme was MRGSHHHHHHGSACELGTA-, where the final alanine corresponds to residue 2 of the native protein (numbering according to (*1*)). DNA sequencing (Protein and Nucleic Acid Laboratory, University of Leicester) confirmed that no spurious mutations had arisen during the PCR. A silent mutation (relative to

the database sequence) in the coding region was observed at valine-391 (GTG to GTA).

6.3.2 Bacterial Expression of Recombinant IDO and Variants

For expression of rhIDO, bacterial strain SG13009 p[REP4] (Qiagen) containing the expression vector pQKS7 was grown in Lennox-LB broth medium (Fisher). All Lennox-LB media used to grow *E. coli* were supplemented with 100 μg/ml ampicillin, 50 μg/ml kanamycin, and 50 mg L-tryptophan per litre of media. SDS-PAGE analysis was used to monitor the reaction.

Agar plates containing ampicillin (100 μg/ml) and kanamycin (30 μg/ml) were steaked with *E. coli* cells from a -80 °C glycerol stock. The plates were incubated, inverted and grown at 37 °C overnight.

A single colony, picked from a freshly streaked stock plate, was used to inoculate 5 ml of medium and the culture was incubated overnight with shaking (225 rpm, 37 °C). An aliquot of this overnight culture (930 μl) was used added to glycerol (70 μl) to form a new glycerol stock, which was then frozen on dry ice. The overnight culture was subsequently used to inoculate 200 ml of medium, which was incubated as before to late logarithmic phase (~2-3 hours). A 25 ml aliquot of this culture was used to inoculate 1 L of medium, incubated as before, until the absorbance at 600 nm (OD_{600}) reached approximately 0.9 (~3 hours). The temperature was then reduced to 27 °C and 1 ml of 200 mM phenylmethylsulfonyl fluoride (in isopropanol), 2 ml of 0.5 M EDTA (pH 8.0) and 2 ml of 3.5 mM hemin (in 10 mM NaOH) were added. Induction of cells must take place at 27 °C: induction at 37 °C led to isolation of recombinant enzyme with an atypical UV-visible spectrum, possessing a significant shoulder to the Soret peak. When the OD_{600} nm of the culture reached ≈1.0, 1 M IPTG was added (1 ml, to a final concentration of 1 mM) and the incubation continued overnight. Cells were collected by centrifugation (10 minutes, 6000 rpm, 4 °C), washed by re-suspension with phosphate-buffered saline, re-pelletted as before and frozen at –20 °C, until needed.

For over-expression of rhIDO variants, the bacterial strain BL21 was found to give the best expression. Cells were grown in LB media (Fisher) supplemented with 100 μg/ml ampicillin, and 50 mg L-tryptophan per litre of media. The protocol for bacterial fermentation was identical to that used for rhIDO except that IPTG

induction was at $OD_{600} \approx 0.6$ instead of 1.0 (final concentration of IPTG = 1 mM). Cells were harvested as for rhIDO.

6.3.3 Isolation and Purification of rhIDO and Variants

Cell Lysis

Cell pellets were resuspended in sonication buffer (50 ml) (see Appendix A) containing two EDTA-free Complete™ tablets (Roche), and stirred with lysozyme (~5 mg) for 20 minutes at room temperature until the liquid became viscous. Complete™ Tablets are a cocktail of protease inhibitors (see Appendix A), used to protect the recombinant protein from proteolysis, as evidenced by SDS-PAGE electrophoresis (Figure 6.2, second component). DNase (~5 mg) was added and the suspension was stirred until it became more fluid. The mixture was sonicated on ice, at maximum power, using 8 × 30 s bursts from a MSE sonicator, followed by a cooling period of approximately one minute. Cell-free extract was obtained through pelleting the cell debris by centrifugation (30 minutes, 20 000 rpm, 8 °C). Samples of the cell pellet and the cell-free extract were taken. The cell-free extract was kept at 4 °C. The cell debris pellet was resuspended in sonication buffer and the sonication and centrifugation was repeated and the cell-free extract pooled and frozen. Samples of the cell pellet and the cell-free extract were taken.

Nickel Resin Column

A Ni^{2+}-nitrilotriacetic acid (NTA) agarose column (Qiagen) was used to isolate the rhIDO protein from the cell-free extract. The cell-free extract was thawed and made up to approximately 250 ml with sonication buffer. A column of 10 ml Ni-NTA Superflow resin (Qiagen) was packed and flushed with water (100 ml). The resin was equilibrated with sonication buffer (100 ml), and the cell-free extract loaded on at a steady flow rate. The resin was then washed with wash buffer (100 ml) (see Appendix A). The column was developed using elution buffer (~100 ml,) which contained 100 mM EDTA (see Appendix A). Elution with low pH (4.5) sonication buffer led to rapid enzyme precipitation; elution with imidazole resulted in binding of imidazole to the heme iron, which may obscure spectroscopic and functional data. Excess EDTA

was removed by dialysis in sonication buffer. The resulting protein was then exchanged into storing buffer (see Appendix A) using an Amicon device (Amicon, Bioseparations, Millipore) with nitrogen under pressure using an ultrafiltration regenerated cellulose membrane (MW cut off 10,000, Amicon). Fractions having A_{404}/A_{280} values > 2 were considered pure. The protein was concentrated to a minimum volume of ~10 ml and frozen in aliquots at -80°C. This procedure revealed the presence of only two components (Figure 6.1(A)).

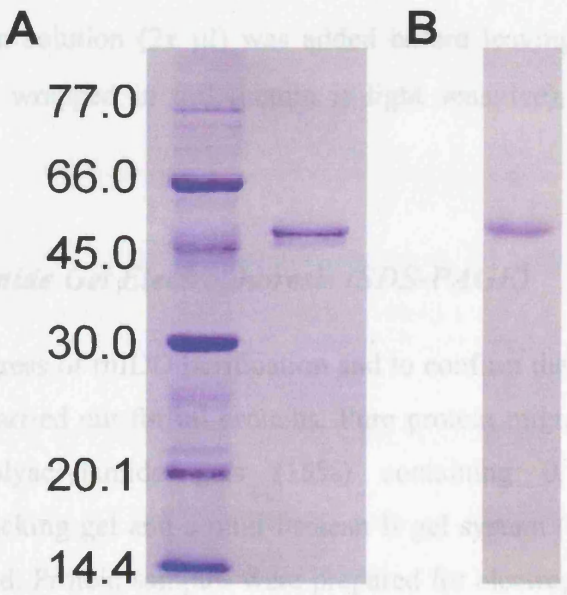

Figure 6.1 Panel A. SDS-PAGE gel of a sample of rhIDO prior to FPLC anion exchange analysis. **Panel B.** SDS-page gel of a purified sample of rhIDO after FPLC anion exchange analysis.

Reconstitution

The protein solution was diluted to 20 ml with reconstitution buffer. Hemin (Sigma) solution (~ 10 mg/ml, 0.1 M NaOH) was prepared. The concentration of the hemin solution was determined by the A_{380} of a dilution of 0.5 µl (of the above solution) in 1.0 ml. The A_{280} of the protein was measured to assess how much hemin to add (Equation (6.4)).

$$x = \frac{[A_{280}(\text{protein}) \times 6 \times 20]}{[A_{380}(\text{hemin}, 0.5\mu\text{l in } 1.0\text{ ml})]} \quad \ldots (6.4)$$

The x µl of hemin solution was titrated into the protein solution by six additions over 30 minutes. Hemin solution (2*x* µl) was added before leaving the protein solution overnight at 4 °C wrapped in foil (hemin is light sensitive), to ensure maximum reconstitution.

6.3.4 Polyacrylamide Gel Electrophoresis (SDS-PAGE)

To follow the progress of rhIDO purification and to confirm the purity of the protein, SDS-PAGE was carried out for all proteins. Pure protein migrates as a single band. Discontinuous polyacrylamide gels (15%) containing 0.1% SDS and 4% polyacrylamide stacking gel and a mini-Protean II gel system (Bio-Rad) at 0.75 mm thickness were used. Protein samples were prepared for electrophoresis by adding an equal volume of reducing sample application buffer (see Appendix A) and boiling for three minutes. The gels were run in SDS running buffer at 50V to load, and then 150 mV until the dye-front reached the end of the gel.

The gels were soaked in staining buffer (see Appendix A) for fifteen minutes, and then destained by soaking in destaining solution (see Appendix A) overnight.

6.3.5 Timed Tryptic Digest

A trypsin solution (0.7 mg/ml in 100 mM potassium phosphate buffer, pH7 .0, 10 µl) was added to an IDO sample (1 mg/ml in 100 mM potassium phosphate buffer,

pH7.0, 100 µl). The resulting solution was mixed at 37 °C. Trypsin inhibitor solutions (from soybean, Sigma, 0.7 mg/ml in the 100 mM potassium phosphate, pH 7.0, 10 µl) were prepared and mixed with sample buffer (see Appendix A, 20 µl). Every minute for 10 minutes, 10 µl of the tryptic reaction were added to one of the above inhibitor solutions, mixed and frozen. At the end of the reaction (after 10 minutes) a SDS-PAGE gel was run.

6.4 Spectroscopic and Analytical Techniques

6.4.1 UV-Visible Spectroscopy

Routine absorbance measurements were conducted using variable-slit Perkin-Elmer Lambda 14, Lambda 35 or Lambda 40 (1 mm slit width) UV-visible spectrometers. Temperature control (25 ± 0.1 °C) was achieved using a thermally-jacketed cell holder that was connected to a circulating water bath (NESLAB RTE-200) or Peltier device (Perkin-Elmer, Peltier thermostatted reference holder, BS0510412). A typical 270-700 nm scan was obtained using a scan speed of 120 nm/minute, acquiring at 0.5 nm intervals, using a 1 ml or 3 ml quartz cuvette of 10 mm path length. Baseline corrections were made against the buffers and solvents used.

6.4.2 Determination of Heme Absorption Coefficients

The total heme content of a heme protein solution and therefore the absorption coefficient of the heme protein can be determined using the pyridine hemochromagen method according to the procedure of Antonini and Brunori (*4*).

An alkaline pyridine solution was prepared from the addition of pyridine (2 ml), 1 M NaOH (600 µl) and distilled water to a final volume of 6 ml. A protein sample with an absorbance of 0.3 – 0.9 in the visible region was required to provide the most reliable data; thus, a spectrum was recorded on a gravimetrically determined sample drawn from the protein stock solution. Pyridine solution (1.5 ml) was added to the protein solution (500 µl of known concentration) to form the pyridine-heme complex. The resulting solution (2 ml) of oxidised hemochromagen (yellow in colour) was divided in two 1 ml aliquots. After five minutes (to enable complete conversion to hemochromagen), the electronic spectrum was recorded using one of the oxidised aliquots. A single crystal of dithionite was added to the oxidised pyridine

hemochromagen solution and the spectrum of the unstable reduced hemochromagen was recorded immediately over the wavelength range 450 – 650 nm. The complete transfer of heme from the protein to the pyridine was checked by determining the absorbance at maximum (λ = 557 nm) and minimum (λ = 540 nm) wavelengths; a ratio of A_{557}/A_{540} = 3.5 is found for protoheme. Absorption coefficients were calculated knowing the absorption coefficient for the pyridine-protoheme complex (ε = 32 mM^{-1} cm^{-1}) using Equation (6.5): where A is the absorbance of the stock solution, c is the concentration of the protein, ε is the molar absorption coefficient and l is the pathlength of the cuvette.

$$A = \varepsilon c l \qquad \ldots (6.5)$$

The experiment was repeated on the other aliquot 24 hours later to check reproducibility. Figure 6.2 shows the pyridine hemochrome spectrum of rhIDO.

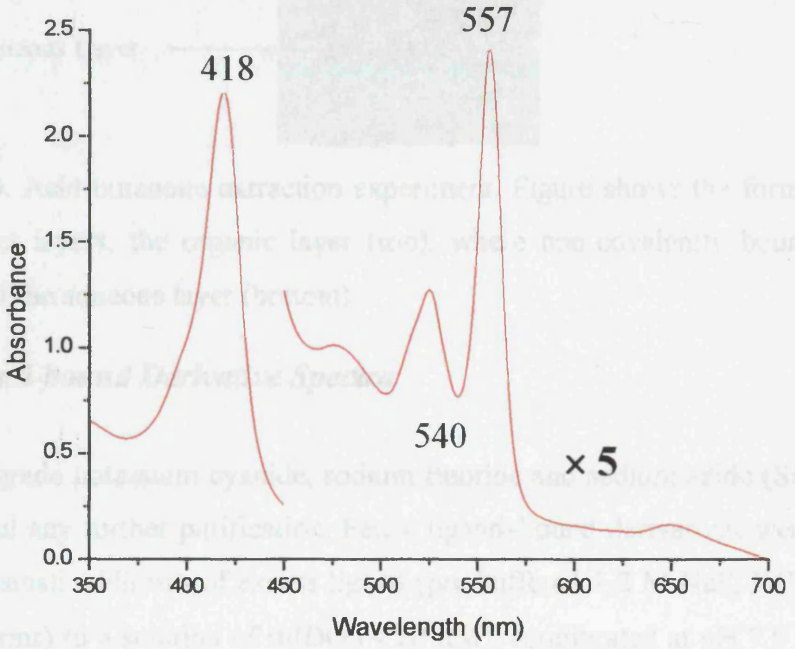

Figure 6.2. Electronic spectrum of the reduced pyridine hemochromagen of rhIDO. The visible region has been multiplied by a factor of 5 for clarity. The ratio of A_{557}/A_{540} = 3.18, which indicates a protoheme structure for the protein.

6.4.3 Acid-Butanone Extraction of Heme

An aqueous solution of protein was titrated with 1 M HCl to a pH of 1.5. An equivalent volume of ice-cold 2-butanone was added with gentle but continuous stirring. After a period of cooling on ice, two distinct layers were observed and a further amount was added to remove more heme.

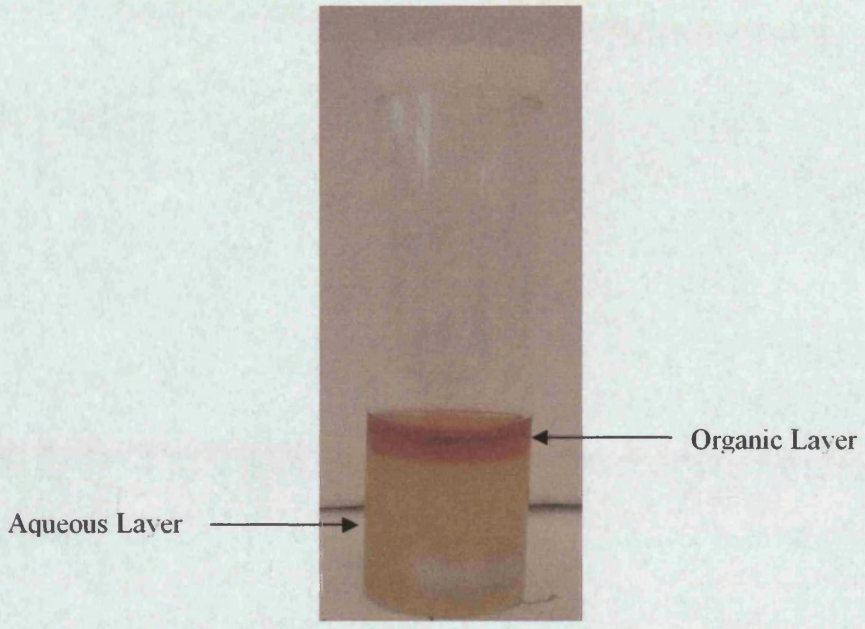

Figure 6.3. Acid-butanone extraction experiment. Figure shows the formation of two distinct layers, the organic layer (top), where non-covalently bound heme travels, and the aqueous layer (bottom).

6.4.4 Ligand-bound Derivative Spectra

Analytical grade potassium cyanide, sodium fluoride and sodium azide (Sigma) were used without any further purification. Ferric ligand–bound derivatives were obtained by making small additions of excess ligand (pre-buffered 1-2 M NaF, KCN or NaN_3 stock solutions) to a solution of rhIDO (~ 20 μM), equilibrated at pH 7.0 (potassium phosphate, 100 mM).

The ferrous-oxy derivative was generated either by passing ferrous rhIDO through a 10 ml column of Sepharose G-25 (Amersham Bioscience) equilibrated with O_2-saturated buffer or by direct bubbling of O_2 gas through a dithionite-reduced sample. The Sepharose columns are used to remove the excess dithionite from the reduced sample.

6.4.5 Ligand Binding Equilibria

Determination of equilibrium dissociation constants, K_D, for the equilibrium given in Equation (6.6),

$$\text{rhIDO} \bullet \text{L-tryptophan} \underset{K_A}{\overset{K_D}{\rightleftharpoons}} \text{rhIDO} + \text{L-tryptophan} \qquad \ldots (6.6)$$

was according previously published procedures (*5, 6*).

The affinity of rhIDO for ligands was measured by spectrophotometric titration. A known amount of ligand was added to the protein solution (the concentration of the protein was determined using its calculated molar absorptivity) in a 1 ml cuvette and the decrease in intensity of the Soret band was measured. The volume of the added ligand was small (0.5 – 2.0 µl) so that the sample dilution was minimal. Each titration curve comprised of 10 – 20 points.

Equilibrium dissociation constants for the protein with high ligand binding affinity (small K_D values) are calculated according to Equation (6.7),

$$\overline{Y} = \frac{[\text{Ligand}]_{free}}{(K_D + [\text{Ligand}]_{free})} \qquad \ldots (6.7)$$

where [Ligand] refers to the concentration of the ligand added, and $\overline{Y}$ is the fractional saturation. Fractional saturation is calculated from the change in absorbance divided by the total change in absorbance, Equation (6.8),

$$\overline{Y} = \frac{(A_i - A_t)}{(A_i - A_f)} = \frac{[\text{rhIDO} \bullet \text{Ligand}]}{[\text{rhIDO}]_{total}} \qquad \ldots (6.8)$$

where A_i is the initial absorbance of the protein solution in the absence of ligand, A_f is the final absorbance at ligand saturation and A_t is the absorbance value at each intermediate point in the titration. The free ligand concentration, $[\text{Ligand}]_{free}$ is then defined by Equation (6.9).

$$[\text{Ligand}]_{free} = [\text{Ligand}]_{total} - [\text{rhIDO} \bullet \text{Ligand}] \qquad \ldots (6.9)$$

Since L-tryptophan is a relatively weak binding ligand, rhIDO was not titrated to saturation at some pHs. Assuming $[Ligand]_{free} = [Ligand]_{total}$, an alternative expression, Equation (6.10), can be derived for weak binding.

$$Abs = \frac{(K_D A_i + [Ligand]_{total} A_f)}{(K_D + [Ligand]_{total})} \quad \ldots (6.10)$$

Use of this relationship avoids the necessity of achieving complete saturation of the protein with ligand.

All binding experiments were carried out at 25 °C ± 0.1 °C. Protein solutions were prepared in potassium phosphate buffers (pH 7.0, 100 mM) and allowed to equilibrate for 10 minutes after each addition of ligand before the spectrum was recorded. Data were entered to an Origin® spreadsheet and fitted to Equation (6.10) to determine the equilibrium constant for weak ligand binding.

6.4.6 pH Titration of rhIDO

Titrations were conducted in potassium phosphate buffer (50 mM) and were carried out by cautious addition of 0.10 M NaOH (~2 µl) to acquire intermediate pH values. Care was taken to avoid any excessive pH jumps and protein precipitation. The pH was recorded before and after measurement of each spectrum and was monitored using a Russell pH-electrode attached to a digital pH-meter (Radiometer Copenhagen, model PHM93). A non-linear least squares fitting program (Origin®) was used to fit the pH-dependent data to the Henderson-Hasselbach equation for a single electron process, Equation (6.11),

$$Z = \frac{A + B \times 10^{(pH-pKa)}}{1 + 10^{(pH-pKa)}} \quad \ldots (6.11)$$

where Z is the absorbance and A and B are the absorbancies of the acidic and basic forms respectively.

6.4.7 Electrospray Ionisation Mass Spectrometry (ESI-MS)

For analysis using electrospray mass spectrometry, a 50 µl aliquot of a stock solution of rhIDO (154 µM, unbuffered) was mixed with 0.1% acetic acid (35 µl) and methanol (65 µl). Activated Dowex (50WX8-200 10N) ion exchange beads, which had been previously washed in ethanol, were then added to this solution. The supernatant was then run by continuous infusion at 5 µl/min, in positive ion electrospray mode using a Micromass Q-Tof Ultima Global mass spectrometer.

6.4.8 Matrix-Assisted Laser Desorption Ionisation – Time of Flight Mass Spectrometry (MALDI-TOF)

MALDI-Tof analyses were carried out by Christof Lenz (Applied Biosystems) using a Voyager-DE STR Biospectrometry Workstation (Applied Biosystems, Framingham/USA) equipped with a 337 nm wavelength nitrogen laser operated at a frequency of 20 Hz (Figure 6.4). Delayed extraction was used for signal focusing, at an acceleration potential of 20 kV. Spectra of the intact protein (154 µM, unbuffered) were acquired in linear mode using external calibration. The protein was diluted in 0.1% TFA/50% acetonitrile (final concentration ≈ 2 pmol/µl) and a 0.5 µl aliquot mixed on a stainless steel MALDI target with the same volume Sinapinic Acid matrix (Sigma, 10 mg/ml) in the same solvent and air-dried. Peptide mass fingerprinting was carried out in reflectron mode after reduction/alkylation of cysteine residues with dithiothreitol/iodacetamide and tryptic digestion (Sequencing Grade Modified Porcine Trypsin, Promega, Mannheim/D). The digestion solution was diluted in 0.1% TFA/50% acetonitrile to give a final concentration of 1 pmol/µl. A 0.5 µl aliquot of the solution was mixed on the MALDI target with the same volume of a solution of α-cyano-4-hxdroxycinnamic acid (HCCA) matrix (Applied Biosystems, 3 mg/ml) in the same solvent and air-dried. A processed list of monoisotopic m/z values was submitted to a MASCOT (Matrixscience Ltd, London/UK) database search against a SwissProt protein sequence database.

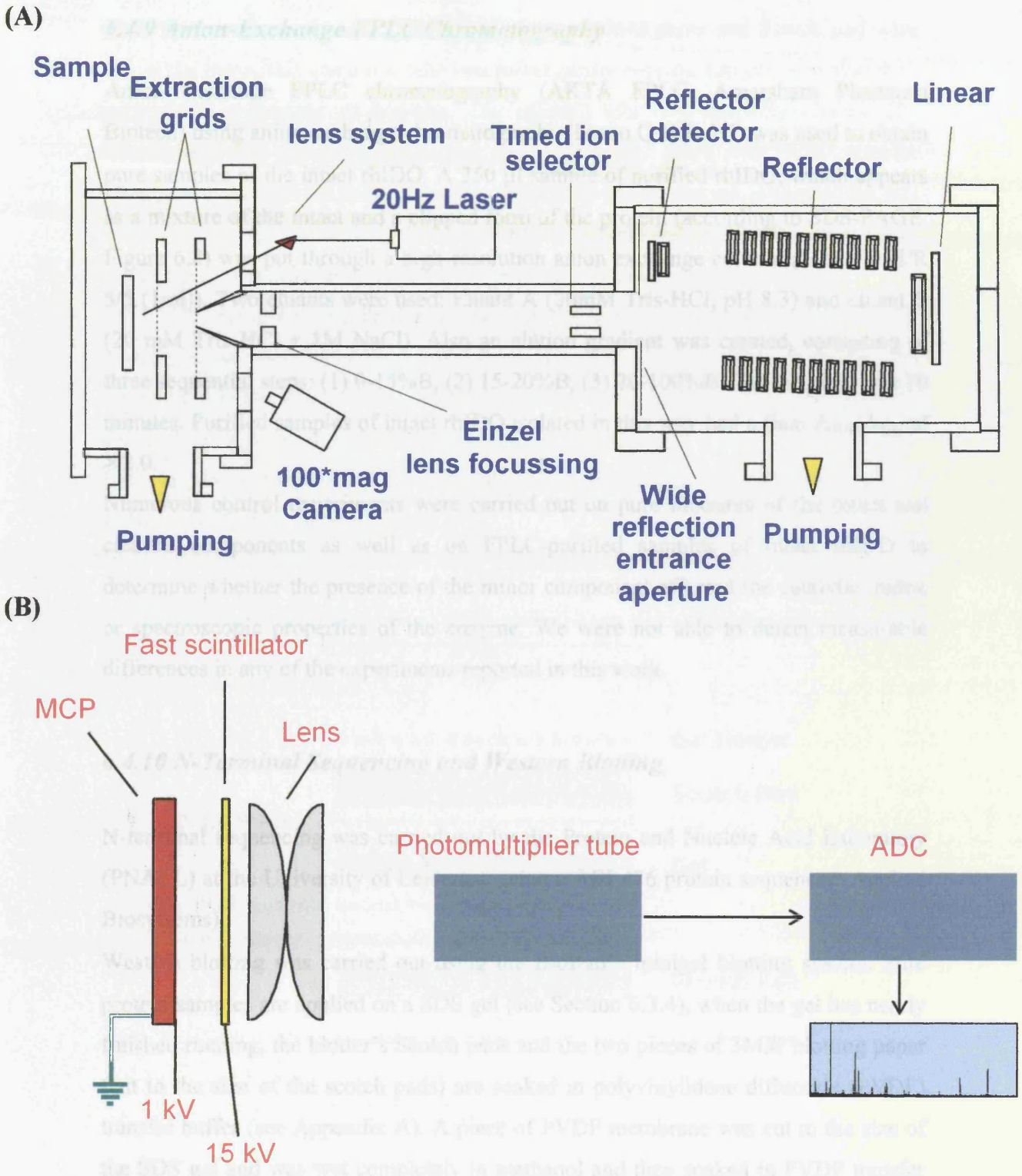

Figure 6.4 (A) Voyager-DE STR workstation layout, Applied Biosystems. **(B)** High current detector.

6.4.9 Anion-Exchange FPLC Chromatography

Anion exchange FPLC chromatography (ÅKTA FPLC, Amersham Phamacia Biotech) using anion exchange chromatography (Mono Q H/R 5/5) was used to obtain pure samples of the intact rhIDO. A 250 μl sample of purified rhIDO, which appears as a mixture of the intact and a clipped form of the protein (according to SDS-PAGE, Figure 6.2) was put through a high-resolution anion exchange column (Mono Q H/R 5/5 (1ml)). Two eluants were used: Eluant A (20mM Tris-HCl, pH 8.3) and eluant B (20 mM Tris-HCl + 1M NaCl). Also an elution gradient was created, consisting of three sequential steps: (1) 0-15%B, (2) 15-20%B, (3) 20-100%B. The run time was 70 minutes. Purified samples of intact rhIDO isolated in this way had a final A_{404}/A_{280} of > 2.0.

Numerous control experiments were carried out on pure mixtures of the intact and cleaved components as well as on FPLC-purified samples of intact rhIDO to determine whether the presence of the minor component affected the catalytic, redox or spectroscopic properties of the enzyme. We were not able to detect measurable differences in any of the experiments reported in this work.

6.4.10 N-Terminal Sequencing and Western Blotting

N-terminal sequencing was carried out by the Protein and Nucleic Acid Laboratoty (PNACL) at the University of Leicester, using a ABI 476 protein sequencer (Applied Biosystems).

Western blotting was carried out using the BioRad™ minigel blotting system. Pure protein samples are applied on a SDS gel (see Section 6.3.4), when the gel has nearly finished running, the blotter's Scotch pads and the two pieces of 3MM blotting paper (cut to the size of the scotch pads) are soaked in polyvinylidene difluoride (PVDF) transfer buffer (see Appendix A). A piece of PVDF membrane was cut to the size of the SDS gel and was wet completely in methanol and then soaked in PVDF transfer buffer until is needed. When the gel has finished running a blotting cassette was used to construct a gel sandwich (Figure 6.5). A presoaked piece of 3MM paper was laid on top of a presoaked Scotch pad, and the SDS gel was placed in the centre of the 3MM paper taking care to remove any air bubbles between the two. The PVDF membrane was then placed on the top of the gel and any air bubbles were removed

gently from between the two. The second piece of 3MM paper and Scotch pad were laid on the top of this and a test tube was rolled gently over the top of the sandwich to remove any remaining air bubbles. The cassette was then carefully closed. The cassette was then placed in the blotter tank, which was filled with PVDF transfer buffer, ensuring that the level of buffer completely covers the gel. The cassette was placed in the tank so that the gel was toward the cathode and the PVDF membrane is toward the anode. The blot was run for 2 hours at 125 mAmps constant current.

The PVDF membrane was then removed form the sandwich and stained (with PVDF staining buffer, see Appendix A) and destained (with PVDF destaining buffer, see Appendix A). The problot was rinsed in distilled water and left to dry between two sheets of 3MM paper in a plastic bag at room temperature.

The two protein bands (transferred on the PVDF membrane) were then excised and subjected to N-terminal sequencing.

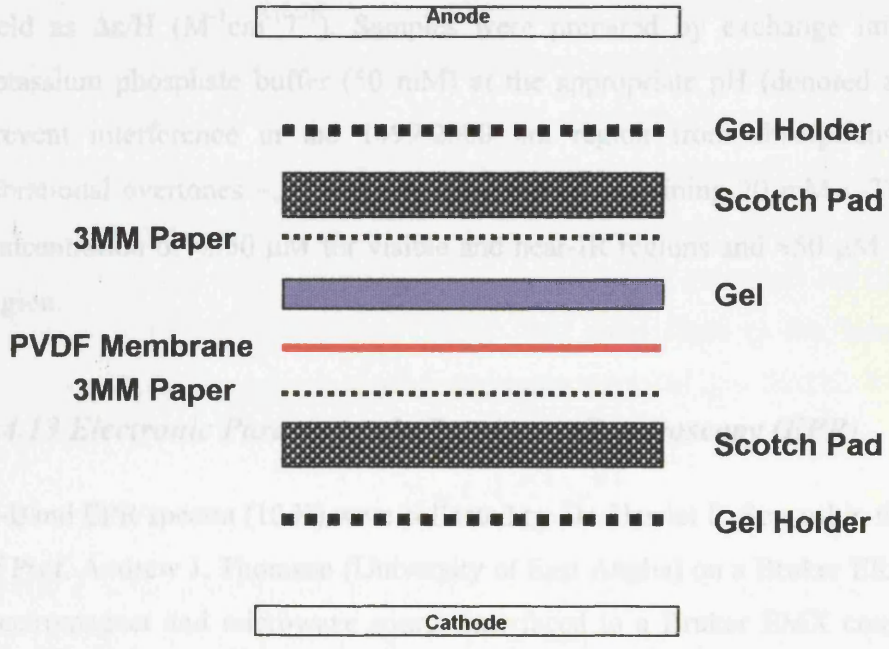

Figure 6.5 Illustration of assembled blotting membranes.

6.4.11 Circular Dichroism Spectroscopy (CD)

CD spectra were recorded on a JASCO J-715 spectropolarimeter (JASCO Corporation, Tokyo, Japan). Sensitivity was 100 millidegrees, the slit width 2 nm, and the scanning speed was 50 nm/min for an accumulation of 2 scans. Samples of the enzyme (20 μM) were prepared by exchange into potassium phosphate buffer (100 mM, pH 8.0 at 25 °C).

6.4.12 Magnetic Circular Dichroism Spectroscopy (MCD)

Magnetic Circular Dichroism spectra were collected by Dr. Harriet E. Seward in the laboratory of Prof. Andrew J. Thomson (University of East Anglia) using the Jasco J810 and J730 models for the UV/Visible and near-IR regions, respectively. An Oxford Instruments SM-1 superconducting solenoid with a 25 mm room temperature bore was used to generate a 6 T magnetic field. MCD intensities are linear with respect to magnetic field at room temperature and are plotted normalised to magnetic field as $\Delta\varepsilon/H$ ($M^{-1}cm^{-1}T^{-1}$). Samples were prepared by exchange into deuterated potassium phosphate buffer (50 mM) at the appropriate pH (denoted as pH*) – to prevent interference in the 1499-2000 nm region from absorptions caused by vibrational overtones –, or into the same buffer containing 20 mM L-Trp, to a final concentration of ≈350 μM for visible and near-IR regions and ≈50 μM for the Soret region.

6.4.13 Electronic Paramagnetic Resonance Spectroscopy (EPR)

X-Band EPR spectra (10 K) were collected by Dr. Harriet E. Seward in the laboratory of Prof. Andrew J. Thomson (University of East Anglia) on a Bruker ER-300D series electromagnet and microwave source interfaced to a Bruker EMX control unit and fitted with an ESR-9 liquid Helium flow cryostat from Oxford Instruments and a dual mode microwave cavity from Bruker (ER-4116DM). Quantification of S = ½ species was carried out by comparison with the spin standard Cu^{2+}(EDTA) using the method of Aasa and Vanngard (*7*).

6.4.14 Electrochemistry

Redox titrations were performed in a Belle Technology glove-box under nitrogen, as described previously (8), with the help of Dr. Kirsty J. Mclean in the laboratory of Prof. Andrew W. Munro (University of Leicester). All solutions were degassed under vacuum with argon ($[O_2]$ < 2 ppm). Solutions of rhIDO (≈ 4 μM in 100 mM potassium phosphate containing 10% glycerol, pH 7.0) or His303Ala (~10 μM in 100mM potassium phosphate containing 10% glycerol, pH 8.0) were titrated electrochemically according to the method of Dutton (*9*) using sodium dithionite as reductant and potassium ferricyanide as oxidant. Mediators (2 μM phenazine methosulfate, 5 μM 2-hydroxy-1,4-naphthoquinone, 0.5 μM methyl viologen, and 1 μM benzyl viologen, all from Sigma) were included to mediate in the range +100 to – 480 mV, as described previously. At least 15 minutes was allowed to elapse between each addition of reductant or oxidant to allow stabilisation of the electrode. Spectra were recorded using a Cary UV-50 Bio UV-Visible scanning spectrophotometer via a fibre optic absorption probe (Varian) immersed in the enzyme solution and connected to the external spectrophotometer. The electrochemical potential of the solution was measured using a Hanna pH 211 meter coupled to a Pt/Calomel electrode (ThermoRussell Ltd.) at 25 °C. The electrode was calibrated using the Fe^{3+}/Fe^{2+} EDTA couple as a standard (+108 mV). A correction factor of +244 mV was used to correct relative to the standard hydrogen electrode; all potentials are quoted against the standard hydrogen electrode (SHE). Data were fitted to the Nernst Equation (Equation (6.12)) for a single electron process.

$$E = E^{\circ} + \frac{RT}{nF} \ln \frac{O}{R} \qquad \ldots (6.12)$$

where, E is the potential of the electrode versus the reference electrode (SHE), E° is the standard redox potential, R is a universal gas constant, T is the absolute temperature, n is the number of moles of electrons involved in the reaction, F is the Faraday constant, and O and R correspond to the concentrations of the oxidised and reduced species respectively.

6.5 Steady State and Pre-Steady State Kinetics

6.5.1 Steady State Kinetics

Samples were assayed for catalytic activity in reactions (25.0 ± 0.1 °C) that consisted of 10 μM methylene blue (Sigma), 10 μg catalase (bovine liver, Sigma), 20 mM L-ascorbate (Sigma) and varying concentrations (0-40 μM) of L-Trp contained in 100 mM potassium phosphate buffer (1 ml total volume) (10). The reaction was initiated by addition of rhIDO (10 μl, ~ 1 μM). Initial reaction rates were monitored by tracking the concentration of N-formylkynurenine, as an increase in absorbance at 321 nm (ε_{321} = 3.75 mM^{-1} cm^{-1} (*11*)). All kinetic profiles were fitted to the Michaelis-Menten Equation (6.13). pH-dependent data were collected using either 100 mM potassium phosphate as above, or glycine-sodium hydroxide buffer at 25.0 °C.

$$V = V_{max} \frac{[S]}{[S] + K_M} \quad \ldots (6.13)$$

Where, V_{max} is the maximal rate, K_M, the Michaelis constant, is the concentration at which the reaction rate is half its maximal value, and [S] is the substrate concentration.

Equation 6.13 means that at low substrate concentrations (*i.e.*, when $K_M >> [S]$) the majority of the enzyme is free and the rate is proportional to the substrate concentration. Hence, the Michaelis-Menten Equation can be rearranged as follows:

$$V = \frac{k_{cat}}{K_M [E][S]} \quad \ldots (6.14)$$

where, k_{cat} is the turnover number for the enzyme (per second). From the above Equation (6.13), we can determine the specific activity of the enzyme, *i.e.* k_{cat}/K_M, which can be used as a comparison of the effectiveness of the enzyme with different substrates.

Results are plotted as rate (mM s^{-1}) *versus* [L-Trp] (μM) to determine V_{max} and K_M values. A plot of rate/enzyme comncentration (V/[E]) *versus* [L-Trp] was used to determine k_{cat} and K_M value. The rate of the enzymic reaction in mM s^{-1} was

determined using Equation 6.15, where the molar absorption coefficient of the product (N-formylkynurenine) at 321 nm is 3.75 mM^{-1} cm^{-1}.

$$\text{Rate}\,(\text{mM s}^{-1}) = \frac{\text{Rate}\,(\text{au min}^{-1})}{\varepsilon_{\text{product}} \times 60} \qquad \ldots (6.15)$$

The Lineweaver-Burk plot or double reciprocal plot is used to linearise data that follows Michaelis-Menten kinetics; the Michaelis-Menten equation is rearranged so that 1/[S] can be plotted against 1/[V] (Equation 6.16).

$$\frac{1}{V} = \left(\frac{K_M}{V_{max}}\right)\left(\frac{1}{[S]}\right) + \frac{1}{V_{max}} \qquad \ldots (6.16)$$

6.5.2 Calculation of the Inhibition Constant K_i

Inhibition studies have been carried out in collaboration with Miss Laura Mcleay, as part of a MChem project, under the supervision of Miss Nektaria Papadopoulou. All tryptophan analogues were purchased from Sigma or Acros Organics. Inhibition studies were carried out at pH 8.0 and 25 °C. The inhibition constant, K_i can be calculated by plotting the slope or intercept of the Lineweaver-Burk plot (whichever changes) against the concentration of the inhibitor (Figure 6.6), this is known as a secondary plot.

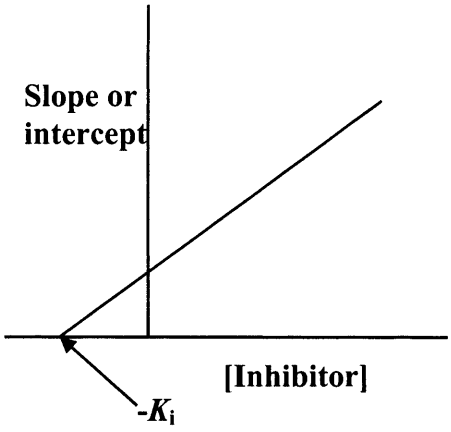

Figure 6.6 A representation of a secondary plot showing how K_i can be calculated.

K_i is the concentration of inhibitor required to inhibit the maximum rate by half, similar to K_M when the inhibitor is not present.

6.5.3 Transient Kinetics

Transient state kinetics were performed using a SX.18 MV microvolume stopped flow spectrophotometer (Applied Photophysics) fitted with a Neslab RTE200 circulating water bath. Reported values of k_{obs} were an average of at least 5 measurements (potassium phosphate, pH 7.0, 25.0 °C). Pseudo-first-order rate constants for the formation of the ferrous rhIDO-oxygen complex (k_1) were monitored at 416 nm – which corresponds to the Soret band of the ferrous-oxy derivative, in a single mixing mode by mixing purified rhIDO (1-3 μM) with varying oxygen (O_2) concentrations. Reduction of the enzyme (ferrous form) was achieved by addition of dithionite (230 μM final concentration). The final dithionite concentration was obtained by conducting a sodium dithionite titration.

The rate constant for the auto-oxidation of the ferrous rhIDO-oxygen complex (k_{auto}) was monitored at 412 nm over a longer timescale in order to monitor the complete conversion of the oxy-complex to the ferric rhIDO derivative.

Pseudo-first-order rate constants for the formation of ferric rhIDO–L-Trp complex (k_3) were monitored at 411 nm (Soret of the rhIDO–L-Trp derivative) in single mixing mode by mixing purified enzyme (1-3 μM) with varying concentrations of L-Trp.

Pseudo-first-order rate constants for the formation of the ternary complex (rhIDO–O_2 –L-Trp) were collected in sequential mixing mode by mixing enzyme (20 μM) with a stoichiometric amount of oxygen (20 μM) in the premixing cell. After a suitable ageing period (200 ms), L-Trp (200 μM) was then rapidly mixed with the oxidised enzyme complex. All data collected were analysed using a non-linear least squares regression analysis on an Archimedes 410-1 microcomputer using spectrakinetics software.

The pH dependence of the rate constants was obtained by using potassium phosphate buffer in the pH range of 5.5 – 8.8 (100 mM). The pH of the solution was checked after mixing to ensure consistency. pH-dependent data were fitted to the Henderson-Hasselbach Equation for a single-proton process (Equation (6.11)).

Monophasic transient traces were fitted to a single exponential process (Equation (6.17)), to obtain pseudo-first-order rate constants,

$$A = Ce^{-k_{obs}t} + b \qquad \ldots (6.17)$$

where A is the absorbance change over time, C is a constant related to the initial absorbance, k_{obs} is the observed rate constant, t represents the time in seconds and b is an offset value to account for a nonzero baseline. Transients that were biphasic were fitted to double exponential process (Equation (6.18)),

$$A = C_1(1 - e^{-k_{obsA}t}) + C_2(1 - e^{-k_{obsB}t}) + b \qquad \ldots (6.18)$$

Where k_{obsA} and k_{obsB} are the rate constants for the fast and slow phases, respectively, C_1 and C_2 are related to the initial absorbance and b is an offset, again to account for a non-zero baseline. All curve fitting was performed using the Origin® software package.

Time-dependent spectra of the various reactions, were performed by multiple wavelength stopped-flow spectroscopy using a photodiode array detector and X-SCAN software (Applied Photophysics). Spectral deconvolution was performed by global analysis and numerical integration methods using PROKIN software (Applied

Photophysics). Precise experimental conditions are given within the various figure legends.

6.5.4 Preparation of O_2-Saturated Solutions

Anaerobic solutions of potassium phosphate buffer (100 mM) (various pHs) containing various concentrations of O_2 were prepared by mixing different volumes of buffer saturated with O_2 gas at 25.0 °C with anaerobic buffer solution. Saturation was achieved by bubbling O_2 for 1 hour in a septum sealed flask at 25 °C. Final O_2 concentrations were calculated on the basis of a saturating concentration of O_2 of ~ 1.2 mM at 25 °C and 1 atm pressure.

6.6 Crystallisation

All the screens for the crystallisation of rhIDO were carried out using the sitting drop method (Figure 6.7) and using 24 well plates (4 × 6 Cryschem plates with 1 ml reservoirs, Hampton Research). Screening of crystallisation conditions used the sparse-matrix factorial search method (*12*) using commercially available kits (MDL screens (I) (http://www.moleculardimensions.com/uk/datasheets/md1-01.htm) and (II) (http://www.moleculardimensions.com/uk/datasheets/md1-02.htm) (Molecular Dimensions Ltd)).

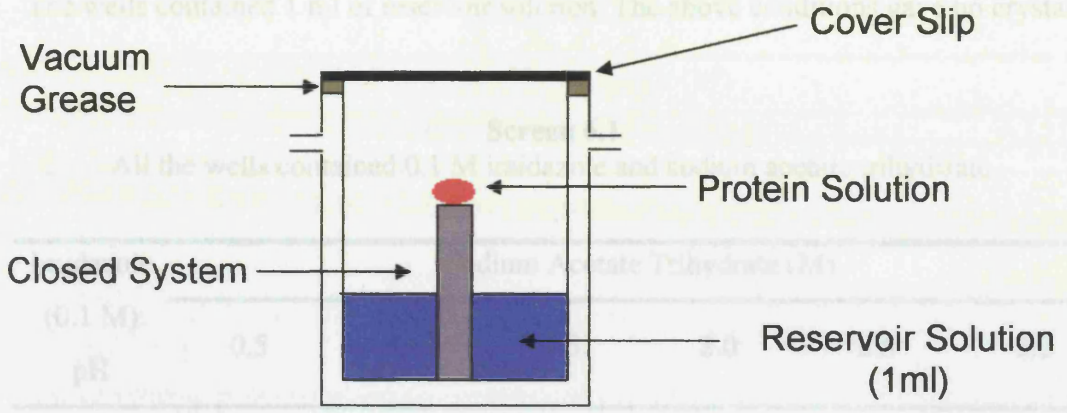

Figure 6.7 Diagrammatic representation of the sitting drop method.

The screens were prepared in a temperature controlled room at 19 °C. The area was dusted before starting and lab coats were worn to prevent fibres contaminating the wells. The protein solution (11 mg/ml in deionised water) was kept in ice throughout. Each MDL solution (1 ml) was added to a separate well. Protein solution (2 µl) was added to the first eight of the small drop wells (4×2). Well solution (2 µl) was added to the drop of protein solution, and the first eight wells were sealed with clear postal tape making sure there were no air bubbles. The process was then repeated to complete the plate. This was done twice for all 100 of the solutions in the MDL kits, one set of plates kept at 4 °C and the other at 19 °C. The above procedure was repeated for protein solutions containing 2 mM L-Trp. The screens were left in temperature controlled rooms with no vibrations.

Two months later, most of the protein solutions in the crystallisation plates have precipitated except in solution number 17 (for the screens prepared in the absence of L-Trp), which contained 0.1 M imidazole pH 6.5 and 1.0 M sodium acetate trihydrate. Hence, screens were set up based around these initial conditions in an attempt to find the ideal crystallising conditions. Two screens were prepared with imidazole and sodium acetate trihydrate (Screens 6.1 and 6.2). All the well solutions were prepared from the same stock solutions and all the buffer pHs were checked as 1 M stock

solutions. The drops were 2 µl of protein solution and 2 µl of well solution as before. The wells contained 1 ml of reservoir solution. The above conditions gave no crystals.

Screen 6.1
All the wells contained 0.1 M imidazole and sodium acetate trihydrrate.

Imidazole (0.1 M) pH	Sodium Acetate Trihydrate (M)					
	0.5	1.0	1.5	2.0	2.5	3.0
6.0						
6.5						
7.0						
7.5						

Screen 6.2
All the wells contained 0.1 M imidazole and sodium acetate trihydrrate.

Imidazole (0.1 M) pH	Sodium Acetate Trihydrate (M)					
	0.5	1.0	1.5	2.0	2.5	3.0
8.0						
8.5						
9.0						
9.5						

A third screen (Screen 6.3) was prepared – both at 19 °C and 4 °C – as previously described that contained only imidazole solutions with varying pHs and concentrations.

Screen 6.3

	Imidazole (M)					
pH	0.025	0.05	0.1	0.125	0.15	0.175
6.5						
7.0						
7.5						
8.0						

After a month small quasi red crystals (bundles of tiny crystals, not large enough to diffract, Chapter 3A, Figure 3A.15) appeared in wells containing 0.15 M and 0.175 M imidazole at pH 7.5 and 8.0. The small red crystals retained their colour and size for a long period of time. The screens were left to further equilibrate in case bigger crystals could grow under these conditions.

6.7 References

1. Dai, W., Gupta, S. L. (1990) *Biochem. Biophys. Res. Comm., 168*, 1-8.
2. Zucker, D. M. (2002), http://biotools/idtdna.com/mfold), St. Louis.
3. Littlejohn, T. K., Takikawa, O., Skylas, D., Jamie, J. F., Walker, M. J., Truscott, R. J. W. (2000) *Protein Express. Purif., 19*, 22-29.
4. Antonini, M., Brunori, E. (1971) *Hemoglobin and Myoglobin and their Reactions with Ligands.*, North Holland Publishers, Amsterdam.
5. Bogumil, R., Hunter, C. L., Maurus, R., Tang, H. L., Lee, H., Lloyd, E., Brayer, G. D., Smith, M., Mauk, A. G. (1994) *Biochem., 33*, 7600-7608.
6. Jones, D. K., Badii, R., Rosell, F. I., Lloyd, E. (1998) *Biochem. J. , 330*, 983-988.
7. Aasa, R., Vanngard, T. (1975) *J. Magn. Res., 19*, 308-315.
8. Munro, A. W., Noble, M. A., Robledo, L., Daff, S. N., Chapman, S. K. (2001) *Biochem., 40*, 1956-1963.
9. Dutton, P. L. (1978) *Methods Enzymol. , 54*, 411-435.
10. Takikawa, O., Kuroiwa, T., Yamazaki, F., Kido, R. (1988) *J. Biol. Chem., 263*, 2041-2048.
11. Shimizu, T., Nomiyama, S., Hirata, F., Hayaishi, O. (1978) *J. Biol. Chem., 253*, 4700-4706.
12. Jancarik, J., Kim, S. -H. (1991) *J. Applied Crystallogr. , 94*, 409-411.

Appendix A

Destain (SDS-PAGE)
7.5% acetic acid
5% methanol

Deuterated Buffer
50 mM D_3PO_4, adjust to required pH using NaOD and DCl

EB Buffer (Qiagen)
10 mM Tris-HCl, pH 8.5

Elution Buffer
50 mM potassium phosphate buffer pH 8.0
300 mM potassium chloride
100 mM EDTA

Lennox-LB Media (Fisher or Sigma)
10 g sodium chloride
10 g tryptone
5 g yeast extract
Adjust to pH 7.0 with 5N sodium hydroxide
20 g glucose per litre
Make up to 1.0 l with deionised water
Autoclave

N3 Buffer (Qiagen)
Contains guanidine hydrochloride and acetic acid

P1 Buffer (Qiagen)
Alkaline buffer that contains RNase

P2 Buffer (Qiagen)
Contains sodium hydroxide

PB Buffer (Qiagen)
Contains guanidine hydrochloride and isopropanol

PE Buffer (Qiagen)
Contains ethanol

Psi Broth
Lennox-LB media autoclaved
Per 100 ml:
Add 1ml of filter sterilised 1M potassium chloride
Add 0.4 ml of filter sterilised 1M magnesium sulphate

PVDF Transfer Buffer
48 mM Tris-HCl
39 mM Glycine

0.03% SDS
10% ethanol
pH 8.3

PVDF Staining Buffer
0.1% w/v Coomasie brilliant blue R-250
50% Deionised water
40% Methanol
10% Acetic acid

PVDF Destaining Buffer
40% methanol
10% acetic acid
50% Deionised water
Stain for five minutes, destain until bands are visible

Resolving Buffer (SDS-PAGE)
0.5 M Tris base
0.4% SDS
Adjust to pH 8.8

Reconstitution Buffer
0.1 M potassium phosphate buffer pH 6.5

Sample Buffer (SDS-PAGE)
125 mM Tris-HCl, pH 6.8
4% SDS
20% w/v glycerol
0.002% bromophenol blue

SDS Running buffer (SDS-PAGE)
25 mM Tris-HCl
192 mM glycine
0.1% w/v SDS

SOC Media
2 g tryptone
0.5 g yeast extract
0.05 g sodium chloride
0.4 g glucose
Make up to 100 ml with deionised water
Autoclave
Add 1ml filter sterilised 1M magnesium chloride
Add 1ml filter sterilised 1M magnesium sulphate

Sonication Buffer
50 mM potassium phosphate buffer pH 8.0
300 mM potassium chloride
2 EDTA-free Complete™ tablets (Roche)

Stacking Buffer (SDS-PAGE)
0.5 M Tris base
0.4% SDS
Adjust to pH 6.8

Staining Buffered (SDS-PAGE)
30% v/v methanol
12% w/v trichloroacetic acid
0.01% w/v Coomassie Blue R
10% w/v sulphosalicylic acid

Storing Buffer
50 mM Tris-HCl pH 7.4
1 mM EDTA

50× TAE Buffer (Agarose gel electrophoresis)
242 g Tris base
37.1 g glacial acetic acid
100 ml of 0.5 M EDTA
900 ml deionised water

Wash Buffer
50 mM potassium phosphate buffer pH 6.0
300 mM potassium chloride

Appendix B

Table I. The forward and reverse oligonucleotides used for sequencing.

Sequencing Primer	T_m (°C)	% GC
PQEF 5′ CGG ATA ACA ATT TCA CAC AG 3′	47.6	40
PQER 5′ GTT CTG AGG TCA TTA CTG G 3′	48.8	47.4
IDOSEF 5′ CAT TTC GTG ATG GAG ACT GCA G 3′	54.7	50
IDOSER 5′ CAA ACT CCT TTG GGT CTT CCC AG 3′	56.9	59.2

Table II. The forward and reverse oligonucleotides used to generate the variants of rhIDO. The mismatched codons are highlighted in red.

Variant	T_m (°C)	% GC
His303Ala Forward: 5′ GCCACCAGCTGCTAGGAACTTCCTGTGC 3′ Reverse: 5′ GCACAGGAAGTTCCTAGCAGCTGGTGGC 3′	58	60.7
His346A Forward: 5′ CCTGAGGAGCTACGCACTGCAAATCGTG 3′ Reverse: 5′ CACGATTTGCAGTGCGTAGCTCCTCAGG 3′	58	57
Lys369* Forward: 5′GGCACTGATTTAATGAATTTCCTGTAAACTGTGAGAAG 3′ Reverse: 5′CTTCTCACAGTTTACAGGAAATTCATTAAATCAGTGCC 3′	62.2	36.8
Lys369Ala Forward: 5′ GAATTTCCTGGCGACTGTGAGAAGTACAACTG 3′ Reverse: 5′ CAGTTGTACTTCTCACAGTCGCCAGGAAATTC 3′	63	46.9
Arg304Ala Forward: 5′ GCCACCAGCTCACGCTAACTTCCTGTG 3′ Reverse: 5′ CACAGGAAGTTAGCGTGAGCTGGTGGC 3′	76.2	59.2

Appendix C

Vector Maps For Section 1.7

1. Vector pβact-CAT from reference (*1*)

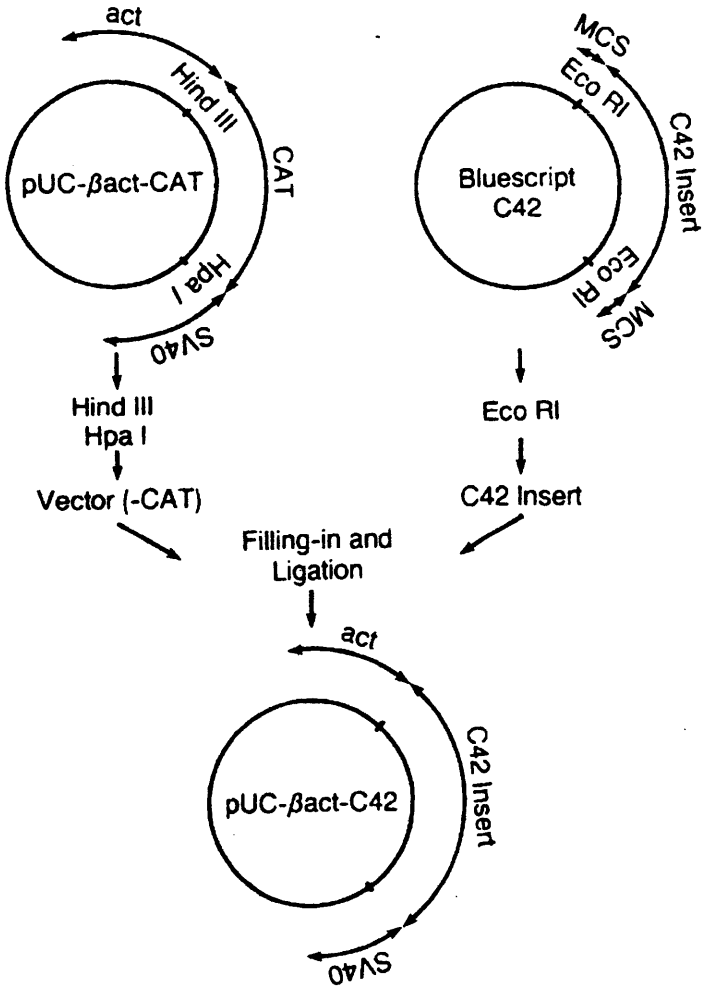

2. Vector pBluescript II KS+ from reference (*1*)

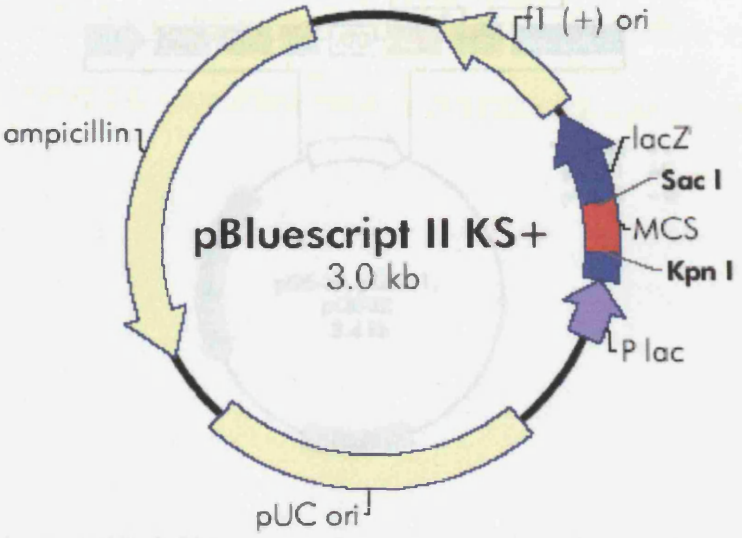

3. Vector pQE-9 from reference (*2*)

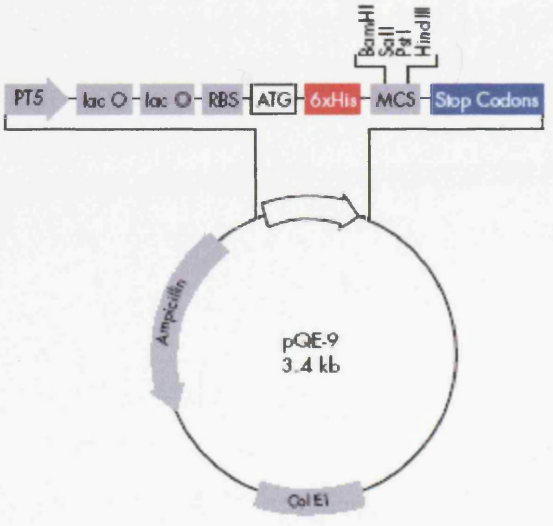

4. Vector pQE-30

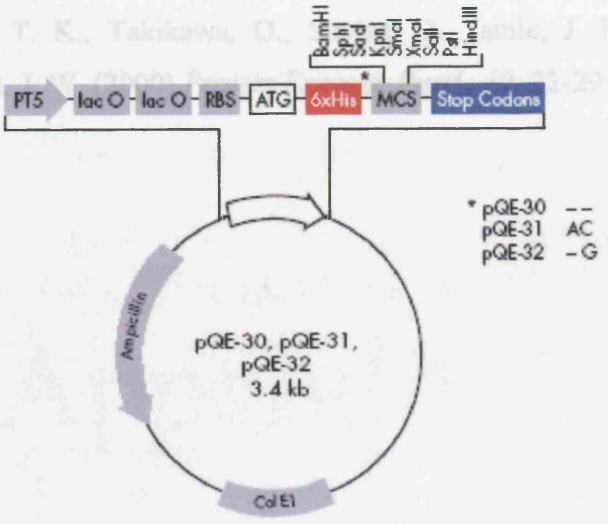

References

1. Dai, W., Gupta, S. L. (1990) *Biochem. Biophys. Res. Comm., 168*, 1-8.
2. Littlejohn, T. K., Takikawa, O., Skylas, D., Jamie, J. F., Walker, M. J., Truscott, R. J. W. (2000) *Protein Express. Purif., 19*, 22-29.

Appendix D

Redox Titrations on the "intact" rhIDO

The first redox titration was performed on the "intact" enzyme (*i.e.* major component as found from SDS-PAGE electrophoresis and successfully separated by anion exchange chromatography). The enzyme behaved well during titration and there was no aggregation observed in the reductive direction (using potassium dithionite), only showing some minor aggregation on re-oxidation with potassium ferricyanide. The process is clearly reversible, with no sign of hysteresis in the oxidative and reductive directions.

In the case of first titration (on the "intact" enzyme), an unusual spectral feature appeared immediately following addition of the mediators to the solution (see Chapter 6, Experimental) (Figure 1(A)). This took the form of a peak at ~389 nm of similar intensity to the Soret band of the oxidised rhIDO. Since there was no real change in the intensity of the Soret of the "intact" rhIDO, it seems impossible that it can be due to a change in heme state. Since the mediators have negligible absorption in the oxidised form, it is impossible that it can be due to them *per se*. Instead, it seems more likely to be due to an impurity in the solution, an interaction between one of the mediators and the rhIDO, or between one of the mediators and a component of the solution. Regardless of the cause, it disappears as soon as small amounts of dithionite are introduced into the solution, prior to their being any significant reduction of rhIDO. After the disappearance of the initial unusual feature, the titration progresses normally and reversibly. On reduction there is loss of intensity of the Soret band and a shift to longer wavelength, along with apparent fusion of the α/β bands (500 and 535 nm, respectively) to give a single feature of greater absorption intensity (Figure 1(B)). Despite appearance of the "unusual" feature early in the titration (before any significant reduction), the data fit well to a single electron Nernst function (Figure 2(A)). Figures 2(A) and 2(B) show plots of data at 407 nm (near oxidised Soret maximum) and 429 nm (where the reduced peak appears) against the applied potential, along with the corresponding fits to a single electron Nernst function. The anaerobic redox titration of the "intact" rhIDO resulted in fully reversible spectral changes of the heme centre. The oxidised form had its Soret spectral maximum at approximately 405 nm, which decreases in intensity and moves to approximately 429 nm on conversion to the ferrous form. An isosbestic point for the transition is located

at 416 nm. Also on reduction, there is an alteration in the α/β region – with a band developing at approximately 558 nm. The enzyme remained stable during the approximately 4 hours required for fully reduction (with potassium dithionite) and re-oxidation (with potassium ferricyanide) and no significant protein aggregation was observed during this time. Data were taken from near the Soret peak in the oxidised form of the enzyme (407 nm) and from the maximum for the reduced form of the enzyme (429 nm) and plotted *versus* the applied reduction potential. Data were fitted to a single electron Nernst function, as described in previous studies (*1*) (Chapter 6, Equation 6.12).

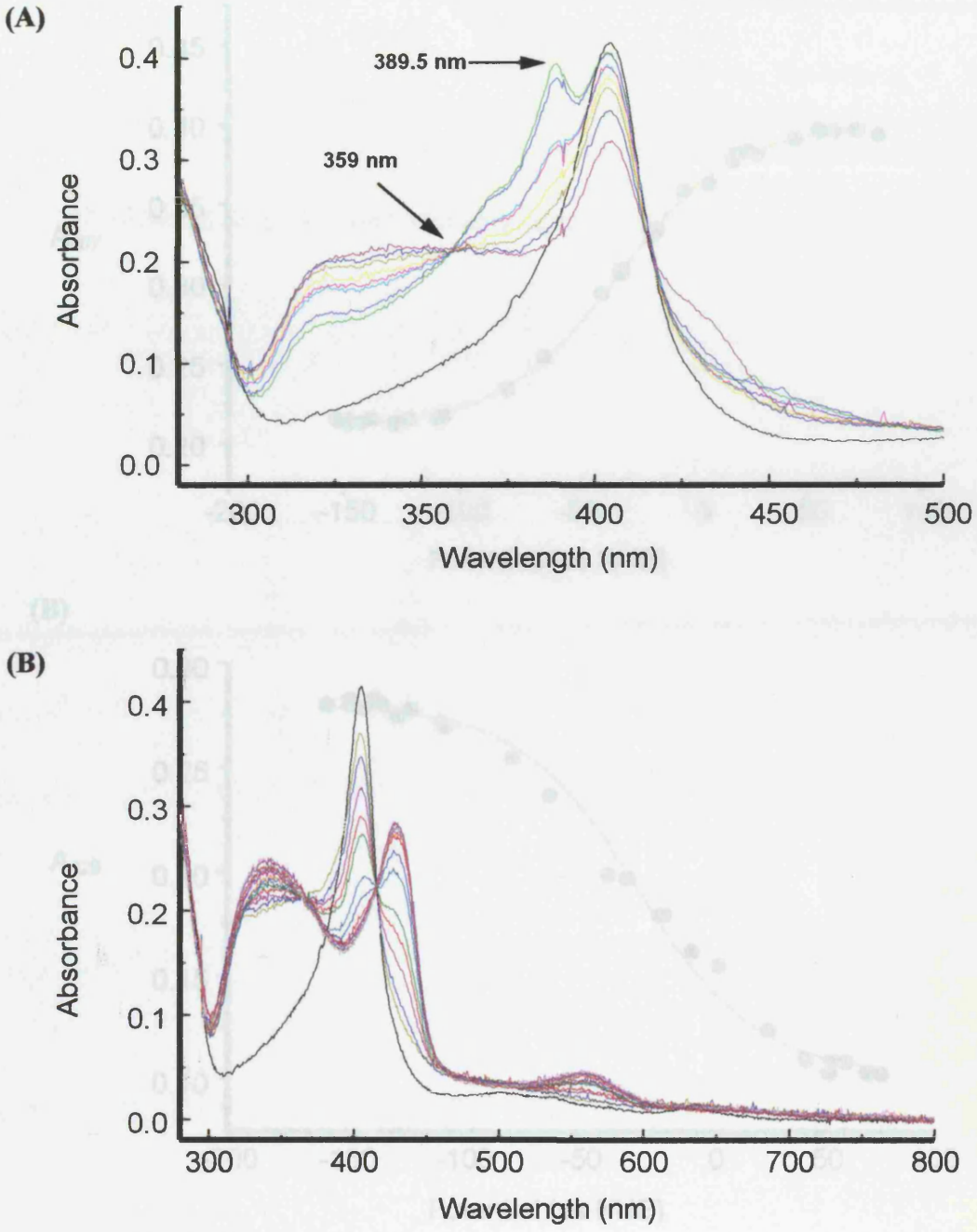

Figure 1 (A) Early spectra in the titration of "intact" IDO. The black line is the starting spectrum, and the green line is the spectrum immediately after addition of the mediators. Subsequent spectra (where feature disappears) are due to small additions of dithionite. An unusual peak appears at 389.5 nm. (B) Spectral changes occurring during redox titration of "intact" IDO. The oxidised Soret band at 405 nm shifts to a reduced form at 429 nm. There is an isosbestic point at ~416 nm for this transition. The previous isosbestic point, noted at ~359 nm still holds. The broad feature at 340 nm develops as the enzyme is reduced.

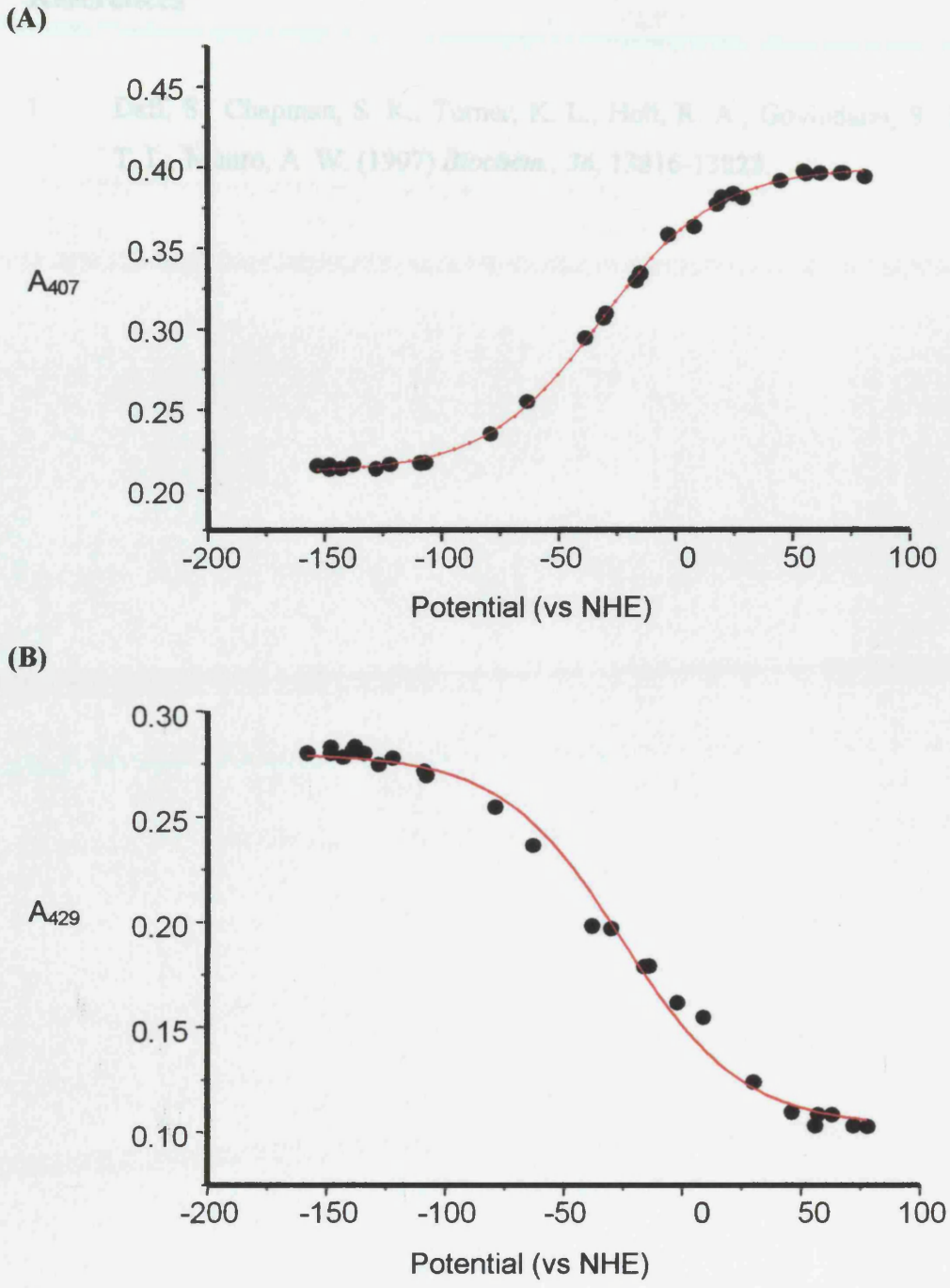

Figure 2 (A) Single electron Nernst plot of data at 407 nm. E^0 value of –31 ± 3 mV for oxidised/reduced transition (RTF = 59 within error). (B) Single electron Nernst plot of data at 429 nm. E^0 value here is –26 ± 4 mV (identical within error to the value obtained from the previous fit).

References

1. Daff, S., Chapman, S. K., Turner, K. L., Holt, R. A., Govindaraj, S., Poulos, T. L., Munro, A. W. (1997) *Biochem., 36*, 13816-13823.

Publication

Redox and Spectroscopic Properties of Human Indoleamine 2,3-Dioxygenase and A His303Ala Variant: Implications for Catalysis†

Nektaria D. Papadopoulou,‡ Martin Mewies,‡ Kirsty J. McLean,§ Harriet E. Seward,§ Dimitri A. Svistunenko,|| Andrew W. Munro,§ and Emma Lloyd Raven*,‡

Departments of Chemistry and Biochemistry, University of Leicester, University Road, Leicester, LE1 7RH, United Kingdom, and Department of Biological Sciences, University of Essex, Wivenhoe Park, Colchester, CO4 3SQ, United Kingdom

Received July 18, 2005; Revised Manuscript Received September 5, 2005

ABSTRACT: Indoleamine 2,3-dioxygenase is an important mammalian target that catalyses the oxidative cleavage of L-tryptophan to *N*-formylkynurenine. In this work, the redox properties of recombinant human indoleamine 2,3-dioxygenase (rhIDO) and its H303A variant have been examined for the first time and the spectroscopic and substrate-binding properties of rhIDO and H303A in the presence and absence of substrate are reported. The Fe^{3+}/Fe^{2+} reduction potential of H303A was found to be -30 ± 4 mV; in the presence of L-Trp, this value increases to $+16 \pm 3$ mV. A variety of spectroscopies indicate that ferric rhIDO at pH 6.6 exists as a mixture of six-coordinate, high-spin, water-bound heme and a low-spin species that contains a second nitrogenous ligand; parallel experiments on H303A are consistent either with His303 as the sixth ligand or with His303 linked to a conformational change that affects this transition. There is an increase in the low-spin component at alkaline pH for rhIDO, but this is not due to hydroxide-bound heme. Substrate binding induces a conformational rearrangement and formation of low-spin, hydroxide-bound heme; analysis of the H303A variant indicates that His303 is not required for this conversion and is not essential for substrate binding. The Fe^{3+}/Fe^{2+} reduction potential of H303A variant is $\approx$70 mV lower than that of rhIDO, leading to a destabilization of the ferrous−oxy complex, which is an obligate intermediate in the catalytic process. In comparison with the properties of other heme enzymes, the data can be used to build a more detailed picture of substrate binding and catalysis in indoleamine 2,3-dioxygenase. The wider implications of these results are discussed in the context of our current understanding of the catalytic mechanism of the enzyme.

The L-kynurenine pathway, which, ultimately, leads to the formation of NAD, is the major catabolic route of L-tryptophan in mammals. The initial, rate-limiting step in this pathway is the oxidative cleavage of L-tryptophan to *N*-formylkynurenine (Scheme 1) and is catalyzed by indoleamine 2,3-dioxygenase (IDO,[1] reviewed in refs *1*−*3*). There is a wealth of evidence linking IDO induction and kynurenine pathway metabolites to various physiological and pathophysiological conditions, including antimicrobial, antiviral, antiparasitic, and antitumor activity, renal allograft rejection, and various neurological disorders (*4*−*8*).

Scheme 1: (A) Reaction Catalyzed by IDO, with IUPAC Numbering Indicated; (B) pH-Dependent Properties of Tryptophan[a]

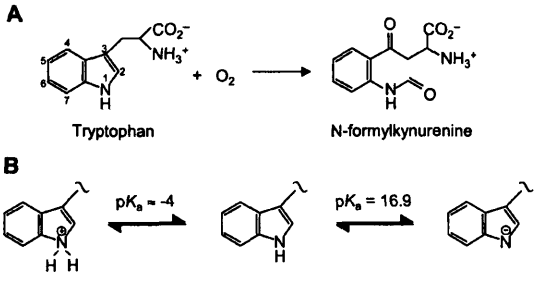

[a] Deprotonation of the NH group of the indole ring occurs with a pK_a of 16.9 (*66*); formation of the doubly protonated species is not favorable [$pK_a \approx -4$ estimated for D-Trp in perchloric acid (*67*)].

IDO is a monomeric, heme-containing enzyme that was first isolated in 1967 (*8*, *9*). It is widely distributed in mammalian tissues. The catalytic mechanism involves reduction of the ferric heme, binding of O_2 to the ferrous heme, and binding of L-Trp, although the precise sequence, O_2 binding followed by L-Trp binding or vice versa, is not known (*10*−*13*). In fact, there is much that we do not understand about this important mammalian target, and there are a number of questions that need urgent attention. There is no crystal structure published; therefore, the nature of the

† This work was supported by The Wellcome Trust (Grant 063688/Z/01/Z to E.L.R.), BBSRC (Studentship to N.P.), University of Essex (Biomedical EPR Facility), and The Royal Society (Leverhulme Trust Senior Research Fellowship to A.W.M.).

* To whom correspondence should be addressed. Telephone: +44-(0)116-228-7047. Fax +44-(0)116-225-3789. E-mail: emma.raven@le.ac.uk.

‡ Department of Chemistry, University of Leicester.

§ Department of Biochemistry, University of Leicester.

|| University of Essex.

[1] Abbreviations: IDO, indoleamine 2,3-dioxygenase; hIDO, human indoleamine 2,3-dioxygenase; rhIDO, recombinant human indoleamine 2,3-dioxygenase; H303A, a site-directed variant of rhIDO in which histidine 303 has been replaced with alanine; EPR, electron paramagnetic resonance; MCD, magnetic circular dichroism; CT, charge transfer; CT_{ls}, low-spin ferric charge-transfer band; CT_1 and CT_2, high-spin ferric charge-transfer bands; SHE, standard hydrogen electrode.

10.1021/bi0513958 CCC: $30.25
Published on Web 10/05/2005

substrate binding and iron−oxygen interactions, the identity of heme active-site residues, and the role of individual residues in catalytic activity and substrate binding are all unknown. In addition, there is no information on the redox properties of the heme for any IDO: this is an important omission because the redox properties of the metal ion are a key determinant in controlling biological function.

To begin to address these deficiencies, we have examined the redox properties (including the influence of substrate on the redox chemistry) and the spectroscopic properties of the substrate-bound and substrate-free IDO. We also present detailed functional data for the H303A variant and an assessment of the likely role of this residue on substrate and dioxygen binding. The results can be used to build a more detailed picture of the possible mechanism of the IDO enzyme, and the collective implications of these results are discussed in terms of our current understanding of the mechanism of IDO catalysis.

EXPERIMENTAL PROCEDURES

Construction of Expression Vector and Bacterial Expression. Construction of the expression vector and expression of rhIDO (*14*, *15*) are described in the Supporting Information.

Mutagenesis. Site-directed mutagenesis was performed using a Quikchange mutagenesis kit (Stratagene) according to the protocol of the manufacturer and confirmed by sequencing the entire IDO-coding region. The PCR product was transformed in Epicurian Coli BL21-Gold (DE3) competent cells (Stratagene) for bacterial expression.

Protein Purification and Handling. The recombinant enzyme is isolated from *Escherichia coli* as the holoenzyme. Cell pellets were resuspended in sonication buffer (50 mM potassium phosphate buffer at pH 8.0 containing 300 mM potassium chloride) containing two EDTA-free Complete tablets (Roche) and stirred with 5 mg of lysozyme for 20 min at room temperature. After 20 min, 5 mg of DNase was added and the suspension was stirred until it became more fluid. The mixture was sonicated on ice using 8 × 30 s bursts from a MSE sonicator. Cell debris was removed by centrifugation (30 min, 20 000 rpm, 8 °C), and the cell-free extract was immediately applied to a 20 mL column of Ni-NTA Superflow resin (Qiagen) previously equilibrated in a sonication buffer. The resin was washed with 100 mL of wash buffer (50 mM potassium phosphate at pH 6.0 containing 300 mM potassium chloride), and the protein was eluted using ~100 mL of elution buffer (sonication buffer containing 100 mM EDTA). The resulting protein was then exchanged into a storing buffer (50 mM Tris-HCl at pH 7.4 and 1 mM EDTA) and frozen in aliquots at −80 °C. This procedure revealed the presence of only two components (see Figure S2A in the Supporting Information), and electrospray mass spectrometry (not shown) showed two peaks at *m/z* 47 170.0 ± 1.8 and 45 643.0 ± 1.7, respectively. The major peak at 47 170.0 corresponds to the calculated mass [*m/z* 47 168.22 (*16*, *17*), Figure S1 in the Supporting Information] of the intact protein including the N-terminal His tag; the minor peak corresponds to the calculated mass [*m/z* 45 637.48 (*16*, *17*)] of a proteolytically cleaved version of the enzyme (clipped at Lys389). MALDI−TOF analyses (not shown) also gave major (*m/z* 47 170 ± 0.24) and minor (*m/z* 45 621 ± 0.23) components; proteolytic digestion followed by further MALDI analyses and database searching [MASCOT (Matrixscience Ltd., London, U.K.)] unambiguously identified both fragments as human IDO. Anion-exchange FPLC (AKTA FPLC, Amersham Pharmacia Biotech) using a Mono Q H/R 5/5 column was used to separate the two components (Figure S2B in the Supporting Information). The buffers used were 20 mM Tris-HCl at pH 8.3 and 20 mM Tris-HCl and 1 M NaCl (buffer B). Purified samples of rhIDO isolated in this way had A_{404}/A_{280} of >2.0.[2] Purification of H303A was as described for rhIDO (A_{408}/A_{280} > 1.2). Samples of rhIDO and H303A were exchanged into a storing buffer (50 mM Tris-HCl at pH 7.4 containing 1 mM EDTA) prior to freezing in aliquots at −80 °C.

Absorption coefficients of ϵ_{404} = 172 mM^{-1} cm^{-1} and ϵ_{408} = 108 mM^{-1} cm^{-1} were determined for ferric rhIDO and H303A, respectively, using the pyridine−hemochromagen procedure (*18*). Ferrous rhIDO was generated by the addition of sodium dithionite. The ferrous−oxy derivative was generated either by passing ferrous rhIDO through a 10 mL column of Sepharose G-25 (Amersham Bioscience) equilibrated with O_2-saturated buffer or by direct bubbling of O_2 gas through a dithionite-reduced sample. For rhIDO, both methods gave identical wavelength maxima for the ferrous−oxy derivative. Other ligand-bound derivatives (azide, cyanide, and fluoride) were obtained by the addition of an excess (typically 2−4 μL) of a concentrated (1 M) solution of ligand to the ferric enzyme (typically 5−25 μM) until no further changes in absorbance were observed.

Steady-State Assays. Samples were assayed for catalytic activity in reactions (25.0 °C) that consisted of 10 μM methylene blue (Sigma), 10 μg of catalase (bovine liver, Sigma), 20 mM L-ascorbate (Sigma), and varying concentrations (0−40 μM) of L-Trp contained in 100 mM potassium phosphate buffer (1 mL total volume) (*19*). The reaction was initiated by the addition of rhIDO (10 μL, ~1 μM). Initial rates were monitored by tracking the increase in the concentration of *N*-formylkynurenine at 321 nm [ϵ_{321} = 3.75 mM^{-1} cm^{-1} (*20*)]. All data were fitted to the Michaelis−Menten equation. pH-dependent data were collected using either 100 mM potassium phosphate as above or glycine−sodium hydroxide buffer.

Electronic Spectroscopy. Electronic absorption spectra (25.0 ± 0.1 °C) were recorded using a Perkin−Elmer Lambda40 UV−vis spectrophotometer. Equilibrium binding constants (μ = 0.05 M) were determined according to published procedures (*21*) using Tris/HCl (pH 8.0−9.5) and phosphate buffers (pH 7.0−8.0). Specifically, this involved preparing samples of protein (≈5−10 μM) and substrate (0.10 M) in the same buffer followed by the addition of small (0.5−2.0 μL) volumes of substrate to the enzyme. Binding constants were determined by monitoring decreases in the absorbance at 406 nm and fitting to eq 1 (*21*)

$$Abs_{406} = (K_D A_i + [\text{L-Trp}]_{tot} A_f)/(K_D + [\text{L-Trp}]_{tot})$$

[2] Numerous control experiments were carried out on pure mixtures of the intact and cleaved components as well as on FPLC-purified samples of intact rhIDO to determine whether the presence of the minor component affected the catalytic, redox, or spectroscopic properties of the enzyme. We were not able to detect measurable differences in any of the experiments reported in this work.

where A_i and A_f are the initial and final absorbancies, respectively, and $[\text{L-Trp}]_{tot}$ is the total concentration of the substrate.

Magnetic Circular Dichroism (MCD) Spectroscopy. MCD spectra were recorded using Jasco J810 and J730 models for the UV−vis and near-IR regions, respectively. An Oxford Instruments SM-1 superconducting solenoid with a 25 mm room-temperature bore was used to generate a 6 T magnetic field. MCD intensities are linear with respect to the magnetic field at room temperature and are plotted normalized to magnetic field as $\Delta\epsilon/H$ (M^{-1} cm^{-1} T^{-1}). Samples were prepared in deuterated sodium phosphate buffer (50 mM) at the appropriate pH (denoted as pH*) or into the same buffer containing 20 mM L-Trp, to a final concentration of ≈350 μM for vis/near-IR regions and ≈50 μM for the Soret region.

Electron Paramagnetic Resonance (EPR) Spectroscopy. X-Band EPR spectra (10 K) were recorded on a Bruker ER-300D series electromagnet and microwave source interfaced to a Bruker EMX control unit and fitted with an ESR-9 liquid Helium flow cryostat from Oxford Instruments and a dual mode microwave cavity from Bruker (ER-4116DM). Quantification of $S = {}^1/_2$ species was carried out by comparison with the spin standard Cu^{II}(EDTA) using the method of Aasa and Vanngard (*22*). Magnetic field magnitude is detected by a Hall probe within the cavity of the instrument. Additionally, the g values of the Cu^{II}EDTA standard (g = 2.32 and 2.075) were used to ensure the correct field values for the detected frequency (observed values identical to those given above). Frequency is monitored within the EMX unit and also with an additional frequency counter attached to the microwave source.

Electrochemistry. Aneorobic ($[O_2]$ < 2 ppm) redox titrations were performed in a Belle Technology glovebox under nitrogen (*23*). Solutions (100 mM potassium phosphate containing 10% glycerol) of rhIDO (≈4 μM, pH 7.0) or H303A (~10 μM, pH 8.0) were titrated electrochemically (*24*) using sodium dithionite as a reductant and potassium ferricyanide as an oxidant. Mediators (2 μM phenazine methosulfate, 5 μM 2-hydroxy-1,4-naphthoquinone, 0.5 μM methyl viologen, and 1 μM benzyl viologen) were used to mediate in the range from +100 to −480 mV (*23*, *25*). Data were fitted to the Nernst equation for a single electron process (*26*). Potentials are quoted against the standard hydrogen electrode (SHE).

RESULTS

Characterization of rhIDO.

UV−Vis Spectroscopy. Wavelength maxima for various ferric and ferrous derivatives of rhIDO are given in Table 1. There are no reported wavelength maxima for human IDO (hIDO); we have therefore compared wavelength maxima with the corresponding maxima for the wild-type rabbit enzyme, for which most of the published data have been obtained. Wavelength maxima are similar in most cases, although there are differences in the cyanide and azide derivatives. The spectrum (Figure 1A) of the ferric form of rhIDO (λ_{max} = 404, 500, 535, and 633 nm) has maxima that are consistent with a mixed population of high- and low-spin heme species. Wavelength maxima of 406 and 630 nm for rhIDO have been previously reported (*15*). This spectrum shows no evidence for formation of ahydroxide-bound heme with increasing pH: there are no substantial changes in peak positions or intensities in the pH range of 5.5−10.7 (data not shown), although there is a drop in the Soret band above

Table 1: Absorption Spectra Maxima for Various Ferric and Ferrous Derivatives of rhIDO[a]

	λ_{max} (nm)		
derivative	rabbit IDO[b]	rhIDO[c]	H303A[d]
ferric	406, 500, 534, 570, 632[e]	404, 500, 535, 633	408, 531, 568
ferric + L-Trp	412, 540, 576[e]	411, 540, 576[f]	411, 531, 568
ferrous	429, 558[e]	425, 527[sh], 558	425, 529, 559
ferrous−oxy	415, 544, 577[g]	412, 539, 576[h]	nd[i]
ferrous−CO	420, 539, 570[j]	419, 539, 565	420, 537, 567
ferric−azide	416.5[j]	414, 535, 572, 634	408, 531, 568
ferric−cyanide	428, 532, 562[j]	419, 540, 570[sh]	417, 533, 563
ferric−fluoride	402, 488, 608[j]	404, 497, 537, 572, 632	407, 531, 568

[a] sh = shoulder. [b] Isolated from rabbit intestine. [c] Spectra were run in sodium phosphate at pH 7.0, μ = 0.10 M, and 25.0 °C, except for footnotes *f* and *g* (see below). [d] Spectra were run in 100 mM potassium phosphate at pH 7.9 and 25.0 °C. [e] Taken from ref *13* (at pH 8.0 and 24 °C). [f] These spectra are pH-dependent and were therefore run in sodium phosphate at pH 8.0, μ = 0.10 M, and 25.0 °C for direct comparison with the published spectra (at pH 8.0). [g] Taken from ref *30* (at 4 °C). [h] Spectrum run in sodium phosphate at pH 8.0, μ = 0.10 M, and 25.0 °C. [i] nd = not detectable. [j] Taken from ref *29* (at pH 6.0 and 25 °C).

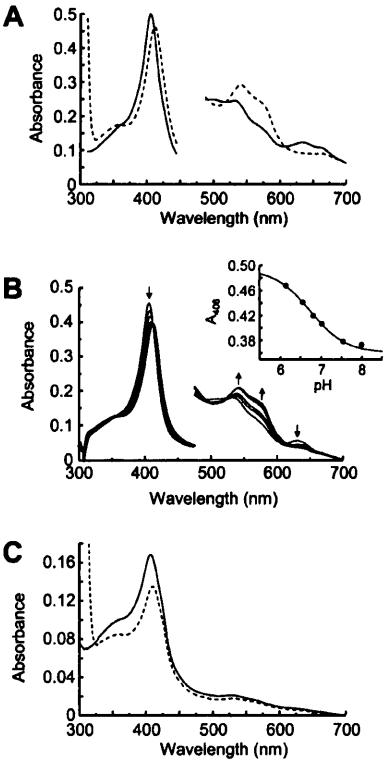

FIGURE 1: (A) UV−vis spectra (pH 8.1 and 25.0 °C) of ferric rhIDO in the absence (—) and presence (- - -) of 20 mM L-Trp. Absorbance values in the visible region have been multiplied by a factor of 5. (B) pH dependence of the UV−vis spectra of rhIDO in the presence of 20 mM L-Trp. (Inset) Fit of the absorbance at 406 nm to a single proton process. Absorbance values in the visible region have been multiplied by a factor of 5. (C) UV−vis spectrum (pH 7.9 and 25.0 °C) of ferric H303A in the absence (—) and presence (- - -) of 20 mM L-Trp.

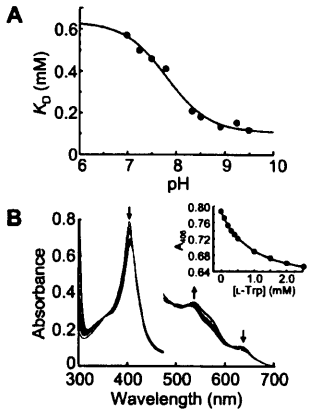

FIGURE 2: (A) Plot of the equilibrium binding constant, K_D, versus pH for binding of L-Trp to rhIDO. Data were fitted to a single proton process. (B) Representative data set for determination of K_D at pH 7.0. The visible region has been multiplied by a factor of 5, and arrows indicate the direction of change in absorbance upon successive additions of L-Trp. (Inset) Fit of data at 406 nm to eq 1 (conditions: 50 mM potassium phosphate at 25.0 °C).

pH ≈8.5. Above pH ≈9 and below pH ≈5, the enzyme was not stable enough to allow meaningful data collection.

Substrate Binding. Binding of L-Trp to ferric rhIDO leads to the formation of a low-spin species (λ_{max} = 411, 540, and 576 nm, Figure 1A). A comparison with other heme proteins [e.g., horseradish peroxidase (pH 12.3), λ_{max} = 414, 543, and 573 nm; horse heart myoglobin (pH 10.9, mixed high spin/low spin), λ_{max} = 411, 485^{sh}, 541, 583, and 593^{sh} nm (*28*)] indicates that the spectrum for rhIDO arises from formation of a low-spin, hydroxide-bound heme. This new substrate-bound species is now pH-dependent (Figure 1B), with low-spin heme dominating at alkaline pH. A pK_a of 6.7 ± 0.1 can be extracted from a plot of the absorbance at 406 nm versus pH (inset of Figure 1B). To quantify the binding interaction, the equilibrium binding constant, K_D, for binding of L-Trp to ferric IDO was measured. At pH 7.0, a value for K_D of 0.57 ± 0.05 mM was determined (not shown). This binding constant varies with pH (Figure 2), indicating that it is sensitive to titration of another group. A fit of these data to a single proton process yields a pK_a of 7.8 ± 0.1.

Steady-State Kinetics. Steady-state oxidation of L-Trp at pH 8.0 gave values for k_{cat} and K_M of 5.2 ± 0.2 s^{-1} and 7.1 ± 1.1 μM, respectively (k_{cat}/K_M = 0.73 μM^{-1} s^{-1}). Steady-state data for rhIDO have been reported (*14*) (but no k_{cat} was reported). There is no reported k_{cat} for hIDO; K_M has been previously reported as ≈20 μM (*19*) and 18 μM (*27*) for hIDO.

MCD Spectroscopy (Ferric rhIDO at Acidic and Alkaline pH). UV−vis and near-IR MCD spectra of rhIDO at pH 6.6 (Figure 3A and 3B, respectively) are characteristic of ferric heme, showing both low- and high-spin features. MCD spectra for rabbit IDO have been published previously (*29*, *30*), but did not include measurements in the near-IR region from which very detailed information can be obtained. For rhIDO, the Soret crossover is at 410 nm and its peak-trough intensity is between the values expected for a purely low-spin (120−160 M^{-1} cm^{-1} T^{-1}) or high-spin (5−25 M^{-1} cm^{-1} T^{-1}) species (*31*). Low-spin bands dominate the visible region, but a negative feature at 641 nm is part of a high-

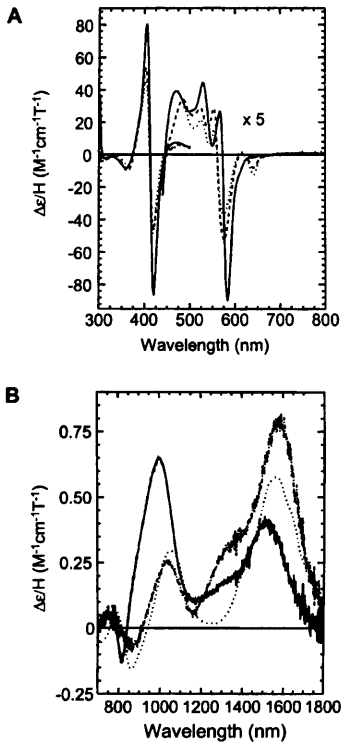

FIGURE 3: Room-temperature MCD at 6 T in the UV−vis (A) and near-IR (B) regions of ferric rhIDO at pH* 6.6 (···, [rhIDO] = 132 μM in both cases), ferric rhIDO at pH* 8.0 (- - -, [rhIDO] = 35 and 169 μM in the Soret and vis/near-IR, respectively), and ferric rhIDO at pH* 8.0 in the presence of 20 mM L-Trp (—, [rhIDO] = 45 and 224 μM, respectively).

spin ligand−metal charge-transfer derivative, CT_2. Spectra in the near-IR region (Figure 3B) are also consistent with a mix of high- and low-spin species. In this case, two CT bands are observed at 1040 and 1570 nm. The 1570 nm band arises from ligand−metal charge transfer from the porphyrin to the ferric d orbitals of low-spin iron (CT_{ls}), and its position is consistent with bisnitrogenous ligation (*32*, *33*). The MCD spectra of high-spin heme species also contain ligand−metal CT bands, CT_1 and CT_2, which shift with changes in the axial ligation (*28*, *34*). The CT_2 band is observed as the negative trough of the derivative in the visible region (see above). The feature at 1040 nm is the positive lobe of the CT_1 derivative, and the negative lobe of this band is obscured by the more intense CT_{ls} band at 1570 nm. This negative lobe obscures in turn with the vibrational sideband of the CT_{ls} feature. Together, the positions of $CT_{1,2}$ are consistent with coordination of a nitrogen ligand and a second, neutral ligand to the heme (e.g., histidine/water). The intensities of the transitions suggest roughly equal populations of high- and low-spin heme at this pH.

At pH 8.0 (Figure 3), there is an increase in intensity in the Soret and visible regions, reflecting an increase in low-spin heme content, and a decrease in the CT_2 band (641 nm), reflecting a decrease in high-spin heme content. In the near-IR region, the 1040 nm feature has decreased to a similar extent (15% of total heme population) and the more intense CT_{ls} feature at 1570 nm now has a vibrational sideband at 1346 nm. There are no major changes in wavelength maxima of the CT bands compared to pH 6.6, which suggests that the two dominant species observed at acidic pH (low-spin

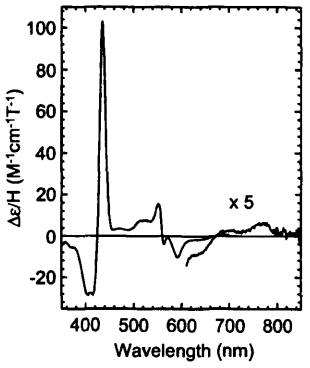

FIGURE 4: Room-temperature MCD spectra at 6 T of ferrous rhIDO (66 μM) at pH* 6.6.

bisnitrogenous and high-spin histidine/water) are unchanged. In contrast to previous work (*35*), there is no evidence at room temperature for the formation of a histidine/hydroxide species at alkaline pH, in agreement with the observation (*vide supra*) that the UV−vis spectrum of rhIDO is pH-independent. Histidine/hydroxide coordination is characteristic of intense $CT_{1,2}$ bands, which are shifted to a lower wavelength compared to histidine/neutral ligand species (*28*, *34*, *36*).

MCD Spectroscopy (Ferric rhIDO + L-Trp). In the presence of L-Trp at pH 8.0, there is a clear increase in intensity throughout the Soret and visible regions, which indicates an increase in low-spin heme. The high-spin CT_2 band at 641 nm (Figure 3A) is diminished in intensity and accounts for only ≈7% of the total heme species. There are shifts in the bands throughout the visible region that indicate formation of a new low-spin species; this is confirmed in the near-IR spectrum, where a new feature at 1000 nm is observed. The shift in peak wavelength from the position of the CT_1 positive lobe, the absence of a corresponding CT_2 band in the visible region, and the clear vibrational sideband in the second CT_{ls} feature suggest that this band is a CT_{ls} feature arising from a new low-spin species rather than from a feature of a high-spin CT_1 band. Its maximum at 1000 nm is similar to that observed for hydroxide-bound myoglobin (1035 nm) (*28*, *37*) and hydroxide-bound horseradish peroxidase at pH 12.3 (1100 nm) (*38*, *39*), both of which have histidine/hydroxide ligation at room temperature. The second CT_{ls} feature at 1515 nm is shifted by ~60 nm from its maximum in the absence of tryptophan but remains in the range expected for histidine/nitrogenous axial ligation, and there are no changes in the corresponding EPR species (g_z = 2.94, *vide infra*) upon binding of L-Trp, which suggests no major changes in the ligation or ligand conformation in this species. The intensity of this band accounts for ≈30% of the heme population.

MCD Spectroscopy (Ferrous rhIDO). The spectrum of ferrous rhIDO (Figure 4) contains an asymmetric Soret feature with a positive peak at 436 nm, positive features at 524, 552, and ~770 nm, and negative features at 532 and 592 nm. The spectrum is similar to ferrous myoglobin (*40*, *41*) and ferrous horseradish peroxidase (*42*), both of which contain five-coordinate, high-spin heme. We therefore assign ferrous rhIDO as containing a five-coordinate high-spin heme as the single species, with histidine as the fifth (proximal) ligand. There is no evidence for low-spin heme, which

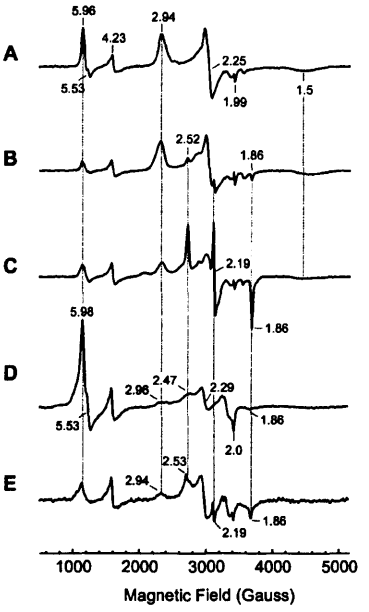

FIGURE 5: Perpendicular mode X-band EPR spectra of ferric rhIDO at pH 6.6 (A), ferric rhIDO at pH 8.0 (B), ferric rhIDO in the presence of 20 mM L-Trp at pH 8.0 (C), ferric H303A at pH 7.5 (D), and ferric H303A in the presence of 20 mM L-Trp at pH 7.5 (E). Conditions: microwave frequency, 9.67 GHz; microwave power, 2 mW; modulation amplitude, 10 G; temperature, 10.8 K; scan speeds and time constants are the same for all spectra. Spectra have been adjusted for differences in the enzyme concentration and receiver gain where required. Gains were typically of the order of 2×10^5−8×10^5.

suggests that any internal (nitrogenous) ligands present in the ferric form are no longer coordinated.

EPR Spectroscopy. EPR spectra for human IDO have not been published, although rabbit IDO has been examined (*29*). The EPR spectrum of rhIDO at pH 6.6 (Figure 5A) contains high- and low-spin species with g values of g = 5.96, 5.53, and 1.99 and g = 2.94, 2.25, and 1.50, respectively.[3] Rhombic g values of 2.94, 2.25, and 1.50 are associated with bishistidine ligation, in which the histidine planes are near parallel (*33*, *43*, *44*). The high-spin signals are slightly rhombic with splitting on the g_{xy} feature at g = 5.7.

At pH 8.0 (Figure 5B), the high-spin signals are diminished with respect to the low-spin species, with the latter accounting for ≈80% of the heme population at 10.8 K. Minor but sharp features at g = 2.52 and 1.86 (middle g value obscured) represent a low-spin species whose g values are consistent with those seen in histidine/hydroxide coordination: because there is no evidence of histidine/hydroxide coordination in the MCD spectra at room temperature (as discussed above, Figure 3), this probably reflects a freezing-induced artifact. There are numerous examples in the heme literature (particularly the peroxidase literature, see for example ref *45*) of water/histidine-coordinated heme producing a fraction of low-spin heme species at cryogenic temperatures for which there is no evidence at room temperature. The factors that influence this are not known.

[3] A minor feature (g = 4.23) is commonly observed for heme proteins and represents high-spin adventitious iron. The splitting on the $g \approx 6$ feature is unusual for six-coordinate (His/H_2O) ligation and may be due to small amounts of buffer-derived phosphate binding to the heme under cryogenic conditions.

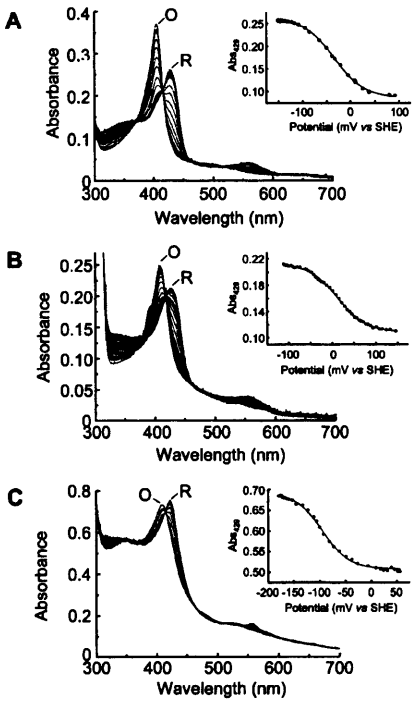

FIGURE 6: (A) Selected absorption spectra obtained during redox titration of rhIDO at pH 7.0. The fully oxidized (O) and fully reduced (R) spectra are indicated. The inset shows a plot of the absorbance at 429 nm against the potential. The solid line is a fit of the data to the Nernst equation for a single electron process. Essentially identical results were obtained by fitting the data at 410 nm. (B) Similar set of absorption spectra collected during redox titration of the substrate-bound form of rhIDO at pH 7.0. The inset shows a plot of absorbance data at 429 nm against the potential, with the corresponding Nernst fit. Fits of the data at 410 nm produced a virtually identical midpoint potential. (C) Redox titration of H303A at pH 8.0, with a fit of the data at 429 nm to the Nernst equation shown in the inset.

Upon addition of L-Trp at pH 8.0, sharp rhombic signals (g = 2.52, 2.19, and 1.86) are observed (Figure 5C) that arise from low-spin heme and are associated with histidine/hydroxide coordination. Minor signals from high-spin heme (g = 5.96) and the other low-spin species (g_z = 2.94) are also present in this spectrum.

Redox Potentiometry. Selected spectra obtained during anaerobic redox titration of rhIDO are shown in Figure 6A. The redox process was clearly reversible, with no sign of hysteresis in the oxidative or reductive directions; spectra collected in the oxidative and reductive stages were near identical at equivalent potentials. Clean isosbestic points were observed, indicating only two absorbing species. Control experiments confirmed that the observed reduction potential was not altered in the presence of the minor (cleaved) component. Upon reduction of rhIDO, there is a decrease in intensity of the Soret band and a shift to a longer wavelength, consistent with the formation of ferrous heme (Table 1). Data were fitted to a single electron process (Nernst equation) at either 407 nm (not shown) or 429 nm (inset of Figure 6A); these analyses at different wavelengths gave results that were within error of one another. The reduction potential (average value from data at 407 and 429 nm) was −30 ± 4 mV.

In the presence of 15 mM L-Trp (Figure 6B), similar absorbance changes were observed. In this case, the reduction potential was 16 ± 3 mV (inset of Figure 6B), an increase of 46 mV over the value for the substrate-free enzyme.

Characterization of the H303A Variant. On the basis of sequence comparisons with IDO-like myoglobins (*46*), IDO is proposed to contain both proximal [assigned as His346 (*14*)] and distal histidine residues. In the absence of crystallographic information, the highly conserved His303 residue is believed to be located near the heme distal pocket.

Electronic and EPR Spectroscopy. The UV−vis spectrum of ferric H303A[4] (λ_{max} = 408, 531, 568 nm, Figure 1C and Table 1) shows that the Soret band has red-shifted compared to rhIDO but is still characteristic of high-spin heme. This spectrum is pH-independent, as observed for rhIDO. The spectrum of ferrous H303A is essentially identical to that of rhIDO (Table 1). Cyanide binds to H303A, as evidenced by the change in the electronic spectrum and its similarity to that of rhIDO. There is a decrease in intensity of the Soret band upon addition of azide to H303A but no corresponding changes in the visible region that indicate formation of the expected low-spin heme. Upon binding of L-Trp at pH 8.0 (Figure 1C), the Soret band shifts to a value (λ_{max} = 411 nm) that is characteristic of low-spin heme formation and that is similar to that observed for rhIDO, but in the visible region, there is no measurable change as observed for rhIDO. EPR analyses indicate that the ferric derivative (Figure 5D) has a much higher proportion of high-spin heme (g = 5.98, 5.53, and 2.00) than for rhIDO. Significantly, the low-spin signals arising from the low-spin, bisnitrogenous species (g = 2.96, 2.29, and 1.50) are very considerably diminished (the very weak signal that does remain probably arises from coordination of another strong field ligand). The low-spin signals (g = 2.47, 2.19, and 1.86) associated with hydroxide ligation in rhIDO are broader for H303A, which suggests the presence of a range of conformers. Addition of L-Trp (Figure 5E) leads to an increase in low-spin heme at g = 2.53, 2.19, and 1.86: these sharp signals are consistent with a hydroxide-bound heme species that is in a defined conformation, rather than a range as observed above. An MCD spectrum of H303A could not be obtained because the sample was unstable during repeated exchange into D_2O.

Steady-State Kinetics. The H303A variant was observed to be capable of steady-state oxidation of L-Trp at pH 8.0 under conditions identical to those used for rhIDO, with values for k_{cat} and K_M of 2.7 ± 0.1 s^{-1} and 15 ± 1.0 μM, respectively (k_{cat}/K_M = 0.18 μM^{-1} s^{-1}). This is in agreement with previous steady-state analyses on the H303A variant (*14*).

Redox Potentiometry. Selected spectra obtained during redox titration of H303A are shown in Figure 6C. Data obtained at 423 nm (to monitor formation of ferrous heme) were fitted to a single electron process (Nernst equation) and gave a reduction potential of −99 ± 2 mV, representing a destabilization of the ferrous heme of almost 70 mV compared to rhIDO.

Formation of Ferrous−Oxy Derivative. To check whether this decrease in reduction potential was functionally significant, we tested whether destabilization of the ferrous derivative may affect stability of the catalytic ferrous−oxy

[4] The H303A variant has been prepared previously (*14*), but no detailed spectroscopic or redox analyses were presented.

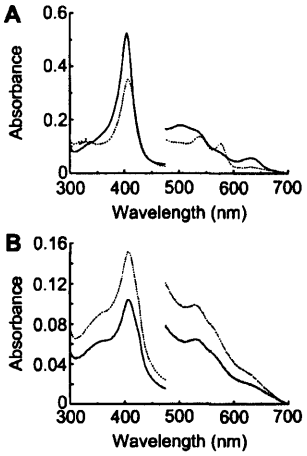

FIGURE 7: UV–vis spectra (100 mM potassium phosphate at pH 7.9 and 25.0 °C) of the ferric (—) and ferrous–oxy (···) derivatives of rhIDO (A) and H303A (B). Absorbance values in the visible region have been multiplied by a factor of 5.

intermediate. Under conditions that resulted in clean formation of the ferrous–oxy complex for rhIDO (see the Experimental Procedures), formation of the ferrous–oxy complex for H303A was not observed. Hence, for rhIDO, a species with wavelength maxima of 412, 539, and 576 nm (Figure 7 and Table 1) was obtained: these maxima are in the range expected for ferrous–oxy heme [e.g., 418, 543, and 581 nm for sperm whale myoglobin (*18*)]. The identical experiment with H303A gave no characteristic oxy peaks in the visible region and no shift in the Soret maximum (Figure 7). In separate rapid-scanning stopped-flow experiments (not shown), no further evidence for transient formation of a ferrous–oxy complex was obtained. Attempts to increase the yield of the ferrous–oxy derivative by addition of imidazole (to 10 mM),[5] which has been shown to recover hydrogen-bonding interactions with bound ligands (*47*), were unsuccessful.

DISCUSSION

Development of our understanding of the detailed mechanism of the IDO enzyme has been hampered by the limited quantities of pure enzyme that can be extracted and purified from readily available sources. For the human enzyme, there is very little functional or spectroscopic information available (*14*, *35*, *46*, *48*, *49*). In this work, we have developed an efficient bacterial expression system for production of hIDO and have used this to examine the redox, spectroscopic, and substrate-binding properties of the enzyme. In this section, the major findings are discussed in the context of our current understanding of the nature of the heme environment, the mechanism of substrate binding, and the redox properties of the IDO enzyme.

Heme Coordination Environment. A summary of the various species present in solution for ferric rhIDO at different pHs and in the presence and absence of the substrate is given in Table 2. Overall, the electronic, MCD, and EPR spectra at acidic pH are clearly consistent with the presence of two distinct species in solution: a high- and low-spin heme

Table 2: Distribution of Heme Species in Ferric rhIDO at Different pH Values in the Presence and Absence of Substrate, as Determined from MCD[a] and EPR Analyses[a]

proximal/ distal ligand	−Trp (%)		+Trp (%)
	pH 6.6	pH 8.0	pH 8.0
His/H_2O (HS)	50	35	7
His/X (LS)	50	65	33
His/OH^- (LS)	nd	nd	60

[a] HS = high-spin heme; LS = low-spin heme; nd = not detected. The percentages stated are derived from MCD intensities, and errors on percentages are estimated as ±5%. Spectra are quantified with the reference to well-characterized model systems [e.g., myoglobin and its complexes and other low-spin compounds (*65*)]. As a guide, a typical high-spin intensity for 100% population of histidine-bound heme is 1 M^{-1} cm^{-1} T^{-1} (peak–trough intensity) and for 100% population of low-spin histidine-ligated heme is between 0.8 and 1.2 M^{-1} cm^{-1} T^{-1} (peak maximum).

species in approximately equal population. The high-spin species is confirmed by MCD as arising from histidine/water ligation. Similar conclusions were reached using resonance Raman spectroscopy (*35*), and His346 has been assigned as the (proximal) ligand in this case (*14*). The low-spin species, which has been observed previously (*29*, *35*), is assigned by MCD as being consistent with bisnitrogenous ligation. Hydroxide ligation, as previously proposed (*35*), is ruled out by the MCD analyses. The identity of the sixth ligand has been a matter of ongoing speculation in the literature (reviewed in ref *1*). EPR data for the H303A variant are useful in this context and are consistent with two possible interpretations: either that His303 is the sixth nitrogenous ligand in this low-spin species or that His303 is located in a region of the protein that is (indirectly) involved in controlling a larger conformational change within the protein structure that leads to formation of this low-spin derivative. It is not known, at this stage, whether the high- and low-spin components are in equilibrium with one another and, if so, on what time scale this occurs. If they are in equilibrium, then a conformational rearrangement of the protein structure would presumably be necessary for the two forms to interconvert (and the fact that significant changes in iron coordination geometry occur upon binding of the substrate indicate that conformational changes of this kind are realistic).[6]

The electronic spectrum of ferric rhIDO is pH-independent, indicating that the distal water molecule does not titrate within the experimentally accessible pH range (pH 5.5–10.7 in our experiments). This is in contrast to the related tryptophan 2,3-dioxygenase enzyme (which catalyses the same reaction as IDO), in which the electronic spectrum is pH-dependent (*52*). The electronic spectra are consistent with the MCD data, which clearly indicate that there is essentially no hydroxide-bound heme at either pH 6.6 or 8.0. There is an increase in low-spin heme at pH 8.0, but this is due to an increase in the bishistidine species and not to the formation of hydroxide-bound heme. An increase in the low-spin component at alkaline pH has also been observed by resonance Raman and assigned as hydroxide-bound heme (*35*). Our data show that this assignment is incorrect, which

[5] Imidazole was not observed to bind to ferric H303A under these conditions (as evidenced by UV–vis spectroscopy).

[6] This is not the only example of a heme protein with mixed coordination geometry. Other examples include leghemoglobin (*50*) and cytochrome *c* at alkaline pH (*51*).

would explain the reported (*35*) failure to detect any ν_{Fe-OH^-} stretching frequency at alkaline pH.

Substrate Binding. MCD and EPR spectra confirm that the predominant species present in the substrate-bound form of rhIDO is hydroxide-bound heme. This is consistent with resonance Raman spectra for the substrate-bound derivative of human IDO (*35*) and previous MCD/EPR spectra for rabbit IDO (*29*). In contrast to the ferric enzyme (*vide supra*), the spectrum of this substrate-bound species is now pH-dependent and a pK_a of 6.7 was derived (Figure 1B). The spectroscopic changes reflect titration of an ionisable residue that affects binding of L-Trp, which explains the appearance of high-spin signals at acidic pH (weaker binding at acidic pH). The pH dependence of the binding interaction can also be determined separately by measuring the change in K_D with pH (Figure 2; pK_a = 7.8). The two pK_a values are in reasonable agreement and are assumed, but not unambiguously confirmed to report, on the same process. This is discussed in more detail below.

A comparison of the pH-dependent properties of substrate-free and substrate-bound rhIDO provides new information that is particularly informative in terms of our understanding of the substrate-binding process. The fact that the spectrum of ferric rhIDO shows no evidence for formation of a hydroxide-bound heme is an unexpected observation in view of the fact that several other heme proteins with known histidine/water coordination, including the closely related tryptophan 2,3-dioxygenase enzyme, have titratable distal water molecules [e.g., myoglobin (*18*), leghemoglobin (*53*), and cytochrome *c* peroxidase (*54*, *55*)]. A conveniently positioned hydrogen-bond acceptor, usually but not exclusively the distal histidine residue, is the normal way in which deprotonation of the bound water is facilitated. Why, then, does the distal water molecule in ferric rhIDO not titrate in a similar manner? The most reasonable explanation is that, in the absence of the substrate, there is no suitable hydrogen-bond acceptor able to stabilize hydroxide formation.[7] (We note that Terentis et al. (*35*) have proposed a direct hydrogen bond between the distal histidine and the distal water molecule in ferric IDO, but this is only consistent with the pH-independent spectrum of the ferric form if the pK_a of the bound water is unaffected by the hydrogen bond or if it is lowered to such an extent as to still be outside the accessible pH range.) The fact that pH-dependent behavior is observed in the tryptophan-bound form presumably means that substrate binding induces a conformational change within the overall protein structure that favors deprotonation, such that a suitable (pH-dependent) hydrogen-bond acceptor is now accessible. One possible scenario that accounts for our observed data is depicted in Scheme 2. Here, the binding of the substrate leads to a hydrogen-bonding interaction between an unspecified active-site acid/base group, the bound substrate, and the distal water molecule. In the absence of the substrate (Scheme 2, left), no such hydrogen-bonding interaction occurs. This would be consistent with the pH-dependent spectrum of the substrate-bound enzyme and the pH dependence of L-Trp binding, because L-Trp can now act as a proton donor/acceptor, shuttling a proton between the distal water molecule and the acid/base group. The pH dependencies observed in this work would therefore be assigned as arising from the titration of one of the residues indicated in Scheme 2, but we cannot unambiguously assign these pK_a values at this stage.[8]

Scheme 2: Proposed Mechanism for Substrate Binding and Hydrogen-Bond Formation in IDO[a]

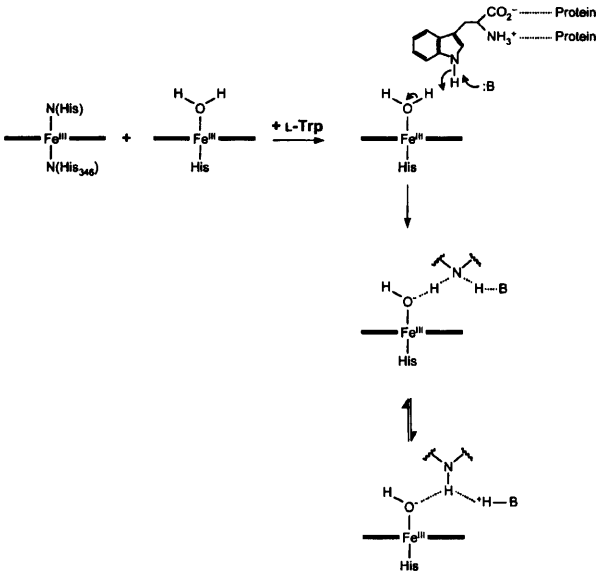

[a] Ferric rhIDO is represented as a mixture of high-spin (water-bound) and low-spin (proposed as histidine-bound) species. Deprotonation of the distal water molecule is induced on substrate binding by favorable hydrogen-bond interactions between the substrate and an active-site acid/base group (the latter only being accessible in the presence of the substrate). Unspecified hydrogen-bonding interactions between the carboxylate and amine groups of the side chain of L-Trp and the protein are also envisaged. Note that the chemistry of the indole ring does not *require* an active-site base to be present for catalysis, because electrophilic addition to the indole ring is possible in the absence of a base.

The fact that H303A is catalytically competent for L-Trp turnover suggests that substrate binding is not critically dependent upon the presence of this residue. This is in agreement with the EPR data for the H303A variant because H303A is observed by EPR to form a low-spin, hydroxide-bound heme upon addition of the substrate. These results clearly indicate that deprotonation of the distal water molecule can occur in H303A and are interpreted as indicating either that His303 does not act as the acid/base acceptor in the wild-type protein or that an alternative proton-transfer mechanism is available in this variant.

Redox Properties and Dioxygen Binding. Table 3 collates the redox data obtained in this work. The reduction potential of IDO has not been previously reported. The magnitude of the observed potential for rhIDO (−30 ± 4 mV) is useful in

[7] This would, necessarily, also have to include the sixth ligand to the heme in the low-spin form which, although it ligates to the heme, must also be unable to induce deprotonation of the bound water molecule in the absence of the substrate. As we have mentioned above, it is likely that conformational changes in the protein structure are involved, such that mobile residues may move in and out of the active-site pocket.

[8] Clearly, the pK_a values of the groups involved need to be in a similar range for proton shuttling to occur. We note that the relevant pK_a values of free L-Trp are out of the physiological range (Scheme 1) but that shifts in the pK_a values could occur upon binding to the enzyme. Formally, however, Scheme 2 does not require complete deprotonation or protonation of L-Trp: we envisage a "concerted" process.

Table 3: Summary of Fe^{3+}/Fe^{2+} Reduction Potentials Obtained in This Paper (Refer to Figure 6)

enzyme	−Trp (mV)	+Trp (mV)
rhIDO	-30 ± 4^a	16 ± 3^a
H303A	-99 ± 2^b	nd[c]

[a] pH 7.0. [b] pH 8.0. [c] nd = not determined.

a functional context. It is lower than those observed in the myoglobins ($E° \approx +50$ mV (reviewed in ref *56*), in which stabilization of the ferrous−oxy complex is required, but is higher than those observed in the heme peroxidases [$E°$ typically in the range from −100 to −250 mV (*57*−*63*)], in which charge separation of the O−O peroxide bond and stabilization of the high-valent ferryl intermediate is required. In the peroxidases, there is a strong hydrogen bond between the proximal histidine and an aspartic acid group: this stabilizes the ferryl intermediate and drives the potential down. Charge separation is not necessary in the globins: in this case, there is no strong hydrogen bond and a higher reduction potential, favoring ferrous heme, is observed. Using resonance Raman techniques, Terentis et al. (*35*) have suggested a strong hydrogen-bonding partner to the proximal ligand in IDO, analogous to the proximal Asp residue in the heme peroxidases, although in this case, the identity of the hydrogen-bonding partner is not known [Asp274 has been suggested, however (*14*)]. On the basis of comparisons with the reported reduction potentials for the peroxidases, the potential for rhIDO is substantially higher than would be expected if a strong hydrogen bond from His346 really does exist.

Upon binding of the substrate, there is a 46 mV increase in reduction potential for rhIDO, reflecting additional stabilization of the ferrous derivative. This increase has not been reported previously and is analogous to but less than the corresponding increase in reduction potential (~130−140 mV) observed in both cytochrome $P450_{cam}$ (*64*) and P450 BM3 (*26*) upon binding of substrates (camphor and fatty acids, respectively). For P450, this large increase in reduction potential acts as a switch, to turn on electron transfer to the ferric heme. For IDO, it is not clear at this stage whether heme reduction precedes substrate binding or vice versa, but a thermodynamic stabilization of the reduced form would clearly favor catalytic reduction prior to substrate binding. We note, however, that the potentials of substrate-free and substrate-bound forms of IDO are more positive than their P450 counterparts (potentials typically in the range from −350 to −400 mV for substrate-free P450s and from −200 to −250 mV for the substrate-bound forms); perhaps, with its higher potential, IDO does not need to depend upon a substrate-induced mechanism for stabilization of catalytically active ferrous heme.

For the H303A variant, there is considerable (≈70 mV) destabilization of the reduced form compared to the wild-type protein. This brings the potential for this variant into the range expected for a heme peroxidase (in which the ferrous form is considerably destabilized). The functional implication of this decrease in potential is clear: the catalytic ferrous−oxy derivative is now too unstable to be detected under conditions that allow its detection in the wild-type protein. A binding orientation for dioxygen in which His303 influences the hydrogen-bonding structure of the bound ligand would be consistent with this observation.

Clearly, there are many questions that remain to be answered, but these data help to build a more informed picture of the detailed mechanism of IDO catalysis and provide a useful and testable framework for further structure/function studies on this important mammalian target.

ACKNOWLEDGMENT

We thank Dr. Sohan Gupta (Hipple Cancer Research Center) for the gift of the IDO cDNA and Professor Andrew Thomson and Dr. Myles Cheesman (University of East Anglia) for the use of EPR/MCD facilities. We are grateful to Dr. Christof Lenz (Applied Biosystems) for MALDI−TOF analyses, Mr. Kuldip Singh for technical assistance, and Dr. Bernard Rawlings (University of Leicester) and Professor Chris Cooper (University of Essex) for insightful discussions.

SUPPORTING INFORMATION AVAILABLE

The construction of the expression vector, mutagenesis/bacterial expression of recombinant IDO, and protein purification; nucleotide sequence of human IDO (Figure S1); (A) SDS−PAGE gel of a sample of rhIDO prior to FPLC analysis, showing molecular weight markers (left), (B) SDS−PAGE gel of a purified sample of rhIDO after FPLC (Figure S2). This information is available free of charge via the Internet at http://pubs.acs.org.

REFERENCES

1. Sono, M., Roach, M. P., Coulter, E. D., and Dawson, J. H. (1996) Heme-containing oxygenases, *Chem. Rev. 96*, 2841−2887.
2. Hayaishi, O, T. O., and Yoshida, R. (1990) Indoleamine 2,3-dioxygenase: Properties and functions of a superoxide utilizing enzyme, *Prog. Inorg. Chem. 38*, 75−94.
3. Thomas, S. R., and Stocker, R. (1999) Redox reactions related to indoleamine 2,3-dioxygenase and tryptophan metabolism along the kynurenine pathway, *Redox Rep. 4*, 199−220.
4. Kerr, S. J., Armati, P. J., Pemberton, L. A., Smythe, G., Tattam, B., and Brew, B. J. (1997) Kynurenine pathway inhibition reduces neurotoxicity of HIV-1-infected macrophages, *Neurology 49*, 1671−1681.
5. Grohmann, U., Fallarino, F., and Pucceti, P. (2003) *Trends Immunol. 24*, 242−248.
6. Aquilina, J. A., Carver, J. A., and Truscott, R. J. W. (1997) *Exp. Eye Res. 64*, 727−735.
7. Munn, D. H., Zhou, M., Attwood, J. T., Bondarev, I., Conway, S. J., Marshall, B., Brown, C., and Mellor, A. L. (1998) Prevention of allogeneic fetal rejection by tryprophan catabolism, *Science 281*, 1191−1193.
8. Yamamoto, S., and Hayaishi, O. (1967) Tryptophan pyrrolase of rabbit intestine, *J. Biol. Chem. 242*, 5260−5266.
9. Higuchi, K., and Hayaishi, O. (1967) Enzymic formation of D-kynurenine from D-tryptophan, *Arch. Biochem. Biophys. 120*, 397−403.
10. Taniguchi, T., Sono, M., Hirata, F., Hayaishi, O., Tamura, M., Hayashi, K., Iizuka, T., and Ishimura, Y. (1979) Indolemine 2,3-dioxygenase−Kinetic studies on the binding of superoxide anion and molecular oxygen to enzyme, *J. Biol. Chem. 254*, 3288−3294.
11. Sono, M. (1990) Spectroscopic and equilibrium studies of ligand and organic substrate binding to indoleamine 2,3-dioxygenase, *Biochemistry 29*, 1451−1460.
12. Sono, M. (1986) Spectroscopic and equilibrium properties of the indoleamine 2,3-dioxygenase tryptophan O-2 ternary complex and of analogous enzyme derivatives−Tryptophan binding to ferrous enzyme adducts with dioxygen, nitric oxide, and carbon monoxide, *Biochemistry 25*, 6089−6097.

13. Sono, M., Tanigushi, T., Watanabe, Y., and Hayaishi, O. (1980) Inoleamine 2,3-dioxygenase—Equilibrium studies of the tryptophan binding to the ferric, ferrous, and CO-bound enzymes, *J. Biol. Chem. 255*, 1339−1345.
14. Littlejohn, T. K., Takikawa O., Truscott, R. J. W., and Walker, M. J. (2003) Asp[274] and His[346] are essential for heme binding and catalytic function of human indoleamine 2,3-dioxygenase, *J. Biol. Chem. 278*, 29525−29531.
15. Littlejohn, T. K., Takikawa O., Skylas, D., Jamie, J. F., Walker, M. J., and Truscott, R. J. W. (2000) Expression and purification of recombinant human indoleamine 2,3-dioxygenase, *Protein Expression Purif. 19*, 22−29.
16. http://ca.expasy.org/tools/peptide-mass.html.
17. Dai, W., and Gupta, S. L. (1990) Molecular cloning, sequencing, and expression of human interferon-γ-inducible indoleamine 2,3-dioxygenase cDNA, *Biochem. Biophys. Res. Commun. 168*, 1−8.
18. Antonini, M., and Brunori, E. (1971) *Hemoglobin and Myoglobin and Their Reactions with Ligands*, North-Holland Publishers, Amsterdam, The Netherlands.
19. Takikawa, O., Kuroiwa, T., Yamazaki, F., and Kido, R. (1988) Mechanism of interferon-γ action, *J. Biol.* Chem. *263*, 2041−2048.
20. Shimizu, T., Nomiyama, S., Hirata, F., and Hayaishi, O. (1978) Indoleamine 2,3-dioxygenase—Purification and some properties, *J. Biol. Chem. 253*, 4700−4706.
21. Patel, N., Jones, D. K., and Raven, E. L. (2000) Investigation of the haem−nicotinate interaction in leghaemoglobin: Role of hydrogen bonding, *Eur. J. Biochem. 267*, 2581−2587.
22. Aasa, R., and Vanngard, T. (1975) *J. Magn. Reson. 19*, 308−315.
23. Munro A. W., Noble, M. A., Robledo, L., Daff, S. N., and Chapman, S. K. (2001) Determination of the redox properties of human NADPH−cytochrome P450 reductase, *Biochemistry 40*, 1956−1963.
24. Dutton, P. L. (1978) Redox potentiometry: Determination of midpoint potentials of oxidation−reduction components of biological electron-transfer systems, *Methods Enzymol. 54*, 411−435.
25. Ost, T. W. B., Miles, C. S., Munro, A. W., Murdoch, J., Reid, G. A., and Chapman, S. K. (2001) Phenylalanine 393 exerts thermodynamic control over the heme of flavocytochrome P450 μ_B3, *Biochemistry 40*, 13421−13429.
26. Daff, S., Chapman, S. K., Turner, K. L., Holt, R. A., Govindaraj, S., Poulos, T. L., and Munro, A. W. (1997) Redox control of the catalytic cycle of flavocytochrome P450 μ_B3, *Biochemistry 36*, 13816−13823.
27. Southan M. D., Truscott, R. J. W., Jamie J. F., Pelosi L., Walker M. J., Maeda H., Iwamoto Y., and Tone S. (1996) Structural requirements of the competitive binding site of recombinant human indoleamine 2,3-dioxygenase, *Med. Chem. Res.* 343−352.
28. Seward, H. E. (1999) Magneto-optical spectroscopy of heme proteins, Ph.D. Thesis, University of East Anglia, Norwich, U.K.
29. Sono, M., and Dawson, J. H. (1984) Extensive studies of the heme coordination structure of indoleamine 2,3-dioxygenase and of tryptophan binding with magnetic and natural circular dichroism and electron paramagnetic resonance spectroscopy, *Biochim. Biophys. Acta 789*, 170−187.
30. Uchida, K., Shimizu, T., Makino, R., Sakaguchi, K., Iizuka, T., Ishimura, Y., Nozawa, T., and Hatano, M. (1983) Magnetic and natural circular dichroism of L-tryptophan 2,3-tryptophan dioxygenases and indoleamine 2,3-dioxygenase, *J. Biol. Chem. 258*, 2526−2533.
31. Cheesman, M. R., Greenwood, C., and Thomson, A. J. (1991) *Adv. Inorg. Chem. 36*, 201−255.
32. McKnight, J., Cheesman, M. R., Thomson, A. J., Miles, J. S., and Munro, A. W. (1993) Identification of charge-transfer transitions in the optical spectrum of low-spin ferric cytochrome P450 *Bacillus megaterium*, *Eur. J. Biochem. 213*, 683−687.
33. Gadsby, P. M. A., and Thomson, A. J. (1990) *J. Am. Chem. Soc. 112*, 5003.
34. Watmough, N. J., Cheesman, M. R., Butler, C. S., Little, R. H., Greenwood, C., and Thomson, A. J. (1998) The dinuclear center of cytochrome bo_3 from *Escherichia coli*, *J. Bioenerg. Biomembr. 30*, 55−62.
35. Terentis, A. C., Thomas, S. R., Takikawa, O., Littlejohn, T. K., Truscott, R. J. W., Armstrong, R. S., Yeh, S., and Stocker, R. (2002) The heme environment of recombinant human indoleamine 2,3-dioxygenase—Structural properties and substrate-ligand interactions, *J. Biol. Chem. 277*, 15788−15794.
36. Patel, N., Seward, H. E., Svensson, A., Gurman, S. J., Thomson, A. J., and Raven, E. L. (2003) *Arch. Biochem. Biophys. 418*, 197−204.
37. Eglinton, D. G., Gadsby, P. M. A., Sievers, G., Peterson, J., and Thomson, A. J. (1983) A comparative study of the low-temperature magnetic circular dichroism spectra of horse heart metmyoglobin and bovine liver catalase derivatives, *Biochim. Biophys. Acta 742*, 648−658.
38. Foote, N., Gadsby, P. M. A., Berry, M. J., Greenwood, C., and Thomson, A. J. (1987) *Biochem. J. 246*, 659−668.
39. Kobayashi, N., Nozawa, T., and Hatano, M. (1977) Magnetic circular dichroism studies on acid and alkaline forms of horseradish peroxidase, *Biochim. Biophys. Acta 493*, 340−351.
40. Bolard, J., and Garnier, A. (1972) *Biochim. Biophys. Acta 263*, 535−549.
41. Springall, J., Stillman, M. J., and Thomson, A. J. (1976) *Biochim. Biophys. Acta 453*, 494−501.
42. Nozawa, T., Kobayashi, N., and Hatano, M. (1976) *Biochim. Biophys. Acta 427*, 652−662.
43. Palmer, G. (1985) The electron paramagnetic resonance of metalloproteins, *Biochem. Soc. Trans. 13*, 548−560.
44. More, C., Belle, V., Asso, M., Fournel, A., Roger, G., Guigliarelli, B., and Bertrand, P. (1999) EPR spectroscopy: A powerful technique for the structural and functional investigation of metalloproteins, *Biospectroscopy 5*, S3−S18.
45. Yonetani, T., and Anni, H. (1987) Yeast cytochrome *c* peroxidase. Coordination and spin states of heme prosthetic group, *J. Biol. Chem. 262*, 9547−9554.
46. Suzuki, T., Kawamichi, H., and Imai, K. (1998) A myoglobin evolved from indoleamine 2,3-dioxygenase, a tryptophan-degrading enzyme, *Comp. Biochem. Physiol., Part B: Biochem. Mol. Biol. 121*, 117−128.
47. Newmyer, S. L., and Ortiz de Montellano, P. R. (1996) Rescue of the catalytic activity of an H42A mutant of horseradish peroxidase by exogenous imidazoles, *J. Biol. Chem. 271*, 14891−14896.
48. Yamazaki, F., Kuroiwa, T., Takikawa, O., and Kido, R. (1985) Human indoleamine 2,3-dioxygenase, *Biochem. J. 230*, 635−638.
49. Aitken, J. B., Thomas, S. E., Stocker, R., Thomas, S. R., Takikawa, O., Armstrong, R. S., and Lay, P. A. (2004) Determination of the nature of the heme environment in nitrosyl indoleamine 2,3-dioxygenase using mutiple-scattering analyses of X-ray absorption fime structure, *Biochemistry 43*, 4892−4898.
50. Jones, D. K., Patel, N. P., Cheesman, M. R., Thomson, A. J., and Raven, E. L. (2002) Leghaemoglobin: A model for the investigation of haem protein axial ligation, *Inorg. Chim. Acta 331*, 303−309.
51. Rosell, F. I., Ferrer, J. C., and Mauk, A. G. (1998) Proton-linked protein conformation swithcing: Definition of the alkaline conformation transition of yeast iso-1-ferricytochrome *c*, *J. Am. Chem. Soc. 120*, 11234−11245.
52. Makino, R., Sakaguchi, K., Iizuka, T., and Ishimura, Y. (1980) Acid−alkaline transition and thermal spin equilibirum of the heme in ferric L-tryptophan 2,3-dioxygenase, *J. Biol. Chem. 255*, 11883−11891.
53. Jones, D. K., Badii, R., Rosell, F. I., and Lloyd, E. (1998) Bacterial expression and spectroscopic characterization of soybean leghaemoglobin *a*, *Biochem. J. 330*, 983−988.
54. Foshay, M. C., Vitello, L. B., and Erman, J. E. (2004) pH dependence of heme iron coordination, hydrogen peroxide reactivity, and cyanide binding in cytochrome *c* peroxidase (H52K), *Biochemistry 43*, 5065−5072.
55. Turano, P., Ferrer, J. C., Cheesman, M. R., Thomson, A. J., Banci, L., Bertini, I., and Mauk, A. G. (1995) pH, electrolyte, and substrate-linked variations in active site structure of the Trp51Ala variant of cytochrome *c* peroxidase, *Biochemistry 34*, 13895−13905.
56. Raven, E. L., and Mauk, A. G. (2001) Chemical reactivity of the active site of myoglobin, *Adv. Inorg. Chem. 51*, 1−49.
57. Conroy, C. W., Tyma, P., Daum, P. H., and Erman, J. E. (1978) Oxidation−reduction potential measurements of cytochrome *c* peroxidase and pH dependent spectral transitions in the ferrous enzyme, *Biochim. Biophys. Acta 537*, 62−69.
58. Goodin, D. B., and McRee, D. E. (1993) The Asp−His−Fe triad of cytochrome *c* peroxidase controls the reduction potential, electronic structure, and coupling of the tryptophan free radical to the heme, *Biochemistry 32*, 3313−3324.
59. Harbury, H. A. (1957) Oxidation−reduction potentials of horseradish peroxidase, *J. Biol. Chem. 225*, 1009−1024.

60. Millis, C. D., Cai, D., Stankovich, M. T., and Tien, M. (1989) Oxidation−reduction potentials and ionization states of extracellular peroxidases from the lignin-degrading fungus *Phanerochaete crysoporium*, *Biochemistry 28*, 8484−8489.
61. Jones, D. K., Dalton, D. A., Rosell, F. I., and Raven, E. L. (1998) Class I heme peroxidases: Characterisation of soybean ascorbate peroxidase, *Arch. Biochem. Biophys. 360*, 173−178.
62. Tanaka, M., Ishimori, K., and Morishima, I. (1998) Structural roles of the highly conserved Glu residue in the heme distal site of peroxidases, *Biochemistry 37*, 2629−2638.
63. Yamada, H., Makino, R., and Yamazaki, I. (1975) Effrects of 2,4-substituents of deuteroheme upon redox potentials of horseradish peroxidases, *Arch. Biochem. Biophys. 169*, 344−353.
64. Sligar, S. G. (1976) Coupling of spin, substrate, and redox equilibria in cytochrome P450, *Biochemistry 15*, 5399−5406.
65. Cheesman, M. R., Watmough, N. J., Gennis, R. B., Greenwood, C., and Thomson, A. J. (1994) Magnetic-circular-dichroism studies of *Escherichia coli* cytochrome *bo*. Identification of high-spin ferric, low-spin ferric, and ferryl (Fe^{IV}) forms of heme *o*, *Eur. J. Biochem. 219*, 595−602.
66. Yagil, G. (1967) The proton dissociation constant of pyrrole, indole, and related compounds, *Tetrahedron 23*, 2855−2861.
67. Andonovski, B. S. (1999) UV study of the protonation of indole-2-carboxylic acid, 3-methylindole, 3-acetylindole, and D-tryptophan in perchloric acid solutions, *Croat. Chem. Acta 72*, 711−726.

BI0513958